Self-Healing Corrosion Protective Sol-Gel Coatings

door

Mina ABDOLAH ZADEH

Master of Science in Materials Science and Engineering,
Sahand University of Technology (SUT), Tabriz, Iran.
Geboren te Macoo, Iran

This dissertation has been approved by the:

Promotor: Prof.dr.ir. S. Van der Zwaag
Copromotor: Dr. S.J. Garcia Espallargas

Composition of the doctoral committee:

Rector Magnificus,	voorzitter
Prof.dr.ir.S. van der Zwaag,	Technische Universiteit Delft, promotor
Dr. S.J. Garcia Espallargas,	Technische Universiteit Delft, copromotor

Independent members:

Prof.dr. S.J. Picken,	Technische Universiteit Delft
Prof.dr. R.A.T.M. van Benthem	Technische Universiteit Eindhoven
Prof.dr. M. Olivier,	Université de Mons, Belgium
Prof.dr. Mikhail Zheludkevich,	Helmholtz-Zentrum Geesthacht, Germany
Prof.dr.ir. H. Terryn,	Vrije Universiteit Brussel, Technische Universiteit Delft

Agentschap NL
Ministerie van Economische Zaken

تقدیم به

همسر مهربان و خانواده عزیزم

Contents

Chapter 1

Introduction

Introduction

Synthetic coatings are of great scientific and technological importance and depending on the intended demand have to fulfil different functionalities [1, 2]. Corrosion is one of the main processes leading to material destruction and economic losses estimated at about 3% of the world's GNP [3]. Although corrosion processes are unavoidable, the cost related to premature product degradation and failure can be significantly reduced using appropriate protection methods such as protective coatings. Protective coatings minimize/control corrosion of the underlying substrate based on one or a combination of three main mechanisms: (i) barrier protection where the coating prevents/reduces ingress of corrosive agents to the metal/coating interface, (ii) cathodic protection where the coating acts as a sacrificial anode and (iii) active protection as a result of inclusion of inhibitors, imparting anodic or/and cathodic protection to the coating [4, 5].

Various coating technologies ranging from solvent and waterborne liquid paints, cataphoretic paints and powder coatings have been around for a relatively long time. Apart from these well-established technologies, lately, sol-gel coatings have attracted considerable interest due to their attractive features such as low processing temperature, high chemical versatility, ease of application, strong bonding to a wide range of metallic substrates and an environmentally friendly mode of deposition. Originally used for the production of glass like structures such as particles, the sol-gel process is now a well-established approach for preparation of organic-inorganic hybrid (OIH) films and coatings with a broad application spectrum [6, 7].

Generally, the sol-gel process can be described as the evolution of an oxide network by continuous condensation reactions of molecular precursors in a liquid medium via hydrolytic or non-hydrolytic procedures. The non-hydrolytic approaches are based on the formation of a colloidal suspension followed by its gelation through condensation of precursor molecules via alkyl halide elimination, ether elimination, ester elimination, etc., depending on the precursor and solvent molecules. The more common hydrolytic approaches are mainly based on hydrolysis and condensation reactions of metal or metalloid alkoxides ($M(OR)_n$), in which M and R represent a network-forming element and an alkyl/allyl group, respectively. While the range of precursor molecules is extremely wide, silicone alkoxides are the most studied ones due to their stability and moderate reaction rates facilitating controlled hydrolysis and condensation reactions [8, 9].

Hydrolysis and condensation are equilibrium reactions and can proceed simultaneously once the hydrolysis reaction is initiated. The structure and properties of the final film or

coating depend on the sequence of these steps which themselves are strongly affected by the precursor molecules and reaction conditions e.g. pH, molar ratios of reactants, solvent, temperature, etc. Prepared sol-gel systems can be applied on metallic substrates using different techniques including dip-coating, spin-coating, spray-coating and electrodeposition followed by a drying/curing step [8, 9].

The potential application of sol-gel coatings as corrosion protective coatings was first reviewed by Guglielmi in 1997 [10]. Since then, numerous papers have been published revealing promising results regarding improvement of organic coatings adhesion to substrate and protection of various metallic substrates against corrosion.

Ideally, the coatings would prevent corrosion of the underlying substrate during its entire intended service life. Yet, despite the substantial advances in coating performance, even the best protective coatings can fail to fulfil their functionalities due to damages resulting from (local or global) mechanical and chemical attacks as well as thermal cycles [2, 11]. Implementation of self-healing approaches into the protective coatings can guarantee longer service life and reduced maintenance cost by autonomous or non-autonomous healing of local damages at different scales. However, self-healing in corrosion protective coatings is slightly different from that of the bulk/structural polymers or decorative coatings. In the latter cases, healing is referred to as restoration of mechanical or aesthetic properties by providing enough material to repair/fill in the defect volume. While in corrosion protection, recovery of the lost protective function is considered to be the most crucial form of healing. Therefore incorporation of discrete active/healing agents such as corrosion inhibitors and binders into the coating system enabling surface protection of the damage as well as introduction of reversible chemistries empowering damage closure and sealing can be considered as extrinsic and intrinsic healing approaches in corrosion protective coatings, respectively. The extrinsic and intrinsic self-healing coatings can be further subcategorized into several groups considering their architecture, healing mechanism, and healable damage size-scale [1, 2, 12-14]. As depicted in Figure 1.1, depending on the chosen strategy the healing process (i.e. leakage of the active agents to the damage site or flow of the coating network) can be activated using different stimuli.

Passive protection

Sol-gel coatings, in particular silane based ones, have been successfully applied as corrosion protective pre-treatments (thickness < 1 μm) and coatings (thickness > 5 μm) on a range of metallic substrates such as aluminium alloys, steel, copper, magnesium, titanium, galvanized and stainless steel and tin. However, efficient corrosion protection
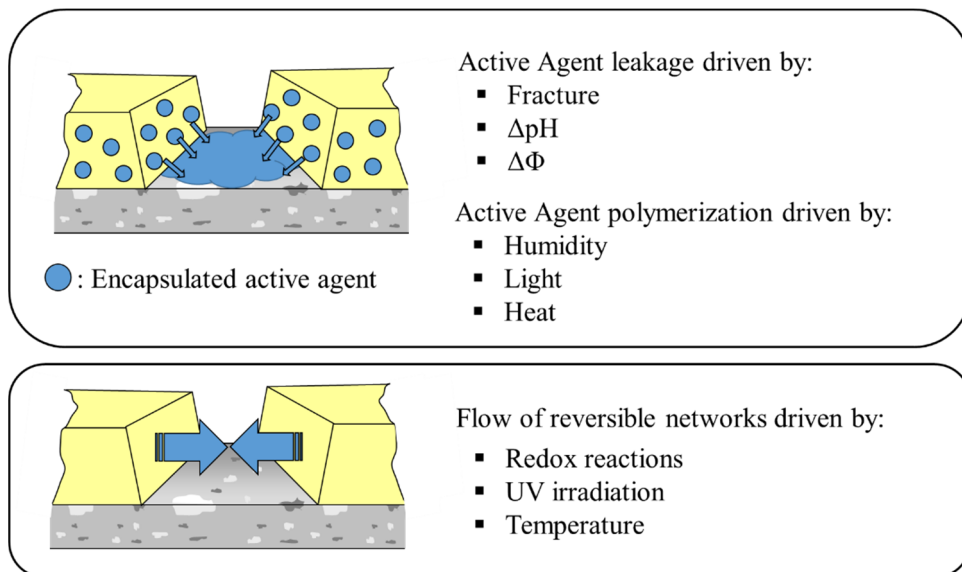
Figure 1.1. Schematic representation of extrinsic (top figure) and intrinsic (bottom figure) healing approaches in corrosion protective coatings.

can only be achieved by (i) proper surface preparation of the substrate leading to the formation of a high density of covalent bonds between the sol-gel coating and the metal surface and (ii) a fine balance between the application conditions and the employed ingredients [15]. The final properties of sol-gel coatings depend on the starting materials and the processing conditions e.g. pH and temperature [8]. Introduction of organic groups into inorganic sol-gel networks can facilitate preparation of thick and crack-free hybrid coatings, eliminating the drawbacks associated with the conventional inorganic sol-gel coatings [6].

In spite of high corrosion protection potential, silanes are electrochemically inactive, unless they carry electrochemically active functional groups. As a consequence, silane based OIH sol-gel coatings do not provide active protection. The protection they offer is generally based on passive protection through formation of a well adherent barrier layer. Depending on the nature of the precursor molecules the OIH coatings can be hydrophobic. Hydrophobic OIH coatings can reduce the kinetics of the corrosion processes by delaying penetration of water and other electrolytes towards the metal/coating interface. However, a prolonged exposure of the OIH coatings to water/electrolyte will eventually result in moisture penetration to the metal/coating

interface. Considering the reversible nature of hydrolysis and condensation reactions involved in the creation of the coating, water penetration can promote hydrolysis of the bonds formed during condensation reaction. Unless the condensation reactions are promoted via a drying step, water/moisture ingress can result in coating failure/delamination [6, 16]. Modification of formulation parameters can nonetheless lead to an improvement of general passive protective properties. The effect of different parameters such as nature of organic components, ratio of organic/inorganic components, etc will be analysed in the following sections.

Critical formulation parameters

Organic-inorganic components

The OIH sol-gel coatings can be prepared over a wide compositional range. Based on the type of the organic component to be added to the inorganic network and the interactions between organic and inorganic counterparts, the sol-gel derived OIH materials can be classified into five groups.

As Figure 1.2 shows, the OIH sol-gel coatings can be prepared by addition of either organic oligomers/polymers (Types I & II) or monomers (Type III) to inorganic sols. In the absence of the covalent bonds, the organic and inorganic counterparts of the OIHs are connected to each other through physical bonds (Types (I) and (III)). Despite the presence of weak dispersion forces and Van der Waals interactions between organic and inorganic components of such OIHs, the physical bonds are not stable enough for long-term applications involving weathering. Formation of strong covalent bonds between organic and inorganic components can significantly improve corrosion protective properties of the OIH coatings. This can be achieved by end-capping of oligomers/polymers with functional groups capable of reacting with the inorganic network (Type II) or by application of organically modified metal/metalloid alkoxides with general formula of $R'_x\text{-}M(OR)_{n-x}$ as starting material (Types IV and V). R' can be either a non-functional group such as methyl, ethyl, etc (Type V) or a functional group such as epoxy, vinyl, methacrylic, isocyanate, mercaptane, furan, etc (Type IV), which can undergo further polymerization. The OIH sol-gel coatings containing functional groups outperform pure sol-gel or polymeric coatings due to higher crosslink density and better mechanical properties, respectively [7, 17, 18].
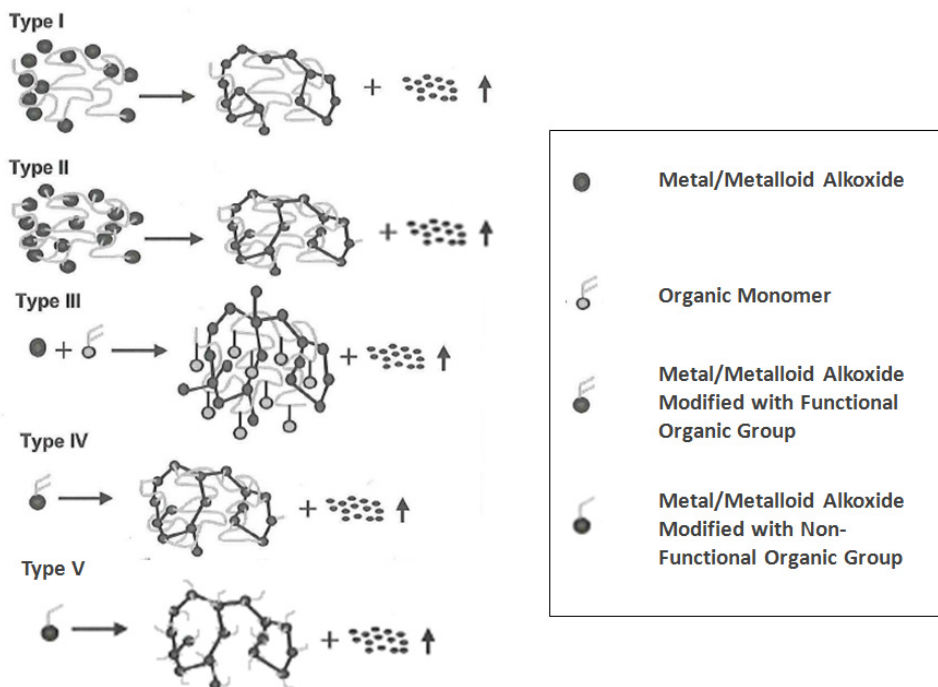
Figure 1.2. Different classes of OIH materials [18].

Different functional groups impart different corrosion protective properties to OIH coatings. Moreover, the corrosion protective properties of the OIH coatings dramatically depend on the presence, the type and the number of the reactive groups of the adopted crosslinking agent [18]. Not only the nature of organic components but also their content in the hybrid sol-gels plays a significant role in the final properties of the hybrid system. An increase in the organic content of the hybrid coatings leads to formation of less porous and thicker films appropriate for barrier protection of metals. However, a high concentration of organic component can lower the adhesion and the mechanical properties of the final coating. In other words, although hybrid coatings potentially do exhibit higher corrosion resistance than their inorganic or organic counterparts, there is an optimum ratio for inorganic-organic components to deliver maximum corrosion resistance. The optimum organic/inorganic ratio (OOIR) varies depending on the precursors employed and on the coating application technique. The coating application method not only affects the OOIR but also the maximum achievable thickness of the hybrid sol-gel coatings [6, 18-20].

Curing temperature

Drying/curing of the sol-gel coatings is an important stage in sol-gel process which dramatically affects the coating final properties. Measurement of linear shrinkage and weight loss of sol-gel derived materials as a function of temperature provides valuable information on the effect of the curing treatment. A plot of these parameters versus temperature yields a curve with three distinct regions (Figure 1.3) for high temperature curing of sol-gels. Region (I) in the curve (T < 200 °C) is associated with a sharp decrease in material weight due to solvent evaporation/desorption. Region (II) shows a linear shrinkage and weight loss at intermediate temperatures (200-500 °C) which can be attributed to further condensation reactions and decomposition of organic components, respectively. Finally, region (III) shows the collapse of pores formed as a result of solvent evaporation and loss of organic compounds leading to fast shrinkage. Therefore, an increase of the curing temperature up to 500-700 °C can result in a lower corrosion resistance sol-gel coating unless the heating rate is small enough to avoid cracks formation [6, 17].
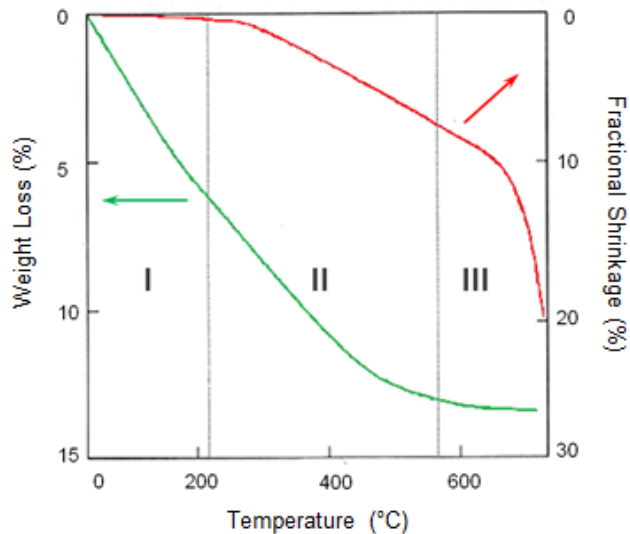
Figure 1.3. Stages of curing process [18].

Sol-gel coatings can also be cured at/or near room temperature. Low temperature drying is normally employed for curing of hybrid sol-gel coatings entrapping organic compounds. Although compact crack-free films can be obtained, room temperature cured sol-gel coatings exhibit higher water sensitivity compared to those cured at higher temperatures. Higher cure temperatures (up to 200 °C) promoting condensation reactions and formation of dense OIH coating improve the barrier properties [6, 17, 18]. Aging of the prepared sol prior to application of the OIH on the metallic substrate has reported to also strongly affect the corrosion protection properties of the resulting coatings. Aging of the sol can promote the condensation reactions of the precursors, increasing the viscosity of the sol which can eventually lead to formation of thick coating with a high defect density [18, 21].

Micro/nano particles

Incorporation of ceramic particles such as silica, ceria, zirconia, alumina, titania, zeolite, Na-Montmorillonite and hydrotalcite as mechanical reinforcement was among the first proposed approaches for modification of OIH sol-gel coatings. The improved mechanical properties, increased thickness and lower crack sensitivity achieved by addition of controlled amount of the particles resulted in enhanced corrosion protection of the underlying substrate. However, the particle size and surface modification proved to be critical, as agglomeration of the embedded particles promoted by gelation process could lead to coating rupture and deterioration of the coating barrier properties [18].

Moreover, the critical pigment volume concentration (CPVC) beyond which coating physical/mechanical properties start to degrade, must always be taken into account. Yet, even for concentrations below the CPVC, a strong interaction between particle and matrix interfaces is required [12, 18, 20]. Furthermore, the sol-gel process can be beneficially employed for particle surface modification with desired functional groups in order to enhance/impart the necessary chemical/physical interactions between the particles and the coating matrix for good particulate composite formulations. In addition, micro/nano particles not only can be added but also can be formed in-situ in the OIH coatings, eliminating some of the challenges associated with CPVC and the strong interfacial forces between matrix and particles [18, 22].

Active corrosion protection

Extrinsic self-healing OIH sol-gel coatings

Despite the effective barrier protection of metallic substrates by OIH sol-gel coatings, these systems are prone to failure as water ingress is just a matter of time. Incorporation of active species such as binding agents and corrosion inhibitors which add active protection mechanisms to the system can improve the protective properties of the OIH sol-gel coatings. The controlled leakage of the active species to the damaged sites passivates/seals the underlying substrate from the surrounding corrosive media through chemical or physical interactions forming thin and dense layers on the substrate. The OIH sol-gel coatings containing discrete active species can be classified as extrinsic self-healing coatings [2, 12-14, 18, 23, 24].

The (organically modified) metal/metal oxides (i.e. the precursors of the OIHs) can be employed in the preparation of robust micro-/nanocontainer such as polyurea/silica microcapsules [25], mesoporous silica [26], zirconia [27] and titania nanoparticles [28] entrapping active species. Moreover, they can be utilized as humidity [29] and photo sensitive [30] binding agents. The use of encapsulated binding agents based on OMSAs has already been explored in corrosive protective organic coatings and it is only a matter of time that the concept is also implemented in the OIH sol-gel coatings.

In contrast, the implementation of corrosion inhibitors in OIH sol-gel coatings has been studied extensively. Corrosion inhibitors can either be added (i) directly to the coating formulation, or (ii) immobilized in carriers to reduce the possible interactions with the matrix and control release of the inhibitor. Despite the pros and cons associated with either of the approaches, the second approach is the one that is leading to major developments.

Direct addition of inhibitor

The most common way of inclusion of corrosion inhibitors into sol-gel systems is mixing them with the coating formulation. The most important factor to be taken into account in such systems is the solubility of inhibitor in the corrosive media. While a low solubility of inhibitor can lead to a weak self-healing effect due to the low concentration of active agents at damaged site, a high solubility will limit prolonged healing effect as a result of rapid leach out of the active agents from coating. In addition, a high solubility of the inhibitor can lead to coating degradation by blistering and delamination processes due to an increased osmotic pressure which promotes water ingress into coating/substrate interface. Despite the potential drawback of this class of extrinsic self-healing sol-gel

9

coatings, they have been extensively studied for protection of different metallic substrates due to ease of preparation. The corrosion inhibitors used can be divided according to their nature into (i) inorganic and (ii) organic inhibitors [12, 14, 18].

i) Inorganic inhibitors

Active ions with well-known corrosion inhibition ability have attracted considerable interest as replacement for toxic Cr(VI) based inhibitors. Inclusion of rare earth metal (REM) and transition metal inhibitors such as Ce, La and Zr in the OIH coatings led to the improved electrochemical performance of such OIH coatings compared to the unloaded ones [31-33]. Yet, upon prolonged immersion to aggressive electrolyte, neither La-loaded nor Zr-loaded coatings could mitigate corrosion activity as effectively as the Ce-doped OIH coatings [18]. Incorporation of the active Ce ions not only facilitates preparation of dense and defect free OIH coatings, but also empowers active protection mechanism via selective leaching of Ce ions to the damage site (fully/partially) restoring the coating's protective properties. However, the final properties of the Ce loaded coatings are strongly affected by the nature/type of the precursor molecules employed for synthesis of the OIH sol-gel coatings, the salt used as the source of the Ce ions, the amount of Ce ions to be added into a sol-gel system and their valence number [18].

ii) Organic Inhibitors

Organic inhibitors which are usually designated as film forming agents, mitigate corrosion by adsorption on the metal surface and formation of hydrophobic layers. Organic inhibitors prevent corrosion by either increasing the anodic or cathodic polarization resistance of the corrosion cell or retarding diffusion of corrosive agents to the metallic surface. However, their inhibition efficiency depends on the chemical composition, molecular structure, and affinity for the metal surface.

Organic inhibitors such as phosphonic acid, 2-mercaptobenzothiazole (MBT), 2-mercaptobenzimidazole (MBI), benzotriazole (BTA), etc. have been successfully incorporated into sol-gel systems to improve their corrosion protection properties by inducing active protection. In several cases, release of organic molecular species from the OIH sol-gel matrix is based on a pH-triggered release mechanism. One of the advantageous features of pH- triggered desorption processes is that they can provide an intelligent release of corrosion inhibitors only at damaged areas which generally experience local pH changes originating from localized corrosion processes [18, 34].

Indirect addition of inhibitor

Although incorporation of corrosion inhibitors into sol-gel coatings is a promising route in the development of active corrosion protective OIH coatings, there are inevitable drawbacks associated with direct mixing of active agents into coating formulation. Firstly, it is quite difficult to control leach-out of entrapped inhibitors especially when they are poorly soluble within the coating matrix. Secondly, inhibitors can chemically interact with the coating matrix losing their own activity and lowering the barrier properties of the matrix. These drawbacks have motivated researchers to think of new ways of inhibitor introduction, enabling isolation of active agents from coating components. This can be achieved either by encapsulation of active species or complexing them with other chemicals.

i) Cyclodextrin-inhibitor complexes

A quite simple approach for inhibitor entrapment/immobilization is based on the complexation of organic molecules with β-cyclodextrin. Cyclodextrins are cyclic oligosaccharides that possess a unique molecular cup-shaped structure with a hydrophilic exterior and a hydrophobic interior cavity. They are capable of forming complexes with various organic guest molecules which fit within their cavities. Organic aromatic and heterocyclic compounds are normally the main candidates for the inclusion complexation reaction. 2-mercaptobenzothiazole (MBT) and 2-mercaptobenzimidazole (MBI) were successfully loaded in β-cyclodextrin. Although the complexation process delayed immediate response to corrosion, a lower inhibitor release rate resulted in pro-longed self-healing potential of the OIH coatings loaded with such complexes rather than the inhibitors alone [18, 35].

ii) Micro-nanocontainers

Ceramic particles such as silica, alumina, etc. are generally electrochemically inactive and therefore incapable of imparting self-healing properties to the OIH coatings. However, they can be employed as micro-/nano-containers to immobilize corrosion inhibitors. The selected inhibitors can be entrapped on the carriers through controlled hydrolysis of the relevant precursors in the inhibitor containing aqueous solutions. The inhibiting ions can also be immobilized on the surface of commercially available particles via immersion of the so-called particles in an inhibitor-containing solution. Activation of the nanoparticles with inhibitive species not only can bestow active corrosion properties to the OIH coatings but also can prevent particle agglomeration by stabilization of the particle surface charge. As in the case of cyclodextrin complexes, incorporation of the

inhibitor loaded particles in OIH coatings was more efficient than direct inhibitor loading in imparting long term self-healing function [18].

Cationic and anionic active species can also be entrapped within the layers or the structural cages of the ion-exchangeable particles via cation/anion exchange process. The release process of the entrapped inhibitors in such containers is stimulated by corrosion activities involving pH changes and presence of ionic species (M^{n+}, H^+, Cl^-, OH). Selective leaching of the inhibitive ions to the damage site and entrapment of aggressive Cl^- ions can reinforce the protective oxide layer, guaranteeing the long term protection for the metallic substrate [18]. In an effort to make environmentally friendly coatings which outperform those based on carcinogenic Cr(VI) additions, combinations of corrosion inhibitors have been explored following the promising results exhibited by hybrid organic-inorganic inhibitors [36].

Mesoporous silica nanoparticles with a high inhibitor loading capacity resulting from their high surface area and large pore volume have been loaded successfully with different organic inhibitors. The OIH coatings containing inhibitor loaded mesoporous nanoparticle outperformed both the un-doped coatings and those directly loaded with the same corrosion inhibitor. The pH-triggered release mechanism is based on the electrostatic repulsion between silica nanoparticles and inhibitor molecules, i.e. at pH values different from neutral, both the silica particles and the inhibitor molecules gain the same charge (positive at pH < 6 and negative at pH > 6). To boost the release of the inhibitors in acidic and alkaline media, the mesoporous silica nanoparticles can be modified using α-cyclodextrin (α-CD)/aniline supramolecular complex and cucurbit[n]uril (CB[n])/bisammonium supramolecular complex, respectively. The employed supramolecular nanovalves (i.e. α-CD/aniline and (CB[n])/bisammonium) can effectively tune the release of the entrapped inhibitor depending on the pH, inducing self-diagnosis and self-healing characteristics to the OIH sol-gel coatings. Although not applied in protective coatings yet, different silica/polymer nanotubes with a high aspect ratio and inhibitor loading capacity, capable of regulating the release process with various triggering agents such as pH, temperature and redox reaction have been developed, opening new possibilities in feedback-active self-healing coatings.

Despite the improved active protection of metallic substrates achieved by inclusion of inhibitor loaded carriers, the architectural aspects of the OIH coatings affecting the position of the embedded carriers with respect to the substrate should be taken into account. While increasing the distance between the carriers and metal surface can lead

to better barrier properties, it can delay the active corrosion protection as a result of increased diffusive path of the entrapped inhibitors [18].

In an effort to increase the inhibitor loading capacity of the OIH coatings, a porous TiO_x layer was deposited on the metallic substrate through controlled hydrolysis of tetra isopropyl orthotitanate. Using a template-based synthesis procedure, titania nanoparticles were self-assembled on AA2024-T3 substrate, forming a cellular network capable of loading large quantities of n-benzotriazole. The inhibitor loaded porous layer was subsequently coated with the OIH sol-gel coating. Electrochemical characterization of prepared samples using EIS revealed a well-defined multiple self-healing ability resulting in an effective long-term active corrosion protection of the underlying substrate [18].

iii) Entrapment of inhibitors in nano-containers in a LBL configuration

Application of *Layer-by-Layer (LbL) assembled shells* on the surface of micro/nanocontainers has led to the development of containers with regulated storage/release of the inhibitor. The LbL method is based on the adsorption of oppositely charged layers on the surface of a template material. Entrapment of corrosion inhibitors in polyelectrolyte multi-layer systems via LbL method has several advantages. It can isolate the inhibitor avoiding its negative effect on the integrity of the coating. Additionally, such a system can provide an intelligent release of the corrosion inhibitor as permeability of the polyelectrolyte assemblies is regulated by changes in pH and humidity. The change of pH is the most preferable stimulus to initiate the release of corrosion inhibitors. Upon restoration of neutral pH values, the polyelectrolyte shell will close, ceasing the inhibitor release/leakage [14].

Negatively charged ٣:O$_2$ particles were coated with successive layers of poly(ethyleneimine) (١٢٤١) / poly(styrene sulfonate) (PSS)/BTA/PSS/BTA, yielding an inhibitor content of about 95 mg per gram of SiO_2 nanoparticles. The limited loading capacity of the nanoparticles can be overcome via the application of porous structures and nanocontainers with higher aspect ratio such as halloysite nanotubes. Halloysites are two-layered aluminosilicate nanotubes with nominal internal diameter, and length of 15, and 300-800 nm, respectively. In analogy to the silica nanoparticles, the LBL self-assembly method was adopted for the development of multi-layer polyelectrolyte nano-shells on the surface of halloysite nanotubes and smart end-caps regulating the inhibitor release process [18].

LBL self-assembly of polyelectrolytes not only can regulate the inhibitor release events, but also can empower loading of different inhibitors in a single container. 2-

mercaptobenzothiazole (MBT) and Ce(III), were loaded in LDHs via anion-exchange and LBL procedures, respectively. Although deposition of successive polyelectrolyte layers altered the inhibitor release mechanism, the OIH coatings loaded with the two inhibitor containing LDH nanoparticles exhibited an improved barrier and active protection [18, 37].

Intrinsic self-healing sol-gel coatings

Intrinsic self-healing coatings not requiring the addition of discrete healing agents but relying on a suitable generic modification of the polymer architecture to achieve complete healing even in the case of multiple damage events at specific locations, are ultimately the most promising type of self-healing coating even if they need some controlled supply of an external stimulus. Intrinsic self-healing approaches are based on local temporary mobility leading to damage closure upon flow of the polymeric matrix (coating). Most of the intrinsic healing approaches developed to date are based on reversible physical and/or chemical bonds.

Deformation recovery in networks

In analogy to polymer coatings, OIH sol-gel coatings exhibit visco-elasto-plastic behaviour. Therefore, any deformation in OIHs consists of viscous response, plastic flow, and elastic deformation. The time-independent component of the response affiliated with the stored energy can be employed for partial deformation recovery, referred to as elastic recovery. The plastic and the time-dependent viscous component of the deformation can also contribute to healing via the so-called shape memory effect although the extent of damage and healing will be affected by the network crosslinking density [11, 18].

The energy applied a slightly crosslinked coating during surface deformation is generally lost in the process of viscous flow, unless residual stresses due to viscoelastic (or viscoplastic) deformation are present. Therefore, restoration of the coating topology via flattening/levelling of the scratch profile is generally achieved by temperature assisted healing processes. In case of a highly crosslinked coating, as most of the OIH coatings, any surface damage is also formed as a result of material transport from the indented area to the sides. Yet, in contrary to the former case, depending on whether the yield strength of the coating is exceeded, all or part of the applied energy will be stored in the polymer network in the vicinity of the scratch (elastic and/or plastic response). Upon removal of the external mechanical stress, the stored elastic energy will be relieved, and the scratch will fully/partially bounce back into a flat level surface. The timescale of such a process

is determined by the mobility of the polymer network chains, i.e. the glass transition temperature (T_g). It is obvious that formation of tensile cracks along the scratch path can drastically alter the process as fracture will release a large fraction of the stored elastic energy. Therefore the energy will be no longer available for a directed bounce-back movement [11, 18].

Stress relaxation in reversible non-covalent networks

Self-healing polymeric systems based on reversible non-covalent bonds, e.g. hydrogen bonds and ionomers have been extensively studied in recent years. In contrast to permanent covalent bonds, dissociation and association of monomers and/or polymeric segments in the polymers based on the reversible non-covalent bonds are governed by a dynamic equilibrium ruled by thermodynamics. Reorganization of the polymeric network as a result of re-association of the reversible bonds provides these polymers with a latent healing potential in case of local structural damage. The time scale of the dynamic equilibrium plays a crucial role in the healing performance of such polymers. When the dissociation/re-association time scale is larger than that of the deformation, the reversible network will behave equivalent to a covalent network but when it is much shorter the reversible network will not show the structural integrity of a covalently cross-linked material [18].

Accumulation of internal stresses as a result of physical aging is a well-known phenomenon in covalently crosslinked coatings [38]. The residual stresses as a result of plasticity can be relieved via thermal treatment or viscoelasticity. Covalently crosslinked polymers can undergo limited viscoelastic stress relaxation at temperatures higher than T_g, Due to presence of physical constraints i.e. the covalent crosslinks, polymer segments can only be stretched up to a maximum extent, yielding partial relaxation. Reversible networks are not limited by such a degree of maximal extent of relaxation and will constantly creep, provided that the timescale of bond dissociation/re-association is equal to or shorter than the stress relaxation time constant (τ). The creep behaviour exhibited by the reversible network can empower relaxation of both internal stresses and imposed external stresses, preventing escalation of the damage from the microscopic to the macroscopic level and hence inducing an autonomous healing potential into the coating system [18].

Although to date no OIH coating capable of full stress relaxation has been reported in the literature, recently an OIH ionomer showing this desired behaviour has been synthesised through implementation of a butyltin oxo-cluster macrocation, $[(BuSn)_{12}O_{14}(OH)_6]^{2+}$ functionalized with two 2-acrylamido-2-methyl-1-

propanesulfonate anions (AMPS), as a physical crosslinking agent in poly(n-butyl acrylate) (pBuA). Sacrificial domains with reversible ionic bonds developed at the hybrid interface play a double role. The interactions are strong enough to induce crosslinking and consequently rubber-like elastic behaviour; and labile enough to enable dynamic bond dissociation/re-association leading to an efficient network rearrangement and hence healing at room temperature [39].

Although not yet studied from a stress-relaxation and self-healing point of view, heat and corrosion resistant urethane/urea/siloxane copolymers as well as anti-fouling urea-siloxane OIH coatings have been successfully applied on aluminium alloys. Considering the properties of the organic component in such OIHs, such as flexibility and presence of hydrogen bonding moieties, these OIH coatings can be optimized (e.g. by variation of organic/inorganic components ratio) for self-healing coating applications [18].

Reversible covalent networks

Several intrinsic self-healing approaches based on reversible covalent bonds using Diels-Alder/r Diels-reactions, thiol/disulphide exchange, disulphide bond reshuffling, radical based thiol-ene reactions, alkoxyamine bonds, dynamic urea bonds, dynamic boronic esters and reversible acylhydrazone formation have been successfully implemented in polymers and polymer coatings [18].

Peng et al [40] recently introduced an OIH coating based on mercapto- and vinyl-functionalized OMSAs for the protection of copper substrates. The increased crosslinking density of the developed OIH achieved through the in-situ condensation of silanol groups and thiol-ene click reactions led to improved protective performance of the coating compared to the one solely crosslinked with Si-O-Si bonds. Despite the reported heat and UV irradiation induced stress relaxation in polymeric coatings based on thiol-ene crosslinks, the OIH coating developed has not been thermo-mechanically examined yet [18]. The effect of the inorganic network based on Si-O-Si bridges on thermomechanical properties of OIH networks containing thiol-ene moieties has been documented [18, 41]. Despite the limited relaxation behaviour of the OIH network compared to the pure organic one imposed by irreversible covalent bonds, the OIH networks exhibited a reasonable stress relaxation behaviour and increased mechanical properties although they have not examined as a coating yet.

In addition to the inclusion of reversible covalent bonds in the backbone or side- chains of covalently crosslinked networks, blending of thermosets with thermoplastics of low melting point particularly polycaprolactone (PCL) has been reported to induce shape recovery and self-healing functionality to polymeric coatings. This principle has been

further explored by combing it with Diels–Alder chemistry (DASMASH) yielding thermo-remendable shape memory polyurethanes. PCL has also been incorporated in corrosion protective OIH coatings. While this leads to a well-documented thick and defect free OIH coatings having an improved potential bioactivity, the effect on scratch-healing has not yet been studied [18].

Up to very recently no corrosion protective intrinsic healing sol-gel coatings have been reported in the literature. To address this issue, in the first part of thesis we focused on development and characterization of an intrinsic healing containing reversible tetra-sulphide groups.

Scope and outline of the thesis

Inspired by the state of the art and the recent advances in the field of self-healing corrosion protective coatings, the current thesis addresses novel routes to self-healing corrosion protective sol-gel coatings via intrinsic and extrinsic healing approaches extending the service life of the coating and the underlying substrate by multiple damage closure/sealing and metal surface protection, through incorporation of reversible tetra-sulfide groups and inhibitor loaded containers, respectively.

In *Chapter 2*, the synthesis and characterization of the first generation of healable organic-inorganic hybrid (OIH) sol-gel polymers containing reversible tetra-sulfide groups is described. The effect of the reversible group's content and the crosslinking density on the thermal, mechanical and healing properties of the developed OIH sol-gel polymers are presented.

In *Chapter 3* the macroscopic flow kinetics of the OIH sol-gel polymer exhibiting the highest healing efficiency in chapter 2 are evaluated under air and nitrogen flow to unravel the mechanisms involved in the healing process. Furthermore, to correlate the reversible group's state to the observed macroscopic flow and healing capability of the OIH sol-gel polymer, the evolution of the reversible groups during the healing stage is monitored using a hot-stage coupled Raman spectrometer.

In *Chapter 4*, the time-resolved behaviour of the OIH sol-gel polymer containing thermo-reversible tetra-sulfide groups and the related deep impact on mechanical, viscoelastic and healing properties are presented. A hyphenated experimental procedure combining rheology and FTIR spectroscopy is employed to correlate the thermally

accelerated chemical reactions to the evolving rheological properties of the OIH sol-gel polymer. Additionally, the effect of the evolving network on the interfacial healing potential of the OIH sol-gel polymers is assessed using a fracture mechanics based protocol.

In *Chapter 5* the potential application of the OIH sol-gel polymer as protective coating is evaluated. To this aim the developed polymer is applied on AA2024-T3 substrate and its wetting, adhesion and barrier properties are assessed. Furthermore, the adhesion and barrier restoration potential of the coating systems are studied using mechanical and electrochemical techniques.

In *Chapter 6* application of the AC/DC/AC procedure as a fast electrochemical technique for evaluation of the OIH sol-gel coating's durability and the healing extent of scratch induced interface is described. The intact and healed OIH sol-gel coatings are assessed using the AC/DC/AC procedure and the results were compared to those obtained using conventional EIS.

In *Chapter 7*, preparation and characterization of stimuli responsive extrinsic healing corrosion protective coatings containing combination of cationic and anionic inhibitor doped containers is described. The loading procedure of the selected inhibitors in the ion-exchangeable carriers, the triggered inhibitor release and the potential synergism between the employed inhibitors in surpassing corrosion of the AA2024-T3 substrate are addressed.

References:

[1] D.G. Shchukin, D. Borisova, H. Mohwal, Self-healing coatings, in: W.H. Binder (Ed.) Self-healing polymers from principles to applications, Wiley-VCH Verlag GmbH & Co. KGa, Weinheim, Germany, 2013.
[2] S.J. García, H.R. Fischer, S. van der Zwaag, A critical appraisal of the potential of self healing polymeric coatings, Progress in Organic Coatings, 72 (2011) 211-221.
[3] I. Gurrappa, I.V.S. Yashwanth, Chapter 2 - The Importance of Corrosion and the Necessity of Applying Intelligent Coatings for Its Control, in: A. Tiwari, J. Rawlins, L.H. Hihara (Eds.) Intelligent Coatings for Corrosion Control, Butterworth-Heinemann, Boston, 2015, pp. 17-58.
[4] M.G. Fontana, Corrosion Engineering, 3 ed., Hill International Editions Series in Material Science and Engineering, Singapore, 1987.
[5] A.W. Peabody, Peabody's Control of Pipeline Corrosion, 2 ed., NACE International The Corrosion Society, Houston, Texas, 2001.

[6] M.L. Zheludkevich, I.M. Salvado, M.G.S. Ferreira, Sol-gel coatings for corrosion protection of metals, Journal of Materials Chemistry, 15 (2005) 5099-5111.

[7] R.B. Figueira, C.J.R. Silva, E.V. Pereira, Organic–inorganic hybrid sol–gel coatings for metal corrosion protection: a review of recent progress, Journal of Coatings Technology and Research, 12 (2015) 1-35.

[8] C.J. Brinker, G.W. Scherer, Sol-Gel Science: The Physics and Chemistry of Sol Gel Processing, Academic Press, INC.1990.

[9] M. Niederberger, N. Pinna, Aqueous and Nonaqueous Sol-Gel Chemistry, Metal Oxide Nanoparticles in Organic Solvents Synthesis, Formation, Assembly and Application, Springer-Verlag London Limited2009, pp. 7-18.

[10] M. Guglielmi, Sol-gel coatings on metals, Journal of Sol-Gel Science and Technology, 8 (1997) 443-449.

[11] R.T.M. van Benthem, W. Ming, G. de With, Self Healing Polymer Coatings, in: S. van der Zwaag (Ed.) Self Healing Materials, Springer Netherlands2007, pp. 139-159.

[12] S.K. Ghosh, Self-Healing Materials: Fundamentals, Design Strategies, and Applications,, Wiley-VCH 2009.

[13] A.E. Hughes, I.S. Cole, T.H. Muster, R.J. Varley, Designing green, self-healing coatings for metal protection, NPG Asia Materials, 2 (2010) 143-151.

[14] M.L. Zheludkevich, M.G.S. Ferreira, Self-healing anticorrosion coatings, in: L. Fedrizzi, M.F. Montemor (Eds.) Self-Healing Properties of New Surface Treatments, European Federation of Corrosion Series, Maney Publishing, UK, 2011.

[15] J. Kron, K.J. Deichmann, K. Rose, Sol–gel derived hybrid materials as functional coatings for metal surfaces, in: L. Fedrizzi, M.F. Montemor (Eds.) Self-Healing Properties of New Surface Treatments, European Federation of Corrosion, UK, 2011.

[16] W.J. van Ooij, D. Zhu, M. Stacy, A. Seth, T. Mugada, J. Gandhi, P. Puomi, Corrosion Protection Properties of Organofunctional Silanes-An Overview, Tsinghua Science & Technology, 10 (2005) 639-664.

[17] J.D. Wright, N.A.J.M. Sommerdijk, Sol-Gel Materials: Chemistry and Applications, Taylor & Francis Book Ltd2001.

[18] M. Abdolah Zadeh, S. van der Zwaag, S.J. Garcia, Routes to extrinsic and intrinsic self-healing corrosion protective sol-gel coatings: a review, Self-Healing Materials, 2013, pp. 1.

[19] D. Wang, G.P. Bierwagen, Sol-gel coatings on metals for corrosion protection, Progress in Organic Coatings, 64 (2009) 327-338.

[20] S. Zheng, J. Li, Inorganic-organic sol gel hybrid coatings for corrosion protection of metals, Journal of Sol-Gel Science and Technology, 54 (2010) 174-187.

[21] K.A. Yasakau, J. Carneiro, M.L. Zheludkevich, M.G.S. Ferreira, Influence of sol-gel process parameters on the protection properties of sol–gel coatings applied on AA2024, Surface and Coatings Technology, 246 (2014) 6-16.

[22] M.L. Zheludkevich, R. Serra, M.F. Montemor, I.M.M. Salvado, M.G.S. Ferreira, Corrosion protective properties of nanostructured sol-gel hybrid coatings to AA2024-T3, Surface and Coatings Technology, 200 (2006) 3084-3094.

[23] M.L. Zheludkevich, R. Serra, M.F. Montemor, K.A. Yasakau, I.M.M. Salvado, M.G.S. Ferreira, Nanostructured sol-gel coatings doped with cerium nitrate as pre-treatments for AA2024-T3: Corrosion protection performance, Electrochimica Acta, 51 (2005) 208-217.

[24] D.G. Shchukin, H. Möhwald, Self-Repairing Coatings Containing Active Nanoreservoirs, Small, 3 (2007) 926-943.

[25] G. Wu, J. An, D. Sun, X. Tang, Y. Xiang, J. Yang, Robust microcapsules with polyurea/silica hybrid shell for one-part self-healing anticorrosion coatings, Journal of Materials Chemistry A, 2 (2014) 11614-11620.

[26] D. Borisova, H. Mohwal, D.G. Shchukin, Mesoporous Silica Nanoparticles for Active Corrosion Protection, ACS Nano, 5 (2011) 1939-1946.

[27] M. Wang, M. Liu, J. Fu, An intelligent anticorrosion coating based on pH-responsive smart nanocontainers fabricated via a facile method for protection of carbon steel, Journal of Materials Chemistry A, 3 (2015) 6423-6431.

[28] P. Kluson, P. Kacer, T. Cajthaml, M. Kalaji, Preparation of titania mesoporous materials using a surfactant-mediated sol-gel method, Journal of Materials Chemistry, 11 (2001) 644-651.

[29] S.J. Garcia, H.R. Fischer, P.A. White, J. Mardel, Y. Gonzalez-Garcia, J.M.C. Mol, A.E. Hughes, Self-healing anticorrosive organic coating based on an encapsulated water reactive silyl ester: Synthesis and proof of concept, Progress in Organic Coatings, 70 (2010) 142-149.

[30] Y.-K. Song, Y.-H. Jo, Y.-J. Lim, S.-Y. Cho, H.-C. Yu, B.-C. Ryu, S.-I. Lee, C.-M. Chung, Sunlight-Induced Self-Healing of a Microcapsule-Type Protective Coating, ACS Applied Materials & Interfaces, 5 (2013) 1378-1384.

[31] K.A. Yasakau, M.L. Zheludkevich, S.V. Lamaka, M.G.S. Ferreira, Mechanism of Corrosion Inhibition of AA2024 by Rare-Earth Compounds, The Journal of Physical Chemistry B, 110 (2006) 5515-5528.

[32] S.J. García, J.M.C. Mol, T.H. Muster, A.E. Hughes, T.M.J. Mardel, H.T.T. Markely, J.H.W. de Wit, Advances in the selection and use of rare-earth based inhibitors for selfhealing organic coatings, Self-Healing Properties of New Surface Treatments, European Federation of Corrosion Series, Maney Publishing, UK, 2011, pp. 148–183.

[33] M.F. Montemor, M.G.S. Ferreira, A review on the use of nanostructured and functional organosilane coatings modified withcorrosion inhibitors as environmentally friendly pre-treatments for metallic substrates, in: L. Fedrizzi, M.F. Montemor (Eds.) Self-Healing Properties of New Surface Treatments, Maney Publishing, UK2011.

[34] A.J. Vreugdenhil, M.E. Woods, Triggered release of molecular additives from epoxy-amine sol-gel coatings, Progress in Organic Coatings, 53 (2005) 119-125.

[35] A.N. Khramov, N.N. Voevodin, V.N. Balbyshev, R.A. Mantz, Sol-gel-derived corrosion-protective coatings with controllable release of incorporated organic corrosion inhibitors, Thin Solid Films, 483 (2005) 191-196.

[36] S.J. Garcia, T.A. Markley, J.M.C. Mol, A.E. Hughes, Unravelling the corrosion inhibition mechanisms of bi-functional inhibitors by EIS and SEM–EDS, Corrosion Science, 69 (2013) 346-358.

[37] J. Carneiro, A.F. Caetano, A. Kuznetsova, F. Maia, A.N. Salak, J. Tedim, N. Scharnagl, M.L. Zheludkevich, M.G.S. Ferreira, Polyelectrolyte-modified layered double hydroxide nanocontainers as vehicles for combined inhibitors, RSC Advances, 5 (2015) 39916-39929.

[38] D.Y. Perera, P. Schutyser, Effect of physical aging on thermal stress development in powder coatings, Progress in Organic Coatings, 24 (1994) 299-307.

[39] F. Potier, A. Guinault, S. Delalande, C. Sanchez, F. Ribot, L. Rozes, Nano-building block based-hybrid organic-inorganic copolymers with self-healing properties, Polymer Chemistry, 5 (2014) 4474-4479.

[40] S. Peng, Z. Zeng, W. Zhao, J. Chen, J. Han, X. Wu, Performance evaluation of mercapto functional hybrid silica sol–gel coating on copper surface, Surface and Coatings Technology, 251 (2014) 135-142.

[41] K.M. Schreck, D. Leung, C.N. Bowman, Hybrid Organic/Inorganic Thiol–Ene-Based Photopolymerized Networks, Macromolecules, 44 (2011) 7520-7529.

Chapter 2

Synthesis of healable dual organic-inorganic hybrid sol-gel based polymers containing reversible tetrasulfide groups

Introduction

Sol-gel derived organic-inorganic hybrid materials combining desirable properties of their building blocks have lately attracted considerable interest. Their extended abilities to tune the properties by controlling the system chemistry and structure makes them a suitable candidate for designing healable materials via extrinsic and intrinsic healing approaches [1-4]. Incorporation of 1-, 2- and 3-dimensional inorganic nano-materials containing healing agents into polymeric matrices is a well-studied method in composites and coatings [5-7]. Yet, despite the ability of such systems for autonomous healing of damage, they fail to reproduce the healing event in a previously damaged zone.

Intrinsic healing approaches (i.e. not requiring the inclusion of discrete capsules filled with a healing agent) based on reversible chemistries have attracted considerable attention due to their attractive features such as multiple healing capability and the possibility to incorporate the relevant reversible moieties directly into the polymer network [8, 9]. Although the intrinsic self-healing behavior would be advantageous for the life-time extension, its implementation generally leads to a decrease in the mechanical behavior of the final network which can be even more detrimental for the life-time. The major challenge in self-healing polymer design remains the development of a self-healing polymer which has sufficient mechanical properties yet heals at modest temperatures [10, 11]. Intrinsic healing approaches based on reversible non-covalent bonds such as ionic interactions [12] have been successfully introduced to hybrid materials.

Although reversible non-covalent bonds can lead to multiple healing, individually they are not as strong as reversible covalent bonds. However, the strong covalent bonds demand higher energy to initiate the healing process. Therefore, achieving efficient healing as well as adequate mechanical properties requires a fine compromise in the bond strength. The versatility of sulfur chemistry alongside with the relatively low bond strength of sulfur-sulfur (S-S) bonds makes this type of chemistry a suitable candidate to induce multiple healing properties in polymeric systems [13]. The healing process in such systems which is mainly based on S-S bonds re-shuffling and can be triggered using a range of stimuli such as temperature [14-17], shear forces [18], reduction reactions [19, 20] and UV-irradiation [21, 22]. In addition, nucleophilic reagents such as phosphine [23] and thiol groups can facilitate scission of S-S bonds [24, 25].

In addition to thermoplastics (polyethylene) and elastomers (polyurethanes) containing reversible disulfide bonds [14, 26, 27] thermoset rubbers containing reversible disulfide bonds have been prepared previously by end-capping of poly-sulfides with epoxide groups followed by ring-opening polymerization (ROP) using different crosslinking

agents [15, 16, 28, 29]. The dynamic nature of the disulfide bonds provides the driving force for partial recovery of the initial mechanical strength upon thermal trigger, provided that the concentration of disulfide bonds is high enough. However, a drawback of these materials is that they are not mechanically robust. Additionally, tuning the content of the reversible bonds in such thermoset rubbers is not straight forward. Sol-gel derived hybrid materials containing reversible groups, in which separate parts of the polymer network take care of the mechanical robustness and the healing behavior could offer new and more successful approaches.

In this chapter a new intrinsic sol-gel based self-healing polymer capable of restoring its cohesive integrity upon damage is described. Our approach is based on reversible tetrasulfide groups incorporated into a crosslinked polymeric matrix through sol-gel chemistry. Tetrasulfide groups with an average dissociation energy of 36 kcal mol^{-1} can provide higher re-shuffling rates compared to disulfide bonds having a dissociation energy of 64 kcal mol^{-1} [30]. The reversible bonds provide adequate chain mobility in the crosslinked network upon thermal stimulus. Through these systems, the dominant role of the reversible tetrasulfide groups and crosslinking density on the healing performance of the developed hybrid sol-gel polymers is revealed.

Experimental procedure

Materials

Epoxy resins based on Epikote^{TM} 828 (184-190 g.eq^{-1}) and Ancamine$^{®}$2500 curing agent (105-110 g.eq^{-1}) were provided by AkzoNobel Aerospace Coatings (ANAC) and used as received. (3-Aminopropyl)trimethoxysilane (97%, MW=179.29 g.mol^{-1}) and pentaerythritol tetrakis(3-mercaptopropionate) (>95%, MW=488.66 g.mol^{-1}), from hereon called APS and tetra-thiol respectively, were purchased from Sigma-Aldrich, The Netherlands, and used without further purification. Bis[3-(triethoxysilyl)propyl]tetrasulfide (99%, MW=538.95 g.mol^{-1}, total sulfur content>20%), from hereon called BS, and ethanol were purchased from Capture Chemicals, China, and VWR, The Netherlands, respectively and used as received.

Preparation

The healable dual organic-inorganic sol-gel based polymers, referred hereafter as healable hybrid sol-gel polymers were prepared in a multi-step process in which the order of

addition of the ingredients is a key factor. The organically modified silicone alkoxides (OMSAs) were sequentially (APS followed by BS) added to the epoxy resin with an OMSAs:epoxy resin weight ratio of 1:1 and stirred using a magnetic stirrer at 300 rpm for 3 h at room temperature. The content of the reversible tetrasulfide groups was tuned by changing BS:APS molar ratio (1:1, 2:1 and 3:1). The aliphatic amine based organic crosslinker (Ancamine®2500, with an average functionality of 4) was then added to the mixture, keeping the amine hydrogen equivalent of Ancamine®2500 (AHE_{Anc}) to epoxy equivalent (EE) ratio at 1.1 to ensure full conversion and the mixture was stirred in a high speed mixer at 2500 rpm for 5 min. Tetra-thiol was then added in a tetra-thiol:epoxy resin weight ratio 0.56:1 to overcome phase separation problems and to facilitate cleavage of tetrasulfides via thiol-oligosulfide exchange reactions. Yet, the tetra-thiol can also act as secondary crosslinker for epoxy [31, 32]. The exact contribution of the tetra-thiol in each of its potential roles could not be unraveled due to the complexity of the new network. Nevertheless, it is likely that the thiol groups participate in all possible reactions as will be concluded from the Raman studies presented in chapter 3.

After addition of tetra-thiol the mixture was mixed in the high speed mixer for 40 s at 2500 rpm. The resulting mixtures were cast on Teflon plates using a 600 μm calibrated standard aluminum single doctor blade and cured for 2 h at 70 °C, yielding a crosslinked network as demonstrated by the presence of a rubbery plateau in the dynamic thermo-mechanical analysis (DMTA) (as presented in chapter 3). The chemical structure of the OMSAs and an idealized form of the resulting hybrid network are presented in Figure 2.1.

In order to evaluate the effect of the crosslinking density on macroscopic flow capabilities of the hybrid sol-gel films, two more sets of samples were prepared by separately increasing the crosslinking density of the inorganic and organic networks. To increase the inorganic crosslinking density, BS and APS mixtures (molar ratio of 3:1) were pre-hydrolyzed prior to addition of epoxy resin to initiate inorganic crosslinking by formation of Si-O-Si bridges [1-4, 33].

Organically modified silicone alkoxides (OMSAs)

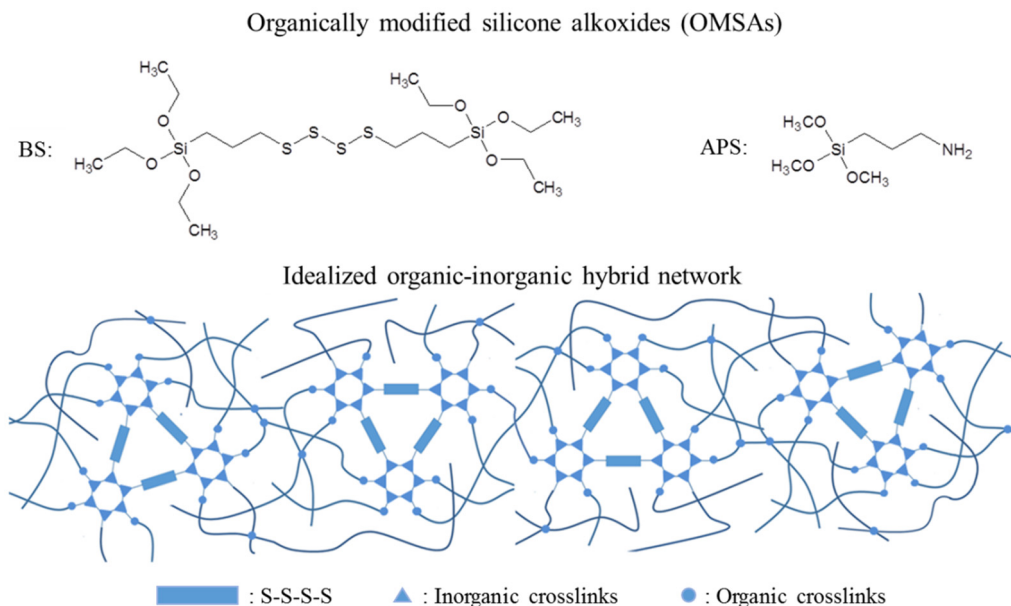Idealized organic-inorganic hybrid network

Figure 2.1. Chemical structure of the precursors used in synthesis (a) and idealized structure of the formed hybrid sol-gel polymers containing reversible bonds (b).

The hydrolysis was carried out by drop-wise addition of 4.67 molar equivalent of DI water (r_W=H_2O/Si-OR) into the mixture containing 25.67 molar equivalent of pure ethanol ($r_{Ethanol}$ = C_2H_5OH/Si-OR). The mixture was stirred for 22 h at room temperature (T ≈ 25 °C) to initiate the inorganic crosslinking by formation of Si-O-Si bonds [34]. The remainder of the process followed as for the un-hydrolyzed samples. The organic crosslinking density was increased by addition of Ancamine°2500 in stoichiometric amount required to ring open oxirane rings (i.e. $AHE_{Anc.}$/EE ratio of 1). Epikote 828 based epoxy films with epoxy resin:Ancamine:tetra-thiol weight ratio of 1:0.58:0.56 were prepared and examined as crosslinked [31, 35, 36] non-healing reference samples. All films had a similar final thickness of about 600 µm. Table 1 sums up the different polymer film compositions evaluated in this work. The sample codes listed in the first column of table 1 will be used along the chapter.

Table 2.1. Composition of the prepared healable hybrid sol-gel polymers

Code	OMAS (BS:APS) (Molar Ratio)	Pre-Hydrolysis of OMAS	Epoxy Resin:OMAS (weight ratio)	$AHE_{Anc.}/EE$ [a]	Epoxy resin:tetra-thiol (weight ratio)
Ref	N.A.[b]	N.A.	N.A.	1.1	1:0.56
1	1:1	No	1:1	1.1	1:0.56
2	2:1	No	1:1	1.1	1:0.56
3a	3:1	No	1:1	1.1	1:0.56
3b	3:1 [c]	Yes	1:1	1.1	1:0.56
3c	3:1 [d]	No	1:1	1	1:0.56

[a] : $AHE_{Anc.}$ and EE stand for amine hydrogen equivalent of Ancamine and epoxy equivalent, respectively.

[b] : N.A. stands for not applicable   [c]: Higher inorganic network crosslinking density

[d] : Higher organic network crosslinking density

Characterization

Thermal properties

Thermogravimetric analysis (TGA) TGA measurements were performed with Perkin Elmer Pyris Diamond TG/DGA analyzer under nitrogen atmosphere (gas flow 100 ml min^{-1}). Samples of 5-10 mg weight were heated from 25 to 550 °C at a heating rate of 20 °C.min^{-1} to determine the thermal stability of the healable hybrid sol-gel polymers.

Differential scanning calorimetry (DSC) DSC measurements were performed using a PerkinElmer Sapphire DSC under nitrogen flow. Samples of approximately 10 mg weight were heated from -100 to 100 °C at a heating rate of 20 °C.min^{-1}. For each sample, two cool-heat runs with the same heating/cooling rates were performed and the glass transition temperature (T_g) of the hybrid sol-gel films were determined using the inflection point of the DSC curves for the second heating run.

Mechanical properties
Tensile properties: The mechanical properties of the prepared healable hybrid sol-gel films were evaluated at room temperature using a Zwick 1455 tensile testing machine.

Samples of $70 \times 5 \times 0.6$ mm³ were tested in tension with a 1 kN load cell, a cross-head speed of 5 mm.min⁻¹ and a gauge length of 50 mm.

Density: The density of the reference and the hybrid sol-gel polymers were measured using a METTLER TOLEDO hydrostatic balance applying the Archimedes principle. Circular films with an average thickness and diameter of 600 µm and 5 mm were weighed in air and distilled water at room temperature to yield the polymer density based on the following equation:

$$\rho = \frac{A}{A-B}(\rho_0 - \rho_l) + \rho_l \qquad\qquad \text{Eq. 2.1}$$

Where ρ, ρ_0 and ρ_l represent the densities of polymer, water and air at the test temperature and A and B stand for the measured weight of polymer in air and under water, respectively.

Healing properties

Gap closure properties: The healing process of intrinsic self-healing polymers is a multi-step phenomenon in which the approach of cut surfaces is a critical step. The surface approach applies to ability of the polymer to undergo macroscopic flow and bring the cut surfaces in contact, creating an interface to be healed. To quantify the thermo-mechanical induced flow of the polymer leading to gap closure, hybrid sol-gel films of 15×4 mm² were cut in two pieces at room temperature. The cut pieces were placed in parallel 500 ± 20 µm apart from each other between two glass plates under a constant pressure of 30 kPa. The ability of the healable hybrid sol-gel films to close the artificial gap over 10 minutes was investigated at 20, 50, 70 and 90 °C in an air circulation oven. The gap size evolution was monitored with a Leica DMLM microscope in transmission mode and images captured with inbuilt Axio Cam ICc 3 digital camera. AxioVision software was employed for the analysis of micrographs and gap area quantification. Assuming a uniform thickness of the samples, the gap closure efficiency was calculated using the following equation:

$$Gap\ Closure\ Efficiency\ (\%) = \left(\frac{A_0 - A_t}{A_0}\right) \times 100 \qquad\qquad \text{Eq. 2.2}$$
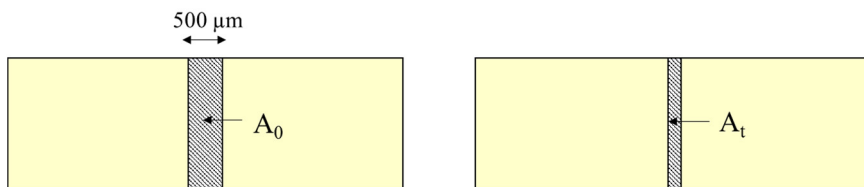
Figure 2.2. Schematic representation of the gap closure process as a function of time in case of isothermal healing.

where A_t and A_0 represent the gap area between the cut pieces at time (t) and (0), respectively (Figure 2.2). Using this approach the role of the tetrasulfide content and the crosslinking density of the hybrid sol-gel films on the gap closure efficiency was evaluated.

Single edge notched tension (SENT) To evaluate the degree of interfacial strength recovery achieved during the healing process SENT tests were performed at room temperature on pristine and healed samples. SENT specimens were prepared by casting the hybrid polymers in a mould of $80 \times 25 \times 8$ mm³. A 2 mm long notch was made in the middle of the specimen edge using a sharp razor blade. The samples were tested using a Zwick 1455 tensile testing machine with a 1 kN load cell, a cross-head speed of 10 mm min⁻¹ and a gauge length of 50 mm till a final crack length of 150 mm was achieved. The tested samples were then placed in a Teflon mould designed to correctly align the two crack planes (Figure 2.3) and the mould with sample was placed in an air circulation oven at 70 °C for 2 h. The healed samples were subsequently notched at the previously damaged site and tested using the same methodology.
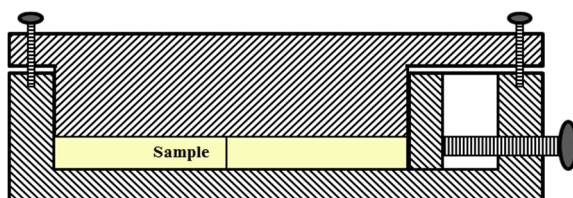

Figure 2.3. Schematic representation of the set-up used for healing of SENT samples.

Results & Discussion

Thermal properties

Implementation of reversible tetrasulfide groups in hybrid sol-gel polymers implies that the healing process of such polymers can be activated using a range of stimuli such as temperature [13]. Depending on the presence or absence of nucleophilic agents such as thiol groups and the crosslinking density of the polymeric network, the reversible sulfur-sulfur (S-S) bonds can be cleaved in a temperature range of 60-90 °C [14]. Therefore, thermal stability of the healable polymers containing S-S bonds in the aforementioned temperature range is crucial.

The thermal stability of the prepared hybrid sol-gel films was evaluated using TGA and the obtained results are summarized in table 2.2. As shown in table 2.2, no significant difference in thermal stability was observed for the studied films. However, it was found that an increase in BS content led to a slight increase in the thermal stability up to a BS:APS molar ratio 2:1 beyond which the stability decreased. Increasing the crosslinking density of either organic or inorganic networks with a fixed BS:APS molar ratio (i.e. 3:1) led to a slightly higher thermal stability. In all cases, the TGA results revealed that the developed films are thermally stable at the temperatures chosen for the healing process of hybrid sol-gel polymers (20 to 90 °C).
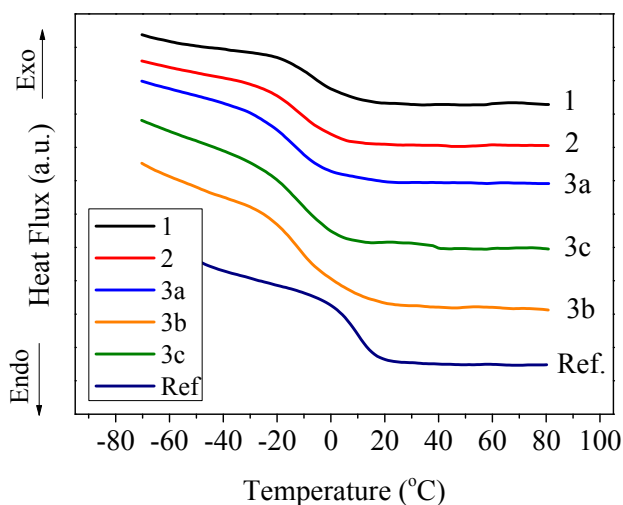

Figure 2.4. DSC curves of healable hybrid sol-gel films with different tetra-sulfide content and crosslinking density.

The completion of the curing reactions in the non-healing reference epoxy and the healable hybrid sol-gel films was demonstrated using DSC (Figure 2.4). As shown in Figure 2.4, the DSC curves of the prepared films exhibited no residual exothermic peak characteristic of the curing reactions. Completion of the curing reactions indicates that further annealing at the healing temperatures would not lead to further curing neither in the non-healing reference epoxy nor in the healable hybrid sol-gel polymers. Formation of a crosslinked network as a result of curing reactions in the epoxy based polymers (tested as non-healing reference) was addressed in a number of publications [31, 35, 36]. The formation of the crosslinked network in the hybrid sol-gel polymers was illustrated by presence of a rubbery plateau in the dynamic thermo-mechanical analysis (DMTA) data as shown in chapter 3. Moreover, all the films showed T_g values below room temperature (i.e. 25 °C). The non-healing reference system showed a T_g value at +10 °C which is approximately 20 °C higher than that of healing systems which had T_g values between -9 and -13 °C (see table 2.2). Variations in BS content (and therefore reversible tetrasulfide groups) and crosslinking density had a minimal effect on T_g.

Table 2.2. Thermal weight loss, T_g and Young's modulus of the prepared hybrid sol-gel films.

Code	Weight loss (°C)		T_g (°C)	E (MPa)	ρ (g.cm^{-1})
	1%	10%			
Ref	120	237	10	25	1.21
1	96	232	-13	10	1.20
2	105	245	-11	55	1.20
3a	96	232	-11	35	1.20
3b	114	245	-9	145	1.23
3c	104	246	-11	62	1.22

Mechanical properties

The effect of the tetrasulfide group content and the crosslinking density on the mechanical properties of the prepared hybrid films is shown in Figure 2.5. As Figure 2.5a shows, the toughness and the stress at break initially increased by increasing BS content but decreased again when the BS:APS ratio was 3:1. The elastic modulus values (summarized in Table 2.2) showed the same trend as toughness and stress at break.

In the preparation stage of healable hybrid polymers, sol-gel chemistry was employed to introduce intrinsic healing functionality into a cross-linked epoxy matrix through BS. The amine functionality of APS was used to provide compatibility with epoxy resin, resulting in homogenous hybrids with well-dispersed silica phase. Yet, the APS content in the hybrid sol-gel polymers was proved to be a critical factor. The amine functionality of APS, not only provides the required compatibility between the organic and inorganic networks, but also can dramatically affect the degree of hydrolysis and condensation of silicone alkoxides [37]. Acceleration of condensation reactions in presence of basic amine groups will consume the hydroxyl functionality of silanol groups which could otherwise increase the compatibility of the organic and inorganic networks and the hybrid polymers effective crosslinking density through ring opening reactions of oxirane rings of organic phase [38].
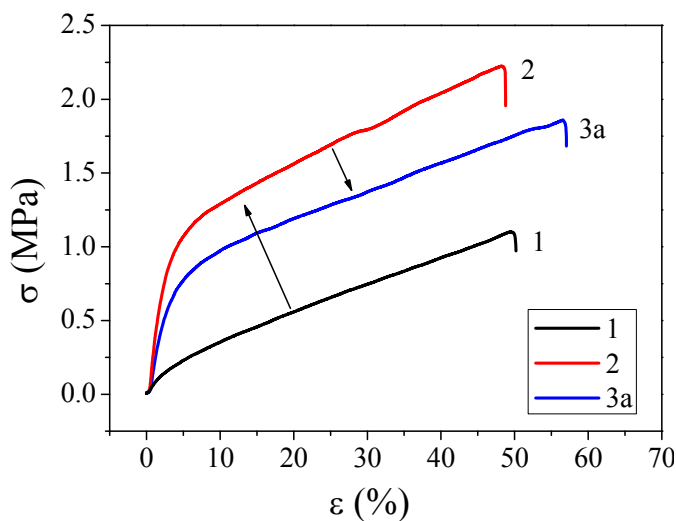

Figure 2.5. Stress-strain curves of free standing hybrid sol-gel films with different tetrasulfide content. Arrows indicate increase of tetrasulfide content.

The elastic modulus values summarized in Table 2.2 can be employed to estimate the effective crosslinking density of the hybrid sol-gel polymers based on the elasticity theory.

$$\nu_E = \frac{E}{3\rho RT}$$

Eq.2.3

Where ν_E, E, ρ, R and T stand for the effective crosslinking density, elastic modulus, density, universal gas constant and temperature, respectively. The density of the hybrid sol-gel polymers are calculated using the Archimedes' principle and are summarized in Table 2.2. As shown in Table 2.2, the densities of the hybrid sol-gel polymers containing different content of the reversible tetrasulfide groups were equivalent (1.20 g.cm^{-1}). Therefore, the elastic modulus of these polymers can be taken as a measure of their effective crosslinking density. In other words, the higher elastic modulus of the hybrid sol-gel polymer with composition 2 compared to those of 1 and 3a points to its higher effective crosslinking density, further confirming the pronounced effect of the amine content on the final properties of the hybrid sol-gel polymers [39].

As Table 2.2 shows the calculated densities of the hybrid sol-gel polymers with different content of the reversible groups (1, 2 and 3a) were slightly lower than the non-healing reference polymer. Investigation of the fractured surfaces of the mechanically tested films revealed different features for the non-healing reference epoxy and the hybrid sol-gels with compositions of 1, 2 and 3a. The SEM micrographs of the fracture surfaces of the aforementioned samples are presented in Figure 2.6. Unlike the non-healing reference epoxy, the hybrid sol-gels with different content of the reversible groups exhibited a porous structure. Despite the small differences the average pore diameter in the hybrid sol-gel polymers was 100 nm independent of the content of the reversible tetra-sulfide groups. The porous structure of the hybrid sol-gel polymers can result from hydrolysis and condensation of the un-hydrolyzed OMSAs involving evolution of water and alcohol [1, 3, 33]. The observed features can justify the slightly lower density of the hybrid sol-gel polymers (1, 2 and 3a) compared to the non-healing reference epoxy.
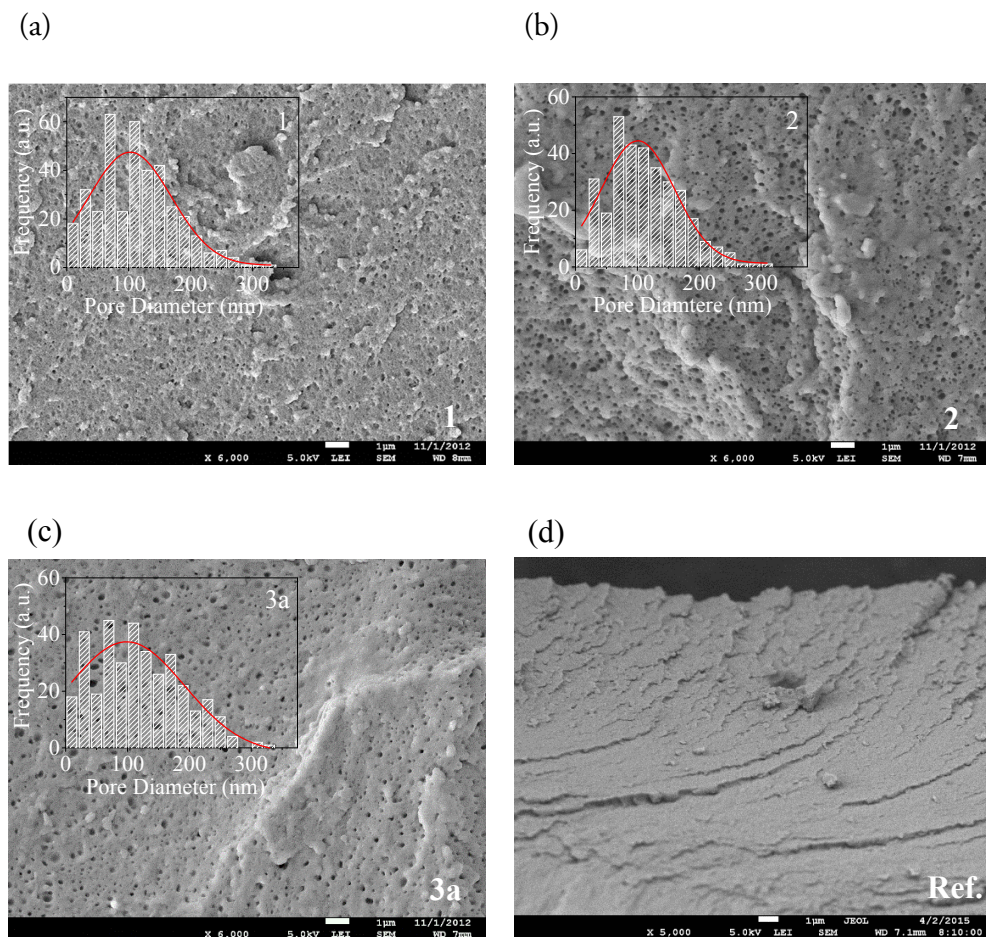
Figure 2.6. SEM micrographs of the hybrid sol-gel coatings with composition 1 (a), 2 (b), 3a (c) and the non-healing reference epoxy (d).

Figure 2.7 shows that the increase of the crosslinking density by increasing the inorganic (sample 3b in Table 2.1) and the organic crosslinks (sample 3c) led to an increase of the elastic modulus and stress at break (figure 3b). The inorganic crosslinks were found to have the largest effect. Formation of Si-O-Si bridges promoted by pre-hydrolysis of the OMSAs led to a significant increase in the crosslinking density of the hybrid sol-gel

polymers as illustrated by rather high elastic modulus of the sample 3b. The increased crosslinking density of either of the inorganic and organic networks resulted in slight increase of the hybrid sol-gel polymer density. In analogy to the samples with different tetra-sulfide content, the increase in the effective crosslinking density of the samples 3b and 3c compared 3a was reflected by a noticeable increase in their elastic modulus (Table 2.2).
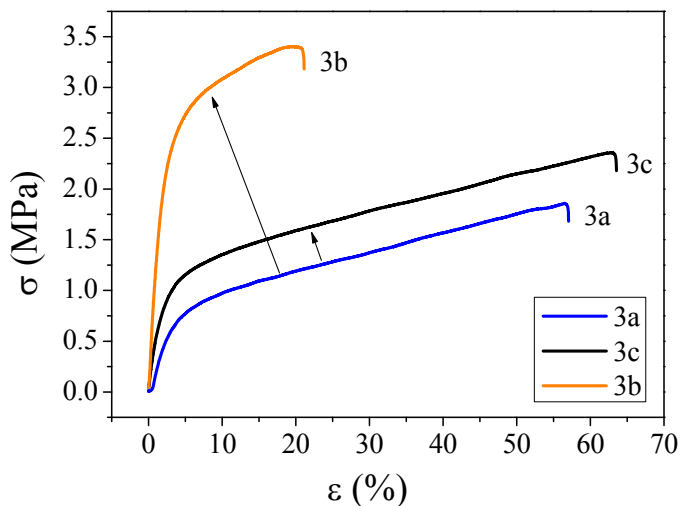
Figure 2.7. Stress-strain curves of free standing hybrid sol-gel films with different crosslinking density. Arrows indicate increase of crosslinking density.

Healing properties

The effect of the tetrasulfide content and crosslinking density on the gap closure efficiency of the hybrid sol-gel films after 10 minutes heating at four different temperatures is shown in Figure 2.8. The results indicate that all systems containing tetrasulfide groups show a clear macroscopic flow upon application of thermo-mechanical stimulus. The extent of gap closure and therefore healing of the samples depend on the sol-gel network architecture. Figure 2.8 a shows that the gap closure efficiency achieved in 10 min at all the tested temperatures was strongly influenced by the reversible bond content. While the tetrasulfide free reference epoxy films exhibited

no reduction in the gap area, significant healing was observed at higher BS:APS molar ratios without significant alteration of T_g, with 70 °C being the optimum healing temperature for all the systems. The gap closure efficiency were weakly affected by the tetrasulfide content when the BS:APS molar ratio was beyond 2:1. At the lowest BS content, 100% healing was not reached at any of tested temperatures independent of the healing time.

Although the increase in the mechanical properties by increasing crosslinking density is a well-known phenomenon [40], its effect on the healing potential has not been yet reported, while this could be a key parameter towards the development of more rigid but still healing polymers. The effect of the crosslinking density on the gap closure efficiency for the hybrid sol-gel films with the highest BS content exhibiting the highest gap closure efficiency is shown in figure 2.8 b. As shown in Figure 2.8 b, a higher crosslinking density lowered the gap closure efficiency for a given heating time (e.g. 10 min). The decrease in gap closure efficiency occurred independently of the temperature and the nature of the crosslinks.

The results presented in Figures 2.5, 2.7 and 2.8 clearly show that when the content of reversible bonds is constant (Figures 2.7 and 2.8 b), increasing the rigidity of the network lowers the gap closure efficiency. Nevertheless, the same trend is not applicable when the content of reversible groups is modified. For the samples containing different content of reversible groups, the highest gap closure efficiency does not correspond to the lowest mechanical properties (sample 1), but it increases as a function of reversible bond content (Figures 2.5 and 2.8 a). This suggests that despite the significant effect of the mechanical properties on the healing performance of the hybrid sol-gel films, the controlling factor is the content of reversible bonds (i.e. tetrasulfide groups).
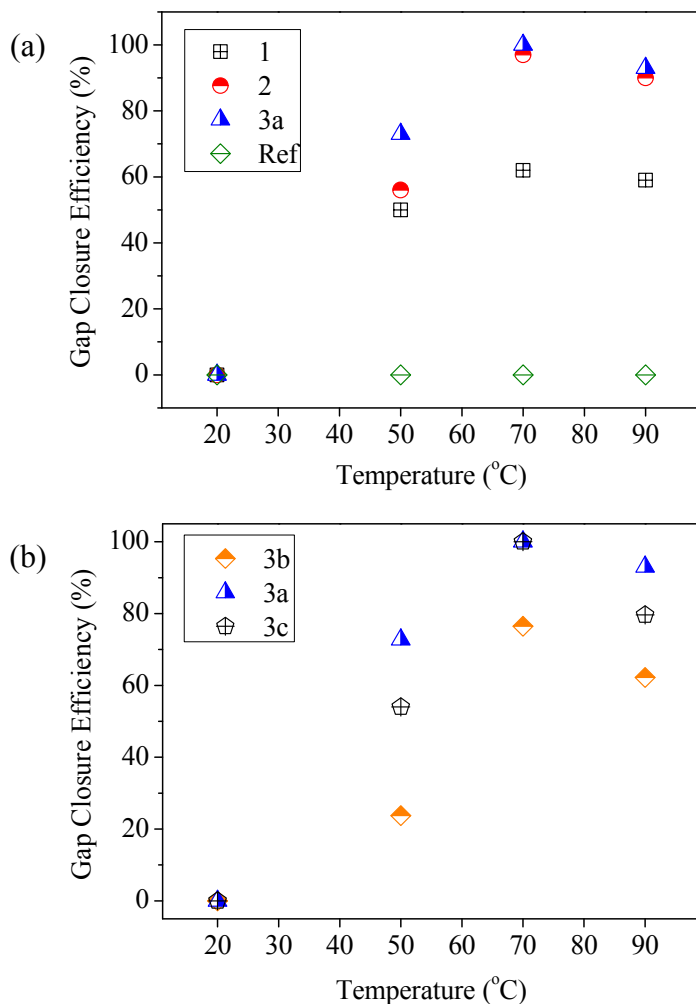
Figure 2.8. Effect of tetrasulfide content (a) and crosslinking density (b) on gap closure efficiency as function of healing temperature after 10 min healing time.

The gap closure is the first step in the healing process of the hybrid sol-gel films which is driven by the cleavage of reversible groups leading to sufficient flow. Yet, the polymer gap closure does not immediately imply a full recovery of the interfacial strength due to presence of the non-reversible bonds. To evaluate the strength recovery at the interface, SENT test was performed as exposed in experimental section. Figure 2.9 shows the results of the strength recovery tests for 3 separate samples with composition 3a which

showed the highest gap closure efficiency and contained the highest amount of reversible groups responsible for the healing. As seen in the figure, the healing treatment resulted in a recovery of about 70% of the failure load, notwithstanding the complete optical disappearance of the healed interface. The newly formed crack formed at the location of the first crack.
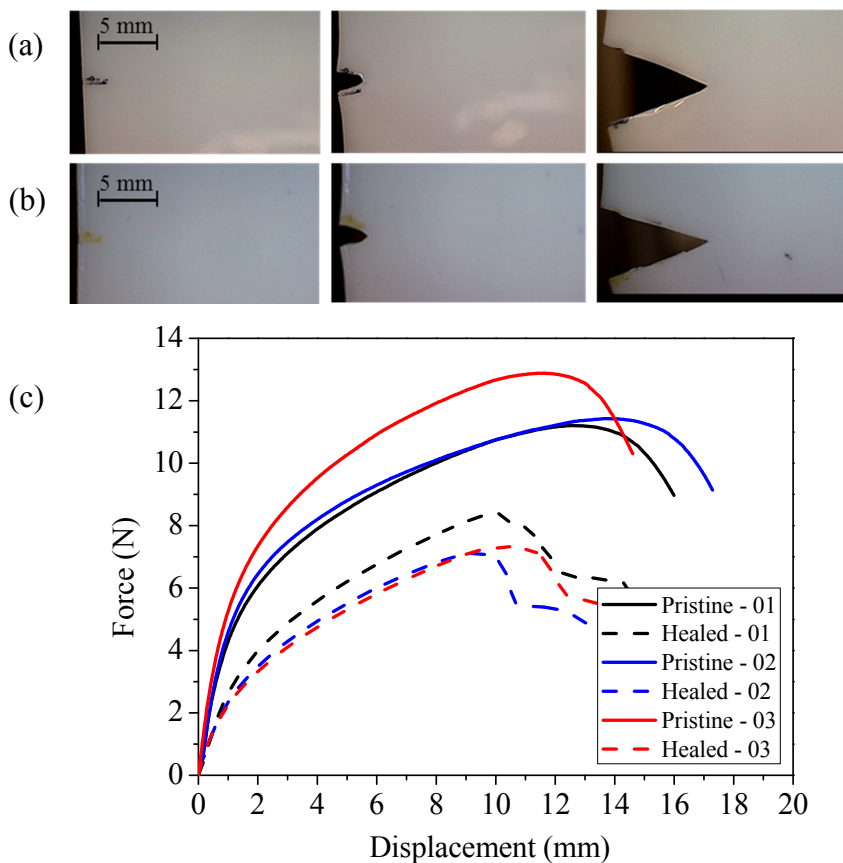

Figure 2.9. Evolution of crack opening during SENT test for pristine (a) and healed sample (b) and force-displacement curves of three pristine and healed samples of composition 3a (c).

Conclusions

In this chapter, the synthesis and characterization of first generation of healable hybrid sol-gel polymers containing reversible tetra-sulfide groups is described. The prepared hybrid sol-gel polymers exhibited thermal stability in the S-S bond cleavage temperature window and a significant gap closure capability at modest temperatures. The gap closure efficiency of prepared polymer was strongly affected by healing temperature, crosslinking density and content of reversible tetra-sulfide groups. Evaluation of mechanical and macroscopic flow properties of the healable hybrid sol-gel films revealed that despite the significant effect of the mechanical properties on the healing performance of the hybrid sol-gel films, the controlling factor in their gap closure and therefore healing performance is the content of reversible bonds (i.e. tetrasulfide groups).

References:

[1] J.D. Wright, N.A.J.M. Sommerdijk, The chemistry of sol-gel silicates, Sol-Gel Materials: Chemistry and Applications, Taylor & Francis Book Ltd, UK, 2001.

[2] G. Kickelbick, Introduction to Hybrid Materials, in: G. Kickelbick (Ed.) Hybrid Materials: Synthesis, Characterization, and Application, WILEY-VCH, Darmstadt, Germany, 2007, pp. 1-48.

[3] D.A. Loy, Sol–Gel Processing of Hybrid Organic–Inorganic Materials Based on Polysilsesquioxanes, in: G. Kickelbick (Ed.) Hybrid Materials: Synthesis, Characterization, and Application, WILEY-VCH, Darmstadt, Germany, 2007, pp. 225-254.

[4] R. Corriu, N. Trong Anh, Nanostructured Materials, Molecular Chemistry of Sol-Gel Derived Nanomaterials, John Wiley & Sons, Ltd2009, pp. 91-144.

[5] D.G. Shchukin, H. Möhwald, Self-Repairing Coatings Containing Active Nanoreservoirs, Small, 3 (2007) 926-943.

[6] M.L. Zheludkevich, M.G.S. Ferreira, Self-healing anticorrosion coatings, in: L. Fedrizzi, M.F. Montemor (Eds.) Self-Healing Properties of New Surface Treatments, European Federation of Corrosion Series, Maney Publishing:, UK, 2011.

[7] M. Abdolah Zadeh, S. van der Zwaag, S.J. Garcia, Self-healing corrosion protective sol-gel coatings based on extrinsic and intrinsic healing approaches, Advances in Polymer Science, (2015).

[8] S. Zwaag, Self healing materials: an alternative approach to 20 centuries of materials science, Springer Science+ Business Media BV2008.

[9] W.H. Binder, Self-healing polymers: from principles to applications, John Wiley & Sons2013.

[10] M. AbdolahZadeh, C. Esteves, A. Catarina, S. Zwaag, S.J. Garcia, Healable dual organic–inorganic crosslinked sol–gel based polymers: crosslinking density and tetrasulfide content effect, Journal of Polymer Science Part A: Polymer Chemistry, 52 (2014) 1953-1961.

[11] S.J. Garcia, Effect of polymer architecture on the intrinsic self-healing character of polymers, European Polymer Journal, 53 (2014) 118-125.

[12] F. Potier, A. Guinault, S. Delalande, C. Sanchez, F. Ribot, L. Rozes, Nano-building block based-hybrid organic-inorganic copolymers with self-healing properties, Polymer Chemistry, 5 (2014) 4474-4479.

[13] B. Gyarmati, Á. Némethy, A. Szilágyi, Reversible disulphide formation in polymer networks: A versatile functional group from synthesis to applications, European Polymer Journal, 49 (2013) 1268-1286.

[14] M. Mochulsky, A.V. Tobolsky, Chemorheology of polysulfide rubbers, Industrial & Engineering Chemistry, 40 (1948) 2155-2163.

[15] J. Canadell, H. Goossens, B. Klumperman, Self-healing materials based on disulfide links, Macromolecules, 44 (2011) 2536-2541.

[16] U. Lafont, H. van Zeijl, S. van der Zwaag, Influence of Cross-linkers on the Cohesive and Adhesive Self-Healing Ability of Polysulfide-Based Thermosets, ACS Applied Materials & Interfaces, 4 (2012) 6280-6288.

[17] H.P. Xiang, H.J. Qian, Z.Y. Lu, M.Z. Rong, M.Q. Zhang, Crack healing and reclaiming of vulcanized rubber by triggering the rearrangement of inherent sulfur crosslinked networks, Green Chemistry, (2015).

[18] J.J. Griebel, N.A. Nguyen, A.V. Astashkin, R.S. Glass, M.E. Mackay, K. Char, J. Pyun, Preparation of Dynamic Covalent Polymers via Inverse Vulcanization of Elemental Sulfur, ACS Macro Letters, 3 (2014) 1258-1261.

[19] J. Kamada, K. Koynov, C. Corten, A. Juhari, J.A. Yoon, M.W. Urban, A.C. Balazs, K. Matyjaszewski, Redox responsive behavior of thiol/disulfide-functionalized star polymers synthesized via atom transfer radical polymerization, Macromolecules, 43 (2010) 4133-4139.

[20] J.A. Yoon, J. Kamada, K. Koynov, J. Mohin, R. Nicolaÿ, Y. Zhang, A.C. Balazs, T. Kowalewski, K. Matyjaszewski, Self-Healing Polymer Films Based on Thiol–Disulfide Exchange Reactions and Self-Healing Kinetics Measured Using Atomic Force Microscopy, Macromolecules, 45 (2012) 142-149.

[21] H. Otsuka, S. Nagano, Y. Kobashi, T. Maeda, A. Takahara, A dynamic covalent polymer driven by disulfide metathesis under photoirradiation, Chemical Communications, 46 (2010) 1150-1152.

[22] Y. Amamoto, H. Otsuka, A. Takahara, K. Matyjaszewski, Self-Healing of Covalently Cross-Linked Polymers by Reshuffling Thiuram Disulfide Moieties in Air under Visible Light, Advanced Materials, 24 (2012) 3975-3980.

[23] R. Caraballo, M. Rahm, P. Vongvilai, T. Brinck, O. Ramstrom, Phosphine-catalyzed disulfide metathesis, Chemical Communications, (2008) 6603-6605.

[24] T. Oku, Y. Furusho, T. Takata, A Concept for Recyclable Cross-Linked Polymers: Topologically Networked Polyrotaxane Capable of Undergoing Reversible Assembly and Disassembly, Angewandte Chemie International Edition, 43 (2004) 966-969.

[25] M. Pepels, I. Filot, B. Klumperman, H. Goossens, Self-healing systems based on disulfide-thiol exchange reactions, Polymer Chemistry, 4 (2013) 4955-4965.

[26] A.V. Tobolsky, R.B. Beevers, G.D.T. Owen, The viscoelastic properties of crosslinked poly(ethylene tetrasulfide). I, Journal of Colloid Science, 18 (1963) 353-358.

[27] G.D.T. Owen, W.J. MacKnight, A.V. Tobolsky, Urethane Elastomers Containing Disulfide and Tetrasulfide Linkages, The Journal of Physical Chemistry, 68 (1964) 784-786.

[28] V.R. Sastri, G.C. Tesoro, Reversible crosslinking in epoxy resins. II. New approaches, Journal of Applied Polymer Science, 39 (1990) 1439-1457.

[29] G.C. Tesoro, V. Sastri, Reversible crosslinking in epoxy resins. I. Feasibility studies, Journal of Applied Polymer Science, 39 (1990) 1425-1437.

[30] I. Kende, T.L. Pickering, A.V. Tobolsky, The Dissociation Energy of the Tetrasulfide Linkage, Journal of the American Chemical Society, 87 (1965) 5582-5586.

[31] B. Ellis, Chemistry and technology of epoxy resins, Springer1993.

[32] A. Brandle, A. Khan, Thiol-epoxy 'click' polymerization: efficient construction of reactive and functional polymers, Polymer Chemistry, 3 (2012) 3224-3227.

[33] L.L. Hench, J.K. West, The sol-gel process, Chemical Reviews, 90 (1990) 33-72.

[34] W.J.v. Ooij, D. Zhu, Electrochemical Impedance Spectroscopy of Bis-[Triethoxysilylpropyl]Tetrasulfide on Al 2024-T3 Substrates, Corrosion, 57 (2001) 413-427.

[35] D. Katz, A. Tobolsky, Rubber elasticity in a highly crosslinked epoxy system, Polymer, 4 (1963) 417-421.

[36] D. Braun, H. Cherdron, M. Rehahn, H. Ritter, B. Voit, Polymer synthesis: theory and practice: fundamentals, methods, experiments, Springer Science & Business Media2012.

[37] C.J. Brinker, G.W. Scherer, Sol-gel science: the physics and chemistry of sol-gel processing, Academic press2013.

[38] T.L. Metroke, O. Kachurina, E.T. Knobbe, Spectroscopic and corrosion resistance characterization of GLYMO–TEOS Ormosil coatings for aluminum alloy corrosion inhibition, Progress in Organic Coatings, 44 (2002) 295-305.

[39] Y.S. Lipatov, T.T. Alekseeva, Phase-separated interpenetrating polymer networks, Springer2007.

[40] K.P. Menard, Dynamic mechanical analysis: a practical introduction, CRC press2008.

Chapter 3

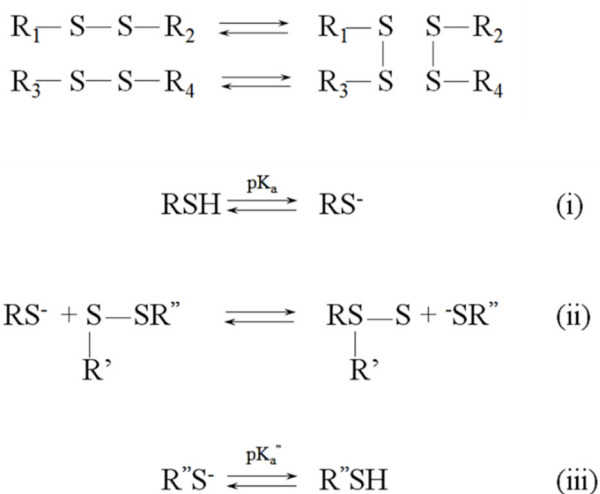## An insight into healing mechanism and kinetics of dual organic-inorganic sol-gel based polymers

Introduction

In the previous chapter it was demonstrated that small quantities of reversible tetrasulfide groups can induce enough mobility in the crosslinked network of hybrid sol-gel polymers to initiate macroscopic flow upon application of thermo-mechanical stimulus. A few approaches for incorporation of the reversible tetrasulfide groups in polymer networks have been reported in literature [1-7]. In analogy to the hybrid sol-gel polymers presented in the previous chapter, the rheological properties of the resulting polymers are strongly affected by the content of reversible bonds, the crosslinking density and the temperature [8-11]. The significant stress-relaxation ability of such crosslinked polymers was explained by tetrasulfide interchange mechanism. The proposed mechanism involves scission of the reversible sulfur-sulfur (S-S) bonds followed by their recombination to yield an unstressed chain (schematic 3.1a) [1-3, 8-11].

$$R_1-S-S-R_2 \rightleftharpoons R_1-S \quad S-R_2$$
$$R_3-S-S-R_4 \rightleftharpoons R_3-S \quad S-R_4$$

$$RSH \underset{}{\overset{pK_a}{\rightleftharpoons}} RS^- \qquad\qquad (i)$$

$$RS^- + \underset{R'}{S-SR''} \rightleftharpoons RS-S + {}^-SR'' \qquad (ii)$$
$$\underset{R'}{|}\phantom{S-SR'' \rightleftharpoons RS-S + {}^-}\underset{R'}{|}$$

$$R''S^- \underset{}{\overset{pK_a^{''}}{\rightleftharpoons}} R''SH \qquad\qquad (iii)$$

Schematic 3.1. Reshuffling of the reversible sulfur-sulfur (S-S) bonds via S-S interchange (a) and in presence of nucleophilic thiol groups (b).

Yet, the kinetics and mechanism of cleavage of tetrasulfide groups can be altered by nucleophilic agents such as thiol groups. In presence of small traces of thiol groups (0.01 wt%) the scission of tetrasulfide linkages might proceed via thiol-oligosufilde exchange

mechanism (schematic 3.1b) [9, 12]. In this case the exchange reactions consist of three consequent steps including i) ionization of thiol to thiolate anion ii) nucleophilic attack of thiolate anion on a sulfur atom of the tetrasulfide moiety and iii) protonation of the product thiolate anion [13, 14]. The kinetics and the resulting equilibrium constants of the exchange reactions are dominated by structure and therefore by the dissociation constant (pK_a) of thiol groups and their concentration [14, 15]. The oxidation of thiol groups under oxidative conditions particularly at high temperatures and basic pH values is a known phenomenon. The thermally accelerated oxidation of thiol groups can lead to a change in their concentration and therefore in the kinetics of thiol-oligosulfide exchange reactions [16-22].

In this chapter the gap closure kinetics of hybrid sol-gel polymers exhibiting the highest healing efficiency in chapter 2 were further evaluated under air and nitrogen flow to unravel the mechanisms involved in the healing process. Furthermore, to correlate the reversible groups state to the observed macroscopic flow and healing capability of the hybrid sol-gel polymers, the evolution of the reversible groups during the healing stage was monitored using a hot-stage coupled Raman spectrometer.

Experimental procedure

Materials

Epoxy resins based on Epikote[TM] 828 (184-190 g eq[-1]) and Ancamine®2500 curing agent (105-110 g eq[-1]) were provided by Akzo Nobel Aerospace Coatings (ANAC) and used as received. (3-Aminopropyl)trimethoxysilane (97%, MW=179.29 g mol^{-1}) and pentaerythritol tetrakis(3-mercaptopropionate) (>95%, MW=488.66 g mol^{-1}), from hereon called APS and tetra-thiol respectively, were purchased from Sigma-Aldrich, The Netherlands, and used without further purification. Bis[3-(triethoxysilyl)propyl]tetrasulfide (99%, MW=538.95 g mol^{-1}, total sulfur content>20%), from hereon called BS, and ethanol were purchased from Capture Chemicals, China, and VWR, The Netherlands, respectively and used as received.

Preparation

The healable hybrid sol-gel polymers were prepared as described in chapter 2. The organically modified silicone alkxodies (OMSAs) were sequentially (APS followed by BS) added to the epoxy resin with the OMSAs:epoxy resin weight ratio of 1:1, keeping

BS:APS molar ratio at 3:1. The mixture was stirred using a magnetic stirrer at 300 rpm for 3 h at room temperature. The organic crosslinker (Ancamine®2500) was then added keeping the amine hydrogen equivalent (AHE) to epoxy equivalent (EE) ratio at 1.1 and the mixture was stirred in a high speed mixer at 2500 rpm for 5 min. Tetra-thiol was then added to the mixture in a tetra-thiol:epoxy resin weight ratio 0.56:1 and the mixture was mixed in the high speed mixer for 40 s at 2500 rpm. The resulting mixtures were cast on Teflon plates using a 600 µm calibrated standard aluminum single doctor blade and cured for 2 h at 70 °C.

Characterization

Gap closure kinetics

The thermo-mechanical induced flow of the polymer leading to gap closure under air and N_2 flow was quantified by cutting the hybrid sol-gel films of 15×4 mm^2 in two pieces at room temperature. The cut pieces were placed 500 ± 20 µm apart from each other in a set-up designed to enable temperature, pressure and atmosphere control inside the test chamber. The designed set-up consisted of a DC power supply, a temperature control unit and a healing cell. The healing cell composed of three separate chambers. Over the course of the measurement, the sealed upper chamber was filled with compressed air with a regulated pressure enabling pneumatic pressure control in the middle chamber where the sample was placed. The atmosphere in the middle chamber was controlled by constant flux of air/N_2 at a flow rate of 40 mm.min^{-1}. The healing cell was heated up using a ring heater located in the lower chamber of the cell. The temperature in the middle chamber was monitored using a k-type thermocouple connected to the temperature control unit empowering temperature regulation with a precision of ± 1 °C.

The ability of the hybrid sol-gel polymer to close the gap under constant pressure of 40 kPa was studied at five different temperatures: 50, 60, 70, 80 and 90 °C under air and N_2 flow. A Keyence digital optical microscope with a depth-of-field and high resolution was employed for in-situ monitoring of the sample during the heating course. Images were captured in transmission mode every minute during the first 10 minutes and then every 5 minutes up to 20 minutes. The micrographs were analyzed using VHX-2000 software for gap area quantification. Assuming a uniform thickness of the samples, the gap closure efficiency was calculated using equation 2.1.

Meso-scale flow (Thermo-mechanical properties)

Thermo-mechanical analysis The thermo-mechanical properties of the films with the were evaluated using: (i) a Perkin Elmer Pyris Diamond DMTA analyzer to monitor the changes in the storage (E') and loss modulus (E'') as a function of temperature in the range of 20 to 90 °C. Samples were tested in tensile fixture at a constant heating rate of 2 °C min^{-1}, a frequency of 1 Hz, and a tension amplitude of 10 µm under air flow; and (ii) creep measurements on a stress-controlled Thermo-Fisher rheometer using a 20 mm parallel-plate geometry at 50, 70, and 90 °C and a constant shear stress of 50 Pa and nitrogen flow.

Raman spectroscopy Raman spectroscopy tests were performed using a U1000–high resolution double spectrometer from HORIBA Jobin Yvon with acquisition time of 1 min on a measurement spot of 1 mm diameter. The spectral region from 445 to 3260 cm^{-1} was collected using a laser with an excitation line of 632 nm at eight different temperatures in the interval of 20 to 90 °C with step of 10 °C. The temperature of the sample was controlled by a Linkam Scientific Instruments THMS600 hot-stage coupled to the Raman set-up, under atmospheric air or under a nitrogen flow (30 ml min^{-1}). The samples were heated from room temperature to the desired temperature at heating rate of 20 °C min^{-1} and kept at that temperature for 10 min for stabilization, prior to collection of the spectra.

Four spectral bands were chosen to evaluate the occurring chemical reactions: one for S-S stretching (v_{S-S} = 510 cm^{-1}) [23], one for C=O stretching ($v_{C=O}$ = 1743 cm^{-1}) [23], one for S-H stretching (v_{S-H} = 2570 cm^{-1}) [23, 24] and one to serve as the internal standard (v_{C-C} = 1186 cm^{-1}) [23, 25]. The spectra were baseline corrected and the peak area ratios (A v_{S-S}/ A v_{C-C}) were calculated to determine the S-S bond content.

Results & Discussion

Gap closure kinetics

As discussed in chapter 2, the gap closure performance of the healable hybrid sol-gel polymers is not only affected by the content of the reversible bonds and the crosslinking density but also by the healing temperature. To further investigate the observed behavior, the gap closure kinetics of the hybrid sol-gel polymers with BS:APS molar ratio of 3:1

showing the highest gap closure efficiency was studied in the temperature range of 50 to 90 °C under air and N_2 flow for maximum exposure time of 20 minutes. Figure 3.1 shows that the gap closure rate clearly depends on the healing temperature. Notwithstanding the differences in rate, full gap closure was obtained at all temperatures above 60 °C under both air and N_2 flow. At lower temperatures, 100% gap closure was not obtained for the maximum healing time used.
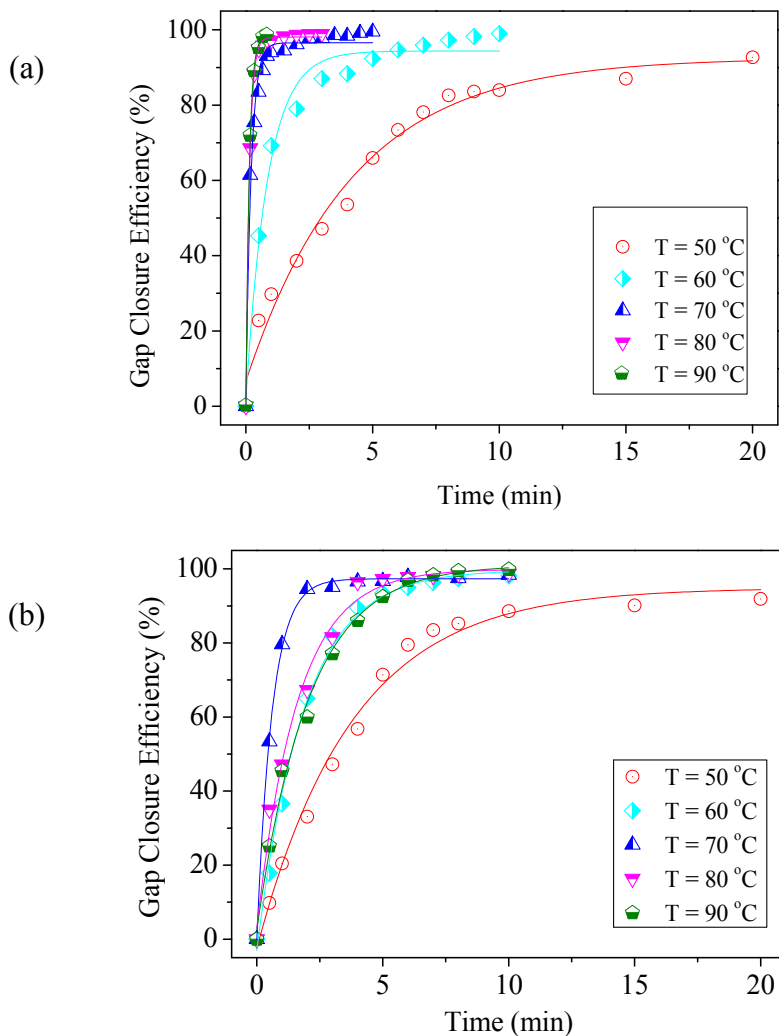

Figure 3.1. Gap closure kinetics of healable hybrid sol-gel polymers with BS:APS molar ratio 3:1 under N_2 (a) or air (b) flow.

As shown in Figure 3.1a for healing experiments under N_2 an increase in healing temperature led to an increase in gap closure rate, although beyond 70 °C the temperature dependence weakened. However, when testing was performed under an air flow (Figure 3.1b) the gap closure kinetics at 80 and 90 °C were slower than that at 70 °C, revealing an optimum gap closure kinetics around 70 °C. The lower healing kinetics at higher temperatures is indicative of presence of at least two competitive phenomena/reactions in the polymer during the thermally triggered healing process. While one set of reactions i.e. breaking of reversible tetrasulfide groups may provide the required chain mobility for the polymeric network and favor the macroscopic flow upon application of thermal stimulus, thermally accelerated side reaction can result in formation of new crosslinks and ultimately hinder the polymer flow.

To better correlate the observed temperature dependent macro-scale flow to the mobility of the networks formed, additional DMTA and creep tests were performed on the sample. The dynamic thermo-mechanical analysis of the healable hybrid sol-gel polymer (Figure 3.2) showed a gradual and continuous decrease in loss modulus (E") with the temperature while the storage modulus (E') decreased until reaching the rubbery plateau around 70 °C. This result indicates that beyond 70 °C there is no effect of the temperature on the elastic response of the material which points to the beneficial effect of the irreversible network. This is reflected in the rather high values for E' and E" (10^7 Pa) at high temperatures given the reversible nature of the part of the network.
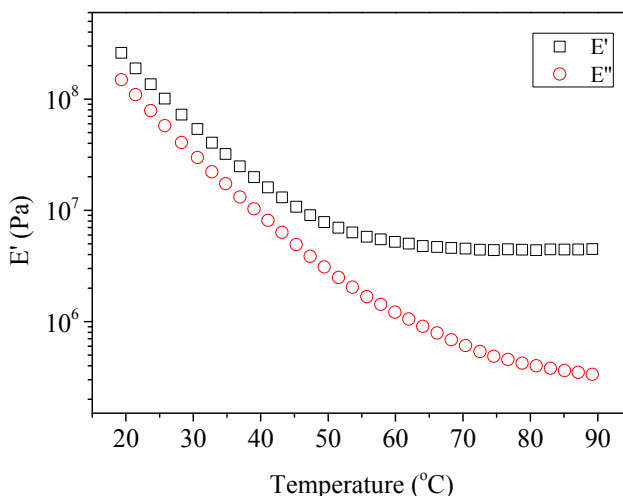

Figure 3.2. Temperature dependence of storage (E') and loss (E") modulus of healable hybrid sol-gel polymers with BS:APS molar ratio 3:1 under air flow.

The decrease of E', E" with increasing temperature up to 70 °C is in line with the results obtained from gap closure tests carried out at different temperatures. However, the absence of significant differences in elastic properties at 70 and 90 °C and the increased chain mobility at higher temperatures offers no explanation for the decrease in gap closure kinetics observed at the highest healing temperature under air flow.
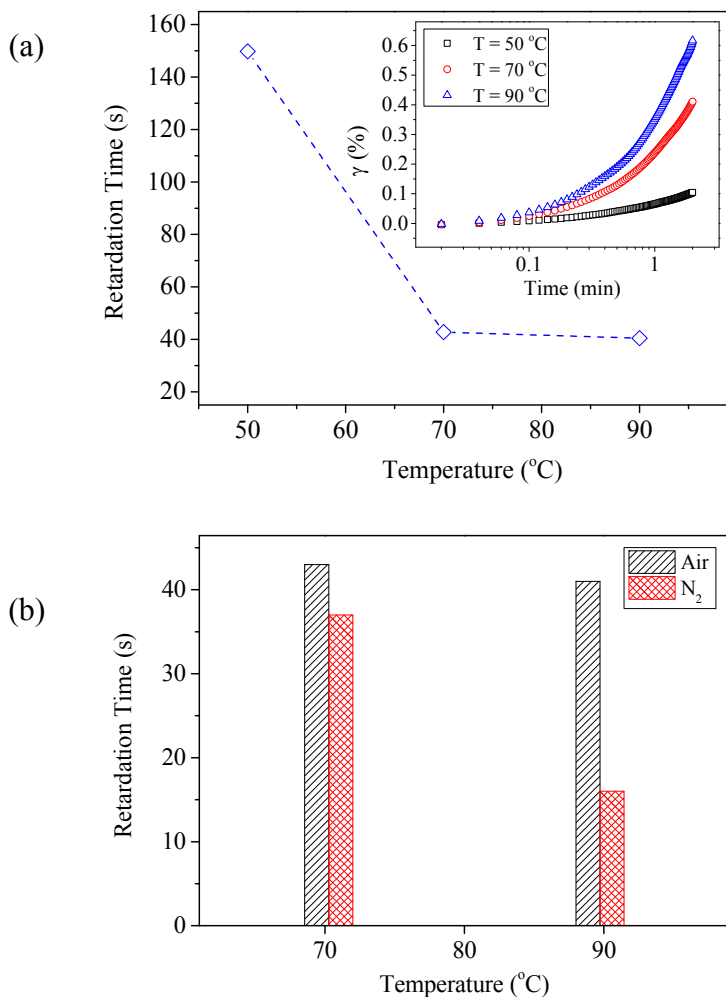

Figure 3.3. Deformation of the healable hybrid sol-gel polymer as a function of time (inset, a) and temperature dependence of retardation time under air flow (a) and retardation times at 70 and 90 °C in air and N$_2$ atmosphere (b).

The creep experiments performed at 50, 70 and 90 °C under air confirmed the temperature dependent flow behavior of the healable hybrid sol-gel polymers. Unlike the differences in gap closure rates, the creep tests revealed that the deformation of the samples increases as a function of temperature (Figure 3.3a). Retardation times derived using Burgers model showed a 3 fold decrease by increasing the temperature from 50 to 70 °C, yielding higher flow rates at 70 °C. Yet, the differences in gap closure rates at 70 and 90 °C were not reflected in the retardation times, as the retardation times were found to be equal suggesting a similar flow behavior which should lead to potentially equal gap closure rates at these temperatures.

The potential effect of thermally activated side reaction on meso-scale flow properties of the healable hybrid sol-gel polymers was further investigated by performing creep tests at 70 and 90 °C under N_2 flow. As shown in Figure 3.3b, the retardation time at 70 °C was only slightly affected by the testing atmosphere, while a significant decrease in retardation time was observed at 90 °C in the absence of oxygen. The reduced network mobility and therefore meso-scale flow of the hybrid sol-gel films in air, reflected by the lower retardation time in N_2 compared to that in air at 90 °C, can justify the lower healing kinetics observed at highest healing temperature. Yet, to get a better insight into the mechanism involved in meso-scle flow of the hybrid sol-gel films, hot-stage coupled Raman spectroscopy was employed to follow the evolution of tetrasulfide groups upon heating.

The Raman spectra of the healable hybrid sol-gel polymers at eight different temperatures is shown in Figure 3.4a. The characteristic resonance of S-S stretching ($v_{S-S} = 510$ cm^{-1}) [23] was chosen for the identification and qualitative quantification of S-S bonds at different temperatures. Using the C-C stretching band ($v_{C-C} = 1186$ cm^{-1}) [23, 25] as the internal standard, the normalized peak area of S-S vibration ($A\,v_{S-S}(T) / A\,v_{C-C}(T)$) was used to calculate the amount of S-S links at each temperature. The calculated peak ratios were further normalized with respect to their initial value at room temperature according to equation 3.1 and the obtained values are plotted as a function of temperature in Fig. 3.4.

$$Relative\ Content\ of\ S-S\ Bonds\ (\%) = \frac{\left[A_{v\,S-S}\,(T) \Big/ A_{v\,C-C}\,(T) \right]}{\left[A_{v\,S-S}\,(RT) \Big/ A_{v\,C-C}\,(RT) \right]} \times 10 \quad \text{Eq. 3.1}$$
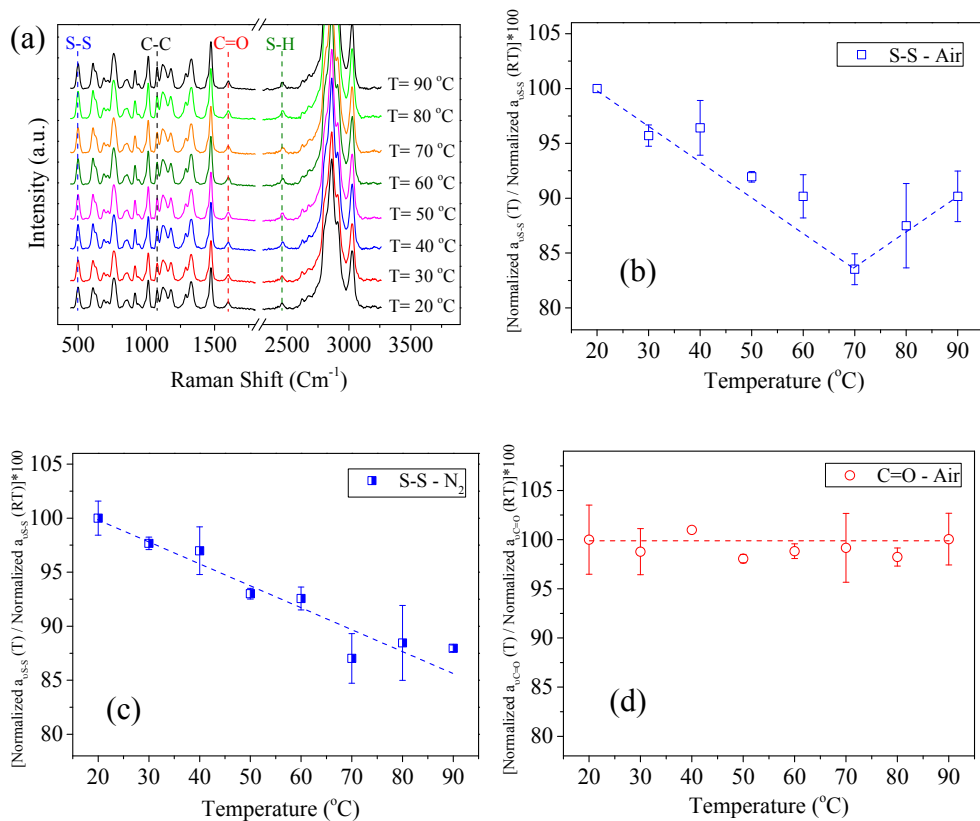
Figure 3.4. Raman spectra of healable hybrid sol-gel polymer at different temperatures (a) and [Normalized Peak Area (T) /Normalized Peak Area (RT)] for S-S under air flow (b) S-S under N_2 flow (c) and C=O under air flow (d).

As Figure 3.4b shows, the amount of S-S bonds decreased linearly with temperature up to a temperature of 70 °C. Upon a further temperature increase, the content of S-S bonds increased when the measurement was performed in air. A similar dependence has been observed in proteins [18] but has not been reported for (self-healing) polymers. The increase in S-S bond content at elevated temperatures can be attributed to oxidation of thiol groups. Presence of thiol groups in the polymer network was confirmed by Raman spectroscopy (υ_{S-H} = 2570 cm^{-1}) [23, 24] at all the tested temperatures. Under oxidative conditions thiol groups can undergo oxidation reactions according to Eq. 3.2. The degree of conversion of such reactions is strongly pH and temperature dependent. The

50

basic pH values as well as high temperatures strongly promote oxidation of thiol group to disulfide bonds [15, 16, 18-21].

$$-SH + HS- \xrightarrow{O_2} -S-S-$$ Eq. 3.2

Unlike the temperature dependence of the content of S-S bonds in air, the tests performed under N_2 flow revealed a continuous decrease in their content as a function of temperature. This observation can provide further confirmation for the significant role of testing atmosphere on the thermally accelerated side reactions such as oxidation of thiol groups.

The amount of S-S bonds showing Raman activity at a certain temperature is an indication of the state of those bonds at that temperature. The minimal amount of these bonds at 70 °C under air flow indicates that a higher proportion of these reversible bonds are broken at this temperature, yielding a higher chain mobility for the system and enabling the macroscopic flow required to close the artificial gap. To confirm the selective breaking of S-S bonds using temperature as the triggering agent, the changes in the content of C=O bonds ($v_{C=O} = 1743$ cm^{-1}) as a function of temperature were also monitored using the same criteria, revealing no significant changes in the content of carbonyl groups (Figure 3.4d).

Although participation of the tetrasulfides groups in temperature triggered healing of the developed hybrid polymers is undeniable, the mechanisms involved in the breaking stage of such bonds are not fully understood yet. The bond cleavage can result from an interchange between the tetrasulfide links [1-3, 10, 11] or it can be due to thiol-oligosulfide exchange reactions [26-28]. Although thiol-disulfide exchange reactions in solution has been confirmed by GC-MS, the occurrence of such reactions in solid state in polymers has yet not been reported.

The healing mechanism based on the temperature triggered cleavage of reversible bonds was further investigated by a set of experiments involving multiple healing cycles at three different temperatures (50, 70 and 90 °C) and collection of Raman spectra upon heating the samples to the desired temperature and cooling them down to room temperature for four consecutive cycles.

The ability of the hybrid sol-gel polymers to undergo multiple healing events was assessed by aging the samples at any of the selected temperatures for a time equivalent to those required to reach full healing (gap closure) in air. The temperature program employed for aging of the samples and collection of Raman spectra is shown in Figure 3.5.
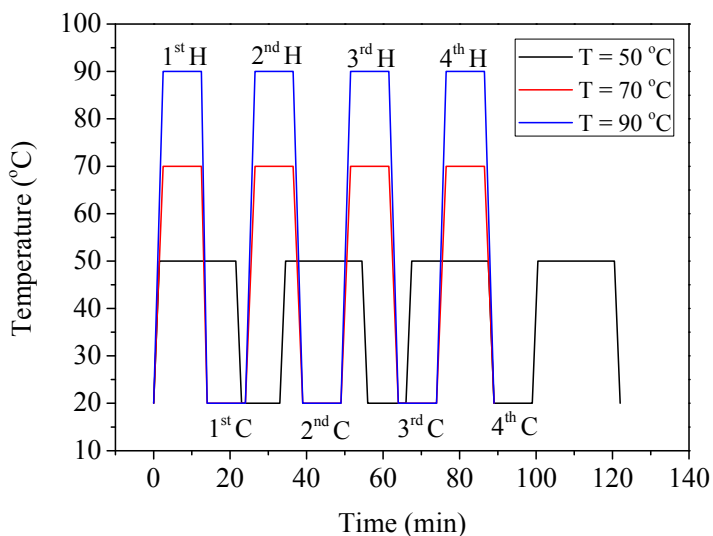
Figure 3.5. The schematics of the temperature program employed for aging of the hybrid sol-gel polymer and collection of Raman spectra; H and C in the plot represent the heating and cooling steps of the cycles, respectively.

The gap kinetics for four consecutive cycles and the content of S-S bonds corresponding to the heating and cooling steps of the cycles are shown in Figure 3.6. As Figures 3.6a and 3.6b show, the gap closure kinetic curves for all the consecutive healing cycles at both 50 and 70 °C overlapped, demonstrating the ability of hybrid sol-gel films to undergo multiple healing events with no decrease in their healing characteristics. Nevertheless, the gap closure kinetics at 90 °C showed a clear slow down after every single healing cycle at this temperature, although full gap closure was achieved for all the four cycles after 10 minutes annealing at 90 °C (Figure 3.6c).
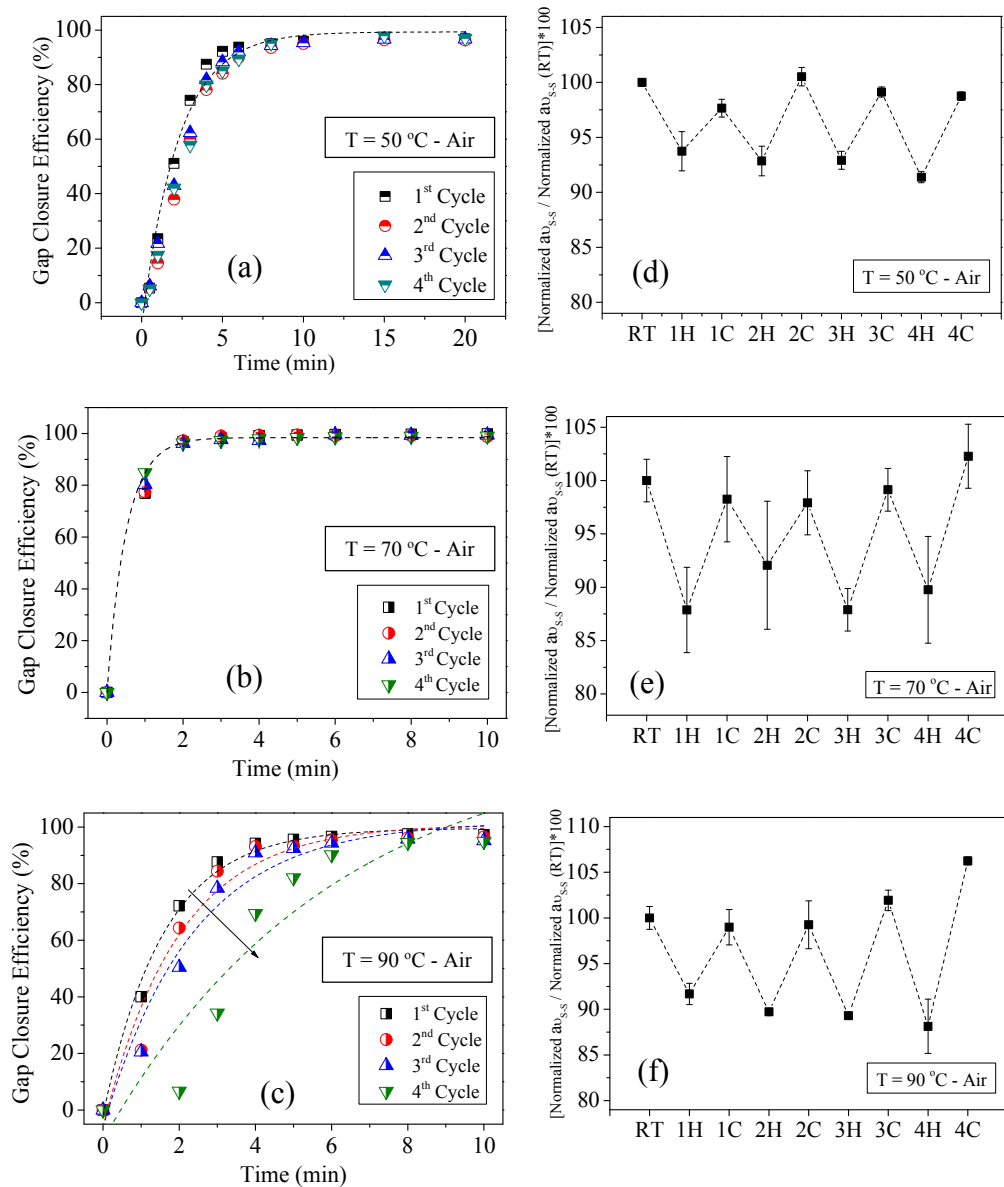
Figure 3.6. Gap closure kinetics of the hybrid sol-gel polymer for four consecutive healing cycles at 50 °C (a) 70 °C (b) 90 °C (c) and percentage of S-S bonds calculated as [Normalized Peak Area (T) /Normalized Peak Area (RT)] at 50 °C (d) 70 °C (e) and 90 °C (f) under air flow upon four heat and cool cycles (b). H and C stand for heat and cool cycles, respectively.

The amount of the S-S bonds present in the hybrid sol-gel polymers after each heating and cooling step was quantified using the peak area criteria described earlier. As can be seen in Figures 3.6d, 3.6e and 3.6f, in spite of differences in the content of detected S-S bonds upon heating to 50, 70 and 90 °C, heating the hybrid sol-gel polymers lowered the content of the these bonds for all the heating steps indicating their cleavage using thermal stimulus. Upon cooling the samples from 50 and 70 °C, the amount of the S-S bonds increased, reaching their original value at room temperature, suggesting complete reformation of these thermo-reversible bridges. Interestingly, cooling the hybrid sol-gel polymers from 90 °C led to a gradual increase in the amount of S-S bonds compared to their initial value at room temperature after each cycle (heating + cooling step). This suggests that in addition to reformation of broken thermo-reversible bonds, an additional source contributes to formation of new S-S bonds, further confirming oxidation of thiol groups to S-S groups according to Eq. 3.2 in presence of oxygen at high temperatures [18].

Oxidation of thiol groups during thermal cycling will increase the crosslinking density of hybrid sol-gel polymers via formation of new S-S bonds. As argued in the previous chapter, a higher crosslinking density leads to a lower gap closure efficiency. Yet, the new crosslinks (S-S bonds) are thermo-reversible, implying that their negative effect on flow properties represented by gap closure kinetics will fade over time as long as the required thermal energy for scission of S-S bonds is provided (as it was pointed out by full gap closure of the hybrid sol-gel films after the 4th healing cycle despite the slower kinetics Figure 3.6c).

The gap closure efficiencies of hybrid sol-gel films after 2, 5 and 10 minutes annealing at 90 °C are plotted for four healing cycles against the corresponding fraction of S-S bonds in the beginning of each healing cycle (Figure 3.7). The fraction of new S-S bonds (compared to the original population) is calculated using equation 3.3. As Figure 3.7 shows, an increase in the amount of the S-S bonds (i.e. the new crosslinks) leads to a linear decrease in the measured gap closure efficiencies. However, the observed effect is more pronounced at early stages of gap closure test (e.g. 2 minutes) and tends to level-off over time (e.g. after 5 and 10 minutes). This can be attributed to the thermo-reversible nature of the S-S bonds; over time and upon providing enough thermal energy the newly formed thermo-reversible crosslinks can break boosting the kinetics of gap closure process.

$$Fraction\ of\ newof\ S-S\ Bonds\ (\%) = \left(\frac{A_{v\ S-S}\ (T) \big/ A_{v\ C-C}(T)}{A_{v\ S-S}(RT) \big/ A_{v\ C-C}(RT)} - 1 \right) \times 100$$
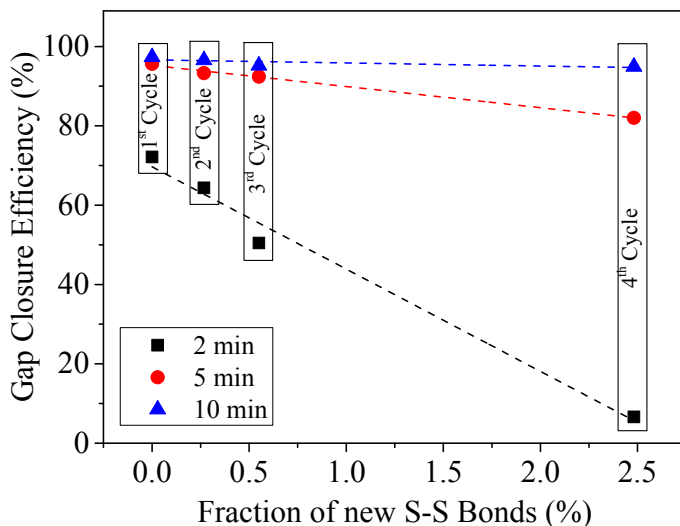
Eq. 3.3

Figure 3.7. Gap closure efficiencies after 2 (■), 5 (●) and 10 minutes (▲) at 90 °C in air for 4 healing cycles as a function of fraction of new S-S bonds (respect to the original population) present in the hybrid sol-gel films.

To eliminate/reduce the oxidation of thiol groups, the hybrid sol-gel polymers were aged at 90 °C using the procedure described earlier but now under N_2 flow. Evaluation of gap closure kinetics of these series of samples under air flow revealed equivalent kinetics for four consecutive cycles (Figure 3.8a). Additionally, the content of S-S bonds decreased upon heating and restored their initial value at room temperature upon cooling for all the heating and cooling steps. Notwithstanding the effect of thermally accelerated oxidation reactions on gap closure kinetics of hybrid sol-gel films, the results presented in Figure 3.6 and 3.8 confirm the reversible nature of tetrasulfide groups and correlate it to the multiple healing capability of such polymers.
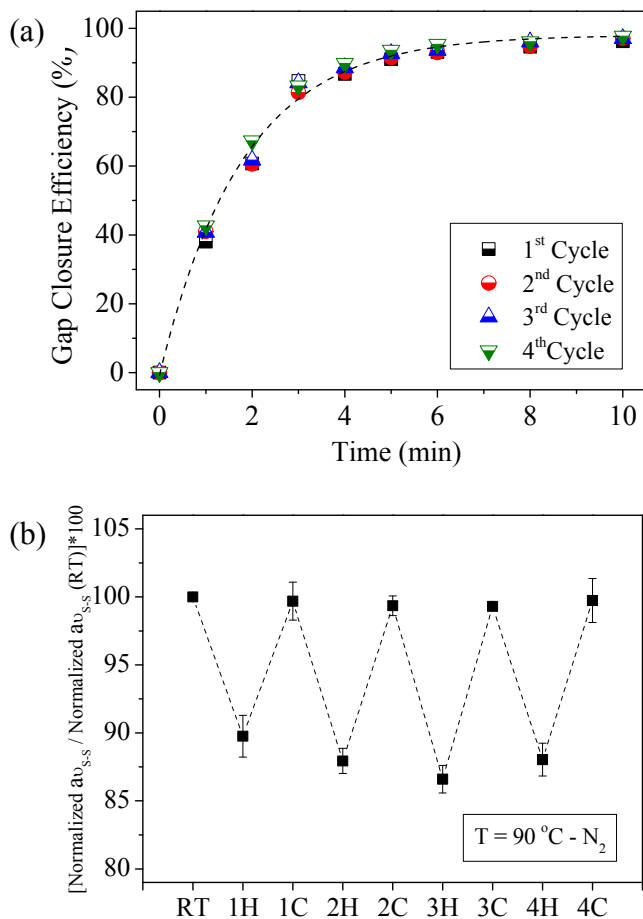
Figure 3.8. Gap closure kinetics of hybrid sol-gel polymers for four consecutive healing cycles at 90 °C (a) and percentage of S-S bonds calculated as [Normalized Peak Area (T) /Normalized Peak Area (RT)] under air N_2 upon four heat and cool cycles (b). H and C stand for heat and cool cycles, respectively.

Conclusions

In this chapter several experimental procedures were employed to unveil the mechanisms involved in the healing process of the hybrid sol-gel polymer. Dynamic thermo-mechanical analysis of the hybrid sol-gel polymer complemented by hot-stage coupled

Raman spectroscopy suggests the increased mobility of the system achieved by thermally triggered selective breaking of S-S bonds as the main mechanism involved in the healing process.

Faster gap closure kinetics of the hybrid sol-gel polymer at 70 °C compared to 80 and 90 °C in air revealed presence of two sets of competing phenomena in the polymer during the thermally triggered healing process; i) cleavage of reversible tetrasulfide groups as well as increased chain mobility favoring macroscopic flow, ii) thermally accelerated oxidation of thiol groups resulting in formation of new thermo-reversible crosslinks and hindering the polymer flow. Yet, as a result of thermo-reversible nature of the new crosslinks, despite the lower kinetics, full gap closure was achieved at temperatures higher than the optimum healing temperature in air.

References:

[1] A.V. Tobolsky, R.B. Beevers, G.D.T. Owen, The viscoelastic properties of crosslinked poly(ethylene tetrasulfide). I, Journal of Colloid Science, 18 (1963) 353-358.
[2] G.D.T. Owen, W.J. MacKnight, A.V. Tobolsky, Urethane Elastomers Containing Disulfide and Tetrasulfide Linkages, The Journal of Physical Chemistry, 68 (1964) 784-786.
[3] W.J. MacKnight, G.E. Leroi, A.V. Tobolsky, Physical chemistry of crosslinked polysulfide elastomers, Journal of Chemical Education, 42 (1965) 4.
[4] V.R. Sastri, G.C. Tesoro, Reversible crosslinking in epoxy resins. II. New approaches, Journal of Applied Polymer Science, 39 (1990) 1439-1457.
[5] G.C. Tesoro, V. Sastri, Reversible crosslinking in epoxy resins. I. Feasibility studies, Journal of Applied Polymer Science, 39 (1990) 1425-1437.
[6] J.J. Griebel, N.A. Nguyen, A.V. Astashkin, R.S. Glass, M.E. Mackay, K. Char, J. Pyun, Preparation of Dynamic Covalent Polymers via Inverse Vulcanization of Elemental Sulfur, ACS Macro Letters, 3 (2014) 1258-1261.
[7] K. Kishore, K. Ganesh, Polymers containing disulfide, tetrasulfide, diselenide and ditelluride linkages in the main chain, Polymer Synthesis/Polymer Engineering, Springer Berlin Heidelberg1995, pp. 81-121.
[8] M.D. Stern, A.V. Tobolsky, Stress‐Time‐Temperature Relations in Polysulfide Rubbers, The Journal of Chemical Physics, 14 (1946) 93-100.
[9] M. Mochulsky, A.V. Tobolsky, Chemorheology of polysulfide rubbers, Industrial & Engineering Chemistry, 40 (1948) 2155-2163.
[10] A. Tobolsky, W. MacKnight, M. Takahashi, Relaxation of disulfide and tetrasulfide polymers, The Journal of Physical Chemistry, 68 (1964) 787-790.
[11] A. Tobolsky, W. MacKnight, M. Takahashi, Relaxation of Disulfide and Tetrasulfide Polymers, Rubber Chemistry and Technology, 39 (1966) 524-529.
[12] B. Gyarmati, Á. Némethy, A. Szilágyi, Reversible disulphide formation in polymer networks: A versatile functional group from synthesis to applications, European Polymer Journal, 49 (2013) 1268-1286.

[13] A. Fava, A. Iliceto, E. Camera, Kinetics of the Thiol-Disulfide Exchange, Journal of the American Chemical Society, 79 (1957) 833-838.

[14] J. Houk, G.M. Whitesides, Structure-reactivity relations for thiol-disulfide interchange, Journal of the American Chemical Society, 109 (1987) 6825-6836.

[15] H.F. Gilbert, Thiol/disulfide exchange equilibria and disulfide bond stability, Methods Enzymol., 251 (1995) 8-21.

[16] W.H. Sawyer, Heat Denaturation of Bovine β-Lactoglobulins and Relevance of Disulfide Aggregation, Journal of Dairy Science, 51 (1967) 323-329.

[17] K. Shimada, J.C. Cheftel, Sulfhydryl group/disulfide bond interchange reactions during heat-induced gelation of whey protein isolate, Journal of Agricultural and Food Chemistry, 37 (1989) 161-168.

[18] F.J. Monahan, J.B. German, J.E. Kinsella, Effect of pH and temperature on protein unfolding and thiol/disulfide interchange reactions during heat-induced gelation of whey proteins, Journal of Agricultural and Food Chemistry, 43 (1995) 46-52.

[19] M.H. Morel, J. Bonicel, V. Micard, S. Guilbert, Protein Insolubilization and Thiol Oxidation in Sulfite-Treated Wheat Gluten Films during Aging at Various Temperatures and Relative Humidities, Journal of Agricultural and Food Chemistry, 48 (2000) 186-192.

[20] M.A. de la Fuente, H. Singh, Y. Hemar, Recent advances in the characterisation of heat-induced aggregates and intermediates of whey proteins, Trends in Food Science & Technology, 13 (2002) 262-274.

[21] M.V. Trivedi, J.S. Laurence, T.J. Siahaan, The role of thiols and disulfides in protein chemical and physical stability, Current protein & peptide science, 10 (2009) 614-625.

[22] M. Conte, K. Carroll, The Chemistry of Thiol Oxidation and Detection, in: U. Jakob, D. Reichmann (Eds.) Oxidative Stress and Redox Regulation, Springer Netherlands2013, pp. 1-42.

[23] P. Larkin, IR and Raman Spectra-Structure Correlations: Characteristic Group Frequencies, Infrared and Raman spectroscopy; principles and spectral interpretation, Elsevier2011.

[24] M. Kieninger, O.N. Ventura, Calculations of the infrared and Raman spectra of simple thiols and thiol–water complexes, International Journal of Quantum Chemistry, 111 (2011) 1843-1857.

[25] R. Marques de Melo, M.A. Bottino, R.K.H. Galvão, W.O. Soboyejo, Bond strengths, degree of conversion of the cement and molecular structure of the adhesive–dentine joint in fibre post restorations, Journal of Dentistry, 40 (2012) 286-294.

[26] T. Oku, Y. Furusho, T. Takata, A Concept for Recyclable Cross-Linked Polymers: Topologically Networked Polyrotaxane Capable of Undergoing Reversible Assembly and Disassembly, Angewandte Chemie, 116 (2004) 984-987.

[27] J.A. Yoon, J. Kamada, K. Koynov, J. Mohin, R. Nicolaÿ, Y. Zhang, A.C. Balazs, T. Kowalewski, K. Matyjaszewski, Self-Healing Polymer Films Based on Thiol–Disulfide Exchange Reactions and Self-Healing Kinetics Measured Using Atomic Force Microscopy, Macromolecules, 45 (2012) 142-149.

[28] M. Pepels, I. Filot, B. Klumperman, H. Goossens, Self-healing systems based on disulfide-thiol exchange reactions, Polymer Chemistry, 4 (2013) 4955-4965.

Chapter 4

Time resolved evaluation of healable dual organic-inorganic sol-gel based polymers

Introduction

In the previous chapters a healable dual organic-inorganic sol-gel based polymer containing dynamic tetrasulfide groups was presented. The thermo-reversible tertasulfide groups enabled thermo-mechanical induced tuneable flow of the crosslinked network while the irreversible organic and inorganic crosslinks preserved network integrity during the healing event. The developed polymeric system demonstrated remarkable macroscale damage closure (flow) capabilities with an optimal healing kinetics at 70 °C, followed by partial restoration of interfacial strength.

The structure of the polymer network at the healed interface plays a crucial role on its mechanical strength. Therefore, a deep insight into the contributing phenomena in the interfacial healing process is essential for potential applications in engineering fields such as coatings and adhesives. The healing performance of the polymeric systems is strongly affected by the chemistry and the structure of the polymer, e.g. content of the reversible bonds, crosslinking density, chain stiffness and intra-molecular interactions [1-4]. Moreover, for engineering applications such as protective coatings, evaluation of the long term performance of the material is essential.

To date there is not a testing protocol able to clearly separate and quantify the impact of these different processes on the healing mechanism. The standard tensile tests are usually employed to evaluate the healing performance of the different polymeric systems [5, 6]. Yet, the tensile procedure fails to distinguish the different processes taking place at the interface. Testing protocol based on fracture mechanics principle can potentially lead to a better understanding of the phenomena involved during the healing process, as recently demonstrate by Grande et al [7].

Based on the results presented in the previous chapters, the healable hybrid sol-gel polymer shows a clear elasto-plastic behaviour. Hence, accurate quantification of the fracture toughness is feasible using a nonlinear fracture mechanics protocol. Several approaches ranging from modifications of the original linear elastic fracture Griffith's criterion (e.g. Irwin, Dugdale or Barenblatt) to evaluation of the essential work of fracture or J-integral are proposed in literature [8-11]. The later method, originally developed by Rice and Cherepanov, is adopted to evaluate the fracture behaviour of materials including non-linear effects such as plasticity, hyper-elasticity, etc [12, 13]. The J-integral evaluation can be carried out using different notched sample geometries. However geometrical correction factors should be taken into account to effectively estimate the fracture properties of a given material [8, 14]. In most of the published works SENT and DENT are the common test geometries due to related easy test

procedure and data interpretation [15]. Yet, the later specimen type is selected because of further consistency and reproducibility [16, 17].

Although the healing performance of the polymers based on sulphur chemistry has been well documented in literature [18], the effect of the evolution of such dynamic networks on their interfacial healing efficiencies has not been addressed. Based on the results presented in the previous chapter, an effect of aging condition on the properties of the developed polymer is foreseeable. Therefore, a comprehensive study of the time-evolution of the polymer structure and mechanical properties is required for long-term applications in complex engineering systems.

In this chapter, the time-resolved behaviour of the sol-gel based polymer containing thermo-reversible tetra sulphide groups and the related deep impact on mechanical, viscoelastic and healing properties are presented. Rheological measurements were performed to evaluate the time/frequency dependent properties exhibited by the polymer through the application of the well-known time-temperature superposition (TTS) principle [19]. Aging kinetics of the polymer was followed by monitoring the evolution of the dynamic shear moduli at different temperatures. Furthermore, to investigate the effect of aging on the hybrid sol-gel polymer bulk properties and its interfacial healing performance, flow and fracture tests were carried out on both freshly prepared and aged samples, highlighting a different healing degree between the two samples. A possible explanation of such as experimental observation is also proposed correlating the availability of reversible bonds within the broken interface to the restored fracture properties and the global polymer network arrangement to the evolving bulk properties.

Experimental procedure

Materials

Epoxy resin based on Epikote[TM] 828 (184-190 g eq[-1]) and Ancamine®2500 curing agent (105-110 g eq[-1]) were provided by Akzo Nobel Aerospace Coatings (ANAC) and used as received. (3-Aminopropyl)trimethoxysilane (97%, MW=179.29 g mol^{-1}) and pentaerythritol tetrakis(3-mercaptopropionate) (>95%, MW=488.66 g mol^{-1}), from hereon called APS and tetra-thiol respectively, were purchased from Sigma-Aldrich, The Netherlands, and used without further purification. Bis[3-(triethoxysilyl)propyl]tetrasulfide (99%, MW=538.95 g mol^{-1}, total sulfur

content>20%), hereon BS, was purchased from Capture Chemicals, China and used as received.

Polymer preparation

The polymers were prepared as described in chapter 2. The organically modified silicone alkxodies (OMSAs) were sequentially (APS followed by BS) added to the epoxy resin with the OMSAs:epoxy resin weight ratio of 1:1, keeping BS:APS molar ratio at 3:1. The mixture was stirred using a magnetic stirrer at 300 rpm for 3 h at room temperature. The organic crosslinker (Ancamine®2500) was then added to the mixture keeping the amine hydrogen equivalent (AHE) to epoxy equivalent (EE) ratio at 1.1 and the mixture was stirred in a high speed mixer at 2500 rpm for 5 min. Tetra-thiol was then added in a tetra-thiol:epoxy resin weight ratio 0.56:1 and the mixture was further mixed in the high speed mixer for 40 s at 2500 rpm. The resulting mixture was casted in a PTFE mould to obtain polymeric films of 80 x 25 x 2 mm and subsequently was cured for either 2 or 48 h at 70 °C in an air circulated oven yielding fresh and aged samples, respectively.

Characterization

DMTA: Dynamic mechanical thermal analysis (DMTA) measurements with in-situ FTIR were performed using a Haake Mars III, Thermofisher rheometer coupled with Nicolet iS10 FTIR spectrometer. Circular samples of 20 mm diameter were tested in oscillatory shear mode using parallel-plate geometry.

TTS: Storage (G') and loss (G'') shear moduli were measured as a function of temperature, frequency and time. A shear strain amplitude of 0.5% was employed to stay in the linear viscoelastic range of the prepared hybrid sol-gel based polymer.

The frequency sweep scans were performed at different temperatures in a range of 25 °C and 60 °C with a temperature step of $\Delta T = 5$ °C. Storage (G') and loss (G'') modulus master curves were then generated applying the time temperature superposition principle (TTS).

Kinetics: The dynamic shear modulus was measured at a frequency of 1 Hz at seven different temperatures in the range of 50-110 °C with a step of 10 °C. The evolution of the dynamic shear modulus was followed for at least 2 hours at the each of the test temperatures. Simultaneous rheological and FTIR data were collected at every 10 minutes during the experiment. The time-resolved evolution of Si-O-Si bonds was

followed by monitoring the changes in peak area of its characteristic resonance ($\upsilon_{Si-o-Si}$ = 1036 cm^{-1}).

Raman spectroscopy Raman spectroscopy tests were performed using a U1000–high resolution double spectrometer from HORIBA Jobin Yvon with acquisition time of 1 min on a measurement spot of 1 mm diameter. The spectral region from 445 to 3260 cm^{-1} was collected using a laser with an excitation line of 632 nm at room temperature.

Gap closure test: Gap closure experiments were performed in order to study the flow behaviour of the polymer under different testing conditions. The testing protocol introduced in Chapter 3 was adopted.

Tensile: The tensile mechanical properties of the prepared films were evaluated at room temperature using a Zwick 1455 tensile testing machine. The dog-bone shaped samples were tested in tension with a 1 kN load cell, a cross-head speed of 10 mm.min^{-1} and a gauge length of 20 mm.

Fracture: To evaluate the degree of interfacial strength recovery of fresh and aged polymers achieved during the healing process, double edge notched tension (DENT) tests were performed at room temperature on pristine and healed samples. DENT specimens were prepared by casting the hybrid polymers in a mould of 45 × 25 × 2 mm. Two 10 mm long notch was made in the middle of the specimen edge using a sharp razor blade. The samples were tested using a Zwick 1455 tensile testing machine equipped with a 1 kN load cell, a cross-head speed of 10 mm.min^{-1} and a gauge length of 25 mm. The tested samples were then placed in a Teflon mould designed to correctly align the two crack planes and the mould with sample was placed in an air circulation oven at 70 °C for a given time (2 h). The healed samples were subsequently notched at the previously damaged sites and tested using the same methodology. All experiments were recorded with a camera in order to detect the crack initiation and to follow its propagation.

Results & Discussion

Thermal dynamic analysis

Oscillatory rheological measurements and subsequent application of the TTS principle for fresh polymer (i.e. hybrid sol-gel polymer cured for 2 h) demonstrated evolution of

an irreversible network manifested by a constant and gradual increase in the storage shear modulus (G') of the polymer after certain temperatures (Figure 1.a). A possible explanation of the behaviour exhibited by the fresh polymer is occurrence of some side reactions above this temperature (e.g. oxidation and condensation of silanol groups). According to these results, the validity of the TTS in a wide temperature range is questionable, thus application of the TTS principle for the fresh polymer was limited up to 60 °C. Additionally, shift factor (a_t) for the fresh material was fitted with an Arrhenius law up to 60 °C (Figure 4.1 c) [19]:

$$\log(a_t) = \frac{E_a}{R}\left(\frac{1}{T} - \frac{1}{T_0}\right)$$ Eq. 4.1

where E_a is the activation energy, R is the universal gas constant, and T_0 is a reference temperature. Fitting the shift factor of the fresh polymer yielded an E_a of about 19 kcal.mol^{-1} which is in good agreement with the one reported in literature for tetra-sulphide containing polysulphide rubbers [20].

On the other hand, the aged polymer (i.e. hybrid sol-gel polymer cured for 48 h at 70 °C) showed a different behaviour, as demonstrate in Figure 1.b. In this case, no further evolution of the storage modulus was detected at the higher temperatures during the frequency sweep experiments indicating a stabilisation of the mechanical properties due to the aging process. The application of the TTS principle was then possible in all the studied temperature range. In this case, a higher E_a (31.7 kcal.mol^{-1}) was obtained from the temperature dependent a_t indicating a lower tendency to relax upon deformation.

Comparing the obtained master curves for fresh and aged polymers (Figure 4.1 a) indicates that the aged polymer has higher elastic properties (G') in all the frequency range compared to the fresh one, clearly suggesting a lower crosslinking density for the fresh polymer [21]. Additionally, the higher loss modulus (G") of the aged polymer in the studied frequency range implies higher chain mobility potential of the fresh polymer compared to its aged counterpart (Figure 4.1 b). These aspects can play a critical role on the healing process since they have a direct impact on the network mobility.

To evaluate the effect of the network re-arrangement on the healing performance of the studied polymer, understanding the origin of the evolution of the dual network is crucial. Generally, different experimental techniques such as rheology and spectroscopic analysis are employed to study the evolution of the material properties during time/temperature triggered aging processes. In this research work a hyphenated experimental procedure combining rheology and FTIR measurements was used to simultaneously investigate the evolutions of the mechanical properties and chemical reactions under aging conditions.
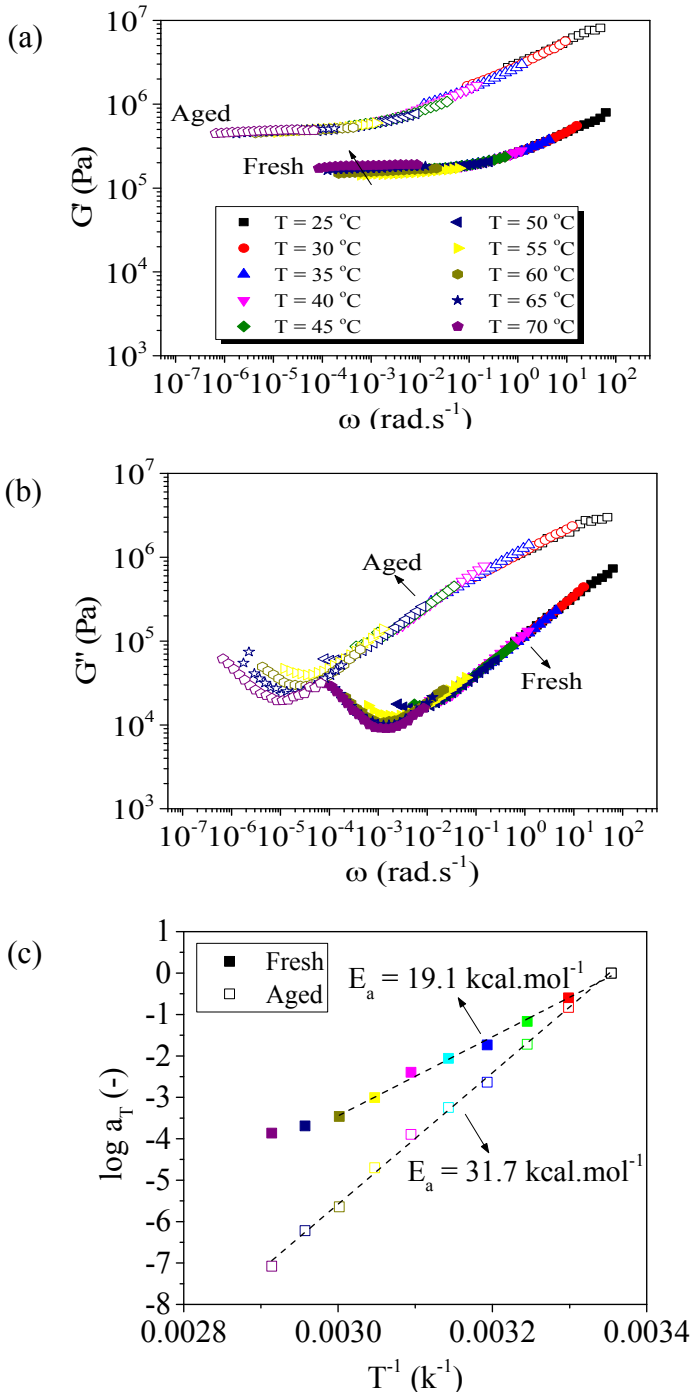
Figure 4.1. G' (a) and G" (b) master curves at 25 °C and shift factor v.s. T^{-1} (c).

From the mechanical point of view, time sweep scans illustrated a gradual increase of the storage modulus (G') depending on the sample temperature (Figure 4.2 a), in particular, higher temperatures resulted in a rapid growth of the storage modulus (G') over the course of the measurements. As Figure 4.2 a shows, below 60 °C, there is no change in the storage modulus for the longest tested time (2 h). However, at temperatures higher than 60 °C, the storage modulus increased linearly without reaching a plateau on the time scale of 2 h. Defining the storage modulus growth rate, as the slope of the different aging curves in Figure 4.2 a, an exponential dependence of it on the aging temperature was obtained (Figure 2.b). The detected G' evolution may indicate the formation of new bonds, stiffening the polymeric network. This behaviour can have a strong effect on the healing kinetic affecting the polymer flow behaviour and potentially also the dynamic of the exchange of the S-S linkages.
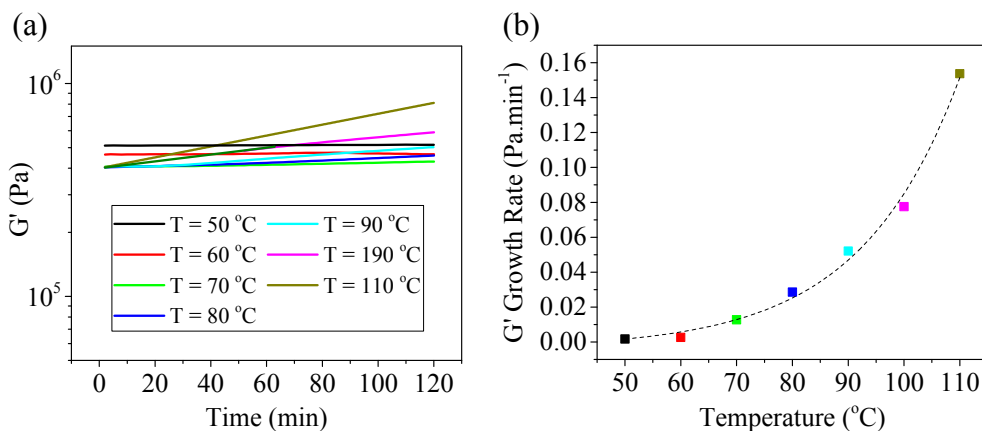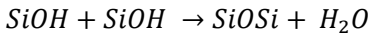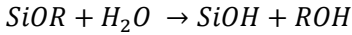

Figure 4.2. The rheological time sweep scans at different temperatures (a) and the corresponding growth rate of the elastic modulus (G').

To clarify the origin of such dynamic behavior, rheological measurements were complemented with FTIR spectroscopy. The FTIR spectra of the fresh polymer during a time sweep rheological scan at 100 °C are presented in Figure 4.3 a. The FTIR spectra of the sample showed several characteristic bands in the spectral range of 4000-500 cm^{-1}; e.g. υ = 3450 cm^{-1} corresponding to O-H and N-H stretching, υ = 2968, 2925 and

2880 cm^{-1} associated with C-H stretching, υ = 1608 and 1450 cm^{-1} assigned to the aromatic ring stretching, υ = 1340 cm^{-1} associated with C-N stretching, υ = 1036 cm^{-1} corresponding to Si-O-Si stretching and υ = 550 cm^{-1} assigned to C-S stretching [22-24].

To get an insight to the nature of chemical reactions proceeding during the thermally triggered aging process, the FTIR spectra were studied in the whole spectral range. As Figure 4.3 b shows, the peaks associated with the organic network (e.g. $\upsilon_{C=C-C}$ = 1450 cm^{-1}, υ_{C-N} = 1340 cm^{-1} and υ_{C-S} = 550 cm^{-1}) exhibited no detectable changes over the course of the measurement. However, the characteristic peaks of the organically modified silicone alkoxides (OMSAs) i.e. υ_{Si-OH} = 956 cm^{-1}, $\upsilon_{Si-OC2H5}$ = 1075 cm^{-1}, $\upsilon_{Si-OCH3}$ = 1100 cm^{-1} and $\upsilon_{Si-O-Si}$ = 1036 cm^{-1} varied considerably over 2 hours at 100 °C. While the intensity of the characteristic resonances of the SiOCH$_3$, SiOC$_2$H$_5$ and SiOH decreased, the one of the Si-O-Si significantly increased during the time sweep rheological scan (Figure 4.3 c). The variation of the aforementioned peak intensities can be explained by the following condensation reactions [25]:

$$SiOR + H_2O \rightarrow SiOH + ROH$$
$$SiOR + SiOH \rightarrow SiOSi + ROH \qquad\qquad\qquad \text{Eq. 4.2}$$
$$SiOH + SiOH \rightarrow SiOSi + H_2O$$

As Eq. 4.2 illustrates, the condensation reactions of the alkoxy silanes (i.e. SiOCH$_3$ and SiOC$_2$H$_5$) and silanol groups (SiOH) results in formation of Si-O-Si bridges, justifying the descending trend in the peak intensities of the former groups and the ascending trend of Si-O-Si resonance.

Using the C-H stretching band (υ_{C-H} = 2969 cm^{-1}) as the internal standard, the amount of SiOCH$_3$, SiOC$_2$H$_5$ and SiOH groups as well as Si-O-Si links at given times and temperatures were calculated using their normalized peak intensities based on the following Eq.:

$$Content\ of\ the\ Groups = {I\left(\nu_{Group}\right)_{T,t}} \Big/ {I\left(\nu_{C-H}\right)_{T,t}} \qquad\qquad \text{Eq. 4.3}$$
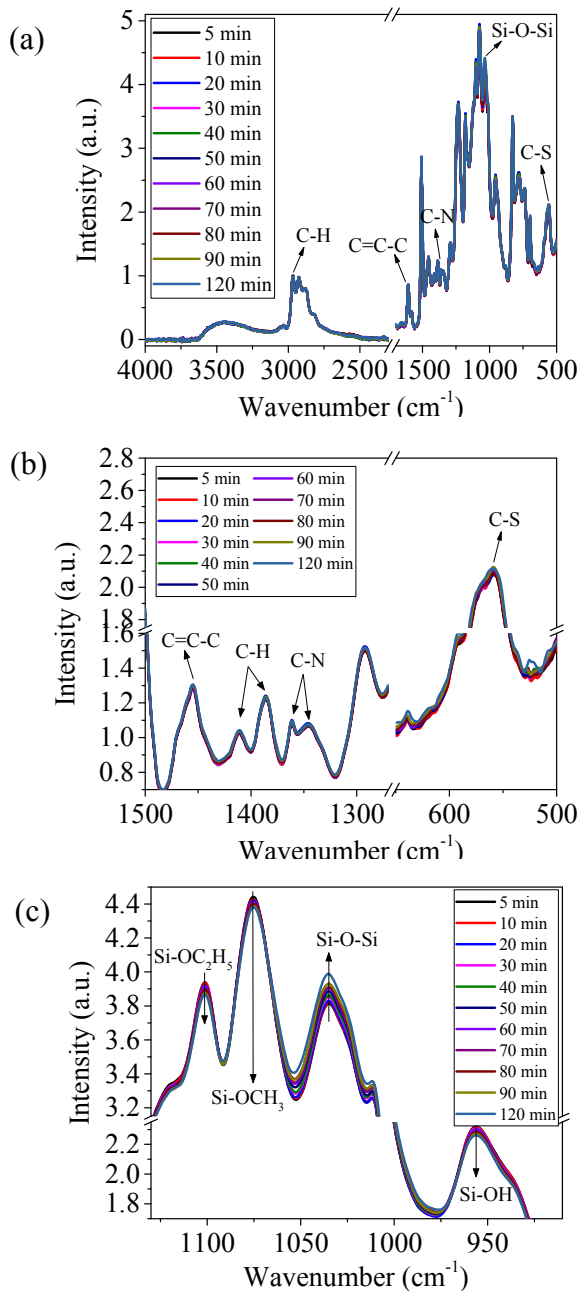
Figure 4.3. The FTIR spectra of the fresh hybrid sol-gel polymer in the spectral range of 4000-500 cm^{-1} (a), 1500-500 cm^{-1} (b) and 1150-900 cm^{-1} (c) measured every 10 minutes during a time sweep rheological scan at 100 °C.

Figure 4.4 shows that apart from 50 and 60 °C for which the content of the studied groups remained constant, the amount of $SiOCH_3$, $SiOC_2H_5$ and SiOH groups decreased linearly over the course of the measurements, though the rate of the change was strongly influenced by temperature. Higher temperatures lead to rapid decay of the aforementioned groups. The observed decrease in the content of the alkoxy silane and silanol groups associated with an increase in the content of the Si-O-Si bridges and therefore the crosslinking density of the inorganic network. In agreement with the rheological time sweep scans, the growth rate of the Si-O-Si links increased exponentially as a function of the testing temperature, manifesting the direct correlation between the content of newly formed irreversible bonds and the enhanced mechanical properties.
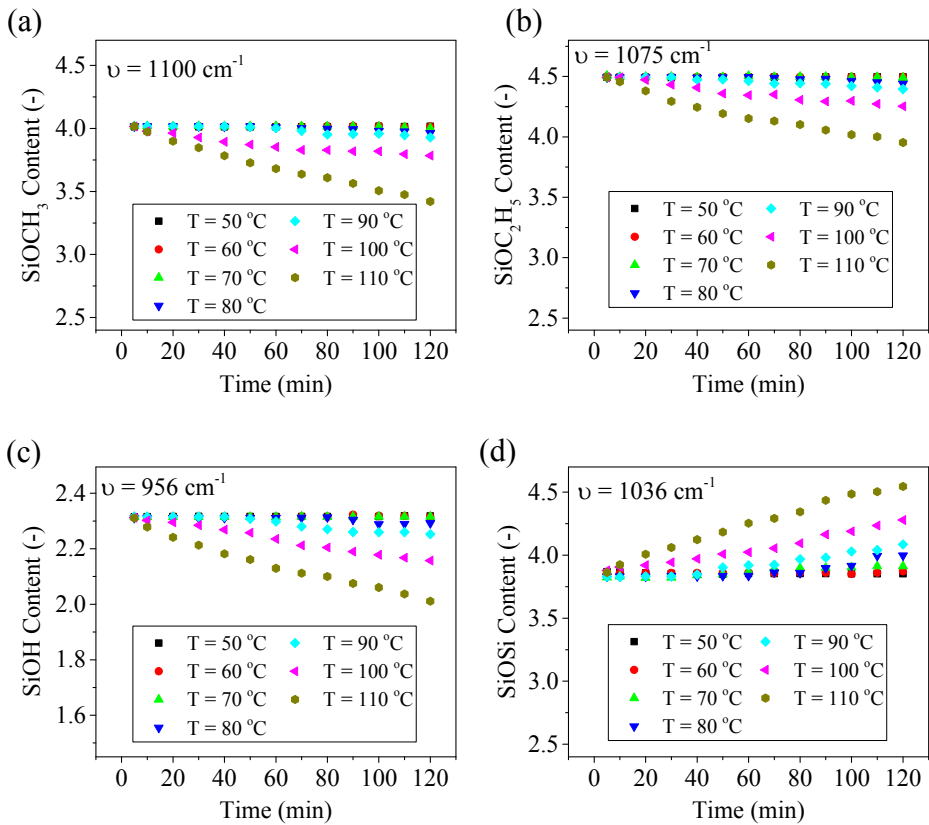

Figure 4.4. The evolution of $SiOCH_3$ (a), $SiOC_2H_5$ (b), SiOH groups (c) and Si-O-Si bonds (d) in the fresh hybrid sol-gel polymer during rheological time sweep scan performed at different temperatures.

The evolution of the storage modulus and the content of the Si-O-Si links in the fresh polymer during a post cure step (48 hours at 70) yielding the aged polymer, was monitored using the FTIR coupled rheometer. As Figure 4.5 a shows the storage modulus (G') of the polymer increased exponentially over 48 hours, reaching a plateau at the end of the measurement. The amount of the Si-O-Si links calculated using the peak intensity criteria (Eq. 4.3) followed the same trend, further confirming the direct correlation between increased crosslinking density due to formation of the irreversible Si-O-Si bridges and the improved mechanical properties demonstrated by higher storage modulus values (G'). The obtained results further illustrate stabilization of the mechanical properties of the aged hybrid sol-gel polymer.

(a) (b)

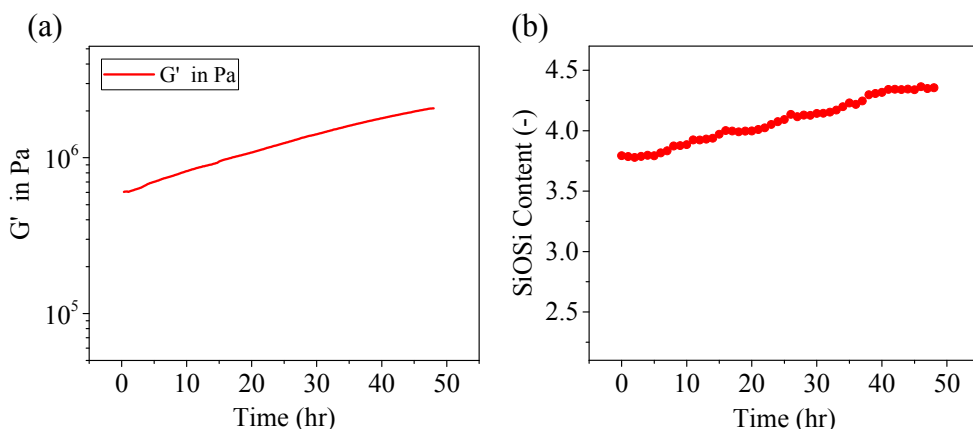Figure 4.5. The evolution of G' (a) and content of Si-O-Si links (b) in the fresh hybrid sol-gel polymer during a rheological time sweep scan performed at 70 °C.

Additionally, as addressed in chapter 3, the post curing step can promote oxidation of thiol groups, yielding a higher concentration of S-S bonds in the aged polymer. Presence of free thiol groups in both fresh and aged samples was confirmed by presence of the characteristic resonance of S-H bonds (υ_{S-H} = 2570 cm^{-1}) [22, 26] in their Raman spectra (Figure 4.6). The characteristic resonance of S-S stretching (υ_{S-S} = 510 cm^{-1}) [22] was chosen for the identification and qualitative quantification of S-S bonds in the two sets of samples. Using the C-C stretching band (υ_{C-C} = 1186 cm^{-1}) as the internal standard,

the amount of S-S and S-H bonds at room temperature were calculated using the peak area ratio as described in chapter 3. While the amount of S-H bonds was 3.8% lower in the aged polymer compared to the fresh one, the content of the S-S links was about 1.5% higher, further confirming temperature triggered oxidation of free thiol groups to S-S.
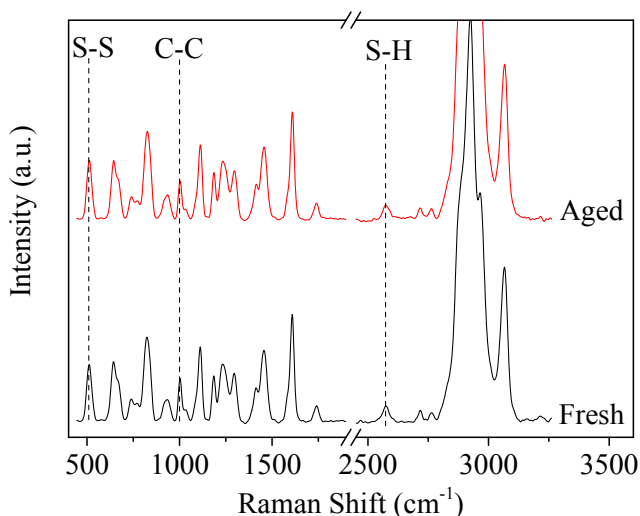

Figure 4.6. Raman spectra of the fresh and healed hybrid sol-gel polymer.

Flow behaviour and tensile properties

As discussed in chapter 2, the gap closure performance of the healable hybrid sol-gel polymers is strongly affected by temperature, content of the reversible bonds and the crosslinking density. To study the effect of the aging on the flow and therefore the healing performance of the hybrid sol-gel polymer, gap closure tests were carried out on both fresh and aged polymers at 70 °C. The gap closure kinetic plots presented in Figure 4.7, clearly show reduced flow of the aged polymer compared to the fresh one. While the fresh sample is able to close a gap with an average width of 500 µm in less than 5 min, the aged material took more than 20 min to cover and close a gap of the same dimension. These results are well in-line with previous rheological measurements, where higher E_a was found for the aged polymer.
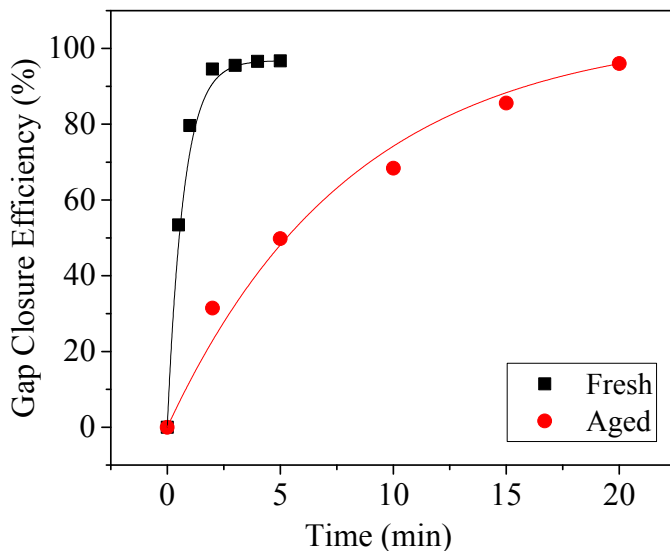
Figure 4.7. The gap closure kinetics of the fresh and aged hybrid sol-gel polymer at 70 °C.

The lower kinetics of the aged polymer can be attributed to the higher crosslinking density achieved by formation of new Si-O-Si bridges, as demonstrated earlier in the FTIR studies. The increased crosslinking density can also lead to enhanced mechanical properties. Figure 4.8 shows that the aged polymer exhibited a yield stress of about 3 MPa, three time higher than the fresh polymer. Moreover a pronounced strain hardening behaviour (slope of the stress-strain curve after yielding) was observed after the aging cycle. On the other hand, the fresh polymer showed an extended plastic region (from ~ 2.5% strain up to the break point) compared to the aged one. All the observed aspects indicate a reduced flow tendency and a less ductile behavior of the aged polymer both at high and room temperatures [27].
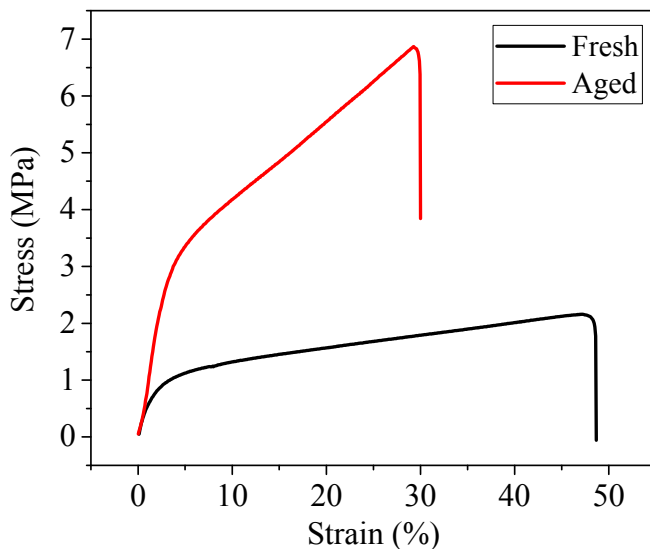
Figure 4.8. Stress-strain plots of the fresh and aged hybrid sol-gel polymer.

Fracture analysis

In a recent publication, experimental procedures based on fracture mechanics were addressed as a useful tool to evaluate the interfacial healing of soft polymers. Accordingly, a fracture mechanics protocol has been employed in this research. Fracture experiments were performed on both the fresh and the aged polymers. The effect of the healing time on the interfacial healing of the hybrid sol-gel polymers was studied by performing the test after different healing time (10 min, 30 min, 1 h, 2 h, 4 h and 12 h).

The load-displacement curves for the virgin DENT samples and the ones healed at 70 °C for different times are presented in Figure 4.9. The healing temperature was selected based on previous results presented in Chapter 2, as an optimum exchange kinetics of the chemical species involved in the recovery of the interfacial properties observed around 70 °C.
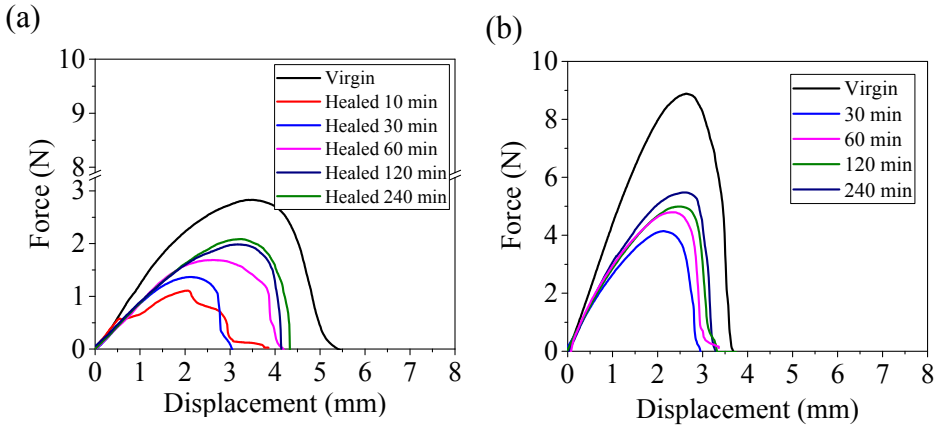
Figure 4.9. Force-displacement plots of the virgin and healed DENT specimens for the fresh (a) and the aged (b) hybrid sol-gel polymer.

As Figure 4.9 a shows, lower mechanical properties were exhibited by the healed DENT specimens of the fresh polymer. Additionally, a preliminary healing time dependent behaviour was detected for the fresh polymer. A similar response was observed for the aged polymer, as shown in Figure 4.9 b.

To estimate the material resistance to crack propagation, the critical J-integral value (J_{IC}) was selected as reference parameter. Crack initiation was detected by image analysis of the recorded video, as illustrated in Figure 4.10. The healing efficiency was calculated based on the following Eq.:

$$Healing\ efficiency\ (\%) = \frac{J_{IC}^{Healed}}{J_{IC}^{Virgin}} \times 100 \hspace{2cm} Eq.\ 4.4$$

where J_{IC}^{Healed} and J_{IC}^{Virgin} are the critical J-integral for healed and virgin samples, respectively.

By analysing the data in terms of recovery of the fracture properties (recovery of J_{IC}), a different trend in the healing efficiency of the fresh and aged polymers was detected (Figure 4.11).
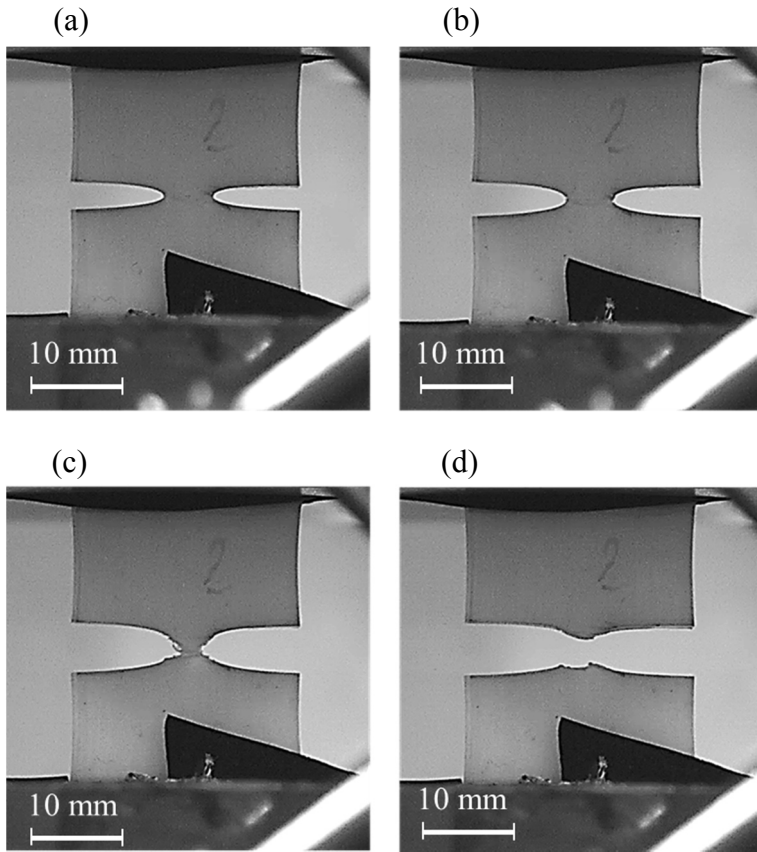
Figure 4.10. Micrographs of the DENT specimen of the fresh hybrid sol-gel polymer during the fracture test corresponding to loading (a), crack initiation (b), crack propagation (c) and failure (d).

As Figure 4.11 shows, the healing efficiency of the fresh polymer continuously increased as a function of healing time from about 20% reaching a plateau of around 60% after 2 hour annealing at 70 °C. Yet, the aged polymer exhibited a great recovery of the fracture property (around 45%) for short healing times (higher than the fresh polymer). Moreover, a lower increment in healing efficiency with healing time for the aged polymer was observed.Although the obtained results seem to be in contrast with the ones obtained in the rheological and flow behaviour studies, they might be explained
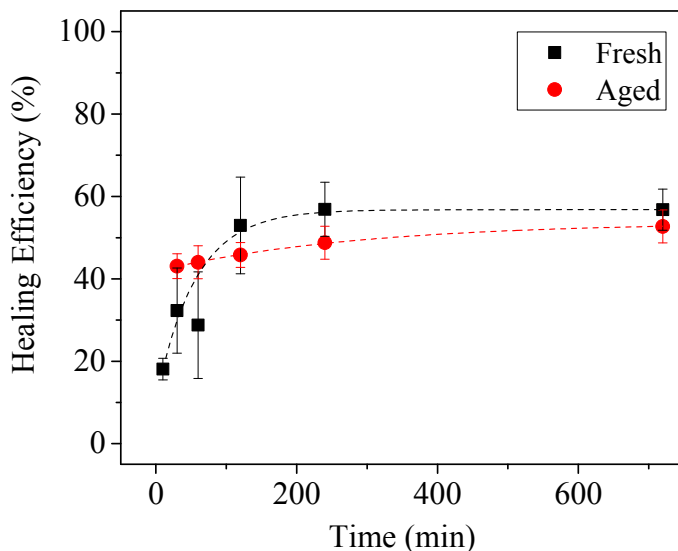
Figure 4.11. Healing efficiencies of the fresh and aged hybrid sol-gel polymers calculated on the basis of their J_{IC} values.

by a higher wetting of the fracture surfaces of the aged polymer due to more intimate contact compared to the fresh one. Smoother fracture surface can be obtained for the aged polymer due to its more "brittle" behaviour observed in tensile experiments. The effect of surface wetting is also reported in literature [1] demonstrating its prominent influence on the kinetics of the healing process in polymeric materials.

Interestingly, both of the fresh and the aged polymers showed a similar degree of healing after the longest healing time, indicating an equivalent extent of chain bridging at the fracture site. It is then possible to assume that the aging of the hybrid sol-gel polymer does not directly affect the dynamic of the reversible bonds, however it clearly has an influence on the global viscoelastic behaviour of the material and potentially on the morphology of the fracture surfaces. Both aspects have a direct impact on the healing process since they affect the capability of the material to flow and to promote an efficient contact between the fracture surfaces.

Conclusions

In this chapter several experimental procedures were adopted to evaluate the effect of aging on the properties of the hybrid sol-gel polymer including its healing efficiency. A fracture mechanics protocol was introduced to assess the recovery of interfacial properties. The simultaneous rheological and FTIR measurements revealed an increased cross-linking density of the hybrid sol-gel polymer due to the thermally triggered aging process as a result of formation of new Si-O-Si links, reducing its flow kinetics. Yet the chemical species involved in the healing (S-S and S-H groups) were not significantly affected, yielding an equivalent degree of interfacial healing for the fresh and aged hybrid sol-gel polymer due to availability of reversible groups at the fracture surface.

References:

[1] R.P. Wool, K.M. O'Connor, A theory crack healing in polymers, Journal of Applied Physics, 52 (1981) 5953-5963.
[2] Y.H. Kim, R.P. Wool, A theory of healing at a polymer-polymer interface, Macromolecules, 16 (1983) 1115-1120.
[3] T. Ge, M.O. Robbins, D. Perahia, G.S. Grest, Healing of polymer interfaces: Interfacial dynamics, entanglements, and strength, Physical Review E, 90 (2014) 012602.
[4] S.J. Garcia, Effect of polymer architecture on the intrinsic self-healing character of polymers, European Polymer Journal, 53 (2014) 118-125.
[5] P. Cordier, F. Tournilhac, C. Soulie-Ziakovic, L. Leibler, Self-healing and thermoreversible rubber from supramolecular assembly, Nature, 451 (2008) 977-980.
[6] A. Rekondo, R. Martin, A. Ruiz de Luzuriaga, G. Cabanero, H.J. Grande, I. Odriozola, Catalyst-free room-temperature self-healing elastomers based on aromatic disulfide metathesis, Materials Horizons, 1 (2014) 237-240.
[7] A.M. Grande, S.J. Garcia, S. van der Zwaag, On the interfacial healing of a supramolecular elastomer, Polymer, 56 (2015) 435-442.
[8] H.-H.-B. von Schmeling, Deformation and Fracture of High Polymers, Definition and Scope of Treatment, Polymer Fracture, Springer Berlin Heidelberg1987, pp. 1-15.
[9] Y.-W. Mai, P. Powell, Essential work of fracture and j-integral measurements for ductile polymers, Journal of Polymer Science Part B: Polymer Physics, 29 (1991) 785-793.
[10] E. Clutton, Essential work of fracture, in: A.P. D.R. Moore, J.G. Williams (Eds.) European Structural Integrity Society, Elsevier2001, pp. 177-195.
[11] X.-K. Zhu, J.A. Joyce, Review of fracture toughness (G, K, J, CTOD, CTOA) testing and standardization, Engineering Fracture Mechanics, 85 (2012) 1-46.
[12] G.P. Cherepanov, Crack propagation in continuous media: PMM vol. 31, no. 3, 1967, pp. 476–488, Journal of Applied Mathematics and Mechanics, 31 (1967) 503-512.
[13] J.R. Rice, A path independent integral and the approximate analysis of strain concentration by notches and cracks, Journal of applied mechanics, 35 (1968) 379-386.

[14] G. Ramorino, S. Agnelli, R. De Santis, T. Riccò, Investigation of fracture resistance of natural rubber/clay nanocomposites by J-testing, Engineering Fracture Mechanics, 77 (2010) 1527-1536.

[15] T.L. Anderson, T. Anderson, Fracture mechanics: fundamentals and applications, CRC press2005.

[16] M. Rink, L. Andena, C. Marano, The essential work of fracture in relation to J-integral, Engineering Fracture Mechanics, 127 (2014) 46-55.

[17] D.R. Moore, J.G. Williams, A. Pavan, Fracture mechanics testing methods for polymers, adhesives and composites, Elsevier2001.

[18] W.H. Binder, Self-healing polymers: from principles to applications, John Wiley & Sons2013.

[19] J.D. Ferry, Viscoelastic properties of polymers, John Wiley & Sons1980.

[20] M. Mochulsky, A.V. Tobolsky, Chemorheology of polysulfide rubbers, Industrial & Engineering Chemistry, 40 (1948) 2155-2163.

[21] K.P. Menard, Dynamic mechanical analysis: a practical introduction, CRC press2008.

[22] P. Larkin, IR and Raman Spectra-Structure Correlations: Characteristic Group Frequencies, Infrared and Raman spectroscopy; principles and spectral interpretation, Elsevier2011.

[23] J. Coates, Interpretation of infrared spectra, a practical approach, Encyclopedia of analytical chemistry, (2000).

[24] B. Stuart, Infrared spectroscopy: Fundamentals and Applications, Wiley Online Library2004.

[25] C.J. Brinker, G.W. Scherer, Sol-gel science: the physics and chemistry of sol-gel processing, Academic press2013.

[26] M. Kieninger, O.N. Ventura, Calculations of the infrared and Raman spectra of simple thiols and thiol–water complexes, International Journal of Quantum Chemistry, 111 (2011) 1843-1857.

[27] B.Z. Jang, D.R. Uhlmann, J.B.V. Sande, Ductile–brittle transition in polymers, Journal of Applied Polymer Science, 29 (1984) 3409-3420.

Chapter 5

Intrinsic healing coatings via dual organic-inorganic sol-gel based polymers

Introduction

Corrosion is one of the main processes leading to material destruction and economic losses, the latter being estimated between 2 to 5% of the world's GNP [1-3]. Although corrosion is inevitable, the costs can be significantly reduced using appropriate protection methods such as application of protective coatings. Passive protective coatings restrict ingress of water and corrosive agents to the metal-coating interface, eliminating electrolyte as an essential element required to initiate corrosion process [4]. Yet such coatings fail to fulfil their protective function upon damage. Implementation of self-healing approaches into the protective coatings can guarantee longer service life and reduced maintenance cost by autonomous or non-autonomous healing of local damages such as cracks and scratches [5, 6].

However, self-healing in corrosion protective coatings is slightly different from that of bulk polymers or decorative coatings. In the latter cases, healing is referred to restoration of mechanical or aesthetic properties by providing enough material to repair/fill in the defect volume. While in corrosion protection, recovery of the lost protective function is addressed as healing. Therefore incorporation of corrosion inhibitors into the coating system enabling surface protection of the damage (to be addressed in chapter 7) and introduction of reversible chemistries empowering damage closure and sealing can be considered as extrinsic and intrinsic healing approaches in corrosion protective coatings, respectively [6-9].

Intrinsically healable polymers based on reversible covalent bonds are of particular interest in protective coating applications. Chemically crosslinked polymeric networks generally offer superior mechanical and barrier properties compared to their linear/non-crosslinked counterparts or physical networks [5, 10]. Incorporation of reversible covalent bonds to the polymeric networks yields an active protection mechanism facilitating multiple restoration events of the barrier properties by damage closure, without sacrificing the chemically crosslinked network structure. Despite the reported short term restoration of barrier properties of the organic coatings based on Diels-Alder [10-13] and shape memory principles [14-17], recovery of other key properties such as adhesion has not been addressed in the literature yet.

In the previous chapters it was demonstrated that the hybrid sol-gel based polymers containing reversible tetrasulfide groups show remarkable macroscale damage closure capabilities upon application of thermo-mechanical stimulus while maintaining their mechanical integrity. In this chapter the potential application of these hybrid sol-gel polymers as protective coating was evaluated. To this aim the developed polymers were

applied on AA2024-T3 substrate and their wetting, adhesion and barrier properties were assessed. Furthermore, the adhesion and barrier restoration potential of the coating systems were studied using mechanical and electrochemical techniques. The studied system presented long-term restoration of the barrier properties as well as recovery of the coating adhesion and surface properties (e.g. hydrophobicity and surface topology) necessary for lifetime extension of corrosion protective coatings.

Experimental procedure

Materials

Epoxy resin based on Epikote^{TM} 828 (184-190 g epoxy eq^{-1}) and Ancamine$^®$2500 curing agent (105-110 g amine eq^{-1}) were provided by Akzo Nobel Aerospace Coatings (ANAC) and used as received. (3-Aminopropyl)trimethoxysilane (97%, MW=179.29 g mol^{-1}) and pentaerythritol tetrakis(3-mercaptopropionate) (>95%, MW=488.66 g mol^{-1}), from hereon called APS and tetra-thiol respectively, were purchased from Sigma-Aldrich, The Netherlands, and used without further purification. Bis[3-(triethoxysilyl)propyl]tetrasulfide (99%, MW=538.95 g mol^{-1}, total sulfur content>20%), hereon BS, and ethanol were purchased from Capture Chemicals, China, and VWR, The Netherlands, respectively and used as received. Unclad AA2024-T3 was received from AkzoNobel and used as metallic substrate.

Coating preparation

Prior to coating application, AA2024-T3 panels of 3×4 cm^2 were ground mechanically using SiC paper (grade 1000) to remove the native oxide layer and further degreased with ethanol [18]. The panels were then immersed in 2 M NaOH solution for 10 seconds and thoroughly rinsed with double distilled water to increase the hydroxyl groups (OH$^-$) density on the AA2024-T3 surface [19].

The dried AA2024-T3 panels were then coated with a non-healing epoxy-amine coating and the healable hybrid sol-gel coatings with different BS:APS molar ratios. The polymers were prepared as described in chapter 2. The organically modified silicone alkoxides (OMSAs) were sequentially (APS followed by BS) added to the epoxy resin with the OMSAs:epoxy resin weight ratio of 1:1, keeping BS:APS molar ratio at 3:1, 2:1 and 1:1. The mixtures were stirred using a magnetic stirrer at 300 rpm for 3 h at room temperature. The organic crosslinker (Ancamine$^®$2500) was then added to the mixture

keeping the amine hydrogen equivalent (AHE) to epoxy equivalent (EE) ratio at 1.1 and the mixture was stirred in a high speed mixer at 2500 rpm for 5 min. Tetra-thiol was then added in a tetra-thiol:epoxy resin weight ratio 0.56:1 and the mixture was further mixed in the high speed mixer for 40 s at 2500 rpm. The resulting mixtures were then cast on the cleaned AA2024-T3 panels using a calibrated standard aluminum single blade at three different thicknesses. The coated samples were dried at room temperature for an hour and cured for 48 h at 70 °C yielding coatings with an average dry thickness of 50 ± 2, 150 ± 5 and 350 ± 10 μm. Epikote based epoxy coatings with epoxy resin:Ancamine:tetra-thiol weight ratio of 1:0.58:0.56 were prepared and examined as non-healing reference samples. More information about the polymer chemistry and healing mechanism can be found in chapter 2.

Coating characterization

Surface hydrophobicity

The degree of hydrophobicity of the prepared coatings as function of the BS content was determined by measuring distilled water-polymer contact angle. The measurements were performed using a CAM 200 Optical Tensiometer from KSV Instruments. To determine the contact angle, distilled water droplets of 5μm were placed on a smooth polymer surface at rate of 1 mm.min^{-1}. Following to equilibration of the droplet for 30 seconds, images of the droplet were taken and the contact angle was determined as the average contact angle (between right and left) from three repeated measurements.

Adhesion properties

Adhesion properties of the prepared coating systems were evaluated using single lap shear test with a Zwick/Roell 250 kN load frame. Test specimens were prepared according to ASTM D-1002 standard by gluing two identical AA2024-T3 plates (L × W × t = 100 × 25 × 2 mm^3) to each other using 0.2 ml of the hybrid sol-gel polymer. The tested sample geometry having an overlap length of 12.5 mm is shown in Figure 5.1. Subsequent to a drying step of 1 h at room temperature, the glued samples were clamped uniformly with a total pressure of 20 kPa and cured at 70 °C for 48 h. After equilibrating the sample at room temperature for at least 2 hours, the glued samples were tested under displacement control at a cross-head speed of 1 mm.min^{-1} till the two AA2024-T3 plates were fully separated from each other.
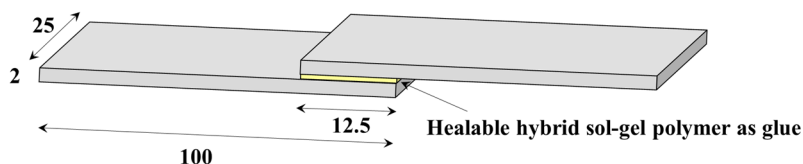
Figure 5.1. Schematic representation of lap shear test geometry.

Barrier properties by electrochemical techniques

Electrochemical properties of the prepared coating systems were investigated using electrochemical impedance spectroscopy (EIS). The EIS measurements were carried out at room temperature in a conventional three-electrode cell configuration consisting of a saturated Ag/AgCl reference electrode, a carbon black rod with a diameter of 50 mm as counter electrode and the sample as the working electrode in a horizontal position (exposed area of ca. 0.8 cm^2). A Faraday cage was employed to avoid the interference of external electromagnetic fields. A stagnant 0.5 M NaCl aqueous solution in equilibrium with air was employed as the testing electrolyte. The measurements were performed using an Autolab PGSTAT 302 N potentiostat/galvanostat coupled to a frequency analyser (FRA) in the frequency range of 10^{-1}-10^5 Hz, with a 10 mV (rms) of sinusoidal perturbation at open circuit potential, acquiring 10 data points per frequency decade. The impedance plots were fitted using the most probable equivalent circuits with the Nova software package from Metrohm-Autolab B.V.

Healing properties

Adhesion recovery

To investigate the adhesive healing capability of the hybrid sol-gel polymers, the specimens tested using test procedure described earlier (single lap shear), were put back together to recover the same bond area. The adhesion of the failed AA2024-T3 adherents was promoted by clamping the samples with a normal pressure of 20 kPa and thermal treatment at 70 °C for 2 h. Following to the thermal treatment, the lap shear test was performed using the same protocol. The adhesive healing efficiency was determined for five thermal treatment-test cycles by monitoring the adhesive strength i.e. strength at break of the samples after each cycle. In attempt to get an insight to the adhesive strength and adhesion recovery potential of the hybrid sol-gel polymers, the single lap shear test with the same sample geometry as described in the section "adhesion properties", was

performed using the free standing cured films with an average thickness of 0.5 mm as the glue. The adhesion of the glue to AA2024-T3 substrates was promoted by clamping the samples with a normal pressure of 20 kPa and thermal treatment for 2 h at 70 °C. The samples were subsequently tested for five consecutive cycles at room temperature using the described protocol.

Superficial scratch healing

To evaluate the superficial scratch healing capability of the hybrid sol-gel coating, controlled superficial scratches (i.e. not reaching the metal surface nor cutting the polymer coating) were created on the 50 μm thick coating using a micro-scratch tester from CSM Instruments equipped with a Rockwell indenter (tip radius = 100 μm). 5 mm long scratches were created at rate of 10 mm.min^{-1} by applying a normal force of 6 N on the coating. The coating topology and the scratch profile were examined with a laser scanning confocal microscope from Olympus (OLS 3100) upon damage and healing events. The superficial healing of the hybrid sol-gel coatings was promoted by a 30 minute annealing step in an air circulation oven at 70 °C, resulting in 100% superficial scratch healing efficiency based on the following equation:

$$Superficial\ healing\ efficiency\ (\%) = 100 - 100 \left(\frac{(V/A)_{A.H.}}{(V/A)_{B.H.}} \right) \qquad \text{Eq. 5.1}$$

Where (V/A) strands for scratch volume to measured surface area ratio before healing (B.H.) and after healing (A.H.) events [20].

Barrier recovery

The ultimate potential of the healable hybrid sol-gel coatings to restore their barrier properties upon damage was evaluated by performing EIS measurements on intact, scratched and healed coating systems. Controlled 3 mm long scratches were created in the 50, 150 and 300 μm thick healable hybrid sol-gel coatings using a CSM micro-scratch tester equipped with a sharp razor blade (Figure 5.2). The penetration depth of the razor in the coating was adjusted based on the coating thickness ensuring that the artificial scratch always reached the metallic substrate. To this aim, the micro-scratch tester was coupled with an electric circuit consisting of a DC power supply and a LED lamp. The circuit was connected to metallic substrate and the razor blade. Prior to scratching, due to the presence of the insulating coating the circuit was in an open state. The direct contact between the blade and the substrate resulting from cutting the

isolating coating throughout its thickness was confirmed by flow of electrons in the closed circuit lighting up the LED lamp.

In addition to the coating thickness, the effect of the scratch width on the barrier recovery potential of the hybrid sol-gel coatings was investigated by employing blades with different nominal thicknesses yielding scratch widths of 25, 35, 50 and 300 μm.
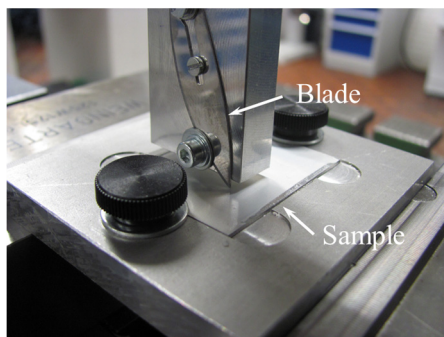

Figure 5.2. The micro-scratch tester equipped with the razor blade.

To activate the gap closure and therefore healing process of the hybrid sol-gel coatings, the scratched samples were clamped uniformly between two glass plates with a pressure of 30 kPa and placed in an air circulation oven at 70 °C for 2 h. The samples were taken out of the oven every 30 minutes during the healing process. The evolution of the scratch profile was monitored using a Leica DMLM microscope in reflection mode and the images were captured with an inbuilt Axio Cam ICc 3 digital camera. The healing process was continued until the two cut surfaces had fused completely. Subsequent to a 60 minute equilibration at ambient temperature, the healed samples were evaluated using EIS for a maximum exposure time of 350 days.

The morphology and composition of the samples across the coating thickness were evaluated by performing SEM/EDS on the cross-section of the cryo-fractured coated AA2024-T3 panels.

Results & Discussion

Hydrophobicity

In protective coatings, a higher hydrophobicity can limit ingress of water and aqueous electrolytes to the metal-coating interface and reduce the kinetics of the corrosion processes on the substrate. [21-23]. Therefore evaluation of the water contact angle as a measure of coating hydrophilicity/hydrophobicity and the effect of a healing treatment on this parameter is of significant importance. The extent of the hydrophobicity of the hybrid sol-gel coatings was studied by measuring distilled water-polymer contact angle. The prepared coatings exhibited static water contact angle (WCA) values higher than 70° (Figure 5.3). As Figure 5.3 shows, the wetting properties of the coating systems were strongly influenced by BS content.
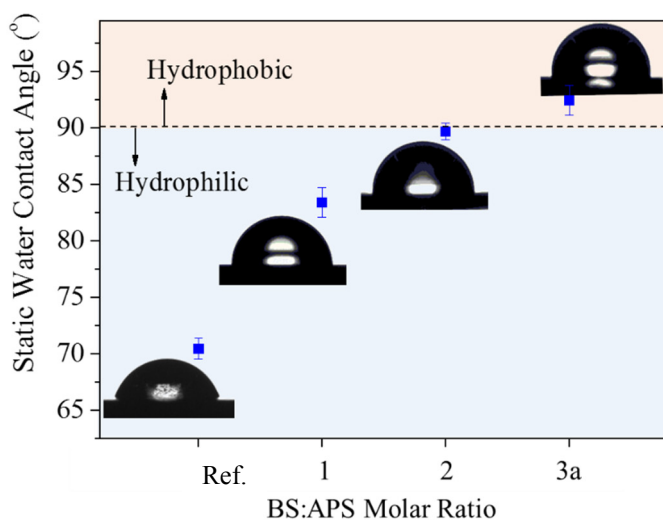

Figure 5.3. The static WCA values of the hybrid sol-gel coatings with different BS:APS molar ratios after 48 h at 70 °C curing conditions.

While the BS-free reference epoxy coating exhibited the lowest WCA (70°), addition of the hydrophobic OMSAs (i.e. BS) to the coating formulation led to a significant increase in the static WCA values ($\Delta\theta$ = 15° ± 2). The WCA of the healable hybrid sol-gel coatings containing reversible tetrasulfide groups increased linearly as a function of BS

content. Yet, defining hydrophilic and hydrophobic surfaces as surfaces with WCAs in the range of 10° < θ < 90° and 90° < θ < 150°, respectively [Intelligent coatings for corrosion control, Tiwari and Adel] only the coating containing the highest BS content (BS:APS molar ratio of 3:1) with static WCA of 93° ± 0.5° can be considered a hydrophobic coating. Additionally, the obtained static WCA values were proved to be independent of the thermal treatment procedure employed for activating the scratch healing of the hybrid sol-gel coatings (i.e. 2 h annealing at 70 °C).

Adhesion properties

In addition to water repellency, strong adhesion to the metallic substrate is a key feature in the protective coating systems [24, 25]. The adhesion strength of the non-healing reference epoxy and the healable hybrid sol-gel coating exhibiting the highest WCA and gap closure efficiency (i.e. BS:APS molar ratio 3:1) was investigated using single lap shear test. The stress-strain plots and micrographs of the tested samples are presented in Figure 5.4. As Figure 5.4a shows no significant difference in lap-shear strength could be detected when comparing the non-healing reference epoxy coating (1.6 ± 0.1 MPa) and the healable hybrid sol-gel coating containing the highest BS content with the BS:APS ratio of 3:1 (1.5 ± 0.05 MPa). Yet, the fractured non-healing epoxy and the healable hybrid sol-gel coating demonstrated different failure modes (Figure 5.4). While the non-healing reference epoxy exhibited adhesive failure, the healable hybrid sol-gel showed mixed adhesive-cohesive failure.

The adhesive failure of the reference epoxy suggests its higher cohesive strength compared to its adhesive strength. On the other hand the alternating crack path in the mixed adhesive-cohesive failure of the healable hybrid sol-gel leaving polymer residue on the surfaces of the both AA2024-T3 panels indicates a higher adhesive strength than the cohesive one. The arrangement/appearance of the polymer residue on the surface of the AA2024-T3 adherent panels after lap shear test can provide a qualitative estimation of the extent of polymer's chemical/physical bonding to the test substrate (AA2024-T3). The distribution of the healable hybrid sol-gel polymer residues on AA2024-T3 adherent is an indication of high interaction of the aforementioned polymer with AA2024-T3. Such high interaction levels can be attributed to the formation of chemical bridges between the silanol groups of OMSAs in the hybrid sol-gel polymer and the aluminum hydroxide groups of the metallic substrate yielding Si-O-Al covalent bonds [26].
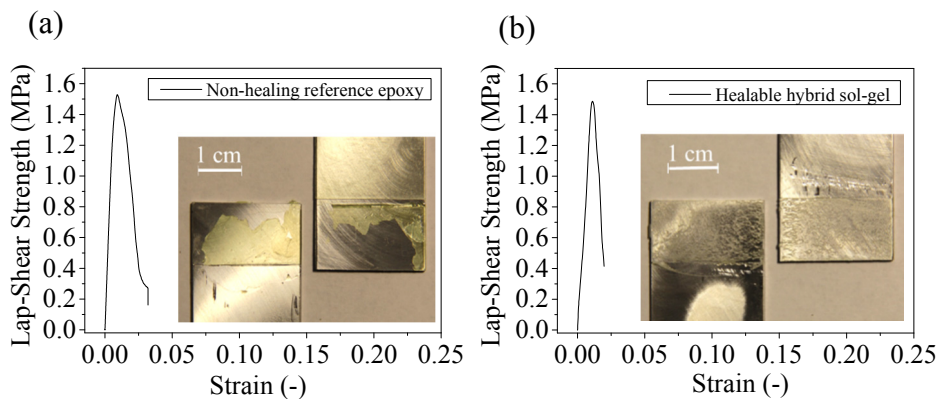
Figure 5.4. Stress-strain plots and micrographs of the non-healing epoxy (a) and a healable hybrid sol-gel coating with BS:APS ratio of 3:1 (b) tested using lap shear test.

An ideal healable corrosion protective coating not only shall recover its cohesive integrity upon damage, but also should restore its adhesion properties in case of delamination. To investigate the ability of the prepared hybrid sol-gel polymer to restore its adhesion properties, five cycles of heat treatment-single lap shear tests were performed as described in the experimental section. The stress-strain plots of the tested samples and their corresponding adhesion strengths are presented in Figure 5.5.

As Figure 5.5.a shows the lap-shear strength of the hybrid sol-gel polymer was maintained in the range of 1.5 ± 0.03 MPa for all the test cycles. Moreover the specimens failed with adhesive-cohesive mode in all the cycles. The constant strength at break showing no significant drop after five consecutive cycles (Figure 5.5.b) demonstrated the ability of the hybrid sol-gel polymer to fully restore the adhesive joint properties. The adhesive recovery of the samples can be explained by the dynamic/reversible nature of the S-S bonds upon heat treatment which allow formation of new bonds/crosslinks restoring the hybrid sol-gel polymer's integrity (mainly cohesive) at broken surfaces. In contrast to the hybrid sol-gel polymer, the reference epoxy specimens did not exhibit any restoration of their adhesive properties as they do not contain any reversible bonds.

To further analyze the hybrid sol-gel polymer capability in recovering its adhesive properties, the AA2024-T3 adherents were glued to each other using the pre-cured hybrid sol-gel polymer (BS:APS molar ratio 3:1) yielding the ASTM D-1002 sample

geometry and tested using the same test procedure. As Figure 5.5 c shows the lap-shear strength of the new set of specimens was in the range of 450 ± 40 kPa for all the test cycles. The lower lap-shear strength of the free standing hybrid sol-gel films compared to the non-cured polymer (Figure 5.4 b) can be ascribed to the lower concentration of the available functional groups for physical/chemical interaction with the metallic substrate due to pre-cure process.
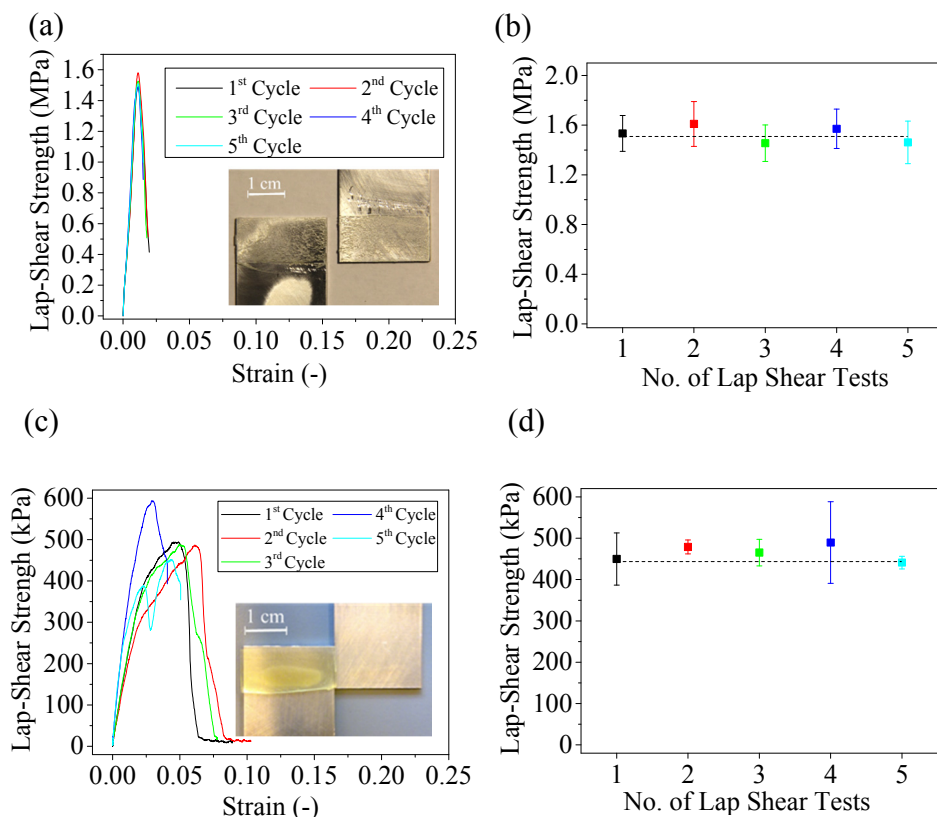

Figure 5.5. The stress-strain plots (a) and the lap shear strength of the healable hybrid sol-gel (b) films tested using lap shear test up to five cycles, the stress-strain plots (c) and the lap shear strength of the pre-cured healable hybrid sol-gel (d) films tested using lap shear test up to five cycles. The inset pictures show the micrograph of the tested sample after the fifth cycle.

The lower interaction of the films with AA2024-T3 adherent panels was further confirmed by adhesive failure of the samples during the lap-shear test. The adhesive failure of the test specimens glued using the pre-cured hybrid sol-gel films indicates that the obtained strength values can mainly be attributed to the adhesive strength of the hybrid sol-gel polymer. Additionally, the constant strength at break for five consecutive test cycles illustrates the ability of the hybrid sol-gel polymer to recover its adhesion strength in case of delamination.

Electrochemical properties

As a corrosion protective coating, the healable hybrid sol-gel polymer must provide an effective barrier layer against ingress of electrolyte and corrosive species to the metal-coating interface. The extent of corrosion protection offered by a 50 μm thick hybrid sol-gel (BS:APS molar ratio of 3:1) and the reference epoxy coatings on AA2024-T3 substrate was evaluated using electrochemical impedance spectroscopy (EIS). The Bode plots of the intact coating systems over the frequency range of 10^{-1}-10^{5} Hz, in 0.5 M NaCl are presented in Figure 5.6. As Figure 5.6 a shows after 1 h exposure to the electrolyte, the intact hybrid sol-gel coating showed a high Bode modulus ($|Z|$) at low frequency range ($|Z|_{0.1\ Hz}$ = 3E9 $\Omega.cm^2$) and almost a pure capacitive response over the measured frequency range, characteristic of an effective barrier layer. The low frequency Bode modulus of the reference epoxy coating was slightly higher than that of the hybrid sol-gel coating ($|Z|_{0.1\ Hz}$ = 7E9 $\Omega.cm^2$), yet it deviated only moderately from the pure capacitive response (Figure 5.6 b).
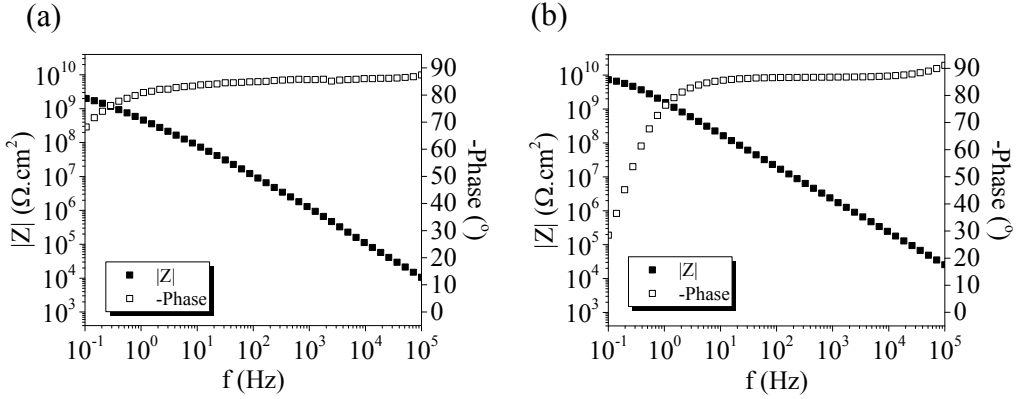
(a)

(b)

Figure 5.6. Bode modulus plots of an intact healable hybrid sol-gel (a) and reference epoxy (b) coating system with an average thickness of 50 μm after 1 h exposure to 0.5 M NaCl over the frequency range of 10^{-1}-10^5 Hz.

EIS is a well-established technique for evaluation of the coating systems [27]. Yet, accurate and quantitative analysis of the electrochemical processes across the coating requires interpretation of the EIS data using a suitable equivalent circuit model. Various elements such as resistors, capacitors and inductors representing different physical processes can be combined in parallel or series to yield the desired equivalent circuit. The resulting equivalent circuit can then be used to fit the experimental EIS data, estimate the defined parameters and monitor the coating behavior over time. The most probable equivalent circuits (MPEC) were selected based on the physical meaning of the selected EC, low relative error and low chi-square [28].

The analysis to select the most probable equivalent circuit (MPEC) led to the EC depicted in figure 5.7.a as the MPEC for the intact coatings. In this EC R_{sol} and R_{coat} correspond to solution and coating resistances respectively while CPE_{coat} represents coating constant phase element (CPE). The insertion of a CPE was proven a necessary step for the fitting during the MPEC selection process. CPE describes a deviation from an ideal capacitor. In coatings this is generally attributed to heterogeneities or porosity in the coating. The impedance of a CPE is given by [28, 29]:

$$Z_{CPE} = Y_0^{-1}(j\omega)^{-n}$$
Eq. 5.2

In which ω, Y_0 and n stand for frequency, admittance of an ideal capacitor and the empirical constant ranging from 0 to 1. The capacitance values of a CPE can be calculated using the following equation [29]:

$$C_{Coat} = Y_0(\omega_{max}^{"})^{n-1}$$
Eq. 5.3

Where $\omega^{"}_{max}$ is the frequency at which the imaginary part of the impedance (Z") is maximum.

The evolution of the coating capacitance and resistance for the hybrid sol-gel and reference epoxy coatings in 0.5 M NaCl solution (derived from fitting the experimental EIS data) is presented in Figure 5.7.b. In all the cases the fitting goodness (χ) was smaller than 5E-3. As Figure 5.7.b shows, the capacitances (C_{Coat}) of the hybrid sol-gel and reference epoxy coatings were in the range of 0.7 and 0.1 nF.cm^{-2}, respectively. Additionally, upon exposure to the electrolyte, the capacitance of the both coating systems slightly increased reaching a plateau of 0.76 and 0.14 nF.cm^{-2} in one day for the hybrid sol-gel and reference epoxy coatings, respectively. The coating capacitance can further be employed to calculate the extent of water uptake using Brasher and Kingsbury Eq. [30]:

$$\Phi = \frac{log\left(C_t/C_0\right)}{log(\varepsilon_w)}$$
Eq. 5.4

Where, C_t, C_0 and ε_w stand for coating capacity at time t and 0, respectively, and water dielectric constant (80 F.m^{-1}). The increase in the hybrid sol-gel and reference epoxy coatings capacitance along the 14 days exposure to the electrolyte is equivalent to a water uptake (Φ) of 0.035 and 0.55, respectively, further confirming the higher hydrophobicity of the hybrid sol-gel coating compared to the reference epoxy (Figure 5.3). Furthermore Figure 5.7.b shows that both of the hybrid sol-gel and reference epoxy coatings exhibited a high resistance (R_{Coat}) in the order of 3.5E9 and 7.5E9 Ω.cm^2, respectively, with no drop in R_{Coat} during the 14 exposure days to the electrolyte.
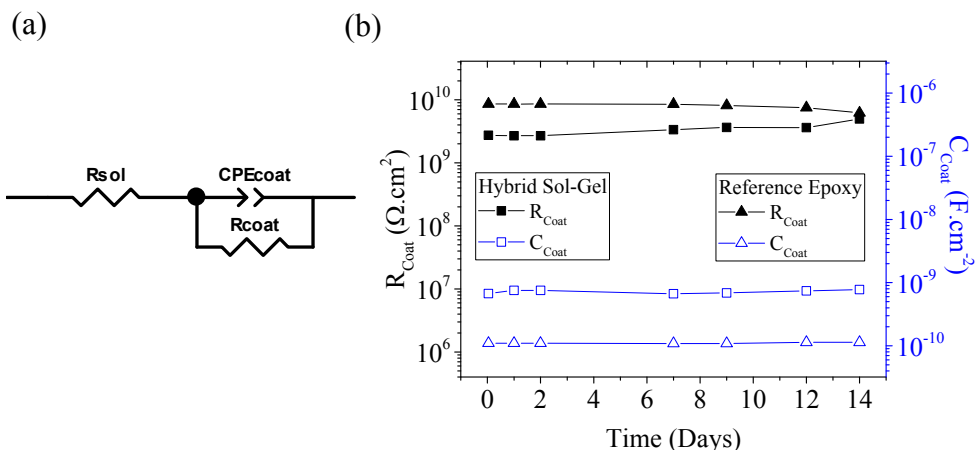
(a) (b)

Figure 5.7. MPEC selected to fit the experimental EIS data (a) evolution of coating resistance (R_{coat}) and capacitance (C_{coat}) for a healable hybrid sol-gel and reference epoxy coatings in 0.5 M NaCl (b).

The high coating resistance (R_{Coat}) together with the low coating capacitance (C_{Coat}) of the hybrid sol-gel coating point at formation of an effective barrier layer on AA2024-T3 substrate in aggressive 0.5 M NaCl solution. Yet, as an intrinsically healable coating, the hybrid sol-gel coating must restore its original properties and function upon superficial and interfacial damages. To evaluate the superficial healing capability of the hybrid sol-gel coating, controlled superficial scratches were created on the 50 μm thick coating as described in the experimental section. The coating topology and the scratch profile upon damage and healing events are presented in Figure 5.8. As Figure 5.8 a shows scratching the hybrid sol-gel coating led to plastic deformation of the polymer creating a uniform scratch with an average depth and width of 20 and 300 μm, respectively (Figure 5.8 c). Upon annealing the damaged coating for 30 minutes at 70 °C, the hybrid sol-gel coating illustrated 100% superficial healing efficiency, as illustrated by a flat scratch profile (Figures 5.8 b and c). Although the reference epoxy showed a comparable initial scratch profile to the one in the healable hybrid sol-gel coating, in this case no significant scratch healing was observed after the annealing step (30 minutes at 70 °C). The absence of the healing is a result of the crosslinked nature of the reference material.
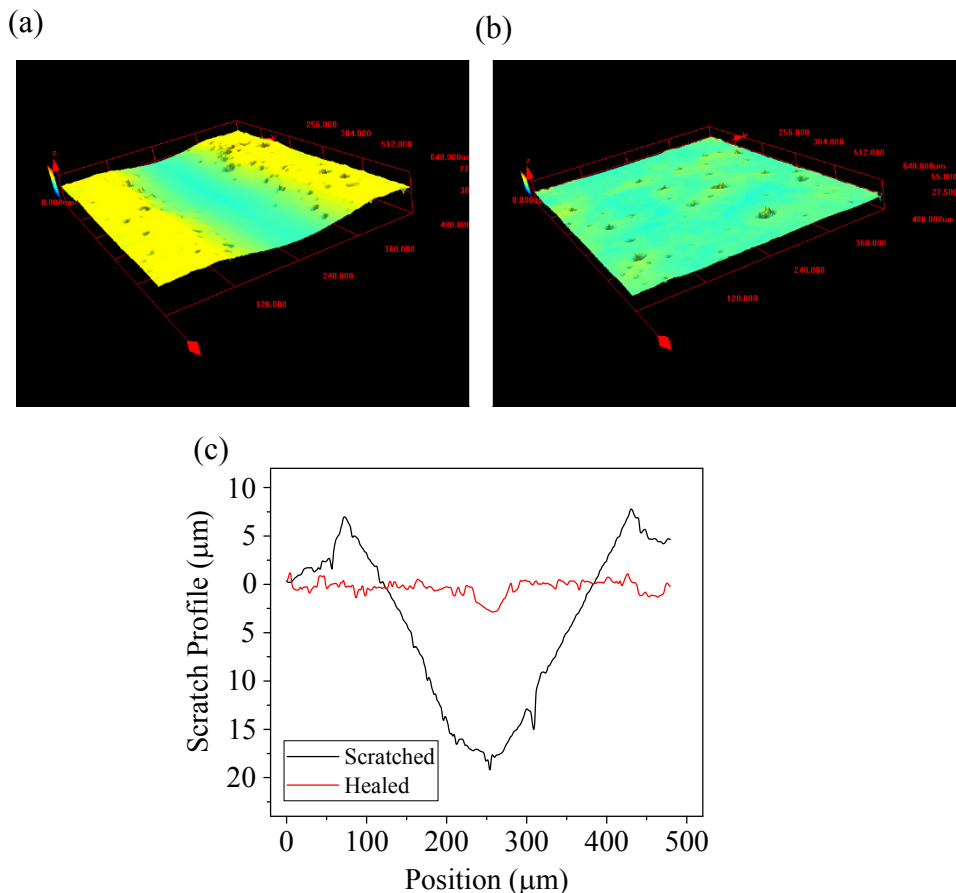
(a)

(b)

(c)

Figure 5.8. Surface topology of a scratched (a) and healed (b) surface of a hybrid sol-gel coating and their corresponding scratch profiles (c). In Figure 5.8 c, 0 represents the coating surface.

Absence of tensile cracks [31] and coating delamination along the scratch path illustrated coatings cohesive and adhesive integrity during the superficial scratch testing. To disrupt the coating systems integrity and function, the coatings were scratched using a micro-scratch tester equipped with a sharp razor blade. The Bode plots of the scratched hybrid sol-gel coating, the evolution of the |Z| at three different frequencies (10^4, 10^2, 10^{-1}) in 0.5 M NaCl solution and the SEM micrograph of the coating cross-section are presented in Figure 5.9.
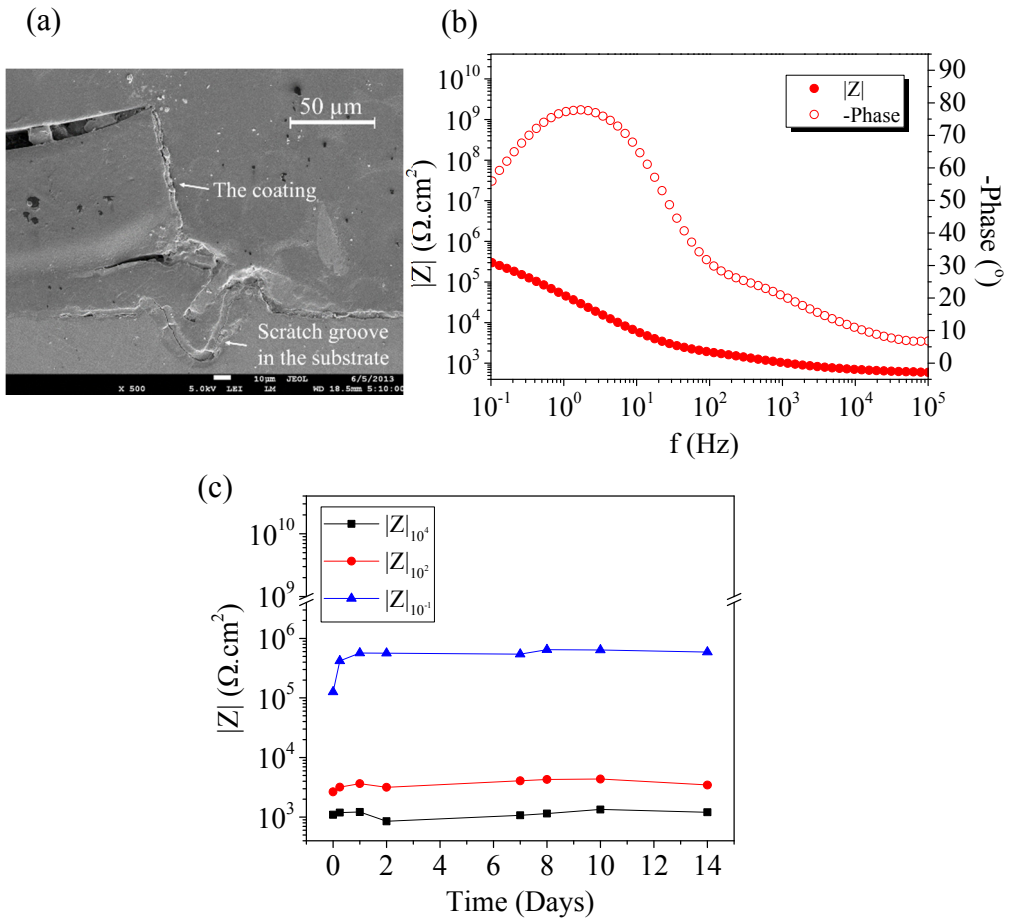
(a)

(b)

(c)

Figure 5.9. SEM micrograph of the scratched hybrid sol-gel coating cross-section (a), its Bode plots after 1 h exposure to 0.5 M NaCl solution (b) and the evolution of the |Z| at three different frequencies of 10^4, 10^2, 10^{-1} Hz over 14 days of exposure (c).

In presence of a scratch reaching the metallic substrate (Figure 5.9 a), the coating lost its barrier function as reflected by the significant drop of the |Z| in the whole frequency range compared to the intact coating. Exposure of the metallic substrate to the aggressive electrolyte at the scratch groove initiated/promoted electrochemical activities at the metal-coating interface affecting the stability of the native oxide layer and polarization resistance of the substrate. The aforementioned processes/phenomenon were captured/detected by appearance of the second and third time constants in the mid and

95

low frequency ranges of the EIS spectra, respectively. The evolution of the |Z| at three different frequencies of 10^4, 10^2, 10^{-1} Hz as a qualitative measure of the coating, oxide and polarization resistances, respectively, in the scratched hybrid sol-gel is shown in Figure 5.9 c. Apart from the small fluctuations in |Z| values of the selected frequencies, the $|Z|_{10}^4$, $|Z|_{10}^2$, and $|Z|_{10}^{-1}$ showed a constant average value of 1E3, 4E3 and 6E5 $\Omega.cm^2$ respectively over 14 days of exposure to the electrolyte. The EIS spectra of the scratched reference epoxy coating were comparable to those of the scratched hybrid sol-gel coating after 14 days of measurement. The significant decrease in the coating resistance of the tested coating systems ($\Delta R \cong 1E6\ \Omega.cm^2$) compared to those of the intact coatings is a clear indications of the coating's lost barrier properties.

In contrast to the reference epoxy the hybrid sol-gel polymer (BS:APS molar ratio of 3:1) exhibited exceptionally high macroscopic flow and gap closure properties as a free standing film (Chapter 2). Yet, when applied as a coating, the polymer's strong adhesion to the substrate might act as a constraint, restricting its macroscopic flow as reported in a number of publications [32, 33]. To study the substrate's potential effect on the flow and hence healing of the hybrid sol-gel coatings, a set of 50 µm thick coatings with different scratch widths (25, 35, 50 and 300 µm) were prepared as described in experimental section. Upon healing (2 h annealing at 70 °C), the coatings were tested using EIS in 0.5 M NaCl solution as all the scratches seemed to be closed by optical observation. The Bode modulus plots of the healed hybrid sol-gel coatings after 1 h exposure to the electrolyte are compared to those of the scratched and intact coatings in Figure 5.10. As Figure 5.10 shows, the EIS spectra of the healed coatings overlapped with that of the intact coating independent of the initial scratch width. Comparison of the EIS spectra of the intact, scratched and healed coating systems suggests complete initial sealing of the scratch induced interface and full restoration of the barrier properties of the hybrid sol-gel coating for short term-exposure. Unlike the hybrid sol-gel coating, the annealing step did not lead to restoration of the reference epoxy coating's barrier properties, as the scratch remained open exposing the metallic substrate to the aggressive electrolyte.
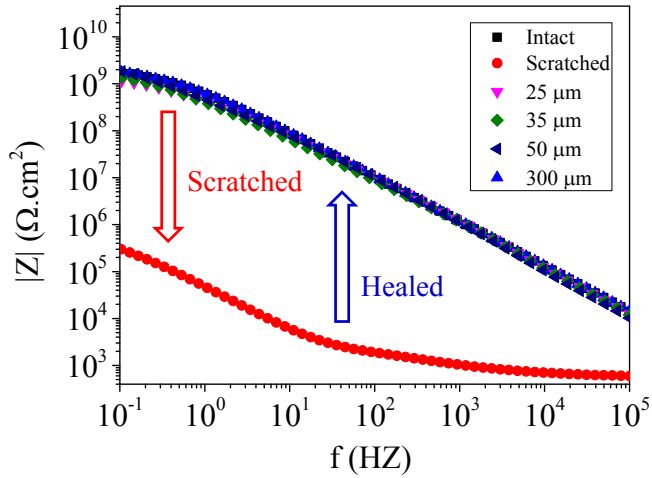
Figure 5.10. Bode modulus plots of the intact, scratched and healed hybrid sol-gel coating with different scratch widths after 1 h exposure to 0.5 M NaCl solution.

The long-term sealing efficiency of the healed coating systems was followed by monitoring their resistance and capacitance over one month exposure to the aggressive electrolyte (0.5 M NaCl). Figure 5.11 (a, b and c) show that the healed coatings with the initial scratch widths of 25, 35 and 50 μm exhibited an average resistance (R_{Coat}) and capacitance (C_{Coat}) of 3E9 $\Omega.cm^2$ and 6E-10 $F.cm^{-2}$, respectively. The consistently high resistance and low capacitance of these healed coatings illustrated their effective barrier protection in 0.5 M NaCl solution. In addition, their comparable R_{Coat} and C_{Coat} to the intact coating, over the course of the measurement (i.e. 30 days) demonstrated their long-term 100% sealing efficiency. However, the coating with the initial scratch width of 300 μm failed to provide long-term sealing. The lost barrier properties of this sample was clearly detected after 10 h exposure to the electrolyte (Figure 5.11 d) by a sudden drop of R_{coat} and increase of C_{coat}.

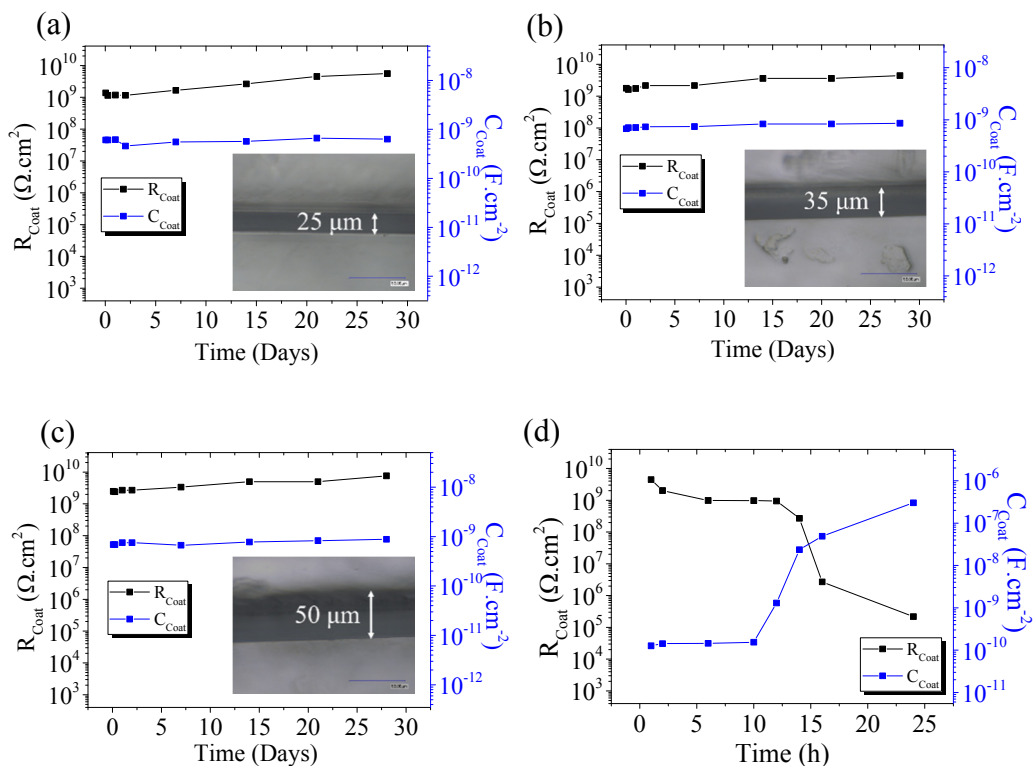Figure 5.11. Evolution of coating resistance (R_{Coat}) and capacitance (C_{Coat}) for 50 µm thick hybrid sol-gel coatings with scratch widths of 25 µm (a), 35 µm (b), 50 µm (c) and 300 µm (d). The inset micrographs show the top-view of the scratched coatings at t = 0.

Figure 5.12 shows the SEM micrographs of the cross-sections of the coatings with different scratch widths (25, 35, 50 µm) after 30 days and 1 day immersion (for the 300 µm scratch width). The healed coating cross-sections revealed fusion of the cut surfaces for the coatings with initial scratch widths of 25, 35 and 50 µm (Figure 5.12 a, b and c), in agreement with their prolonged sealing performance. Unlike the other healed coatings, the one with the widest initial scratch (300 µm) showed clear cracks and delamination along the healed scratch path (Figure 5.12 d), revealing the potential role of the substrate perturbation/deformation in restricting polymer flow and hence healing. Such defects
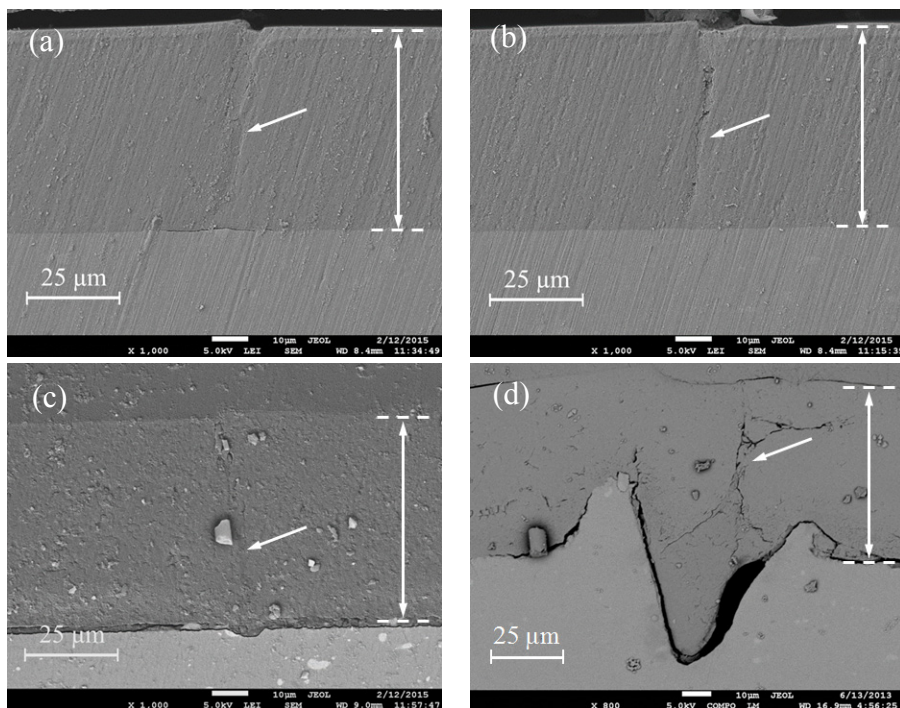
Figure 5.12. SEM micrographs of the healed hybrid sol-gel coating cross-sections with initial scratch width of 25 µm (a), 35 µm (b), 50 µm (c) and 300 µm (d).

provide an easy path for ingress of the electrolyte, facilitating electrochemical (corrosion) processes at the metal-coating interface. The effect of coating thickness on long-term sealing performance of the hybrid sol-gel coating with an initial scratch width of 300 µm is presented in Figure 5.13. Figure 5.13 shows that increasing the coating thickness to 150 and 350 µm minimized/eliminated the substrates perturbation effect on the polymer flow. Yet, the two healed coatings exhibited different long-term sealing performances, suggesting the dominant role of scratch width on the healing of the scratch induced interface. As Figure 5.13 a shows, despite the lower perturbation of the substrate the resistance and capacitance of the 150 µm thick healed coating deviated from those of the intact coating after two days exposure to the electrolyte. The abrupt increase in the healed coating capacitance (ΔC_{Coat} = 1E4 F.cm^{-2}) and the significant decrease in its resistance (ΔR_{Coat} = 1E2 Ω.cm^2) are clear indications of the occurrence of the corrosion processes at metal-coating interface as confirmed by formation of corrosion products beneath the

99

coating layer (Figure 5.13 c). Healing the 350 µm thick coating led to complete fusion of the cut surfaces as revealed by the scar-free cross section of the healed coating revealed by SEM microscopy (Figure 5.13 d). Additionally, the resistance and capacitance of the healed coating overlapped with those of the intact one for one year exposure to the electrolyte, confirming complete sealing of the generated interface and full restoration of the barrier properties of the hybrid sol-gel coating. The obtained data confirm the governing effect of the coating thickness as higher substrate perturbation was overcome by the thicker coating resulting in long-term sealing of the healed interface.

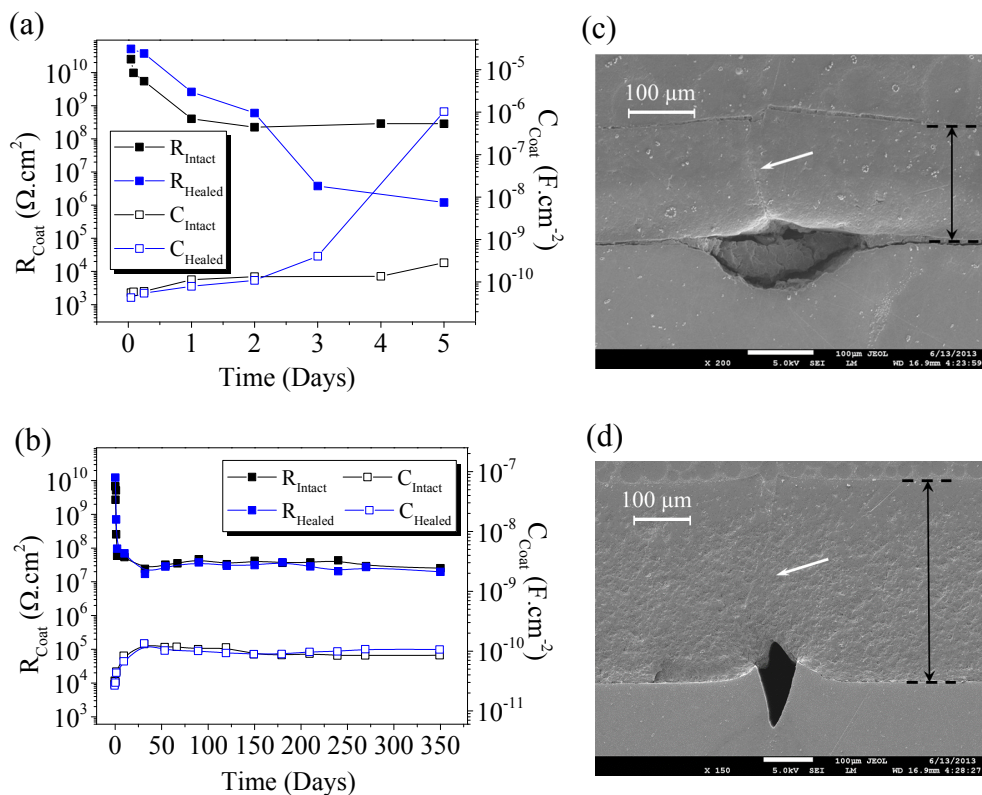

Figure 5.13. Evolution of resistance and capacitance of 150 µm (a) and 300 µm (b) thick hybrid sol-gel coatings in 0.5 M NaCl solution, the cross-sectional SEM micrographs of the 150 µm (c) and 300 µm (d) thick coatings. The initial scratch width in both coatings was 300 µm.

To get an overview on the restrictive effect of the metallic substrate on the polymer's macroscopic flow and hence healing, the studied scratch widths (25, 3, 50 and 300 µm) were normalized by the coating thickness (50, 150, 350 µm). Then the performance of the healed hybrid sol-gel coatings in terms of short- or long-term sealing of the scratch induced interface was plotted versus the thickness normalized scratch widths ($W_{Scratch}$ / $t_{Coating}$). As Figure 5.14 shows, as long as the scratch width is smaller/equal to the coating thickness ($W_{Scratch}$ / $t_{Coating} \leq 1$) the healed coatings exhibited long-term sealing performance. However, increasing the aforementioned to values higher than 2 resulted in short term sealing of the scratch induced interface. In other words the coatings with $W_{Scratch}$ / $t_{Coating}$ values of 2 and 6, endured 48 and 10 hours exposure to the electrolyte, respectively, after which their behaviour deviated from the intact coatings. The results presented in Figure 5.14 confirm the restrictive effect of the underlying substrate on the healing performance of the hybrid sol-gel coating specifically when the artificial scratch is wider the coating thickness by a factor of 2.
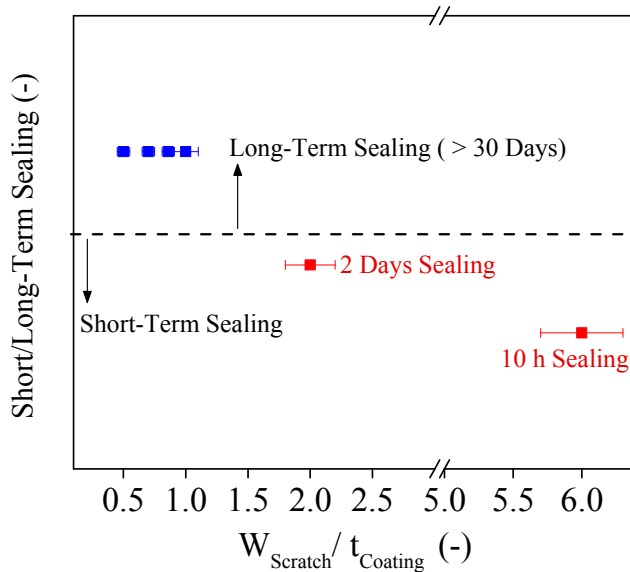
Figure 5.14. Short/Long-term sealing performance of the healed hybrid sol-gel coatings as function of scratch width to coating thickness ratio ($W_{Scratch}/t_{Coating}$).

(a)

(b)

(c)

(d)
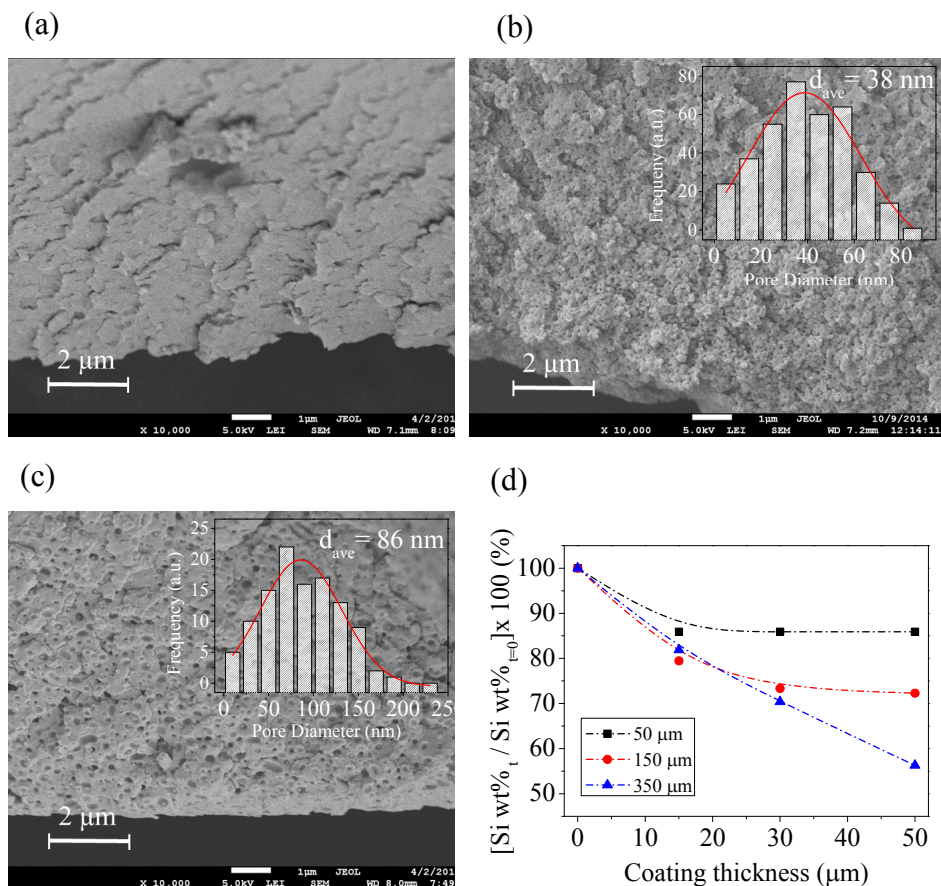
Figure 5.15. SEM micrographs of cryo-fractured hybrid sol-gel coatings with an average thickness of 50 µm (a), 150 µm (b) 350 µm (c) and depth resolved normalized concentration of Si in the fractured coatings (d).

Increasing the coating thickness not only extended the hybrid sol-gel coating capability to fully seal scratches as wide as 300 µm but also led to different coating responses in the electrolyte. In contrast to the 50 µm thick coating, the 150 and 350 µm thick coatings showed a decrease in coating resistance at the early stages of exposure to the electrolyte (when intact). The corresponding increase in the capacitance of the 150 and 350 µm thick coatings is equivalent to a water uptake (Φ) of 0.20 and 0.35, respectively which

is roughly 5 to 10 times higher than that of the 50 µm thick coating (Φ = 0.035). Such an increase cannot be justified by the thickness increase.

For homogeneous coatings obeying Ficks' laws, diffusion coefficient and permeability and hence water uptake are independent of the coating thickness. However, inaccuracy in the thickness measurement, swelling (specifically in more hydrophilic coatings) and the coating formulation can result in deviations from the mentioned rule [34, 35]. As an example a ten and hundred fold increase in the thickness of polyethyleneterephthalate (PET) and polyimide coating, respectively, increased the water uptake by a factor of 2 [35]. Additionally, the structural features arising during the film formation might yield thickness dependent permeability and water uptake. Curing conditions such as relative humidity, temperature, the nature of the substrate, etc, may affect the degree of polymerisation and the arrangement of polymer chains [34, 35].

The potential structural changes along the hybrid sol-gel coating thickness were studied by monitoring the cross-sections of the coatings are after cryoghenic fracture (Figure 5.15). Unlike the 50 µm thick coating (Figure 5.15 a), the other two coatings exhibited a 10 µm thick porous layer next to the substrate. The average pore diameters of 38 and 86 nm in 150 and 350 µm coatings, respectively, are consistent with the higher water uptake of the thicker hybrid sol-gel coating.

Formation of the porous layer in thick hybrid sol-gel coatings can be explained by coating stratification, resulting in a thin silane-reach layer next to the substrate [36-38]. Evolution of volatile side products (e.g. water and alcohols) in condensation reactions of organically modified silicone alkoxides can produce a porous layer [26]. The depth resolved EDS analysis of the cryo-fractured coatings over 50 µm distance from the substrate (starting from the metal-coating interface) revealed stratification of the healable hybrid sol-gel coatings independent of coating thickness (Figure 5.15 d). Yet, silane concentration gradient was increased as a function a coating thickness. The highest silane concentration at metal-coating interface of the 350 µm thick coating further justifies its bigger pores and higher water uptake.

Conclusions

In this chapter application of the hybrid sol-gel polymer as a protective coating for AA2024-T3 substrate is described. The prepared coating with BS:APS molar ratio of 3:1 exhibited a hydrophobic surface, high adhesion strength and an effective corrosion protection in 0.5 M NaCl solution. Upon thermal treatment, the healable hybrid sol-gel

coating demonstrated 100% superficial healing efficiency, full adhesion recovery and complete restoration of its barrier properties. Although the long-term sealing performance of the coating was influenced by the scratch width to coating thickness ratio, the healed coating maintained same protective properties as the intact coating for one year exposure to the aggressive electrolyte, as long as the scratch width was the same range as coating thickness i.e. for $W_{Scratch}/t_{Coating} \leq 1$.

References:

[1] I. Gurrappa, I.V.S. Yashwanth, The Importance of Corrosion and the Necessity of Applying Intelligent Coatings for Its Control, in: A. Tiwari, J. Rawlins, L.H. Hihara (Eds.) Intelligent Coatings for Corrosion Control, Butterworth-Heinemann, Boston, 2015, pp. 17-58.[2] A.A. Ashirgade, Environmentally-Compliant Novolac Superprimers for Corrosion Protection of Aluminum Alloys, University of Cincinnati, 2006.

[3] A.W. Peabody, Peabody's Control of Pipeline Corrosion, 2 ed., NACE International The Corrosion Society, Houston, Texas, 2001.

[4] G.W. Walter, A critical review of the protection of metals by paints, Corrosion Science, 26 (1986) 27-38.

[5] R.T.M. van Benthem, W. Ming, G. de With, Self Healing Polymer Coatings, in: S. van der Zwaag (Ed.) Self Healing Materials, Springer Netherlands2007, pp. 139-159.

[6] S.J. García, H.R. Fischer, S. van der Zwaag, A critical appraisal of the potential of self healing polymeric coatings, Progress in Organic Coatings, 72 (2011) 211-221.

[7] M.L. Zheludkevich, Self-healing Anti-Corrosion Coatings in: S.K. Ghosh (Ed.) Self-Healing Materials: Fundamentals, Design Strategies, and Applications Wiley-VCH2009.

[8] A.E. Hughes, I.S. Cole, T.H. Muster, R.J. Varley, Designing green, self-healing coatings for metal protection, NPG Asia Mater, 2 (2010) 143-151.

[9] D.G. Shchukin, D. Borisova, H. Möhwald, Self-Healing Coatings, Self-Healing Polymers, Wiley-VCH Verlag GmbH & Co. KGaA2013, pp. 381-399.

[10] G. Scheltjens, J. Brancart, I. De Graeve, B. Van Mele, H. Terryn, G. Van Assche, Self-healing property characterization of reversible thermoset coatings, J Therm Anal Calorim, 105 (2011) 805-809.

[11] J. Brancart, G. Scheltjens, T. Muselle, B. Van Mele, H. Terryn, G. Van Assche, Atomic force microscopy–based study of self-healing coatings based on reversible polymer network systems, Journal of Intelligent Material Systems and Structures, (2012).

[12] J. Kötteritzsch, S. Stumpf, S. Hoeppener, J. Vitz, M.D. Hager, U.S. Schubert, One-Component Intrinsic Self-Healing Coatings Based on Reversible Crosslinking by Diels–Alder Cycloadditions, Macromolecular Chemistry and Physics, 214 (2013) 1636-1649.

[13] D.N. Amato, G.A. Strange, J.P. Swanson, A.D. Chavez, S.E. Roy, K.L. Varney, C.A. Machado, D.V. Amato, P.J. Costanzo, Synthesis and evaluation of thermally-responsive coatings based upon Diels-Alder chemistry and renewable materials, Polymer Chemistry, 5 (2014) 69-76.

[14] X. Luo, P.T. Mather, Shape Memory Assisted Self-Healing Coating, ACS Macro Letters, 2 (2013) 152-156.

[15] A. Lutz, O. van den Berg, J. Van Damme, K. Verheyen, E. Bauters, I. De Graeve, F.E. Du Prez, H. Terryn, A Shape-Recovery Polymer Coating for the Corrosion Protection of Metallic Surfaces, ACS Applied Materials & Interfaces, 7 (2015) 175-183.

[16] S. D'Hollander, G. Van Assche, B. Van Mele, F. Du Prez, Novel synthetic strategy toward shape memory polyurethanes with a well-defined switching temperature, Polymer, 50 (2009) 4447-4454.

[17] E.D. Rodriguez, X. Luo, P.T. Mather, Linear/Network Poly(ε-caprolactone) Blends Exhibiting Shape Memory Assisted Self-Healing (SMASH), ACS Applied Materials & Interfaces, 3 (2011) 152-161.

[18] C.C. Morquecho, C.L. Meléndez, M. Flores-Zamora, R. Bautista-Margulis, H.E. Ponce, F.A. Calderón, C.G. Tiburcio, A. Martínez-Villafañe, Electrochemical Impedance Spectroscopy Behavior of Nanometric Al-Cr and Cr-Al Coatings by Magnetron Sputtering, Int. J. Electrochem. Sci, 7 (2012) 1125-1133.

[19] Ö. Özkanat, Molecular interfaces of coated aluminium, S.n., S.l, 2013.

[20] J.M. Vega, A.M. Grande, S. van der Zwaag, S.J. Garcia, On the role of free carboxylic groups and cluster conformation on the surface scratch healing behaviour of ionomers, European Polymer Journal, 57 (2014) 121-126.

[21] A.M.A. Mohamed, A.M. Abdullah, N.A. Younan, Corrosion behavior of superhydrophobic surfaces: A review, Arabian Journal of Chemistry, (2014).

[22] T.L. Metroke, O. Kachurina, E.T. Knobbe, Spectroscopic and corrosion resistance characterization of GLYMO–TEOS Ormosil coatings for aluminum alloy corrosion inhibition, Progress in Organic Coatings, 44 (2002) 295-305.

[23] M. Sheffer, A. Groysman, D. Mandler, Electrodeposition of sol–gel films on Al for corrosion protection, Corrosion Science, 45 (2003) 2893-2904.

[24] W. Funke, The role of adhesion in corrosion protection by organic coatings, Journal of the oil and colour chemists'association 68 (1985) 229-232.

[25] W. Funke, H. Zatloukal, Assessment of the corrosion protection characteristics of paint films and other organic coatings. III. Adhesion at high humidity as a criterion of corrosion protection behaviour, Farbe und Lack, 84 (1978) 584.

[26] W.J. van Ooij, D. Zhu, M. Stacy, A. Seth, T. Mugada, J. Gandhi, P. Puomi, Corrosion Protection Properties of Organofunctional Silanes—An Overview, Tsinghua Science & Technology, 10 (2005) 639-664.

[27] F. Mansfeld, M.W. Kendig, Electrochemical Impedance Spectroscopy of protective coatings, Materials and Corrosion, 36 (1985) 473-483.

[28] S.J. Garcia, T.A. Markley, J.M.C. Mol, A.E. Hughes, Unravelling the corrosion inhibition mechanisms of bi-functional inhibitors by EIS and SEM–EDS, Corrosion Science, 69 (2013) 346-358.

[29] C.H. Hsu, F. Mansfeld, Technical Note: Concerning the Conversion of the Constant Phase Element Parameter Y0 into a Capacitance, NACE International, 2001.

[30] D.M. Brasher, A.H. Kingsbury, Electrical measurements in the study of immersed paint coatings on metal. I. Comparison between capacitance and gravimetric methods of estimating water-uptake, Journal of Applied Chemistry, 4 (1954) 62-72.

[31] G.L. Guerriero, Liquid crystalline thermosetting polymers as protective coatings for aerospace, Aerospace Engineering, Structural Integrity and Composites, Delft University of Technology, 2012.

[32] R. Rey, E. Javierre, S.J. García, S.v. der Zwaag, J.M. García-Aznar, Numerical study of the scratch-closing behavior of coatings containing an expansive layer, Surface and Coatings Technology, 206 (2012) 2220-2225.

[33] J.A. Yoon, J. Kamada, K. Koynov, J. Mohin, R. Nicolaÿ, Y. Zhang, A.C. Balazs, T. Kowalewski, K. Matyjaszewski, Self-Healing Polymer Films Based on Thiol–Disulfide Exchange Reactions and Self-Healing Kinetics Measured Using Atomic Force Microscopy, Macromolecules, 45 (2012) 142-149.

[34] D.Y. Perera, P. Selier, Water transport in organic coatings, Progress in Organic Coatings, 2 (1973) 57-80.

[35] F. Bellucci, L. Nicodemo, Water Transport in Organic Coatings, Corrosion, 49 (1993) 235-247.

[36] A. Seth, W.J. van Ooij, P. Puomi, Z. Yin, A. Ashirgade, S. Bafna, C. Shivane, Novel, one-step, chromate-free coatings containing anticorrosion pigments for metals—An overview and mechanistic study, Progress in Organic Coatings, 58 (2007) 136-145.

[37] L.-K. Wu, J.-T. Zhang, J.-M. Hu, J.-Q. Zhang, Improved corrosion performance of electrophoretic coatings by silane addition, Corrosion Science, 56 (2012) 58-66.

[38] P. Wang, D.W. Schaefer, Why does Silane Enhance the Protective Properties of Epoxy Films?, Langmuir, 24 (2008) 13496-13501.

Chapter 6

Accelerated electrochemical evaluation of intrinsic healing dual organic-inorganic sol-gel coatings by AC/DC/AC

Introduction

Passive protective coatings are among the most widespread approaches for corrosion protection of metallic substrates. Such coatings restrict ingress of water and corrosive species to the metal-coating interface, limiting corrosion initiation [1, 2]. Due to the electrochemical nature of the corrosion processes, electrochemical characterization techniques are well-suited for evaluation of the coating's protective performance. Yet, the traditional direct current (DC) measurements (e.g. polarization curves), where electron-conducting processes are described in terms of ohmic resistance, fail to provide adequate information on poorly conducting coatings [3].

Alternating current (AC) measurements on the other hand offer comprehensive information on the properties of non-conductive (polymeric) coatings [4]. Electrochemical impedance spectroscopy (EIS) as the most common AC method, is a well-established technique for evaluation of coating systems [5-9]. In an EIS measurement, the complex impedance of a coating system is measured over the desired frequency range. In combination with equivalent circuits, the EIS data can provide detailed information on the coating's barrier performance, stability, degree of degradation, thickness, porosity, adhesion and the electrochemical processes occurring at the metal surface [10-14]. Yet, as a result of non-destructive nature of the EIS measurements (provided that the measurement is well-performed), the monitoring process of an intact coating system can be as long as months to years.

To reduce the measurement time, a variant of the EIS technique was introduced in the 90s by Hollaender for rapid assessment of the coated food/beverage cans [15, 16]. Such variant consists of cycles of EIS (AC) – cathodic polarization (DC) – EIS (AC), leading to its common name AC/DC/AC procedure. The procedure was later adopted by Suay, Rodriguez and Garcia for evaluation of water-born and powder coatings as well as cataphoretic paints through introduction of a long relaxation period and adopting it into a 24 h test [17-22].

In the AC/DC/AC test procedure, the coating system's initial state is registered with a first EIS run, then the sample is cathodically polarized at a constant potential (DC) for a given time. The polarization step aims at promoting local cathodic reactions at the metal surface leading to formation of blisters, coating delamination and further corrosion processes around existing defects. Thereafter, a new EIS run registers the coating's new state [15]. The process is generally repeated six times for a 24 h test [22] although more cycles can be implemented depending on the evaluated coating system. As a result of the accelerated aging promoted by electrochemical stresses, such an approach provides

valuable information on the properties of the coating systems in a very short time, simulating much longterm EIS measurements [9, 15, 17-24].

Accelerated screening tests also yielding information on the failure mechanisms are particularly valuable when developing new (self-healing) coatings [25]. In this chapter application of AC/DC/AC procedure as an efficient electrochemical technique for evaluation of the goodness of the healed interface of intrinsic healing coatings is described. To this aim the durability and sealing efficiency of the healable hybrid sol-gel coating were studied using the AC/DC/AC procedure and the results are compared to those obtained using conventional EIS. Furthermore, the cross-section of the hybrid sol-gel coatings tested using these two electrochemical techniques i.e. AC/DC/AC and EIS were further analyzed using scanning electron microscope (SEM), revealing testing technique dependent failure modes of the coatings. The results obtained suggest that the AC/DC/AC procedure is suitable as a fast evaluation technique of the degree of healing achieved in self-healing intrinsic coatings.

Experimental procedure

Materials

Epoxy resin based on Epikote™ 828 (184-190 g eq^{-1}) and Ancamine®2500 curing agent (105-110 g eq^{-1}) were provided by Akzo Nobel Aerospace Coatings (ANAC) and used as received. (3-Aminopropyl)trimethoxysilane (97%, MW=179.29 g mol^{-1}) and pentaerythritol tetrakis(3-mercaptopropionate) (>95%, MW=488.66 g mol^{-1}), hereon, APS and tetra-thiol respectively, were purchased from Sigma-Aldrich, The Netherlands, and used without further purification. Bis[3-(triethoxysilyl)propyl]tetrasulfide (99%, MW=538.95 g mol^{-1}, total sulfur content>20%), hereon BS, and ethanol were purchased from Capture Chemicals, China, and VWR, The Netherlands, respectively and used as received. Unclad AA2024-T3 was received from Akzo Nobel and used as metallic substrate.

Coating preparation

Prior to application of the coating, the AA2024-T3 panels of 3×4 cm^2 were ground mechanically using SiC paper (grade 1000) to remove the native oxide layer and further degreased with ethanol. The panels were then immersed in 2 M NaOH solution for 10

seconds and thoroughly rinsed with double distilled water to increase the surface density of the hydroxyl groups (OH⁻) on the AA2024-T3 substrates [26].

The dried AA2024-T3 panels were coated with healable hybrid sol-gel films. The polymers were prepared as described in chapter 2. The organically modified silicone alkoxides (OMSAs) were sequentially (APS followed by BS) added to the epoxy resin with the OMSAs:epoxy resin weight ratio of 1:1, keeping BS:APS molar ratio at 3:1. The mixture was stirred using a magnetic stirrer at 300 rpm for 3 h at room temperature. The organic crosslinker (Ancamine®2500) was then added to the mixture keeping the amine hydrogen equivalent (AHE) to epoxy equivalent (EE) ratio at 1.1 and the mixture was stirred in a high speed mixer at 2500 rpm for 5 min. Tetra-thiol was then added in a tetra-thiol:epoxy resin weight ratio 0.56:1 and the mixture was further mixed in the high speed mixer for 40 s at 2500 rpm. The resulting mixture was then cast on the cleaned AA2024-T3 panels using a calibrated standard aluminum single doctor blade. The coated samples were dried at room temperature for one hour and cured for 48 h at 70 °C yielding coatings with an average dry thickness of 50 ± 2 μm.

To evaluate the hybrid sol-gel coating sealing efficiency, controlled 3 mm long scratches with an average width of 50 μm were created using a micro-scratch tester equipped with a sharp razor blade as described in chapter 5. The penetration depth of the razor into the coating was adjusted such that the artificial scratch reached the metallic substrate. To activate the gap closure and therefore the healing process, the scratched samples were clamped between two glass plates applying a constant uniform pressure of 30 kPa. The assembly was then placed for a given time (1, 2 or 8 h) in an air circulation oven operating at 70 °C.

Coating characterization

Electrochemical impedance spectroscopy (EIS)

The intact and healed coating systems were electrochemically characterized using EIS. The EIS measurements were carried out at room temperature in a conventional three-electrode cell configuration consisting of a saturated Ag/AgCl reference electrode, a carbon black rod with diameter of 50 mm as the counter electrode and the coated AA2024 substrate as the working electrode. The samples were placed horizontally in the electrochemical cell with an exposed area of around 0.8 cm². A Faraday cage was employed to avoid the interference of external electromagnetic fields. A stagnant 0.5 M NaCl aqueous solution in equilibrium with air was employed as the testing electrolyte. The measurements were performed using an Autolab PGSTAT 302 N

potentiostat/galvanostat coupled to a frequency analyser (FRA) in the frequency range of 10^{-1}-10^5 Hz, with a 10 mV (rms) sinusoidal perturbation respect to the open circuit potential. 10 data points were acquired per frequency decade. The impedance plots were fitted using different equivalent circuits with the Nova software package from Metrohm-Autolab B.V., following the most probable equivalent circuit (MPEC) selection approach [27].

AC/DC/AC

The AC/DC/AC measurements were performed at room temperature following reported and well-established procedures [17, 20, 21]. The tests were performed using a PGSTAT 302 N potentiostat/galvanostat, in a conventional three-electrode cell containing stagnant 0.5 M NaCl aqueous solution as the testing electrolyte. The AC/DC/AC test routine started with the first AC run after 1 hr pre-exposure to the electrolyte for OCP equilibration. The AC measurements (i.e. EIS) were performed using the procedure described above. After the first AC run the test specimens (intact and healed coatings) were cathodically polarized at a constant potential of –4 V for 20 minutes. Subsequent to the cathodic polarization, a potential relaxation period of 3h was implemented. The variation in open circuit potential (OCP) versus time was recorded during the relaxation step. The cycle was completed with a new AC run (EIS). A schematic representation of one EIS-Polarization-relaxation-EIS cycle is shown in Figure 6.1. This test sequence was repeated at least 6 times (lasting 24 h in total).
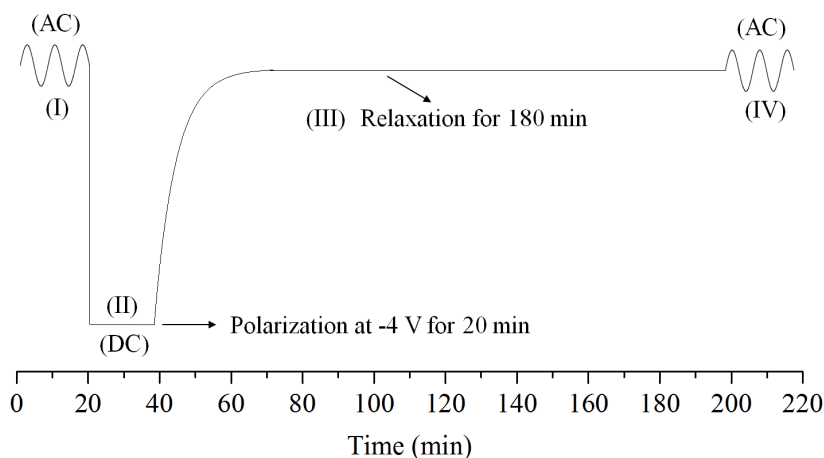

Figure 6.1. Schematic of the AC/DC/AC test procedure, adopted from [17].

Optical microscopy

The intact, scratched and healed hybrid sol-gel coatings were examined using a Keyence VHX-2000 series digital microscope after damage, healing and electrochemical testing. Images were captured in reflection mode with a 500x objective and the micrographs were analyzed using VHX-2000 software.

Scanning confocal microscopy

An Olympus laser scanning confocal microscope (OLS 3100) was employed to analyse the surface topology of the hybrid sol-gel coatings after the AC/DC/AC procedure. The images were captured with 5x and 10x objectives and were analysed using LEXT software.

Scanning electron microscopy

A high resolution JOEL SEM (JSM-7500F) operating at 5 kV was employed to analyze the morphology of the electrochemically tested hybrid sol-gel coatings across the coating thickness.

Results & Discussion

Intact coating performance

As discussed in chapter 5, the healable hybrid sol-gel coating with an average thickness of 50 μm proved to be an effective barrier layer on AA2024-T3 substrate. Electrochemical evaluation of this coating system using EIS revealed no significant variations in the coating resistance and capacitance over 14 days of exposure to a 0.5 M NaCl solution (Figure 5.7). Yet, Figure 6.2 shows that testing this coating system using the AC/DC/AC procedure as a fast assessment technique, led to rapid degradation of the coating's protective performance as illustrated by a gradual decrease in the coating low frequency Bode modulus ($|Z|_{0.1\ Hz}$) as well as the changes in the Bode phase plots with the number of the applied polarization cycles. The change of the Bode phase plot from a capacitive system (initial state) to a resistive/capacitive one upon application of the polarization cycles, is indicative of pore formation process facilitating electrolyte ingress followed by the electrochemical processes at the metal/coating interface.

To quantify the resistance and capacitance of the hybrid sol-gel coatings and the potential delamination processes initiated by polarization cycles , the EIS data of the AC/DC/AC test were fitted using the equivalent circuits (EC) presented in Figure 6.3 a. In the depicted ECs, R_{sol}, R_{coat}, and R_{pol} represent solution, coating and polarization

resistances, respectively, while CPE_{coat} and CPE_{dl} stand for coating and double layer constant phase elements. The CPE_{coat} and CPE_{dl} were employed to calculate the capacitance of the coating (C_{Coat}) and the double layer (C_{dl}) based on Eq. 5.2, respectively. The double layer capacitance (C_{dl}) can be directly correlated to the electrochemically active surface area of the substrate and therefore can provide a measure of coating delamination. Apart from the EIS spectrum acquired prior to the polarization cycles (i.e. the initial EIS), the other EIS spectra were fitted using two-time constant ECs to capture and quantify the electrochemical processes at the metal-coating interface. As Figure 6.3 b shows, fitting the EIS data revealed a decrease of about two orders of magnitude in the coating resistance (R_{Coat}) between the first and the sixth cycle (Figure 6.3 b). The drastic drop in the coating resistance is in-line with the decrease in impedance modulus presented in Figure 6.2, confirming the degradation inflicted to the coating system during the polarization steps.
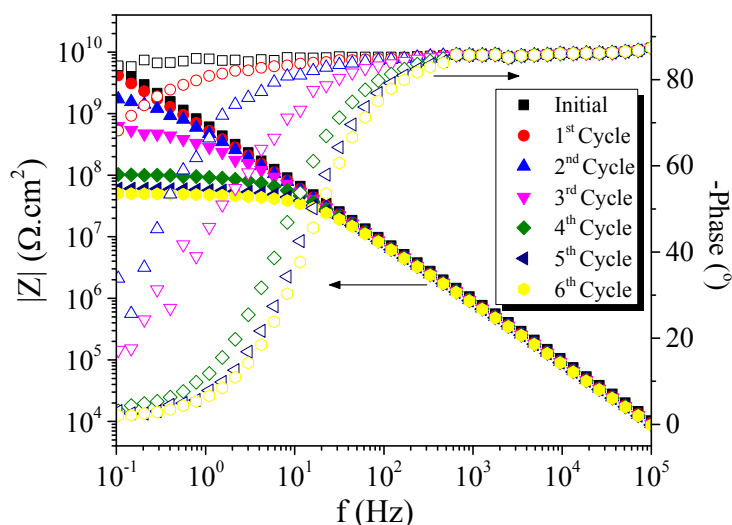

Figure 6.2. Bode modulus plots of an intact coating system with an average thickness of 50 μm, for six consecutive cycles of AC/DC/AC procedure in 0.5 M NaCl solution.

In contract to the behaviour of the coating resistance, its capacitance (C_{Coat}) slightly increased reaching a plateau ($C_{Coat} = 0.3$ nF.cm^{-2}) after one test cycle (Figure 6.3 b). The

insignificant increase in the coating capacitance after six polarization cycles indicated the absence of major defects in the tested coating. Yet, as Figure 6.3 c shows the double layer capacitance (C_{dl}) increased gradually (power law) as a function of the number of applied polarization cycles, suggesting increased electrochemical activities on the surface of the metallic substrate due to an increase in the active area as a result of coating delamination [5, 10-14]. The increase in electrochemical activity level (corrosion processes) was confirmed by the drastic drop of the polarization resistance (R_{pol}) (Figure 6.3 c).

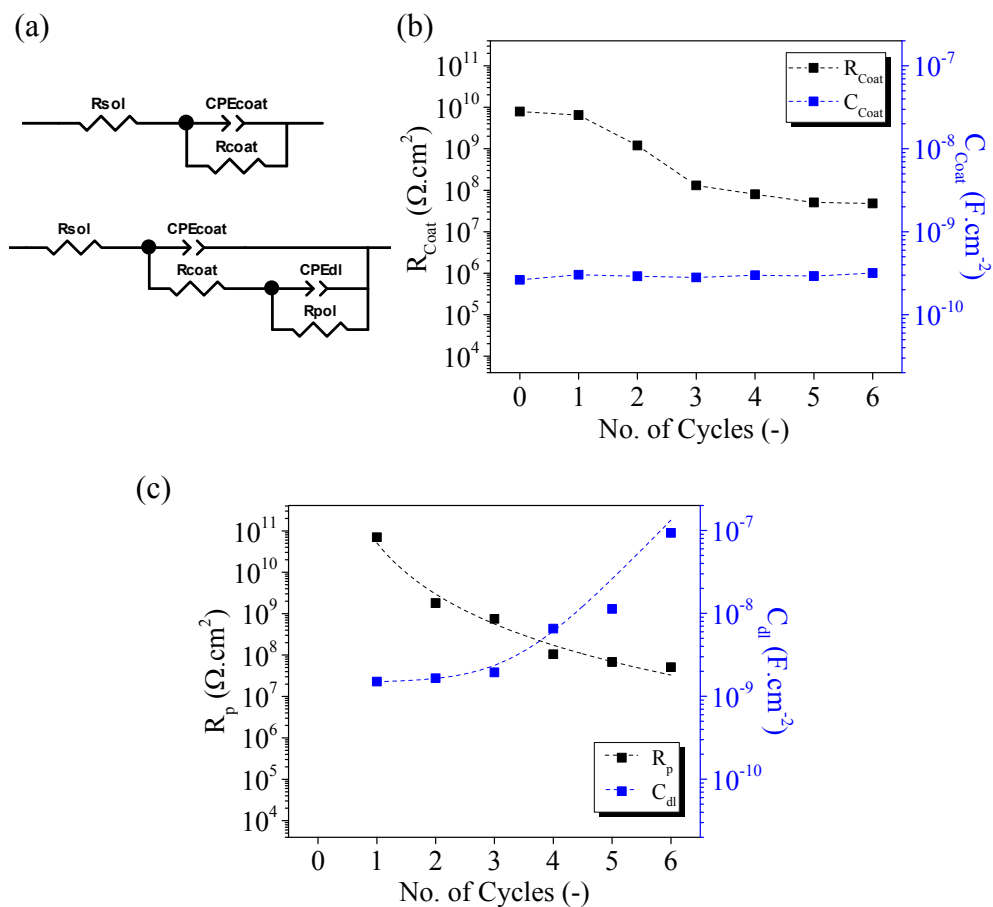Figure 6.3. Equivalent circuits used to fit the experimental EIS data (a), evolution of the hybrid sol-gel coating resistance (R_{coat}) and capacitance (C_{coat}) (b) and polarization resistance (R_p) and double layer capacitance (C_{dl}) (c) for six consecutive of AC/DC/AC procedure in 0.5 M NaCl.

The electrochemical stress (i.e. cathodic polarization steps) applied to the coating system during the AC/DC/AC procedure might lead to the following scenarios [20-22]:

(i) The imposed negative charge on the substrate can force migration of cationic species in the electrolyte (e.g H^+ and Na^+) towards the metal-coating interface, yielding (potentially) a positively charged coating. The accumulated positive charge in the coating layer would later be counter-balanced by absorption of anions such as Cl^-. The flow of ions through the coating can result in pore opening and coating deterioration.

(ii) Evolution of H_2 gas and OH^- groups as a result of cathodic reactions on the substrate at potentials more negative than -1.0 V versus saturated calomel electrode (SCE):

$$2H_2O(l) + 2e^- \rightarrow H_2(g) + 2OH^- \hspace{3cm} \text{Eq. 6.1}$$

The evolution of gaseous species and OH^- groups in the cathodic reaction can promote local delaminations via blisters formation around existing local damages in the coating, as depicted in Figure 6.4. Yet, it is noteworthy that the cathodic reactions will primarily take place if the electrolyte can penetrate to the metal-coating interface. Therefore, the process is strongly affected by coating properties (e.g. permeability, adhesion, presence of damage sites such as local delaminated areas, etc) [19-22].
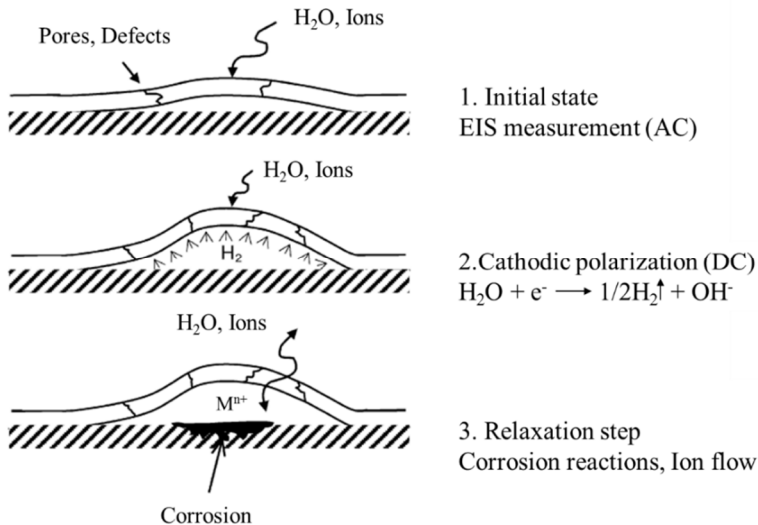

Figure 6.4. Schematic representation of failure mechanism of the coating due to AC/DC/AC testing, adopted from [18].

Deterioration of the hybrid sol-gel coating's protective function upon testing with AC/DC/AC procedure can result from one or both of the aforementioned processes. Evaluation of the surface topology of the coatings tested with AC/DC/AC procedure using optical and confocal microscopy revealed the formation of well-defined blisters on the coating (Figure 6.5). The presence of blisters confirms the occurrence of severe cathodic reactions at the metal-coating interface as observed in the case of cathaphoretic coatings tested using the same procedure [21]. The appearance of the distinct blisters might be explained by presence of original defects (e.g. trapped air bubbles, water rich paths, under film delaminations) in the hybrid sol-gel coating acting as ion-conduction paths necessary for the corrosion processes to occur. Moreover, the localized electrochemical processes in form of pitting corrosion beneath the blisters and a few scattered sites around it are indicative of a severe attack of the coating during the cathodic polarization. (Figure 6.5).

The hybrid sol-gel coating was further studied by analysing the evolution of the coating open circuit potential (OCP) during a 3 h relaxation step (Figure 6.6). The evolution of the coating open circuit potential after the cathodic polarization step (i.e. during the relaxation step) yields valuable information on the processes occurring in the coating and the metal-coating interface in particular evolution of the H_2 (g) and OH^-, promoting coating delamination.

As Figure 6.6 shows the OCP of the hybrid sol-gel coating exhibited single potential relaxation process. However, the steady state OCP of the coating changed with the number test cycles. After the first polarization step (cycle 1), the coating OCP quickly relaxed to its initial value (-0.1 V versus. Ag/AgCl). The observed potential relaxation can be attributed to the flow/migration of electrolyte and ionic species through the coating promoting the pore opening phenomenon [20-22]. After the second polarization (cycle 2) the OCP demonstrated a rather rapid relaxation, reaching a steady state value of -1.0 V versus Ag/AgCl. Such relaxation potential profile has been assigned in literature [20-22] to the presence of electrolyte at the metal-coating interface promoting cathodic reactions according to Eq. 6.1. The obtained data confirms that localized cathodic reactions took place after opening of the ionic conductive paths in the coating during the polarization steps, facilitating further ingress of electrolyte to the metal-coating interface. After the second polarization step (i.e. in the third, fourth, fifth and sixth cycles) the coating exhibited a much slower relaxation behaviour related to extensive cathodic reactions (steady state OCP = -1.2 V vs. Ag/AgCl). The OCP relaxation data further

confirmed pore formation/opening followed by cathodic reaction as the main processes leading to deterioration of the hybrid sol-gel coating during the AC/DC/AC procedure.
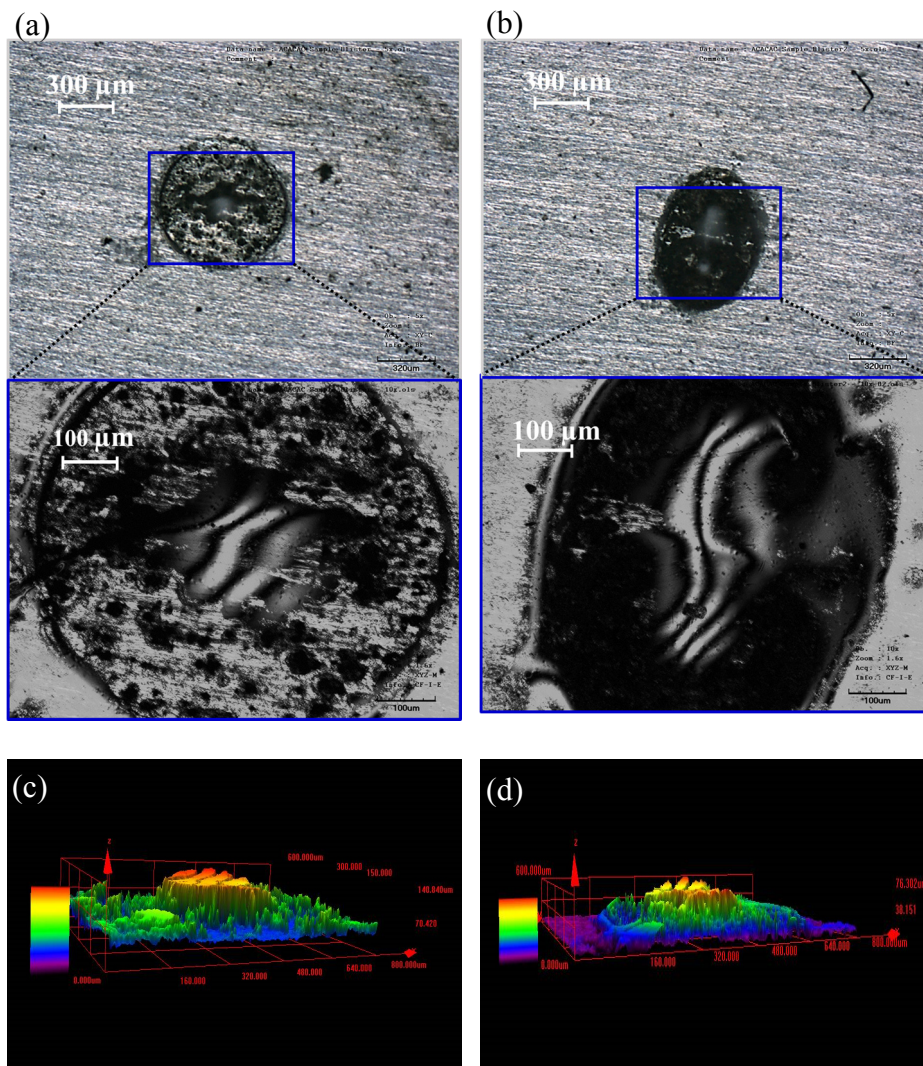

Figure 6.5. Optical micrographs (a) and (b) and surface topology (c) and (d) of two blisters formed on a 50µm thick hybrid sol-gel coating after six consecutive cycles in AC/DC/AC testing.

The effective barrier properties of the hybrid sol-gel coating was illustrated by its stable resistance and capacitance derived from the EIS spectra over 30 days exposure to the aggressive electrolyte (chapter 5). Yet, the information extracted from the AC/DC/AC evaluation of the hybrid sol-gel coatings revealed a rapid decay in the coating protective function as a result of the polarization induced damages. The reduced coating (R_{Coat}) and polarization resistance (R_{pol}) coupled with the potential relaxation profiles suggest that the coating is severely damaged after two AC/DC/DC test cycles lasting 8 h, confirming the capability of the AC/DC/AC procedure in rapid assessment of the long term protective power of a hybrid sol-gel coating.
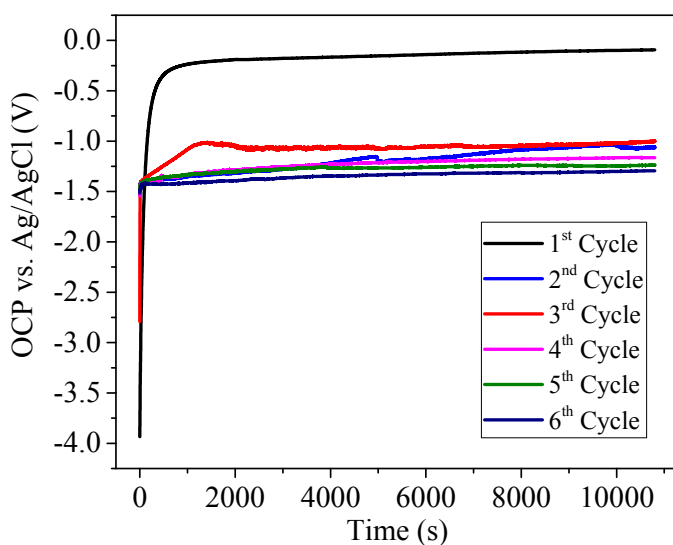
Figure 6.6. Evolution of the open circuit potential (OCP) vs. time for a hybrid sol-gel coating tested with six consecutive AC/DC/AC cycles.

Damaged and healed coatings performance

The Bode modulus plots of the hybrid sol-gel coatings healed for one, two and eight hours at 70 °C and tested using EIS and AC/DC/AC procedures are presented in Figure 6.7. As Figure 6.7 a shows, despite the initial sealing of the scratch induced interface
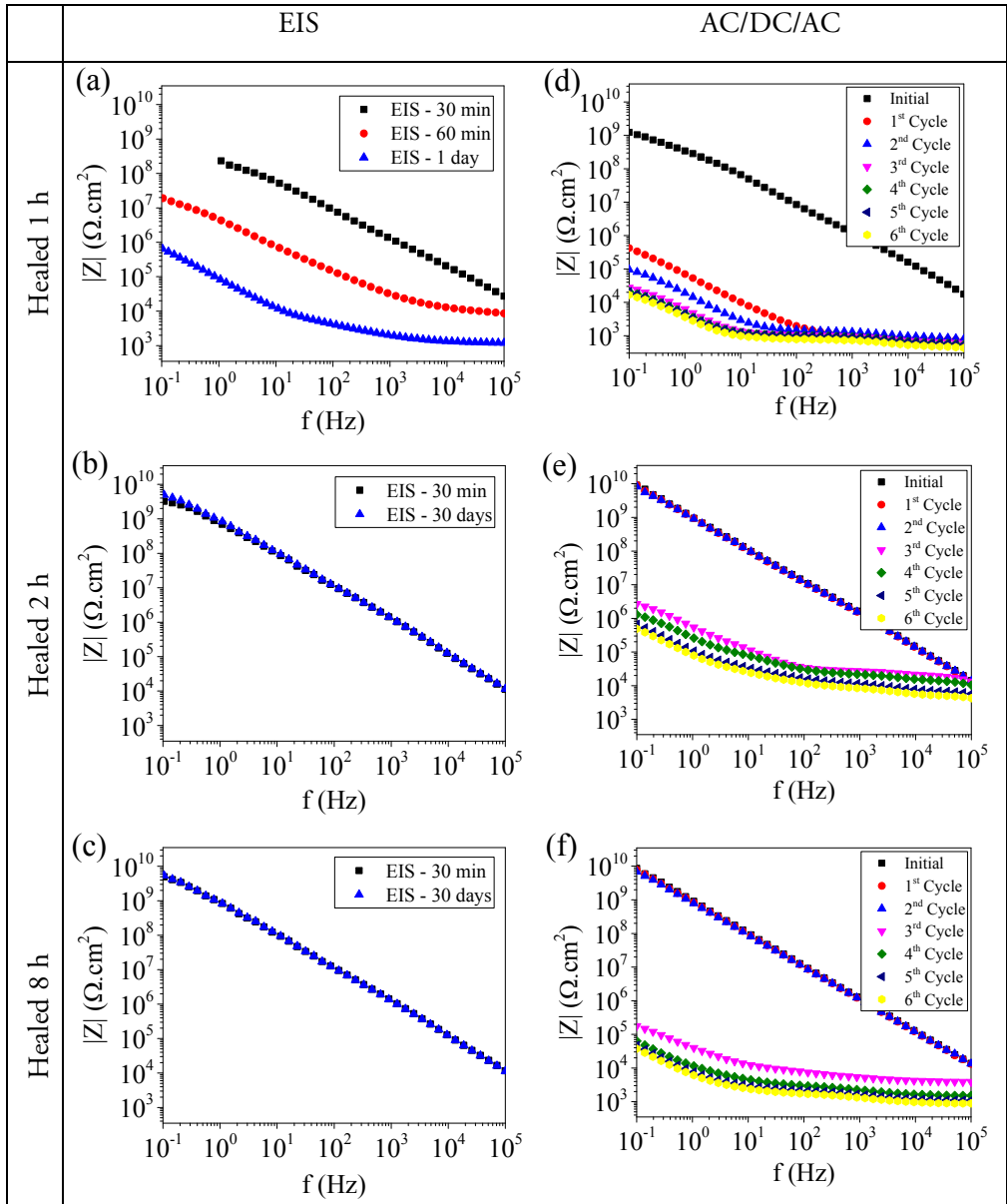
Figure 6.7. Bode modulus plots of hybrid sol-gel coatings healed for 1 h (a) and (b), 2 h (c) and (d), and 8 h (e) and (f) and tested using EIS and AC/DC/AC procedures respectively.

the coating lost its barrier function upon one hour exposure to 0.5 M NaCl solution when tested using non-destructive EIS procedure. This demonstrates the capacity of the EIS in rapidly disclosing the incomplete healing of the interface. Upon longer exposure manifested by high low-frequency |Z| of the hybrid sol-gel coating healed for one hour, (one day), the coating's protective function further deteriorated as reflected by the significant drop of the |Z| in the whole frequency range. Unlike the hybrid sol-gel coating healed for one hour, the ones healed for two and eight hours at 70 °C exhibited long-term sealing of the scratched induced interface. Figures 6.7 b and 6.7 c show that the EIS spectra of these healed coatings after 30 days of immersion in 0.5 M NaCl solution overlapped with those of initial immersion (30 minutes), revealing efficient sealing of the generated interface. Yet, due to the high barrier properties of the coatings healed for two and eight hours, EIS was not able to unveil the differences between them in terms of the goodness of the healed scratch even after one month exposure to the aggressive electrolyte.

Application of electrochemical stress (i.e. cathodic polarization) to the coating system healed for an hour at 70 °C (during AC/DC/AC procedure) led to a substantial decrease in the coating high-frequency |Z|, suggesting failure of the healed interface after one test cycle (Figure 6.7 d). Additional test cycles further promoted corrosion processes at metal-coating interface as illustrated by the continuous decay in the coating's low-frequency |Z| value.

Evaluation of the coatings healed for two and eight hours using AC/DC/AC procedure revealed their different performance compared to the one healed for one hour. In contrast to the coating healed for one hour, the ones healed for two and eight hours could withstand two polarization cycles (Figures 6.7 d and 6.7 e). The third polarization cycle led to failure of the healed interface and loss of coatings barrier properties, as shown by the significant drop of |Z| in the whole frequency range in the third AC run (EIS) of the AC/DC/AC procedure. The equivalent performance of the hybrid sol-gel coatings healed for two and eight hours illustrated by the equal number of the polarization cycles leading to the coating failure, suggests an equivalent degree of scratch healing (goodness of the healed scratch) for the two healed coatings. The obtained results are in line with the interfacial healing efficiencies of hybrid sol-gel polymer samples healed for two and twelve hours when tested using the fracture mechanics protocol (Chapter 4).

The evolution of the coating resistance (R_{Coat}) in the intact and healed hybrid sol-gel coatings tested using different electrochemical techniques (i.e. EIS and AC/DC/AC) are presented in Figure 6.8. As Figure 6.8 shows, apart from the test time span, the EIS and

AC/DC/AC procedures revealed similar behaviour trend in the healed hybrid sol-gel coatings. The coatings healed for one hour lost their barrier properties in the very early stages of the EIS and AC/DC/AC measurements as illustrated by the abrupt decrease in the coating resistance ($\Delta R_{Coat} > 1E4\ \Omega.cm^2$), disclosing insufficient healing of the scratch induced interface. The evolution of the coating resistance in hybrid sol-gel coatings healed for two and eight hours at 70 °C, exhibited their equivalent performances when tested using either of the electrochemical characterization techniques. While the healed coatings (for two and eight hours) maintained their high resistance upon 30 days of testing, they exhibited a drastic drop in the coating resistance ($\Delta R_{Coat} > 1E5\ \Omega.cm^2$) after two cycles of the AC/DC/AC procedure.
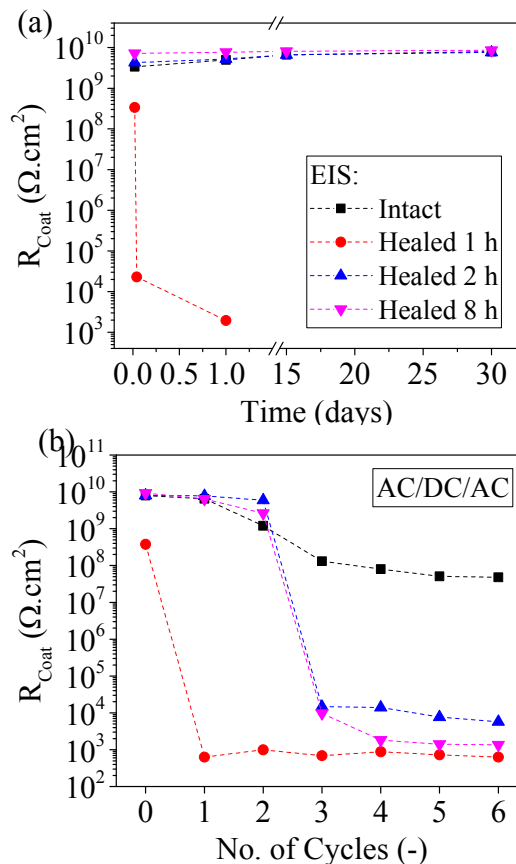

Figure 6.8. Evolution of coating resistance (R_{Coat}) in hybrid sol-gel coatings healed for one (●), two (▲), and eight (▼) hours and the intact coating (■) tested using EIS (a) and AC/DC/AC (b) procedures, respectively.

Furthermore, Figure 6.8 a shows that the intact and healed (for two and eight hours) hybrid sol-gel coatings exhibited identical resistances over the course of EIS measurement, manifesting their long-term 100% sealing efficiency. Yet, using the AC/DC/AC procedure as the electrochemical characterization technique, in addition to the reduced testing time compared to EIS, the resistance of the healed coatings deviated from that of intact one after two test cycles ($\Delta R_{Coat} > 1E3\ \Omega.cm^2$), unveiling different performance and failure modes of the intact hybrid sol-gel coatings.

The divergent resistances of the intact and healed hybrid sol-gel coatings tested using AC/DC/AC procedure, offers a fast estimation of the quality of the healed interface. The lower R_{Coat} of the healed (for two and eight hours) hybrid sol-gel coatings compared to the intact one after two AC/DC/AC cycles indicates the presence of an easy path for electrolyte ingress (possibly) due to failure of the healed interface. The easy penetration of the electrolyte to the metal-coating interface will eventually boost the electrochemical (corrosion) processes at the metal-coating interface, as a result of the enlarged active area. The variations in the substrate active area imposed by the local delamination processes can be monitored by following the evolution of the double layer capacitance (C_{dl}). The double-layer capacitance (C_{dl}) and the coating delaminated/active area can be correlated to using the following equation [10-14]:

$$A_d = \frac{C_{dl}}{C_{dl}^0}$$

Eq. 6.2

Where A_d and C^0_{dl} represents the coating delaminated area and the specific double layer capacitance of the substrate, respectively. Assuming that C^0_{dl} remains constant during exposure to the test electrolyte, the delaminated area [5, 10-14], which is in contact with the electrolyte is directly proportional to the C_{dl}.

The evolution of C_{dl} in the intact and healed hybrid sol-gel coatings evaluated using the AC/DC/AC procedure is presented in Figure 6.9. As Figure 6.9 shows, the C_{dl} of the intact coating increased gradually from 1.5 to 95 $nF.cm^{-2}$ with the number of the applied polarization cycles. The increase in C_{dl} corresponds to an enlarged delaminated area (A_d) which is consistent with the formation of the blisters in the coating, as presented in Figure 6.5. The coating healed for one hour exhibited the highest C_{dl} associated with the largest A_d, after application of the first polarization cycle, suggesting the failure of healed interface. Additional test cycles prompted the corrosion processes at the metal-coating interface as illustrated by gradual increase of C_{dl} and therefore the active delaminated area (A_d).

Unlike the coating healed for one hour, the C_{dl} value of the coatings healed for two and eight hours was in the same range of the intact coating for the first two test cycles, demonstrating efficient sealing of the scratch induced interface. Yet, upon application of the third polarization cycle, the C_{dl} and hence A_d of the healed (for two and eight hours) coatings deviated from that of the intact coating and grew exponentially with the further polarization cycles, disclosing the failure of the healed interface. Despite the slightly higher C_{dl} values of the coating healed for eight hours compared to the one healed for two hours, the equal number of test cycles (i.e. 2 cycles) further confirms an equivalent degree of the scratch healing achieved by annealing the coating for two and eight hours.
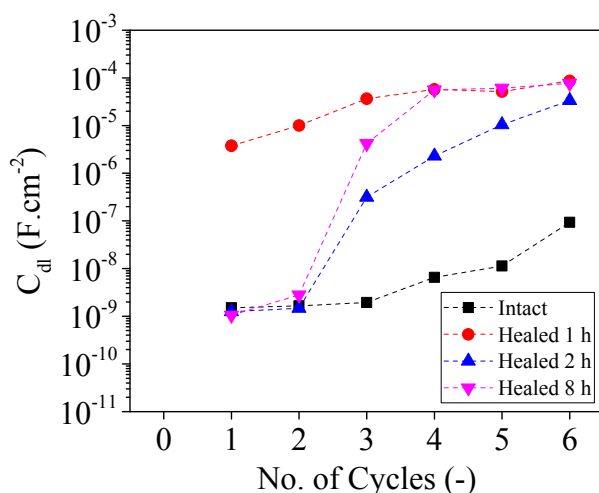

Figure 6.9. The evolution of the double layer capacitance (C_{dl}) in the intact and healed (for 1, 2 and 8 h) hybrid sol-gel coatings evaluated using six consecutive AC/DC/AC test cycles.

The equivalent performance of the hybrid sol-gel coatings healed for two and eight hours at 70 °C was further confirmed by monitoring the evolution of the coating OCP during the 3 h potential relaxation step of the AC/DC/AC tests (Figure 6.10). In analogy to the intact hybrid sol-gel coating, all healed coatings demonstrated a single potential relaxation process. However, the steady state OCP of the coatings varied as a function of healing time and the number of test cycles. A steady-state OCP of -1.0 V versus Ag/AgCl upon the first test cycle for the coating healed for an hour, indicated penetration of the electrolyte to the metal-coating interface followed by cathodic

reactions as a result of the failed scratch induced interface (Figure 6.10 a). In contrast, the coatings healed for two and eight hours exhibited a steady state OCP of -0.1 V for two consecutive test cycles suggesting absence of major defects facilitating ingress of the electrolyte through the coating. However, upon the third polarization, the OCP of the healed coatings dropped to -1.0 V, implying the occurrence of cathodic reactions on metallic substrate as a result of the failure of the healed interface.

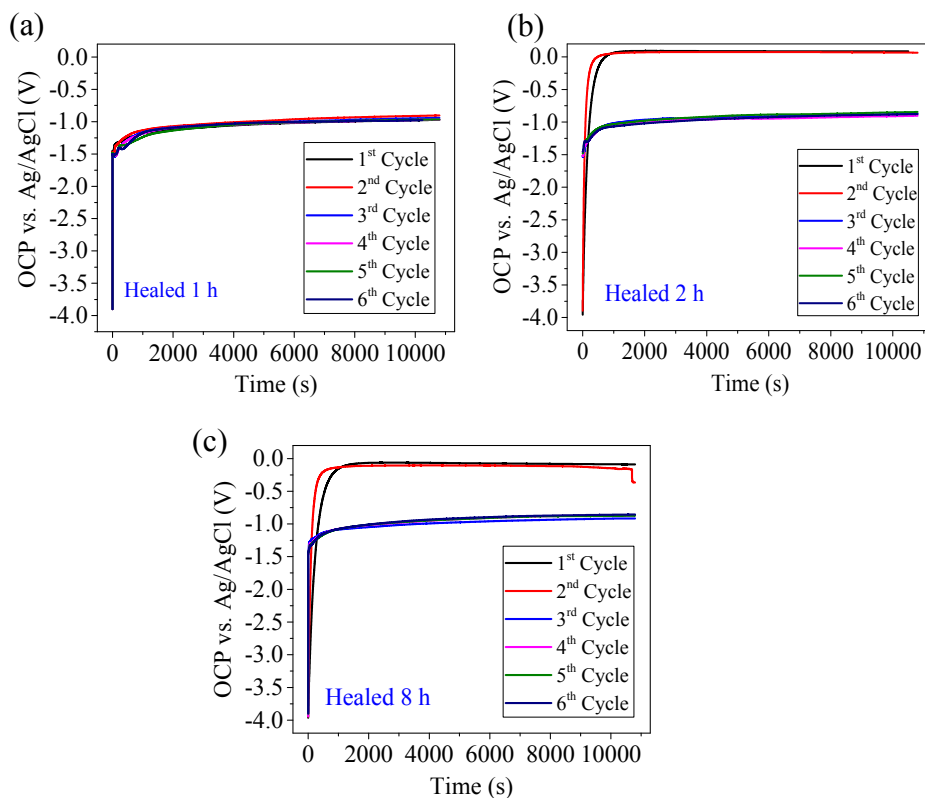Figure 6.10. The evolution of open circuit potential in hybrid sol-gel coatings healed for one (a), two (b) and eight (c) hours, respectively.

The OCP relaxation profiles suggest slightly improved performance of the coatings healed for two and eight hours compared the intact coating, as they showed limited ingress of the electrolyte, and hence the cathodic reactions, for two consecutive test cycles

while the intact coating could only withstand one test cycle. The higher resistance of the healed coatings against penetration of the electrolyte to the metal-coating interface might be attributed to lower defect density (e.g. micro-cracks, pinholes, local delaminations, etc) achieved by the stress-relaxation and healing processes promoted during the thermally-triggered healing of the hybrid sol-gel coatings.

To correlate the electrochemical performance of the hybrid sol-gel coatings to the quality of the healed interface, the surface topology and cross section of the healed coatings after EIS and AC/DC/AC testing were investigated using optical and scanning electron microscopy (Figure 6.11). Presence of a clear gap between the cut surfaces of the coating healed for an hour prior to the EIS measurement, further demonstrated its lost cohesive integrity due to insufficient healing of the scratch induced interface (Figure 6.11 a). Additionally, the optical and SEM micrographs of the coating healed for one hour showed that the AC/DC/AC procedure boosted the electrochemical processes on the metallic substrate resulting in formation of massive corrosion products (confirmed by EDS) along the scratch path beneath the coating layer (Figure 6.11 b).

The absence of the corrosion products (e.g. oxide layer) and the scar-free cross section of the coatings healed for two and eight hours revealed efficient sealing of the scratch induced interface due to fusion of the cut surfaces (Figures 6.11 c and e), in agreement with their long-term sealing efficiency when tested using EIS. However, as Figures 6.11 d and 6.11 f show, testing these coating systems using the AC/DC/AC procedure resulted in failure of the healed interface and formation of the corrosion products beneath the healed scratch. Evolution of ions, gaseous species and bulky corrosion products beneath the coating layer put additional pressure on the coating, facilitating coating failure at its weakest point i.e. the healed interface. The comparable extent corrosion processes (or corrosion products) at the metal-coating interface of the hybrid sol-gel coatings healed for two and eight hours further demonstrated the equivalent degree of the scratch healing in them compared to the one healed for one hour.
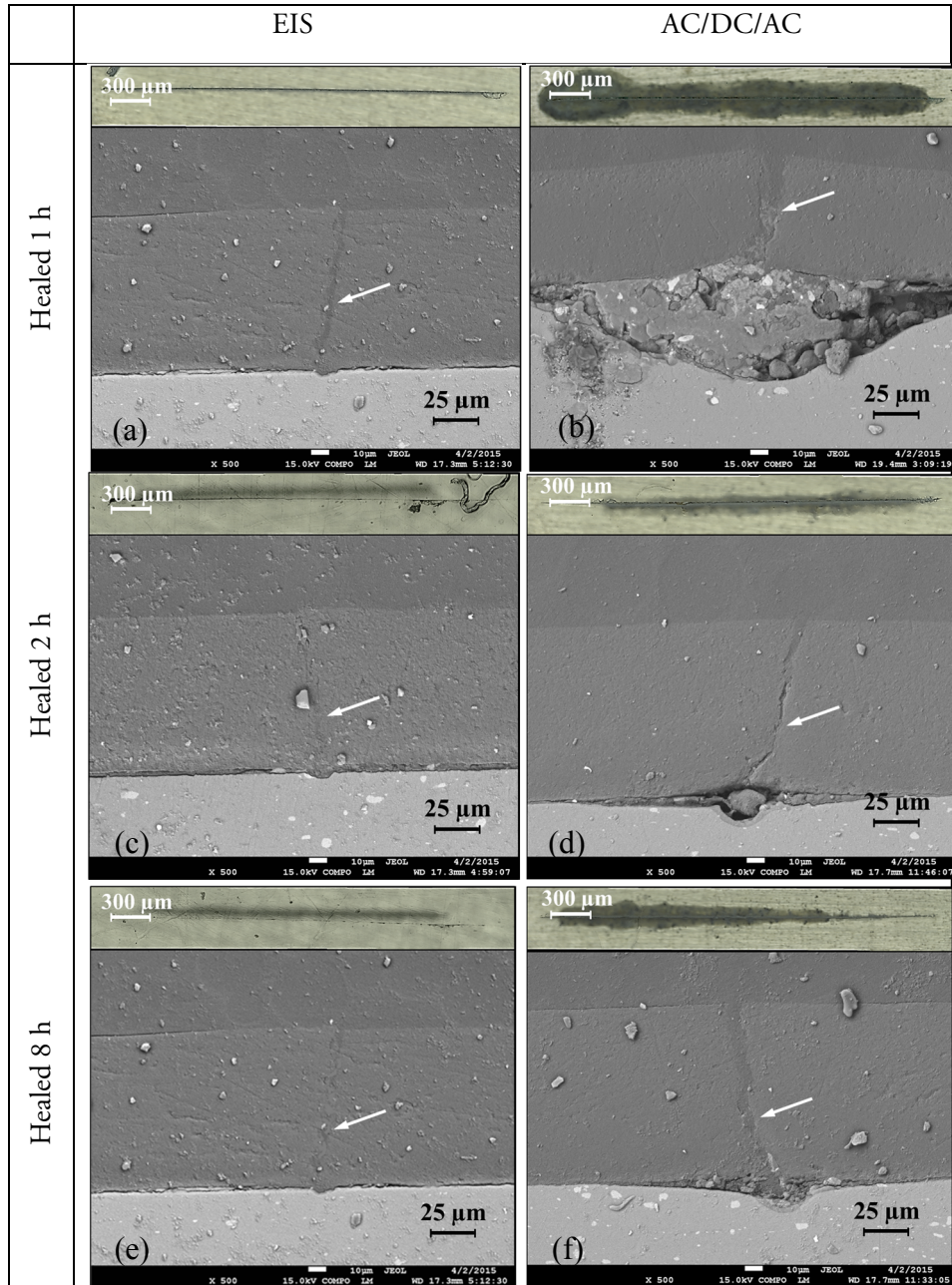
Figure 6.11. The optical micrographs (top) and cross-sectional SEM images of the hybrid sol-gel coatings healed for one (a) and (b), two (c) and (d), and eight hours (e) and (f) and tested using EIS and AC/DC/AC procedure, respectively.

Conclusions

In this chapter application of the AC/DC/AC procedure as a fast electrochemical technique for evaluation of the hybrid sol-gel coating's durability and the healing extent of scratch induced interface is described. Local delamination processes governed by pore opening and cathodic reactions facilitated rapid assessment of the coating durability and sealing efficiency in a short time span (24 h) compared to the conventional EIS measurements requiring more than one month. While healing the coating for one hour at 70 °C proved to be insufficient for full sealing of the scratch, healing it for two and eight hours led to an equivalent degree of protection as the unscratched coating. Complementing the electrochemical evaluation (i.e. the EIS and AC/DC/AC) of the healed hybrid Evaluation of damage formation in pristine and scratched-healed sol-gel coatings with optical and scanning electron microscopy disclosed the dependence of the failure mode on the electrochemical testing method. As a result of the non-destructive nature of the EIS procedure, the healed interface preserved its integrity upon the measurement. Yet, the applied electrochemical stress in the form of cathodic polarization promoted the evolution of ions, gaseous species and corrosion products on the metallic substrate during the AC/DC/AC procedure, facilitating coating failure at its weakest point i.e. the healed interface.

References:

[1] G.W. Walter, A critical review of the protection of metals by paints, Corrosion Science, 26 (1986) 27-38.

[2] M. Stratmann, R. Feser, A. Leng, Corrosion protection by organic films, Electrochimica Acta, 39 (1994) 1207-1214.

[3] G.W. Walter, A critical review of d.c. electrochemical tests for painted metals, Corrosion Science, 26 (1986) 39-47.

[4] F. Mansfeld, M.W. Kendig, S. Tsai, Evaluation of Corrosion Behavior of Coated Metals with AC Impedance Measurements, Corrosion, 38 (1982) 478-485.

[5] F. Mansfeld, Use of electrochemical impedance spectroscopy for the study of corrosion protection by polymer coatings, J Appl Electrochem, 25 (1995) 187-202.

[6] F. Mansfeld, M.W. Kendig, Electrochemical Impedance Spectroscopy of protective coatings, Materials and Corrosion, 36 (1985) 473-483.

[7] U. Rammelt, G. Reinhard, Application of electrochemical impedance spectroscopy (EIS) for characterizing the corrosion-protective performance of organic coatings on metals, Progress in Organic Coatings, 21 (1992) 205-226.

[8] J. Titz, G.H. Wagner, H. Spähn, M. Ebert, K. Jüttner, W.J. Lorenz, Characterization of Organic Coatings on Metal Substrates by Electrochemical Impedance Spectroscopy, Corrosion, 46 (1990) 221-229.

[9] P. Kern, A.L. Baner, J. Lange, Electrochemical impedance spectroscopy as a tool for investigating the quality and performance of coated food cans, Journal of Coatings Technology, 71 (1999) 67-74.

[10] A. Amirudin, D. Thieny, Application of electrochemical impedance spectroscopy to study the degradation of polymer-coated metals, Progress in Organic Coatings, 26 (1995) 1-28.

[11] P.L. Bonora, F. Deflorian, L. Fedrizzi, Electrochemical impedance spectroscopy as a tool for investigating underpaint corrosion, Electrochimica Acta, 41 (1996) 1073-1082.

[12] F. Deflorian, L. Fedrizzi, Adhesion characterization of protective organic coatings by electrochemical impedance spectroscopy, Journal of Adhesion Science and Technology, 13 (1999) 629-645.

[13] M. Kendig, J. Scully, Basic Aspects of Electrochemical Impedance Application for the Life Prediction of Organic Coatings on Metals, Corrosion, 46 (1990) 22-29.

[14] F. Mansfeld, C.H. Tsai, Determination of Coating Deterioration with EIS: I. Basic Relationships, Corrosion, 47 (1991) 958-963.

[15] J. Hollaender, Rapid assessment of food/package interactions by electrochemical impedance spectroscopy (EIS), Food Additives and Contaminants, 14 (1997) 617-626.

[16] J. Hollaender, R. Brandsch, Application of Impedance Methods for Corrosion Protecting Properties of Coated Substrates in Metal Packaging, International Meeting on Corrosion Science and Control Technologies IMCORRRio de Janeiro, Brazil, 1995.

[17] S.J. García, M.T. Rodríguez, R. Izquierdo, J. Suay, Evaluation of cure temperature effects in cataphoretic automotive primers by electrochemical techniques, Progress in Organic Coatings, 60 (2007) 303-311.

[18] S.J. García, J. Suay, Application of electrochemical techniques to study the effect on the anticorrosive properties of the addition of ytterbium and erbium triflates as catalysts on a powder epoxy network, Progress in Organic Coatings, 57 (2006) 273-281.

[19] S.J. García, J. Suay, Anticorrosive properties of an epoxy-Meldrum acid cured system catalyzed by erbium III trifluromethanesulfonate, Progress in Organic Coatings, 57 (2006) 319-331.

[20] S.J. García, J. Suay, A comparative study between the results of different electrochemical techniques (EIS and AC/DC/AC): Application to the optimisation of the cataphoretic and curing parameters of a primer for the automotive industry, Progress in Organic Coatings, 59 (2007) 251-258.

[21] S.J. García, J. Suay, Optimization of deposition voltage of cataphoretic automotive primers assessed by EIS and AC/DC/AC, Progress in Organic Coatings, 66 (2009) 306-313.

[22] M.T. Rodríguez, J.J. Gracenea, S.J. García, J.J. Saura, J.J. Suay, Testing the influence of the plasticizers addition on the anticorrosive properties of an epoxy primer by means of electrochemical techniques, Progress in Organic Coatings, 50 (2004) 123-131.

[23] K.N. Allahar, Q. Su, G.P. Bierwagen, L.D. Hyung, Monitoring Of The Ac-Dc-Ac Degradation Of Organic Coatings Using Embedded Electrodes, NACE International, 2007.

[24] Q. Su, K. Allahar, G. Bierwagen, Embedded electrode electrochemical noise monitoring of the corrosion beneath organic coatings induced by ac–dc–ac conditions, Electrochimica Acta, 53 (2008) 2825-2830.

[25] R.K. Bose, U. Lafont, J.M. Vega, S.J. Garcia, S. van der Zwaag, Methods to Monitor and Quantify (Self-) Healing in Polymers and Polymer Systems, Self-Healing Polymers, Wiley-VCH Verlag GmbH & Co. KGaA2013, pp. 335-359.

[26] Ö. Özkanat, Molecular interfaces of coated aluminium, S.n., S.l, 2013.

[27] S.J. Garcia, T.A. Markley, J.M.C. Mol, A.E. Hughes, Unravelling the corrosion inhibition mechanisms of bi-functional inhibitors by EIS and SEM–EDS, Corrosion Science, 69 (2013) 346-358.

Chapter 7

Extrinsic healing corrosion protective coatings containing cationic and anionic inhibitor doped containers

Introduction

Passive protective coatings are one of the most widespread approaches for corrosion protection of metallic substrates. Their protection mechanism is based on restricting the ingress of water and corrosive species to the metal-coating interface [1]. However upon damage, they fail to fulfil their protective function. Defining self-healing as restoration of any lost functionality, self-healing properties can be extrinsically introduced into corrosion protective coatings by incorporation of corrosion inhibitors into the coating formulation [2-6]. For years, chromate compounds have been the most effective inhibitors for different metallic substrates. Yet, due to environmental regulations their consumption in EU has been banned.

The quest for environmentally friendly alternatives to Cr(VI) compounds has revealed the beneficial aspects of rare earth metals (REM) such as cerium (Ce) in supressing corrosion of Al alloys [7, 8]. Nevertheless, so far no single-species replacement for chromates has been reported. The synergistic effects of inhibitor combinations can offer a promising route to outperform Cr(VI) species. Rare earth organophosphates such as Ce dibutyl phosphate and Ce diphenyl phosphate with corrosion inhibition performances comparable to those of Cr(VI) compounds, are a new class of multifunctional corrosion inhibitors showing synergistic corrosion protection for AA2024-T3 [9-12]. Selective deposition of Ce on S-phase intermetallics and formation of an organic film by the organic part of the inhibitor covering the entire surface is proposed as the most feasible mechanism for synergy of these compounds [12].

Despite the advances in the development of multifunctional inhibitors with synergistic properties, their direct implementation into coatings formulation might associate with inevitable drawbacks such as chemical interactions between inhibitor and matrix followed by coating degradation and loss of inhibitor activity [13]. Entrapment of corrosion inhibitors in inert host structures referred hereafter as micro- and nano-containers not only can isolate active agents from coating components but can also control the release of the inhibitors. Zeolite and clay particles have lately attracted considerable interest as host structures for corrosion inhibitors due to their high loading capacity and ion-exchange capability [14, 15].

Zeolites are microporous aluminosilicate crystals possessing negative surface charge. This negative charge is compensated by cations loosely bonded to their framework [16, 17]. Cationic active species such as Ce and La ions can be entrapped within the structural cages of zeolite particles via cation exchange process [18-20]. The release process of the entrapped inhibitors in such containers is stimulated by corrosion activities involving

pH changes and presence of the cationic species (M^{n+} and H^+). Selective leaching of the inhibitive ions to the damage site can reinforce the protective oxide layer, guaranteeing the long term protection for the metallic substrate. Combination of Ce^{3+} and La^{3+} loaded zeolites in the corrosion protective coatings led to an improved active protection as a result of synergy between the two employed inhibitors [21]. Successive loading of two different inhibitors (Ce^{3+} and diethyldithiocarbamate (DEDTC)) in a single zeolite carrier has also been reported with very promising results based on a two kinetic release concept [22]. The organic-inorganic hybrid coatings containing such carriers exhibited a noticeable improvement in active protection of AA2024 compared to the ones loaded with single inhibitors loaded zeolites.

Layered double hydroxides (LDHs) are a class of anion-exchangeable clay particles consisting of stacks of positively charged mixed-metal hydroxide layers. The positive charge of these frameworks is compensated by intercalation of anionic species between the hydroxide layers [23-25]. Inhibitor doped LDH particles can limit the release events to corrosion triggered phenomena such as pH changes or presence of anions released as a result of corrosion processes. Successful entrapment of anionic inhibitors in LDH has been reported in the literature [26-28]. Although the synergistic effect of anionic inhibitors doped separately in LDH nano-containers has been addressed in a few publications [28], the potential synergy between the cationic inhibitor doped containers and the anionic inhibitors doped ones has not been reported yet.

In the present chapter, preparation and characterization of extrinsic healing corrosion protective coatings containing combination of cationic and anionic inhibitor doped containers is described. To this aim NaY zeolite and Zn-Al LDH were doped with Ce^{3+} and 2-Mercaptobenzothiazole as cationic and anionic inhibitors, respectively. The morphology and composition of the micro-/ nano-containers were studied using a combination of characterization techniques confirming successful loading of the employed inhibitors. Monitoring the inhibitor release profiles of the micro-/nano-containers as a function of NaCl concentration and solution pH provided valuable information on the possible synergistic corrosion protection mechanism. Furthermore, sol-gel and water-based epoxy extrinsic healing coating containing individual inhibitor doped containers as well as their combination were prepared and evaluated using bulk and local electrochemical characterization techniques.

Experimental procedure

Materials

Unclad AA2024-T3 was received from AkzoNobel and used as metallic substrate. A water-based model epoxy-amine coating with fast drying at room temperature was kindly provided by Mankiewicz GmbH. Zirconium(IV) propoxide (70 wt.% in n-propanol, MW = 327.57 g mol^{-1}), 3-glycidoxypropyltrimethoxysilane (> 98%, MW = 236.34 g mol^{-1}) from hereon called TPOZ and GPTMS, respectively, and ethyl acetoacetate (> 99%, MW = 130.14 g mol^{-1}) were purchased from Sigma-Aldrich and used as received for preparation of sol-gel coatings. Cerium(III) nitrate hexahydrate (99%, MW = 434.22 g mol^{-1}), 2-Mercaptobenzothiazole (97%, MW = 167.25 g mol^{-1}) referred hereafter as MBT were purchased from Sigma-Aldrich and used without further purification as corrosion inhibitors. NaY zeolite (CBV 100, SiO_2/Al_2O_3 molar ratio: 5.1, Na_2O Weight %: 13.0) was purchased from Zeolyst International. MBT- loaded Zn-Al layered double hydroxides were kindly provided by CICECO Group from Aveiro University of technology.

Pigment preparation

NaY zeolite

The single inhibitor doped Y zeolite was prepared via exchange of the available Na cations in the Y zeolite cages with Ce^{3+}. The ion exchange process was carried out in a $CeNO_3$ solution containing over 300% excess of Ce^{3+} cations with respect to cation exchange capacity (CEC) of NaY zeolite ensuring maximum exchange of Na caions with Ce^{3+} inhibitors [22]. The exchange process was conducted by addition of NaY zeolite into a 0.3 M $CeNO_3$ solution with volume/particle ratio of 20 ml.g^{-1} at 60 °C. The Ce^{3+} doped NaY zeolites referred hereafter as NaY-Ce, were washed and filtered followed by drying at 60 °C for 24 h, yielding NaY zeolite with 12 ± 0.5 wt.% of Ce^{3+} cations.

Zn-Al LDH

The preparation of the inhibitor loaded Zn-Al LHDs consists of two main steps: (i) the synthesis of LDH precursors and (ii) the ion-exchange reaction with substitution of the inorganic anions by inhibiting MBT anions. The synthesis was carried out under argon atmosphere and all the solutions were prepared using boiled distilled water to avoid contamination with carbonate anions. The Zn:Al ratio of 2:1 was chosen for the synthesis to obtain stable layered compounds. In the first step, a 0.5 M Zn $(NO_3)_2$ ×

$6H_2O$ and 0.25 M $Al(NO_3)_3 \times 9H_2O$ solution (V) 50 mL) was slowly added to 1.5 M $NaNO_3$ (V) 100 mL, pH 10) under vigorous stirring at room temperature. During this reaction, the pH was kept constant (pH 10 ± 0.5) by simultaneous addition of 2 M NaOH. Afterward, the obtained slurry was subjected to thermal treatment at 65 ℃ for 24 h for crystallization of the LDHs, and consequently centrifuged and washed 4 times with boiled distilled water. A small fraction of LDHs was dried at 50 ℃ for XRD and TEM analysis. The remnant was used in the anion-exchange reaction for replacement of nitrate by MBT [27, 28].

The anion-exchange reaction was carried out by dispersing the precursor LDH in an aqueous solution containing the organic anions in double excess. Sodium salts of MBT was previously prepared by neutralization of the aqueous solutions of MBT with an equivalent amount of NaOH. Subsequently, the white gel-like LDH precursors were dispersed in a solution of 0.1 M NaMBT (pH ≈ 10) under an argon atmosphere. The total amount of this solution (120 mL) was split into two portions of 60 mL. The LDH precursors were added to one of these portions followed by centrifugation. This procedure was repeated with the second portion of the organic anion solution. Finally, the organic anion loaded LDH powders were washed four times with boiled distilled water, frozen, and then dried by lyophilization at -78 ℃ [27, 28].

Pigment characterization

Morphology
Scanning electron microscopy (SEM): Particle morphology of the employed micro- and nano-containers were characterized using a high resolution JOEL SEM (JSM-7500F) operating at 5 kV. Additionally, the composition of the inhibitor doped and un-doped containers were studied by energy-dispersive X-ray spectroscopy (EDS) using JSM-7500F operating at 15 kV.

Dynamic light scattering (DLS): The particle size distribution of the micro- and nano-containers and their zeta potentials were measured using a Malvern Zetasizer 4 instrument.

X-ray diffraction (XRD): The structure of the inhibitor doped and un-doped LDH nano-containers were studied by XRD. The measurements were performed using Philips X'Pert difractometer with Cu K_α radiation source.

Fourier transform infrared spectroscopy (FTIR): The FTIR spectra of the samples were recorded using a Bruker IF55 spectrometer, in the spectral region 600-1700 cm^{-1} at a resolution of 4 cm^{-1}.

Release kinetics

The release profiles of inorganic (Ce^{3+}) and organic (MBT) inhibitors from NaY and LDH containers were monitored by UV-Vis spectroscopy using a PerkinElmer Lambda 35 medium performance spectrophotometer in the spectral region of 220-400 nm. Unlike Ce^{3+}, the absorption spectra of MBT show two pH-sensitive peaks within the studied spectral range [29]. Therefore, MBT calibration curves were obtained at two different pH values; the natural pH of the solution and at pH = 10. The calibration was performed at the defined values using absorption peaks of λ = 318 nm and λ = 252 nm for MBT and Ce^{3+}, respectively [29, 30].

To study the release kinetics, the inhibitor doped containers were dispersed in an aqueous solution with volume/particle ratio of 400 ml g^{-1} under constant stirring. The effect of potential release triggering parameters were studied by systematic variation of NaCl concentration and pH values (NaCl concentrations = 0, 0.05 and 0.5 M, pH values = 2, 4, natural pH and 10). The suspensions were continuously stirred at 200 rpm. At definite time intervals, 2 ml samples were taken and filtered for analysis.

Coating preparation

Prior to coating application, AA2024-T3 panels of 3×4 cm^2 were ground mechanically using SiC paper (grade 1000) to remove the native oxide layer and further degreased with ethanol. The panels were then immersed in 2 M NaOH solution for 10 seconds and rinsed with double distilled water to increase the surface density of the hydroxyl groups (OH$^-$) on the AA2024-T3 substrates [31]. The cleaned and dried AA2024-T3 panels were coated with two different types of coating; i) a hybrid SiO$_2$-ZrO$_2$ sol-gel coating and ii) a water-based epoxy coating

Sol-gel coatings: The hybrid sols were prepared by mixing two different sols obtained via controlled hydrolysis of TPOZ and GPTMS in n-propanol. The silane based sol was prepared by drop-wise addition of 0.33 molar equivalent of acidified DI water with pH of 0.5 (r$_W$=H$_2$O/Si-OR) into a GPTMS solution containing 1 molar equivalent of n-propanol (r$_{Ethanol}$ = C$_2$H$_5$OH/Si-OR). The pre-hydrolysis was carried out by stirring the mixture at 300 rpm for 1 h at RT.

The zirconia based sol was prepared by mixing TPOZ (70 wt.% in n-propanol) and ethyl acetoacetate in volume ratio of 1:1 at RT for 20 minutes. The pre-hydrolysis was carried out by addition of 2.62 molar equivalent of acidified DI water with pH of 0.5 ($r_W=H_2O/Zr-OR$) into the mixture and stirring the solution for 1 h at RT [32].

The pre-hydrolysed sols were mixed using a magnetic stirrer for 1 h   followed by 1 h aging after which the hybrid sol-gel solution was ready to be applied on the AA2024-T3 panels. 10 wt.% of inhibitor-free and inhibitor-doped micro-/nano-containers were introduced into hybrid sol-gel solution at the mixing step of TPOZ and GPTMS sols. The cleaned AA2024 plates were immersed in the final hybrid sol-gel solution for 100 s and then were withdrawn at the speed of 18 cm min^{-1}. The coated samples were dried at RT for 30 minutes followed by a two-step curing procedure at 60 and 120 ˚C for 80 minutes yielding samples with average thickness of 4 ± 2 μm.

Epoxy coatings: The coating formulation consists of a water-based epoxy emulsion and a solvent free amine hardener. Prior to the addition of the hardener to the formulation, the resin was loaded with 10 wt% pigment (i.e. micro- and nano-containers) and mechanically stirred at 1000 rpm for 5 minutes to ensure full dispersion of the pigments in the resin. The hardener was then added to the mixture in a resin:hardener weight ratio of 0.7:1 and stirred manually. The resulting mixture was then cast on the cleaned AA2024-T3 panels using a bar coater with a nominal thickness of 50 μm. The coated samples were dried and cured at room temperature for 72 hour yielding coatings with an average dry thickness of 30 ± 5 μm.

To evaluate the contribution of inhibitor doped micro- and nano-containers on the protective properties of the coatings, eight types of formulations were prepared. The composition of the prepared coatings is summarized in table 7.1.

Coating characterization

Electrochemical properties

Electrochemical impedance spectroscopy (EIS): Electrochemical properties of the prepared coating systems were investigated using electrochemical impedance spectroscopy (EIS). The EIS measurements were carried out at room temperature in a conventional three-electrode cell consisting of a saturated calomel reference electrode (SCE), a Pt counter electrode and the sample as working electrode in the horizontal position (exposed area of ca. 3.37 cm^2). A Faraday cage was employed to avoid the interference of external electromagnetic fields. Stagnant 0.05 M NaCl aqueous solution

Table 7.1. Composition of the prepared extrinsic healing coatings.

Sample code	Matrix	Micro-/Nano-container	inhibitor
SG-NaY	SiO$_2$-ZrO$_2$ Sol-Gel	NaY	-
SG-NaY-Ce		NaY	Ce
SG-LDH-MBT		LDH	MBT
SG-NaY-Ce_LDH-MBT		NaY + LDH	Ce + MBT
Ep-NaY	Water-Based Epoxy	NaY	-
Ep-NaY-Ce		NaY	Ce
Ep-LDH-MBT		LDH	MBT
Ep-NaY-Ce_LDH-MBT		NaY + LDH	Ce + MBT

in equilibrium with air was employed as testing electrolyte. The measurements were performed using a Gamry FAS2 Femtostat in the frequency range of 10^{-2}-10^5 Hz, with a 10 mV of sinusoidal perturbation, acquiring 7 data points per frequency decade. All the spectra were recorded at open circuit potential. The impedance plots were fitted using different equivalent circuits with the Echem Analyst^{TM}.

In addition to the coating systems, bare AA2024-T3 panels were tested using EIS in a range of electrolytes containing CeNO$_3$ and MBT in different molar ratios. The electrolytes were prepared using 0.05 M NaCl as background solution. The Ce:MBT molar ratio was systematically varied in the following manner: 99:1, 90:10, 75:25, 50:50 and 25:75.

Scanning vibrating electrode technique (SVET): The cathodic and anodic activities over two circular artificial damages with an average diameter of 150 ± 20 μm in the prepared coating systems were monitored using SVET. The measurements were performed using an Applicable Electronics Inc. (Figure 7.1) equipment controlled with the ASET software from ScienceWares (USA) in a cell containing 5 ml of 0.05 M NaCl solution. The SVET maps were obtained by vibrating a microelectrode with a 20-30 μm spherical platinum black tip at amplitude of 20 μm, at an average distance of 100 μm above the sample surface. The scans consisted of 60 × 60 points over an exposed surface area of 4 × 4 mm^2.
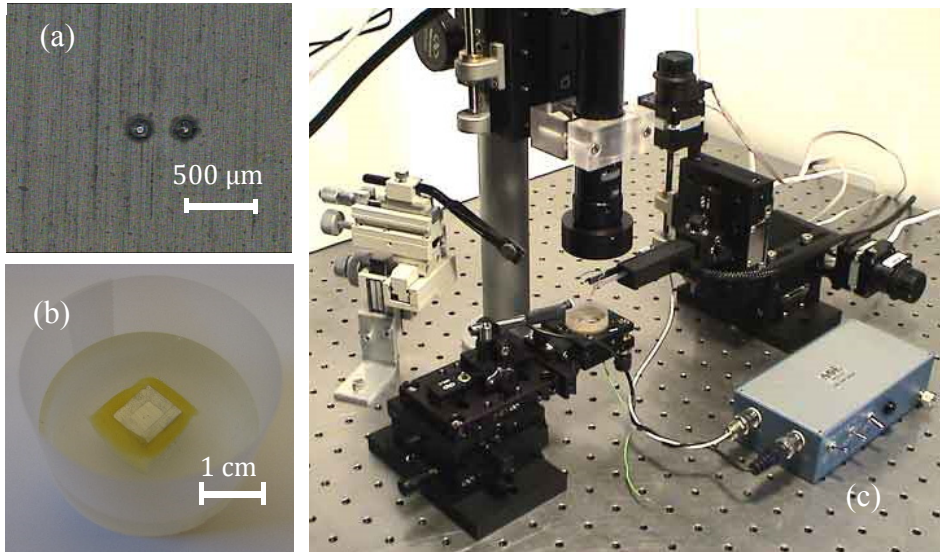
Figure 7.1. Sample surface with two artificial defects (a) the cell (b) and the SVET set-up (c).

Results & Discussion

Ce and MBT compatibility

The synergistic corrosion inhibition of metallic substrates by combination of corrosion inhibitors can only be achieved if the employed inhibitors are compatible. To check the compatibility of the employed inorganic and organic inhibitors, ground and cleaned AA2024-T3 panels were tested using EIS in a range of 0.05 M NaCl solutions containing no inhibitor, 1 mM $CeNO_3$, 1 mM MBT and 0.5 mM $CeNO_3$ + 0.5 mM MBT. The EIS spectra of the AA2024-T3 panels after 1 h exposure to the test electrolytes and evolution of their Bode modulus (|Z|) at frequency of 0.1 Hz are presented in Figure 7.2. As shown in Figure 7.2 a, the sample exposed to the inhibitor free electrolyte exhibited two time constants in the mid and low frequency ranges corresponding to the aluminum oxide layer and the corrosion processes, respectively [12]. Addition of the corrosion inhibitors to the test solution resulted in disappearance of the second time

constant and a significant increase in the |Z| values in both mid and low frequencies, confirming the effective corrosion inhibition provided by the employed inhibitors (Figure 7.2 a). The sample exposed to the combination of the two inhibitors exhibited the highest |Z| value at low frequencies suggesting lower localized corrosion attack and improved corrosion protection due to the compatibility and the potential synergy between Ce^{3+} and MBT.
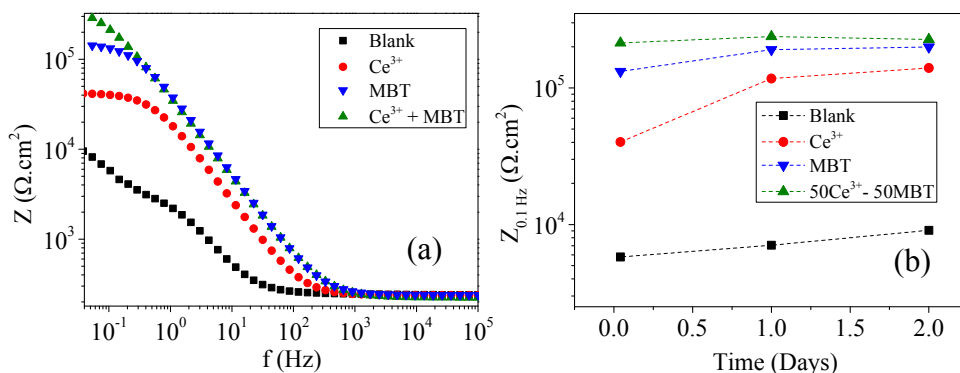

Figure 7.2. The EIS spectra (a) and evolution of Bode modulus (|Z|) at 0.1 Hz for AA2024-T3 panels exposed to inhibitor free (■), 1 mM Ce^{3+} (●), 1 mM MBT (▼) and 0.5 mM Ce^{3+} + 0.5 mM MBT (▲) containing 0.05 M NaCl (b).

To get an insight into the performance and possible inhibition mechanism of the combined inhibitors, the EIS spectra of the AA2024-T3 panels in different test electrolytes were monitored for 2 days. The evolution of the low frequency Bode modulus ($|Z|_{0.1}$) of the tested samples over 2 days of exposure are presented in Figure 7.2 b. The inhibitor free sample showed the lowest $|Z|_{0.1}$ associated with the highest corrosion rate during the course of the measurement. Addition of Ce^{3+} led to a gradual and yet a significant increase in the $|Z|_{0.1}$ of the AA2024-T3 panel. The progressive build-up in $|Z|_{0.1}$ in presence of Ce^{3+} can be explained by the protection mechanism of this REM inorganic inhibitor. The Ce^{3+} cation is believed to suppress corrosion of AA2024-T3 by gradual formation of an insoluble hydroxide or oxide layer on cathodic sites (e.g. S-phase intermetallics) of AA2024-T3 [7, 33, 34]. In contrast to Ce^{3+}, MBT provided a quick protection due to different inhibition mechanism i.e. adsorption on the surface

140

especially on the copper rich domains [35, 36]. The combined inhibitor system yielded a fast and yet slightly higher protection than pure MBT and Ce^{3+}. The higher $|Z|_{0.1}$ values might be attributed to the oxygen scavenging potential of the following reaction:

$$2Ce^{4+} + 2HS - C_7H_3NS \xrightarrow{O_2} 2Ce^{3+} + SNH_3C_7 - S - S - C_7H_3NS \qquad \text{Eq. 7.1}$$
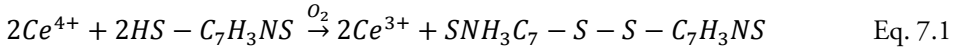
Corrosion of AA2024-T3 in chloride containing aerobic solutions yields a range of pH values favored by different Ce species such as Ce^{3+} and Ce^{4+} [7]. Oxidation of free thiol groups by Ce^{4+} is a well-known reaction used for rapid and sensitive determination of thiol in biological systems [37] yielding Ce^{3+} species. Consumption of oxygen in Eq. 7.1 alongside with the regeneration of Ce^{3+} cations can limit the cathodic reactions (OH^- evolution) and ultimately aluminum dissolution. Hence, Eq. 7.1 might offer an explanation for the improved performance of the combined inhibitor system compared to the pure inhibitors.

The tested samples were further studied using SEM/EDS to unravel their potential morphological and compositional differences. As Figures 7.3 a and b show a continuous cerium oxide layer (confirmed by EDS) covered the sample exposed to pure Ce^{3+} solution. The AA2024-T3 panel exposed to pure MBT solution showed several sulfur-rich strands on sample's surface (Figure 7.3 c and d). The sample exposed to the combined inhibitor system illustrated a combination of the two pure systems, i.e. a continuous cerium oxide layer with sulfur-rich strands on top. Yet, an additional feature was visible on this set of samples. Ceria particles (confirmed by EDS) were found in close vicinity of the sulfur-rich strands/rods (Figures 7.3 e and f), further reinforcing the feasibility of Eq. 7.1

Optimization of Ce^{3+} to MBT ratio

The effect of inorganic (Ce^{3+}) and organic (MBT) inhibitors concentration on the active protection of the AA2024-T3 panels was investigated by systematic variation of Ce^{3+}:MBT molar ratio (99:1, 90:10, 75:25, 50:50, 25:75) in 0.05 M NaCl solution. The evolution of the low frequency Bode modulus ($|Z|_{0.1}$) of AA2024-T3 panels in solutions with different Ce^{3+}:MBT molar ratios is presented in Figure 7.4. As Figure 7.4 shows at the early stages of the measurement (i.e. 1 h), the samples exposed to 50:50 and 75:25
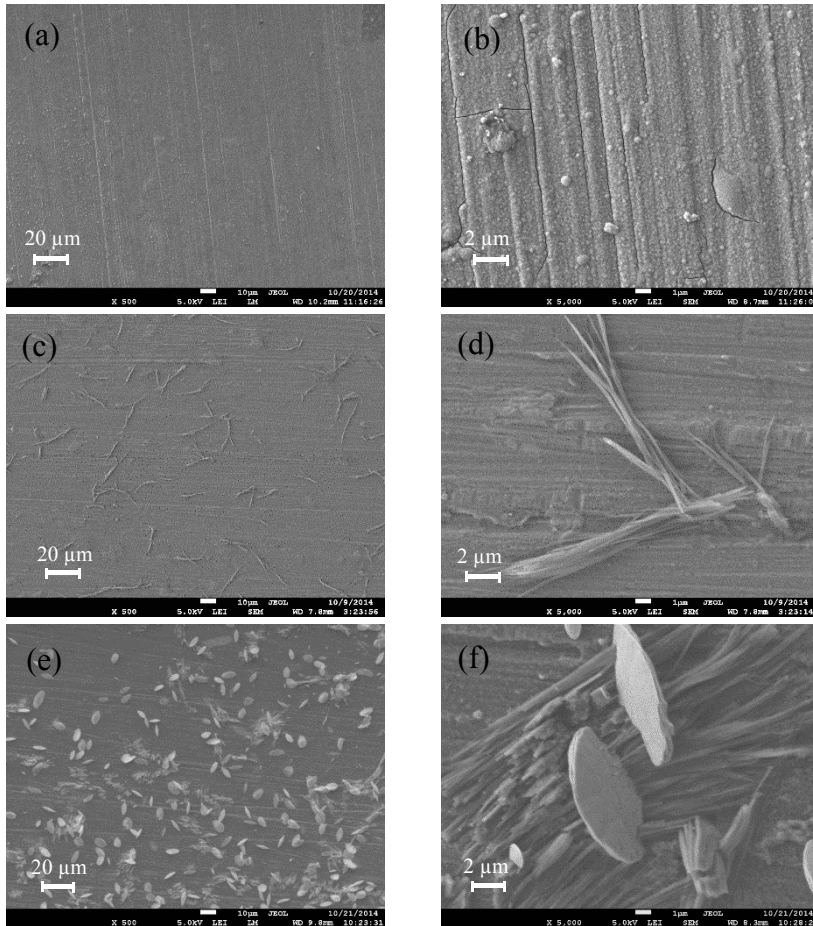
Figure 7.3. SEM micrographs of AA2024-T3 exposed for 14 days to 1 mM CeNO$_3$ at 500x (a) and 5kx (b), to 1 mM MBT at 500x (c) and 5kx (d) and to 0.5 mM CeNO$_3$ + 0.5 mM MBT at 500x (e) and 5kx (f).

molar ratios of Ce^{3+}:MBT exhibited the highest $|Z|_{0.1}$ values, (2.1E5 and 1.6E5 $\Omega.cm^2$, respectively). The $|Z|_{0.1}$ of all the other tested ratios were equivalent to that of pure MBT (1.3E5 $\Omega.cm^2$). Upon longer exposure, the Ce^{3+}:MBT molar ratio dependence of the $|Z|_{0.1}$ values diminished, so that after 1 day all the tested samples exhibited $|Z|_{0.1}$ in the same range (2.2E5 $\Omega.cm^2$). After 14 days of exposure, the samples showed a slight decrease in $|Z|_{0.1}$ approaching that of pure Ce^{3+} (1.3E5 $\Omega.cm^2$).

The results presented in Figure 7.4 show that despite the equivalent performance of the different Ce^{3+}:MBT molar ratios upon long exposure times (i.e. > 1 day), the fast and efficient active protection of AA2024-T3 can only be achieved within a narrow Ce^{3+}:MBT molar ratio range (50:50 and 75:25) with 50:50 being the optimum tested ratio.
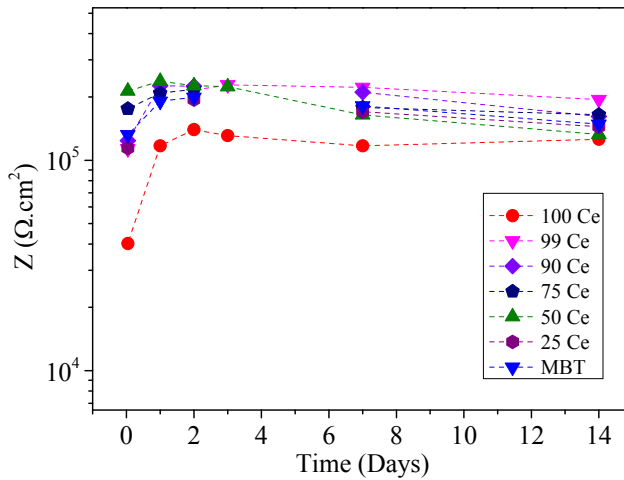

Figure 7.4. Evolution of the low frequency bode modulus ($Z_{0.1\ Hz}$) of AA2024-T3 panels in 0.05 M NaCl solution containing different Ce^{3+}:MBT molar ratios.

Evaluation of carriers

The solution based EIS measurements showed that combining Ce^{3+} and MBT as inorganic and organic inhibitors not only does not deteriorate inhibition efficiency of the single inhibitors but also can lead to improved active protection of AA2024-T3 panels as a result of potential synergy between the two inhibitors. Therefore, a combination of Ce^{3+} and MBT can be incorporated into passive coating formulations to implement healing properties in them. Such coatings referred hereafter as extrinsic healing corrosion protective coatings are capable of restoring their lost protective functionality upon damage. Yet, direct addition of Ce^{3+} and MBT into coating formulation can result in coating instability and inhibitor deactivation [13]. Entrapment

of Ce^{3+} and MBT in ion-exchange host structures such as zeolite and LDH can isolate the active agents from coating components. Furthermore, it can limit the inhibitor release events to the corrosion triggered process such as pH variations, yielding stimuli-responsive extrinsic healing coatings.

NaY Zeolite

The morphology and composition of the un-doped and Ce-doped NaY zeolites were studied using SEM/EDS (Figure 7.5). The SEM micrographs of NaY and NaY-Ce particles exhibit well-defined crystals with an average diameter of < 1µm. The EDS profile of NaY micro-containers (Figure 7.5 a) shows a distinct peak at 1.04 keV associated with the exchangeable Na cations in Y zeolite cages [38]. Substitution of Na with Ce cations in NaY-Ce led to compositional changes confirmed by a substantial decrease in the Na content (from 9.6 ± 0.2 wt.% to 3.1 ± 0.1 wt.%) and appearance of the characteristic peaks of Ce at 4.84, 5.27, 5.60 and 6 keV [38]. Presence of Na characteristic peak in NaY-Ce EDS spectrum indicates incomplete exchange process. The incomplete exchange of Na by Ce cations in NaY-Ce can be attributed to the size limitation of sodalite cages to fit in the hydrated Ce cations. The elemental analysis of NaY-Ce particles by EDS demonstrated successful loading of 12 ± 0.5 wt.% of Ce in Y zeolite. The obtained values are in agreement with ICP-OES analysis of remnant doping solutions yielding 11.2 ± 0.5 wt.% of Ce in NaY zeolites [38].

The effect of Ce doping on size distribution of NaY zeolite containers was further investigated by DLS (Figure 7.5 b). The size distribution of NaY zeolites is strongly affected by their zeta potential. High zeta potential values (either positive or negative) can stabilize particle dispersion by prevention of agglomerate formation as a result of electrostatic repulsion. NaY zeolite particles possess a negative surface charge due to isomorphous substation of alumina by silica resulting in zeta potential values of -47.5 mV. Exchanging monovalent Na cations by trivalent Ce cations shifted the zeta potential of NaY-Ce particles towards more positive values (-37.9 mV). Yet, the obtained values were still negative enough to prevent agglomeration of NaY-Ce particles. The size distribution of NaY and NaY-Ce particles exhibited single peaks centred at 520 ± 50 and 560 ± 50 nm, which are in agreement with the size of particles observed by SEM.
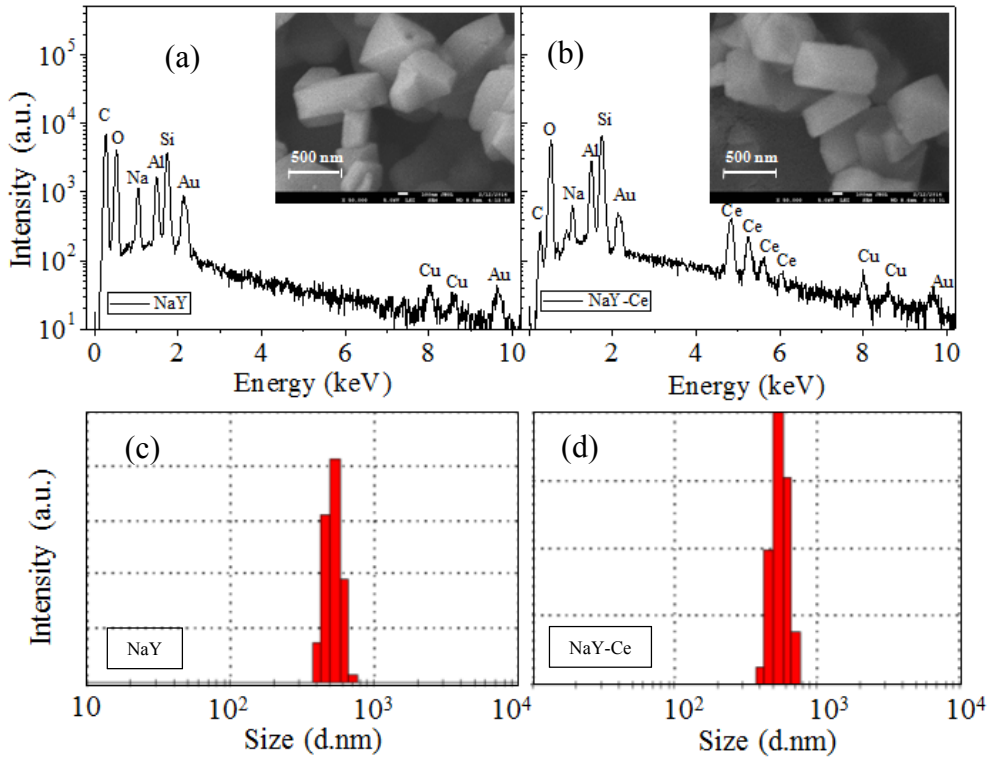
Figure 7.5. EDS spectra and SEM micrographs (picture inset) of NaY (a) and NaY-C and size distribution of NaY (c) and NaY-Ce particles (d).

LDH

The structures of the inhibitor doped and un-doped LDH nano-containers were characterized using XRD (Figure 7.6 a). The XRD pattern of the precursor LDH nano-particles (intercalated with NO_3^- anions) showed well-defined peaks at 2θ = 9.86, 19.92, and 30.00°corresponding to reflection by planes (003), (006), and (009), respectively. Calculation of gallery height based on the thickness of the cationic sheets (0.477 nm) and the basal spacing d (0.9 nm), yielded a value of 0.42 nm. The calculated gallery height is in good agreement with NO_3^- anion size (0.38 nm). The slight difference in the obtained value and NO_3^- anion diameter can be justified by vertical alignment of NO_3^-

planar groups with respect to the host layer. Replacement of NO_3^- by MBT anions via anion exchange process led to structural changes revealed by a shift in the position of peaks toward lower 2Θ angles and a significant decrease in their intensity. The new peak position associate with the basal spacing values of 1.72 nm which is consistent with the relatively bigger size of the intercalating anions i.e. MBT [27].

Intercalation of MBT in LDH precursors was further evaluated by FTIR spectroscopy. The FTIR spectra of the LDH nano-containers and pure MBT in the spectral range of 1700-600 cm^{-1} are presented in Figure 6.3 b. The LDH precursors (containing NO_3^- anions) are generally characterized by a strong absorption band at υ = 1350 cm^{-1} and a few broad peaks below υ = 1000 cm^{-1} corresponding to nitrate and metal-hydroxide stretching modes, respectively. FTIR spectrum of MBT shows several characteristic bands at the studied range; e.g. υ = 669 and 701 cm^{-1} associated with C-S stretching, υ = 745 cm^{-1} assigned to N-H wagging, υ = 1076 cm^{-1} corresponding to C-S stretching in S-C-S and υ = 1248, 1285 and 1329 cm^{-1} associated with C-N stretching modes. Therefore, presence of characteristic absorption bands of C-N (υ_{C-N} = 1248 cm^{-1}) and C-S (υ_{C-S} = 1076 cm^{-1}) stretching as well as N-H wagging (υ_{N-H} = 745 cm^{-1}) [39] in the FTIR spectrum of LDH-MBT nano-particles confirms successful loading/doping of MBT in LDH nano-containers.

The morphology the un-doped and MBT-doped Zn-Al LDHs was also evaluated using SEM. The SEM micrographs of the un-doped (Figure 7.6 c) and MBT-doped LDHs (Figure 7.6 d) show that the prepared LDHs exhibited a plate-like morphology which is retained upon anion-exchange as reported in the literature [28].

Release kinetics

The employed NaY and LDH nano-containers are cation- and anion-exchange compounds, respectively. Therefore, the doped inhibitors i.e. Ce^{3+} and MBT will only be released in presence of cationic and anionic species. Considering chloride concentration and pH changes as relevant corrosion triggering parameters, their effect on the release kinetics of the inhibitors from nano-containers was monitored by spectrophotometry. To this aim the relevant calibration curves were obtained using five standard solutions of known concentrations yielding molar absorptivity constants (ε) of 1.29, 0.047 and 0.054 M^{-1}.cm^{-1} for Ce, MBT at neutral pH and MBT at pH = 10, respectively. The correlation coefficient of the calibration curves in all the cases was higher than 0.999. The obtained ε values were employed to calculate the released inhibitor concentration using Beer-Lambert's law [40].

$$A = \varepsilon \, l \, c \qquad\qquad\qquad\qquad\qquad \text{Eq. 7.2}$$

Where ε, l and c stand for molar absorptivity constant, pass length through the sample and concentration, respectively.
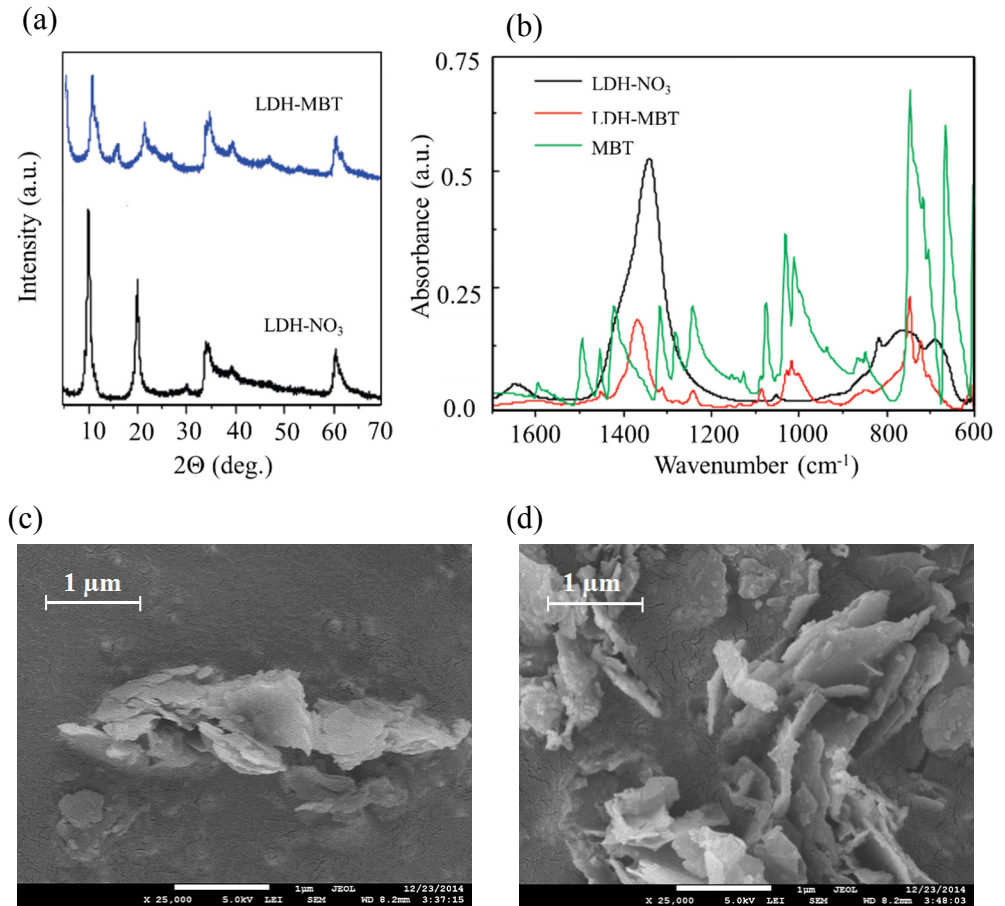

Figure 7.6. XRD patterns of LDH nano-containers intercalated with NO_3 and MBT anions (a), FT-IR spectra of MBT and LDH nano-containers intercalated with NO_3 and MBT (b) and SEM micrographs of un-doped (c) and MBT-doped Zn-Al LDHs at 25 kx.
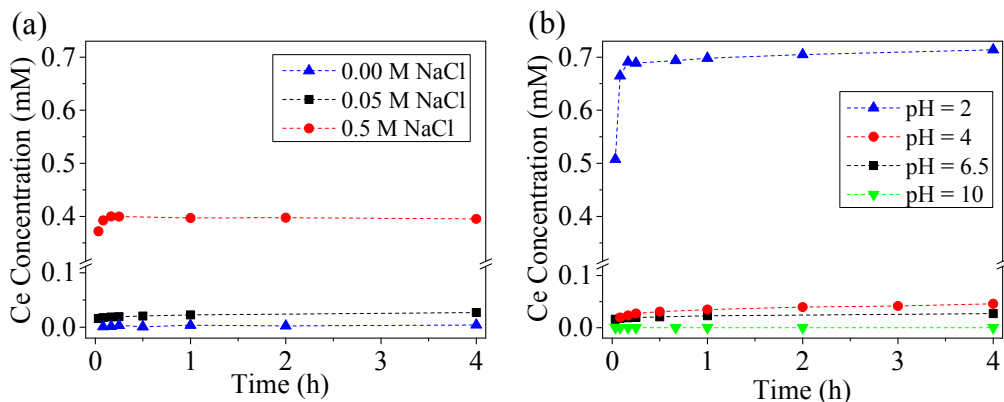
Figure 7.7. Ce^{3+} release profiles at neutral pH in different NaCl concentrations (a) and in 0.05 M NaCl at different pH values (b).

The evolution of Ce^{3+} concentration in solutions with different NaCl concentrations (0, 0.05 and 0.5 M NaCl) and various pH values (2, 4, 6.5 and 10) is presented in Figure 7.7. The release profiles of Ce^{3+} from NaY-Ce micro-containers exhibited similar patterns, yet the amount of the leached inhibitor varied as a function of solution concentration and pH. As Figure 7.7 shows, in the early stages of the exposure the release process took place rapidly increasing the concentration of Ce^{3+} within 30 minutes in the solution. Upon reaching the chemical ion-exchange equilibrium [28], no significant changes in Ce^{3+} concentration was observed. While no release of Ce^{3+} to cation free DI water was detected, increasing NaCl concentration from 0.05 M to 0.5 M boosted the release process (from 0.03 mM Ce in 0.05 M NaCl to 0.4 mM Ce in 0.5 M NaCl) confirming cation-exchange triggered release of the doped inhibitor from the micro-containers (Figure 7.7 a). The release profiles obtained at different pH values exhibited the same features i.e. fast release followed by stabilization of Ce^{3+} concentration upon longer exposure times. However, the extent of release was strongly influenced by solution pH (Figure 7.7 b). At pH = 10 no Ce^{3+} was detected in the solution during the test period. A gradual decrease in pH initiated the release process so that at pH's of 6.5 and 4, the Ce^{3+} plateau concentration was found to be 0.027 and 0.046 mM, respectively. A further decrease in pH down to 2 intensified the release process yielding Ce^{3+} plateau concentration of 0.71 mM. The higher content of H$^+$ cations associated with lower pH values not only stabilizes Ce^{3+} species in the solution [41] but also provides the potential cations for cation-exchange process and release of the doped Ce^{3+} inhibitors.
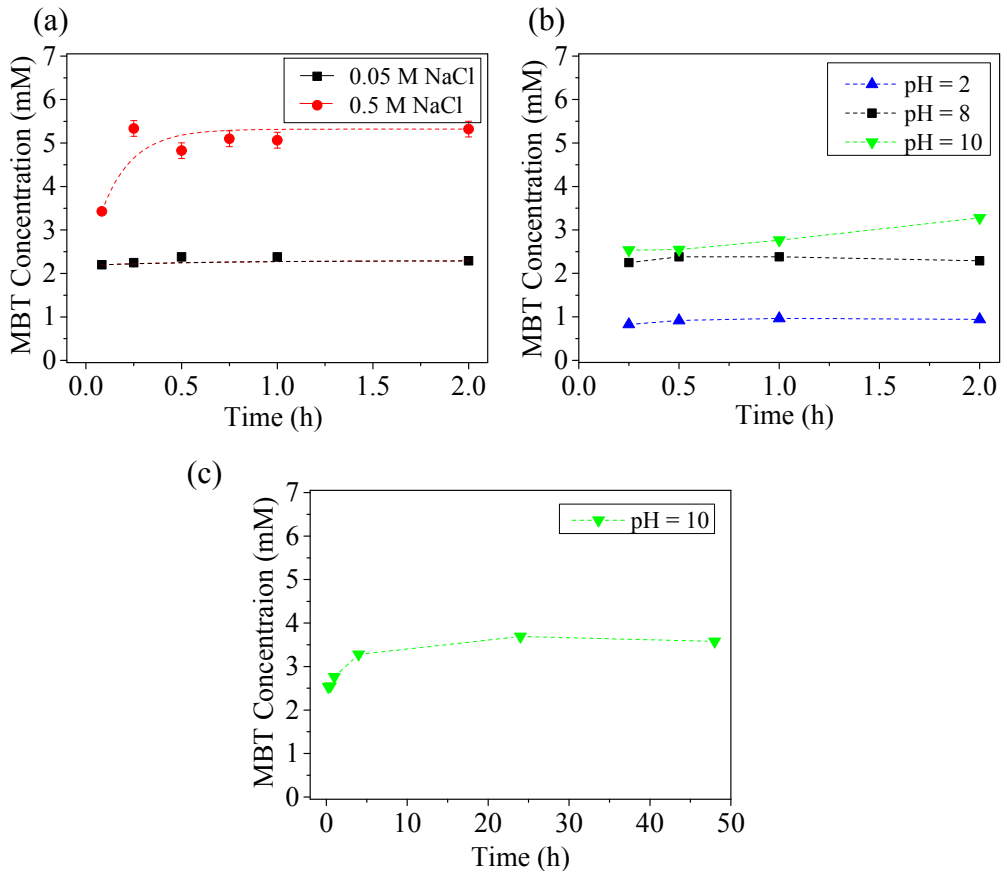
Figure 7.8. MBT release profiles at neutral pH in different NaCl concentrations (a) and in 0.05 M NaCl at different pH values (b).

In analogy to Ce^{3+} release from NaY-Ce micro-containers, the content of the organic inhibitor (MBT) leached out of LDH nano-containers was strongly influenced by NaCl concentration and solution pH (Figure 7.8). An increase in the content of the anions present in the solution either in the form of chloride or hydroxide boosted MBT release from LDH nano-containers. A tenfold increase in the chloride anions concentration shifted the MBT plateau concentration from 2.4 mM to 5 mM (Figure 7.8 a). Similarly, an increase in solution pH from 2 to 10 moved the plateau concentration from 0.96 mM to 3.6 mM (Figure 7.8 b). In all the tested solutions apart from the solution at pH = 10, the plateau concentration was achieved within few minutes, as a result of chemical

ion-exchange equilibrium. In the alkaline NaCl solution with pH = 10, the MBT concentration plateau was only achieved after 24 h (Figure 7.8 c). This observation might be explained by a shift in the aforementioned equilibrium point by high concentration of the hydroxide anions, prolonging the release phenomenon. Upon longer exposure times, MBT concentration in all the tested solutions showed a decrease due to degradation of MBT, forming sub-products such as benzothiazole and 2-hydroxybenzothiazole or dimers i.e. 2-mercaptobenzothiazole disulfide [42].

Extrinsic healing corrosion protective coatings

To evaluate the performance of the combined Ce^{3+} and MBT doped containers in inorganic and organic coating systems, a range of SiO_2-ZrO_2 hybrid sol-gel and water-based epoxy coatings containing 10 wt% NaY, 10 wt% NaY-Ce, 10 wt% LDH-MBT and 5 wt% NaY-Ce + 5 wt% LDH-MBT were prepared. The active protection offered by the doped inhibitors was evaluated by creation of two circular defects with an average diameter of 150 μm reaching the metallic substrate. The EIS spectra and the evolution of high ($|Z|_{10^4}$) and low frequency Bode modulus ($|Z|_{0.1}$) of the tested coating systems are presented in Figure 7.9. At the early stages of the measurement, the EIS spectra of the hybrid SiO_2-ZrO_2 coatings exhibited two time constants in the tested frequency range (Figure 7.9 a) corresponding to the coating and oxide layer responses [12]. Upon prolonged exposure to the electrolyte, a third time constant ascribed to corrosion processes occurring at the metal surface appeared in the EIS spectra of the coating systems. The evolution the high frequency Bode modulus of the hybrid sol-gel coatings (Figure 7.9 b) revealed that apart from a drastic drop of $|Z|_{10^4}$ of the LDH-MBT loaded coating in the beginning of the measurement, all the inhibitor doped sol-gel coatings exhibited $|Z|_{10^4}$ values in the same range, suggesting an equivalent coating response. The $|Z|_{10^4}$ of the sol-gel coating loaded with inhibitor free NaY containers was slightly lower than those of inhibitor containing ones. The poor barrier properties of this coating system can be attributed to the hydrolysis of the inhibitor free zeolite particles in the sol, resulting in a significant increase in the solution pH followed by changes in the coating properties [19].

The low frequency Bode modulus ($|Z|_{0.1}$) of the hybrid sol-gel coatings corresponding to the oxide layer response showed a different trend than that of $|Z|_{10^4}$ (Figure 7.9 c). The coating loaded with the inhibitor free NaY particles showed the lowest $|Z|_{0.1}$ values. Doping NaY containers with Ce^{3+} led to a significant increase in $|Z|_{0.1}$ of the hybrid sol-
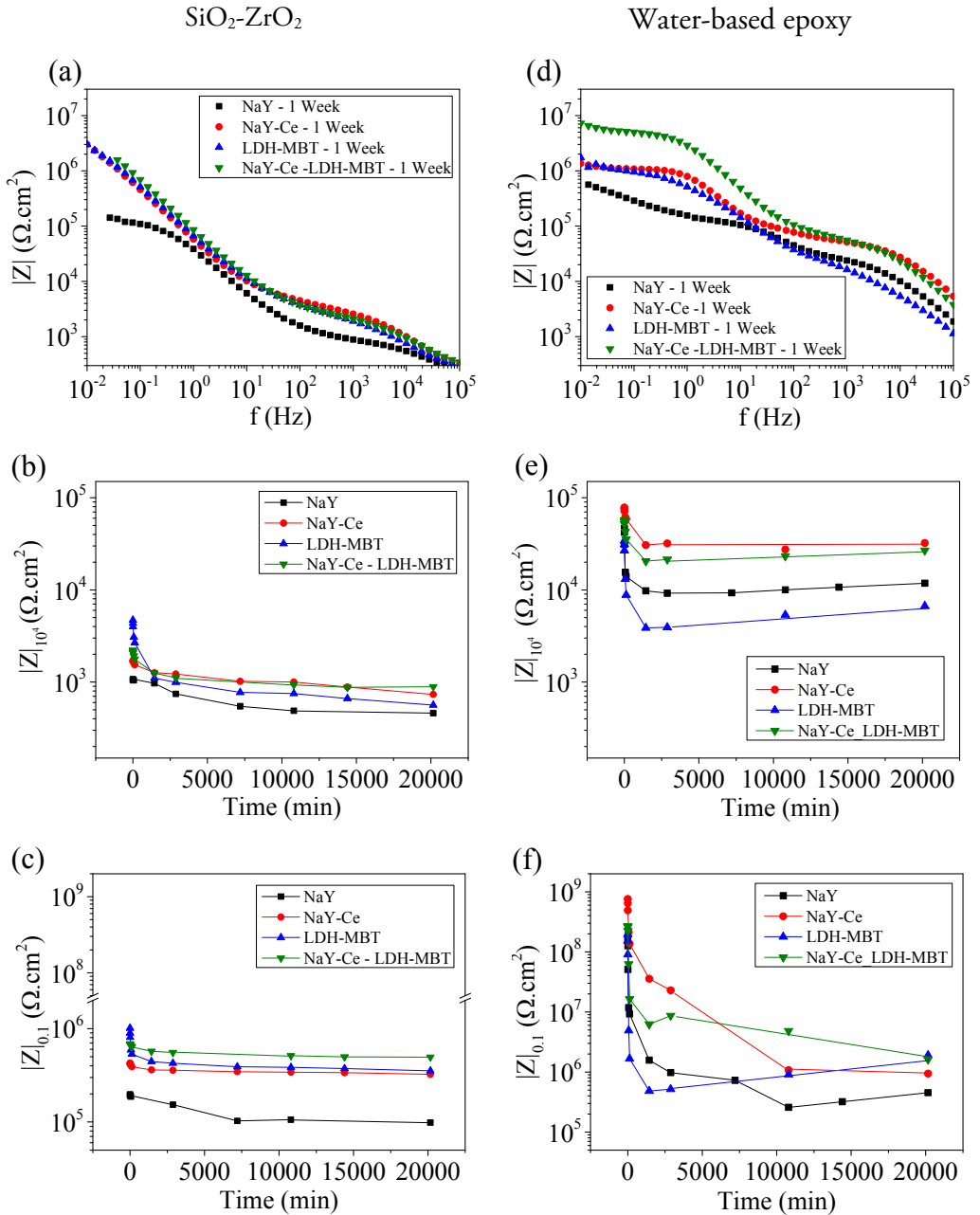
Figure 7.9. The EIS spectra of hybrid SiO_2-ZrO_2 (a) and water-based epoxy coatings (d) after 1 week exposure to 0.05 M NaCl and evolution of Bode modulus (Z) at 0.1 and 10^4 Hz for SiO_2-ZrO_2 (b) and (c) and water-based epoxy coatings (e) and (f), respectively.

gel coatings, suggesting formation of a stable oxide layer with higher resistance. While $|Z|_{0.1}$ of the LDH-MBT loaded sol-gel coatings was in the same range as that of NaY-Ce loaded one, the coatings containing the combination of NaY-Ce and LDH- MBT exhibited the highest $|Z|_{0.1}$ indicating the potential synergism between the inorganic (Ce^{3+}) and organic (MBT) inhibitors in the hybrid sol-gel coatings.

In contrast to the hybrid sol-gel coatings, the EIS spectra of the water-based epoxy coatings showed three well-defined time constants after 1 hour exposure to the electrolyte (Figure 7.9 d). The coating response manifested by the high frequency Bode modulus ($|Z|_{10}{}^4$) showed a different trend compared to the hybrid sol-gel coatings. While the$|Z|_{10}{}^4$ of the NaY-Ce and NaY-Ce + LDH-MBT loaded epoxy coatings were in the same range, loading the coating with pure LDH-MBT significantly lowered the $|Z|_{10}{}^4$ values (Figure 7.9 e). This low coating resistance can be justified by poor LDH-MBT dispersion which interrupted coating integrity due to nano-containers agglomeration.

As a result of poor barrier of the LDH-MBT loaded epoxy coating, in the early stages of the measurement the low frequency Bode modulus ($|Z|_{0.1}$) of this coating was also lower than that of NaY loaded one (Figure 7.9 f). Yet, over time as a result of inhibitor leach-out, the LDH-MBT loaded coating exhibited higher $|Z|_{0.1}$ values than the inhibitor free epoxy coating. The NaY-Ce loaded coating showed the highest $|Z|_{0.1}$ values in the early stages of the measurement, yet it underwent a drastic drop of $|Z|_{0.1}$ upon longer exposure. The $|Z|_{0.1}$ values of the coating containing the combination of the inhibitor doped containers reached a plateau after 1 day, surpassing the $|Z|_{0.1}$ values of the NaY-Ce containing coating after 1 week of exposure to the electrolyte. The obtained results suggest an improved corrosion protection when combination of the two carriers doped with different inhibitors are employed.

To quantify the level of inhibition and corrosion protection offered by the inhibitor doped containers the EIS spectra of the tested coating systems were fitted using equivalent circuits presented in Figure 7.10 a. In the depicted equivalent circuits, R_{sol}, R_{coat}, R_{oxide} and R_{ct} correspond to solution, coating, oxide and charge transfer resistances, respectively. CPE_{coat}, CPE_{oxide} and CPE_{dl} represent coating, oxide and double layer constant phase element, respectively. Figure 7.10 shows that the calculated coating (R_{coat}) and oxide (R_{oxide}) resistances of the tested coatings systems follow the same trend as high and low frequency Bode modulus values (i.e. $|Z|_{10}{}^4$ and $|Z|_{0.1}$) shown in Figure 7.9. As Figures 7.10 b and 7.10 d show, the coating resistance of both hybrid sol-gel and water-based epoxy coatings exhibited an initial decrease followed by stabilization of R_{coat}. Therefore, the evolution of R_{oxide} can provide a qualitative estimation of the inhibition

efficiency of the employed inhibitor loaded containers. The highest R_{oxide} values of the combined inhibitor doped containers (NaY-Ce + LDH-MBT) in the hybrid sol-gel coatings over the course of measurement (Figure 7.10 c) and after 1 week of exposure for the water-based epoxy coatings (Figure 7.10 e) hints the potential synergy between the two inhibitors in the tested coating systems.
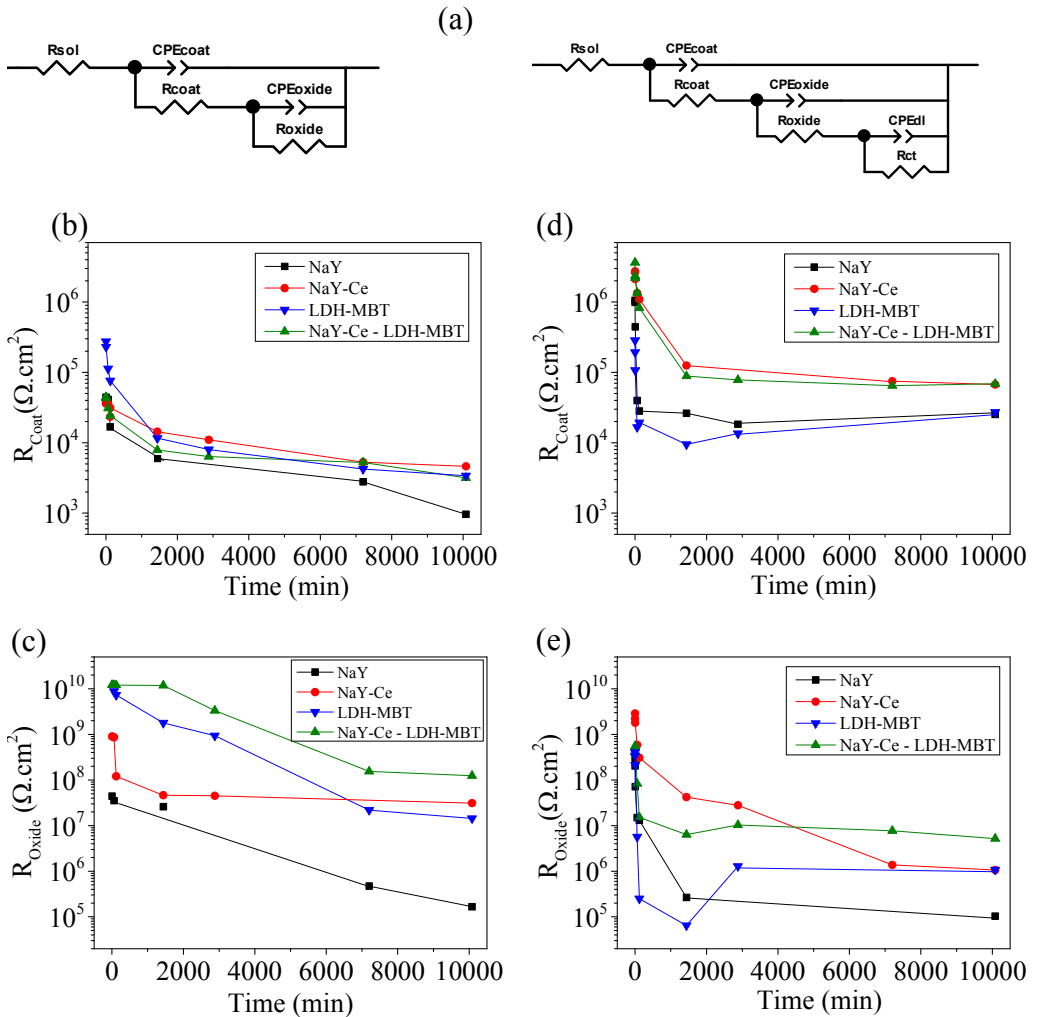

Figure 7.10. Equivalent circuits used to fit the experimental EIS data (a) coating (R_{coat}) and oxide (R_{oxide}) resistances for hybrid sol-gel (b) and (c) and water based epoxy coatings (d) and (e), respectively.

Additionally, the equivalent circuits provide information on the charge transfer resistance (R_{ct}) of the coating systems which can directly be correlated to the active protection provided by corrosion inhibitors using the following equation [43]:

$$IE = \frac{CR_0 - CR_{inh}}{CR_0} \qquad \text{Eq. 7.3}$$

Where IE, CR_0 and CR_{inh} represent inhibition efficiency and corrosion rate of the inhibitor free and the inhibitor containing coatings, respectively. The CR of the inhibitor free and inhibitor containing coatings were calculated using the inverse of the charge transfer resistance (R_{ct}) of the corresponding coating systems. The R_{ct} of the coating systems after 1, 7, 10 and 14 days of exposure to the electrolyte, the fitting goodness (χ^2) and the calculated IEs are summarized in Table 7.2. The fitting goodness for all the coating systems was $\chi^2 < 1 \times 10^{-2}$.

In the hybrid sol-gel coatings the corrosion activity manifested by the third time constant in the EIS spectra was only detected after few days of immersion, therefore the fitting results and the IEs of these coatings are only presented for 7, 10 and 14 days of exposure. As shown in Table 7.2, addition of the single inhibitor doped containers to the hybrid sol-gel coating formulation led to a significant increase in the R_{ct} of the corresponding coating compared to the inhibitor free one, yielding IEs higher than 0.98 and 0.96 for SG-NaY-Ce and SG-LDH-MBT, respectively. Yet, the coating containing the combined inhibitor doped containers exhibited the highest R_{ct} values. The R_{ct} values of the SG-NaY-Ce_LDH-MBT were at least one order of magnitude higher than those of single container loaded ones, with IEs higher than 0.99 demonstrating the improvement in the active protection of the substrate. To ascertain the synergistic corrosion protection offered by combination of the inhibitor doped containers, the synergy parameter (S) was calculated using the following equation [43, 44]:

$$S = \frac{1 - IE_{1+2}}{1 - IE_{12}} \qquad \text{Eq. 7.4}$$

where IE_{12} is the calculated IE for the coating loaded with two inhibitor doped containers and $IE_{1+2}=(IE_1+IE_2) - (IE_1 \times IE_2)$. The values S > 1 indicate the synergistic behaviour of employed inhibitor combination. Therefore S values of 1.47, 1.43 and 1.62 for the SG-NaY-Ce_LDH-MBT coatings after 7, 10 and 14 days of exposure to the electrolyte confirms the synergy between the employed inhibitors.

Table 7.2. Charge transfer resistance (R_{ct}), fitting goodness (χ^2), inhibition efficiency (IE) and synergy parameter (S) for hybrid sol-gel and water-based epoxy coatings after 1, 7, 10 and 14 days exposure to 0.05 M NaCl.

Time	Coating	χ^2	R_{ct} (kΩ.cm^2)	IE (-)	S (-)
7 Days	SG-NaY	9×10^{-2}	588.3	-	
	SG-NaY-Ce	5.64×10^{-3}	48980	0.987	
	SG-LDH-MBT	5.85×10^{-3}	19620	0.970	
	SG-NaY-Ce_LDH-MBT	6.83×10^{-2}	2405×10^{3}	0.999	1.47
10 Days	SG-NaY	1.5×10^{-2}	584.6	-	
	SG-NaY-Ce	5.91×10^{-3}	39070	0.985	
	SG-LDH-MBT	5.63×10^{-3}	19350	0.969	
	SG-NaY-Ce_LDH-MBT	6.83×10^{-4}	1850×10^{3}	0.999	1.43
14 Days	SG-NaY	9×10^{-2}	580.9	-	
	SG-NaY-Ce	5.79×10^{-3}	35760	0.983	
	SG-LDH-MBT	5.06×10^{-3}	15210	0.961	
	SG-NaY-Ce_LDH-MBT	7.3×10^{-2}	1517×10^{3}	0.999	1.62
1 Day	Ep-NaY	2.32×10^{-4}	3516	-	
	Ep-NaY-Ce	1.04×10^{-3}	64410	0.95	
	Ep-LDH-MBT	4.19×10^{-4}	6870	0.49	
	Ep-NaY-Ce_LDH-MBT	6.83×10^{-4}	16560	0.79	0.13
7 Days	Ep-NaY	2.32×10^{-4}	1067	-	
	Ep-NaY-Ce	1.04×10^{-3}	1150	0.07	
	Ep-LDH-MBT	5.17×10^{-4}	2413	0.56	
	Ep-NaY-Ce_LDH-MBT	6.83×10^{-4}	5553	0.81	2.14
10 Days	Ep-NaY	3.40×10^{-4}	1434	-	
	Ep-NaY-Ce	7.25×10^{-3}	1170	-0.22	
	Ep-LDH-MBT	5.17×10^{-4}	3680	0.61	
	Ep-NaY-Ce_LDH-MBT	3.63×10^{-3}	2073	0.31	0.69
14 Days	Ep-NaY	3.40×10^{-4}	176.9	-	
	Ep-NaY-Ce	7.25×10^{-3}	1010	0.82	
	Ep-LDH-MBT	5.17×10^{-4}	6415	0.97	
	Ep-NaY-Ce_LDH-MBT	3.63×10^{-3}	1205	0.85	0.03

The observed synergy between the two inhibitor doped containers not only can be attributed to the oxygen scavenging potential of reaction 7.1, but also can be ascribed to stimuli-triggered release of the inhibitors from the containers. The results presented in the release kinetics section revealed that while release of Ce^{3+} from NaY-Ce was boosted in acidic pHs, release of MBT from LDH-MBT was amplified at basic/alkaline pHs. Therefore by using the combination of the inhibitor doped containers the release events can be expanded to a wide pH range (from very acidic to very basic) promoted by corrosion of AA2024-T3 in the chloride containing aerobic solutions. The released inhibitors can subsequently deactivate cathodic and anodic sites restricting Al dissolution.

In contrary to the hybrid sol-gel coatings, the synergistic behaviour of the two inhibitor doped containers in the water-based epoxy coatings was only observed after 1 week of exposure to the electrolyte (S = 2.14). At the early stages of the measurement, the R_{ct} and therefore the IE of the NaY-Ce loaded coating was higher than the rest of the coating systems. Over time, the coating containing the combination of the inhibitor doped container outperformed the NaY-Ce containing one. The NaY-Ce loaded coating exhibited negative IE (-0.22) after 10 days of exposure, possibly due to depletion of accessible NaY-Ce containers from Ce^{3+} inhibitors.

To get a deeper insight into the synergism kinetics between the two inhibitor doped containers in the water based epoxy coatings, local electrochemical activities over the artificial defects of the coatings was monitored using SVET. The optical micrographs and SVET maps of the extrinsic healing corrosion protective epoxy coatings after 1 and 7 days of exposure to 0.05 M NaCl are presented in Figure 7.11. As Figure 7.11 shows, the coatings containing NaY-Ce (Figure 7.11 a) and LDH-MBT (Figure 7.11 b) exhibited corrosion activity manifested by anodic and cathodic currents (red and blue regions, respectively) in the SVET maps and formation of corrosion products over the defects upon 1 day exposure to the electrolyte. The coating loaded with the combination of the inhibitor doped containers showed no electrochemical activity (Figure 7.11 e) after 1 day of exposure to the electrolyte, possibly due to passivation of the defects by the combined inhibitors.

Prolonged exposure of the coating systems to the electrolyte resulted in sever corrosion of the substrates coated by both NaY-Ce and LDH-MBT loaded ones. The fast evolution of the corrosion processes in these coating systems was demonstrated by well-defined anodic and cathodic regions as well as formation of blisters followed by coating delamination (Figures 7.11 b and d). Although, the coating containing the combined

inhibitor doped containers exhibited anodic and cathodic activities after 7 days exposure to the electrolyte (Figure 7.11 f), the shiny surface of the defects suggested lower corrosion activity compared to the single inhibitor doped coatings.
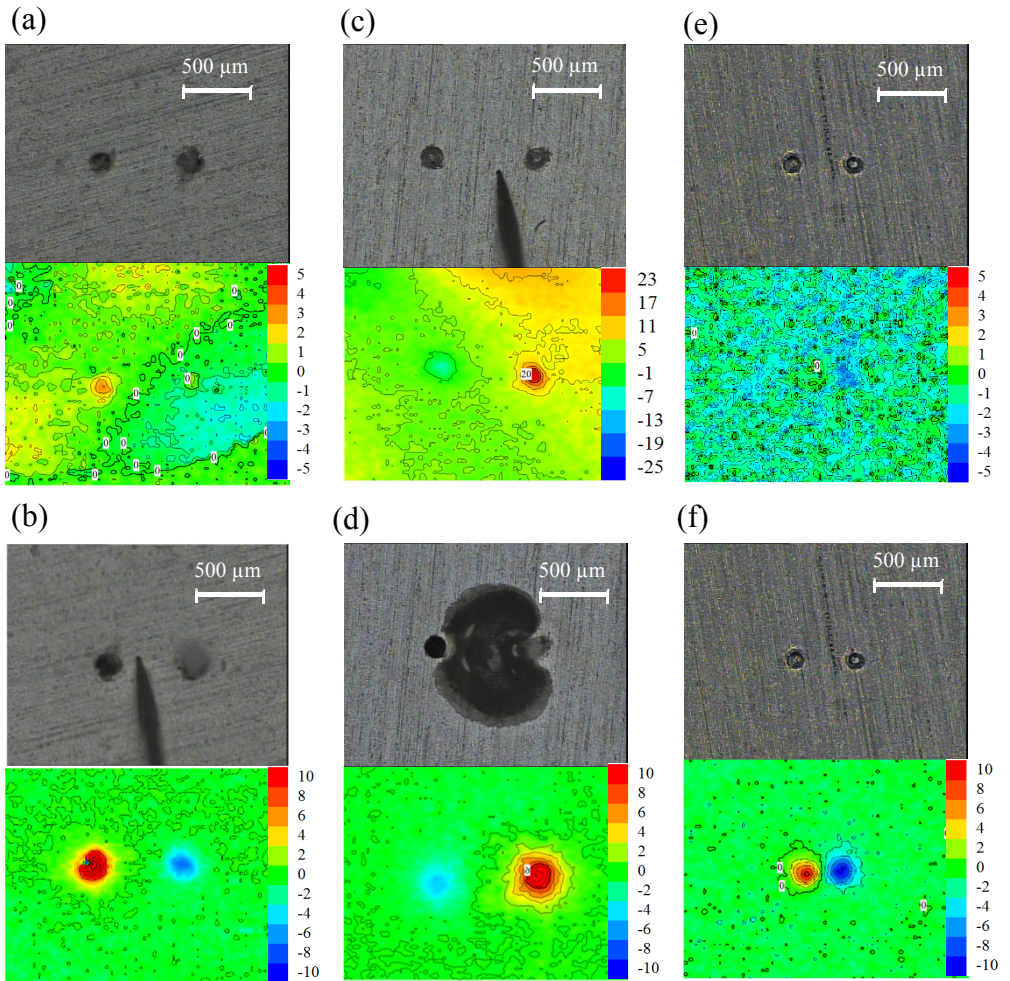

Figure 7.11. Optical micrographs and SVET maps of Ep-NaY-Ce (a) and (b), Ep-LDH-MBT (c) and (d) and Ep-NaY-Ce_LDH-MBT (e) and (f) after 1 and 7 days exposure to 0.05 M NaCl, respectively.
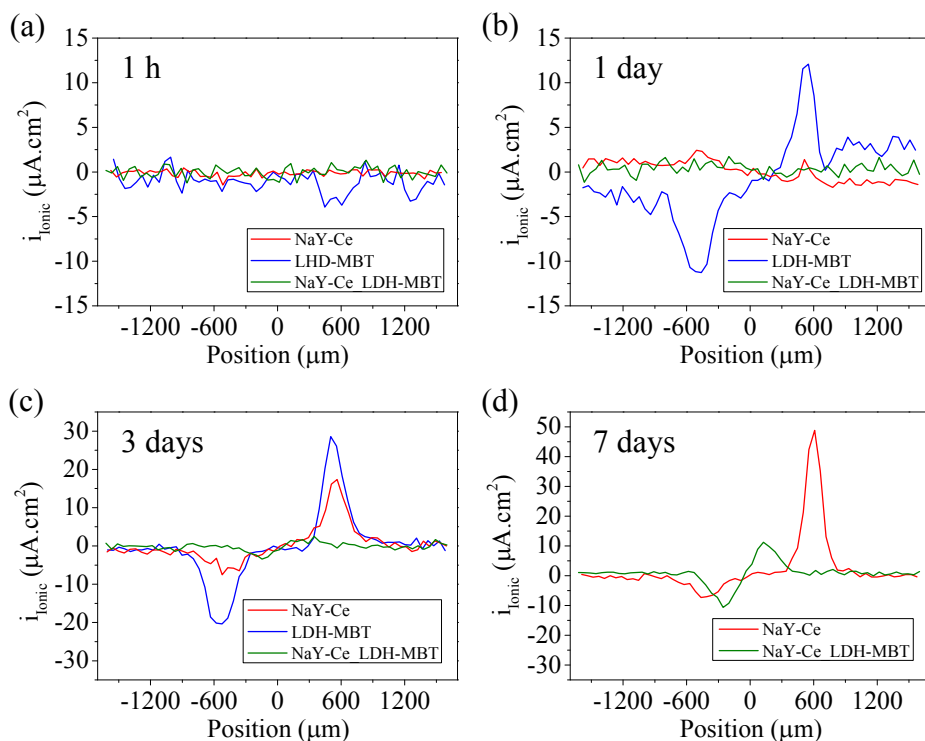
Figure 7.12. Ionic current density profiles of the extrinsic healing corrosion protective epoxy coatings after 1 h (a), 1 day (b), 3 days (c) and 7 days (d) exposure to 0.05 M NaCl, respectively.

The differences in the extent of the active protection provided by loading the inhibitor doped containers in epoxy coatings was further investigated by performing line scans over the artificial defects using SVET. The ionic current density (i_{Ionic}) profiles of the tested coating systems are shown in Figure 7.12.

As Figure 7.12 a shows, at the early stages of the measurement (1 h immersion) no electrochemical activity was detected over the defects of the coating systems. Upon 1 day exposure the coating loaded with LDH-MBT (Figure 7.12 b) exhibited anodic (i_{anodic} = 12 $\mu A.cm^2$) and cathodic ($i_{cathodic}$ = -11.3 $\mu A.cm^2$) activities attributed respectively to dissolution of Al and Mg as a result of corrosion of the intermetallics and the surrounding matrix and reduction of oxygen on copper rich regions [ref]. After 3 days, the corrosion processes were established in NaY-Ce loaded system (i_{anodic} = 17.35 $\mu A.cm^2$) and further

evolved in LDH-MBT containing one (i_{anodic} = 28.5 $\mu A.cm^2$), yet the defects in the coating containing the combined inhibitor doped containers remained passive. Although corrosion of the defects in the later coating system started after 7 days of exposure to the electrolyte, both anodic and cathodic current densities were much lower than those of NaY-Ce loaded coating. Formation of a blister due to reduction of oxygen in the cathodic defect of LDH-MBT loaded coating interrupted the line scan at the same height (100 μm above the sample surface) as the rest of the coatings. The results presented in Figures 7.11 and 7.12 reveal the improved performance of the combined inhibitor doped containers in supressing corrosion of coated AA2024-T3 panels at the defect site, further confirming the synergy between the employed inhibitors.

Optimization of NaY-Ce to LDH-MBT ratio

To find the optimum ratio of the inhibitor doped containers, a range of water-based epoxy coatings containing different weight ratios of NaY-Ce:LDH-MBT (90:10, 75:25, 50:50 and 25:75) were prepared and tested using EIS. The active protection of the AA2024-T3 panels by the coating systems was evaluated by creating an artificial damage in the form of a 3 mm long scratch in the coatings prior to exposure to the electrolyte and fitting the EIS data by a three-time constant equivalent circuit. The EIS spectra and the evolution of oxide (R_{oxide}) and charge transfer ($R_{ct.}$) resistances of the tested coating systems are presented in Figure 7.13. As Figure 7.13 shows, the coating containing NaY-Ce + LDH-MBT with weight ratio of 25:75 exhibited the lowest Bode modulus (|Z|) in tested frequency range over the course of the measurement (Figures 7.13 a and b). The rest of the coating systems showed equivalent high frequency |Z| indicating similar coating responses, while the low frequency |Z| of them were slightly different with the one containing NaY-Ce + LDH-MBT with weight ratio of 90:10 exhibiting the highest values.

The R_{oxide} (Figure 7.13 c) of the coating systems showed a gradual increase over time due to release of the doped inhibitors, reinforcing of the protective oxide layer. The increased resistance of the oxide layer can lower the corrosion rate of epoxy coated AA2024-T3 panels. The reduced corrosion rate of the tested systems was reflected by the gradual increase in their $R_{ct.}$ (Figure 7.13 d). Among the tested coating systems the ones containing NaY-Ce + LDH-MBT with weight ratio of 25:75 and 90:10 exhibited the lowest and highest R_{oxide} and $R_{ct.}$, respectively. This observation might be attributed to the fine balance of between two competing phenomena i.e. release of the MBT from

LDH-MBT and formation the protective cerium hydroxide/oxide layer on the cathodic sites of AA2024-T3 activated by hydroxide groups.

Additionally, based on the results presented in release kinetics section, the maximum content of inhibitor leached out of the NaY-Ce and LDH-MBT containers corresponds to 0.65 ± 0.5 mM Ce^{3+} and 5.5 ± 0.5 mM MBT, respectively. Therefore, the released inhibitor molar ratio in the coating containing NaY-Ce + LDH-MBT in weight ratio of 90:10 might correspond to 1:1 (Ce^{3+}:MBT molar ratio). The aforementioned molar ratio of the two inhibitors exhibited the highest low frequency |Z| in the solution based tests even at the early stages of the measurement (Figure 7.4). Hence the highest R_{Oxide} and $R_{ct.}$ of the coating system containing 90:10 weight ratio of NaY-Ce + LDH-MBT is in agreement with the solution based tests.
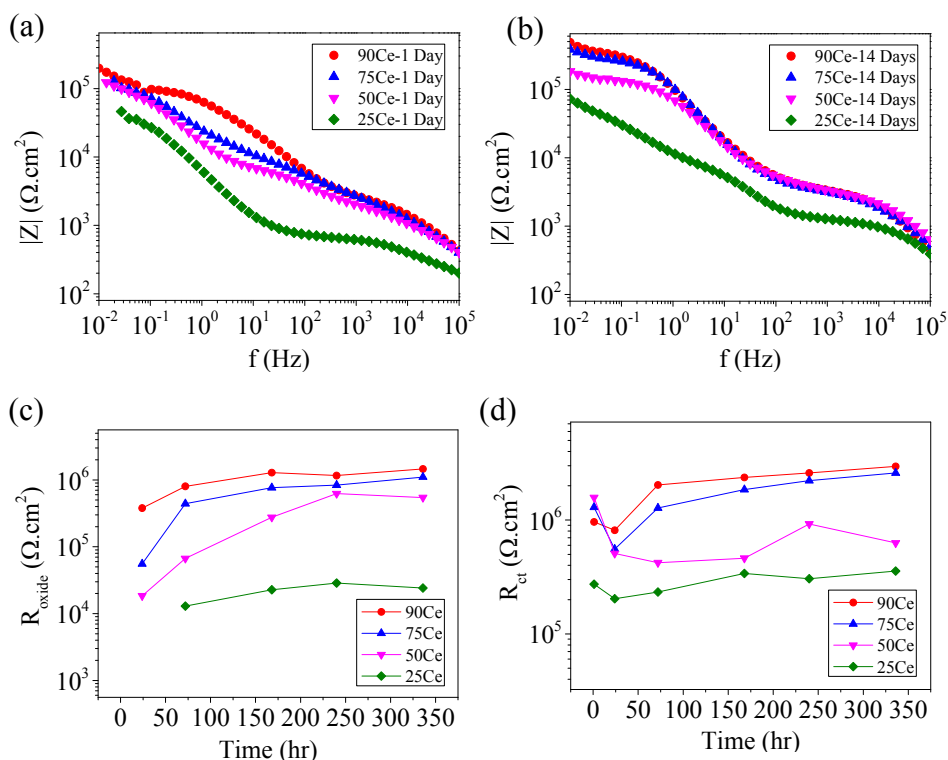

Figure 7.13. The EIS spectra of the epoxy coatings containing different ratios of NaY-Ce:LDH-MBT after 1 day (a) and 14 days (b) and the evolution of R_{oxide} (c) and $R_{ct.}$ (d) of the coating systems in 0.05 M NaCl. (90Ce, 75Ce, 50Ce and 25Ce represent NaY-Ce:LDH-MBT ratios of 90:10, 75:25, 50:50 and 25:75, respectively).

Conclusions

In this chapter, the preparation and characterization of the inhibitor loaded NaY zeolite and LDH containers are described. Ce^{3+} and MBT were successfully loaded in NaY zeolite and LDH containers, yielding NaY-Ce and LDH-MBT with Ce^{3+} and MBT weight percentages of 11% and 10%, respectively. The inhibitor doped containers exhibited stimuli-triggered release phenomenon. An increase in the concentration of the ions (Na^+ and Cl^-) in the test solution promoted the release of the inhibitors via ion-exchange process. The release of Ce^{3+} and MBT from NaY-Ce and LDH-MBT were boosted at low and high pH values, respectively. The combination of the two employed inhibitors presented a constructive effect in the active protection of AA2024-T3 panels with 1:1 being the optimum Ce^{3+}:MBT molar ratio. Incorporation of the single inhibitor doped containers in hybrid sol-gel and water-based epoxy coating provided active protection for the coated AA2024-T3 substrates. Yet, the combination of the inhibitor doped containers in the aforementioned coatings led to an improvement in the active protection of the substrate, confirming the synergy between the two inhibitor doped containers. The active protection offered by the combination of the two inhibitor doped containers was affected by the weight ratio of the NaY-Ce to LDH-MBT with 90:10 being the optimum ratio.

References

[1] G.W. Walter, A critical review of the protection of metals by paints, Corrosion Science, 26 (1986) 27-38.

[2] R.T.M. van Benthem, W. Ming, G. de With, Self Healing Polymer Coatings, in: S. van der Zwaag (Ed.) Self Healing Materials, Springer Netherlands2007, pp. 139-159.

[3] M.L. Zheludkevich, Self-healing Anti-Corrosion Coatings in: S.K. Ghosh (Ed.) Self-Healing Materials: Fundamentals, Design Strategies, and Applications Wiley-VCH2009.

[4] A.E. Hughes, I.S. Cole, T.H. Muster, R.J. Varley, Designing green, self-healing coatings for metal protection, NPG Asia Mater, 2 (2010) 143-151.

[5] S.J. García, H.R. Fischer, S. van der Zwaag, A critical appraisal of the potential of self healing polymeric coatings, Progress in Organic Coatings, 72 (2011) 211-221.

[6] D.G. Shchukin, D. Borisova, H. Möhwald, Self-Healing Coatings, Self-Healing Polymers, Wiley-VCH Verlag GmbH & Co. KGaA2013, pp. 381-399.

[7] K.A. Yasakau, M.L. Zheludkevich, S.V. Lamaka, M.G. Ferreira, Mechanism of corrosion inhibition of AA2024 by rare-earth compounds, The Journal of Physical Chemistry B, 110 (2006) 5515-5528.

[8] S.J. García, J.M.C. Mol, T.H. Muster, A.E. Hughes, T.M.J. Mardel, H.T.T. Markely, J.H.W. de Wit, Advances in the selection and use of rare-earth based inhibitors for selfhealing organic coatings, Self-Healing Properties of New Surface Treatments, European Federation of Corrosion Series, Maney Publishing, UK, 2011, pp. 148–183.

[9] N. Birbilis, R. Buchheit, D. Ho, M. Forsyth, Inhibition of AA2024-T3 on a phase-by-phase basis using an environmentally benign inhibitor, cerium dibutyl phosphate, Electrochemical and solid-state letters, 8 (2005) C180-C183.

[10] T.A. Markley, M. Forsyth, A.E. Hughes, Corrosion protection of AA2024-T3 using rare earth diphenyl phosphates, Electrochimica acta, 52 (2007) 4024-4031.

[11] M. Forsyth, M. Seter, B. Hinton, G. Deacon, P. Junk, New'green'corrosion inhibitors based on rare earth compounds, Australian Journal of Chemistry, 64 (2011) 812-819.

[12] S. Garcia, T. Markley, J. Mol, A. Hughes, Unravelling the corrosion inhibition mechanisms of bi-functional inhibitors by EIS and SEM–EDS, Corrosion Science, 69 (2013) 346-358.

[13] M. Zheludkevich, Self-Healing Anticorrosion Coatings, Self-Healing Materials, Wiley-VCH Verlag GmbH & Co. KGaA2009, pp. 101-139.

[14] M. Abdolah Zadeh, S. Van Der Zwaag, S. Garcia, Routes to extrinsic and intrinsic self-healing corrosion protective sol-gel coatings: a review, Self-Healing Materials, 1 (2013) 1-18.

[15] M. Abdolah Zadeh, S. van der Zwaag, S.J. Garcia, Self-healing corrosion protective sol-gel coatings based on extrinsic and intrinsic healing approaches, Advances in Polymer Science, (2015).

[16] Zeolite Molecular Sieves: Structure, Chemistry, and Use D. W. Breck (Union Carbide Corporation, Tarrytown, New York) John Wiley and Sons, New York, London, Sydney, and Toronto. 1974. 771 pp. $11.95, Journal of Chromatographic Science, 13 (1975) 18A.

[17] R. Xu, W. Pang, J. Yu, Q. Huo, J. Chen, Structural Chemistry of Microporous Materials, Chemistry of Zeolites and Related Porous Materials, John Wiley & Sons, Ltd2010, pp. 19-116.

[18] C. Motte, M. Poelman, A. Roobroeck, M. Fedel, F. Deflorian, M.G. Olivier, Improvement of corrosion protection offered to galvanized steel by incorporation of lanthanide modified nanoclays in silane layer, Progress in Organic Coatings, 74 (2012) 326-333.

[19] S.A.S. Dias, A. Marques, S.V. Lamaka, A. Simões, T.C. Diamantino, M.G.S. Ferreira, The role of Ce(III)-enriched zeolites on the corrosion protection of AA2024-T3, Electrochimica Acta, 112 (2013) 549-556.

[20] S.A.S. Dias, S.V. Lamaka, C.A. Nogueira, T.C. Diamantino, M.G.S. Ferreira, Sol–gel coatings modified with zeolite fillers for active corrosion protection of AA2024 Corrosion Science, (2012) 153-162.

[21] S.A.S. Diasa, S.V. Lamakab, T.C. Diamantino, M.G.S. Ferreira, Synergistic Protection against Corrosion of AA2024-T3 by Sol-Gel Coating Modified with La and Mo-Enriched Zeolites, J. Electrochem. Soc. , 161 (2014) C215-C222.

[22] E.L. Ferrer, A.P. Rollon, H.D. Mendoza, U. Lafont, S.J. Garcia, Double-doped zeolites for corrosion protection of aluminium alloys, Microporous and Mesoporous Materials, 188 (2014) 8-15.

[23] R.G. Buchheit, H. Guan, S. Mahajanam, F. Wong, Active corrosion protection and corrosion sensing in chromate-free organic coatings, Progress in Organic Coatings, 47 (2003) 174-182.

[24] H. McMurray, G. Williams, Inhibition of filiform corrosion on organic-coated aluminum alloy by hydrotalcite-like anion-exchange pigments, Corrosion, 60 (2004) 219-228.

[25] G. Williams, H.N. McMurray, Inhibition of filiform corrosion on polymer coated AA2024-T3 by hydrotalcite-like pigments incorporating organic anions, Electrochemical and solid-state letters, 7 (2004) B13-B15.

[26] M. Kendig, M. Hon, A hydrotalcite-like pigment containing an organic anion corrosion inhibitor, Electrochemical and solid-state letters, 8 (2005) B10-B11.

[27] S. Poznyak, J. Tedim, L. Rodrigues, A. Salak, M. Zheludkevich, L. Dick, M. Ferreira, Novel inorganic host layered double hydroxides intercalated with guest organic inhibitors for anticorrosion applications, ACS applied materials & interfaces, 1 (2009) 2353-2362.

[28] J. Tedim, S. Poznyak, A. Kuznetsova, D. Raps, T. Hack, M. Zheludkevich, M. Ferreira, Enhancement of active corrosion protection via combination of inhibitor-loaded nanocontainers, ACS applied materials & interfaces, 2 (2010) 1528-1535.

[29] F. Li, X. Li, K. Ng, Photocatalytic degradation of an odorous pollutant: 2-mercaptobenzothiazole in aqueous suspension using Nd3+-TiO2 catalysts, Industrial & engineering chemistry research, 45 (2006) 1-7.

[30] P. Ruoff, A. Bjørnstad, M. Jakobsen, The complete UV–visible photoluminescence spectrum of aqueous Ce (III), Chemical physics letters, 291 (1998) 249-251.

[31] Ö. Özkanat, Molecular interfaces of coated aluminium, S.n., S.l, 2013.

[32] K. Yasakau, S. Kallip, M. Zheludkevich, M. Ferreira, Active corrosion protection of AA2024 by sol–gel coatings with cerium molybdate nanowires, Electrochimica Acta, 112 (2013) 236-246.

[33] A. Aldykiewicz, A. Davenport, H. Isaacs, Studies of the Formation of Cerium-Rich Protective Films Using X-Ray Absorption Near-Edge Spectroscopy and Rotating Disk Electrode Methods, Journal of the Electrochemical Society, 143 (1996) 147-154.

[34] V. Palanivel, Y. Huang, W.J. van Ooij, Effects of addition of corrosion inhibitors to silane films on the performance of AA2024-T3 in a 0.5 M NaCl solution, Progress in Organic Coatings, 53 (2005) 153-168.

[35] M. Ohsawa, W. Suëtaka, Spectro-electrochemical studies of the corrosion inhibition of copper by mercaptobenzothiazole, Corrosion Science, 19 (1979) 709-722.

[36] A.N. Khramov, N.N. Voevodin, V.N. Balbyshev, R.A. Mantz, Sol–gel-derived corrosion-protective coatings with controllable release of incorporated organic corrosion inhibitors, Thin Solid Films, 483 (2005) 191-196.

[37] G.-C. Han, Y. Peng, Y.-Q. Hao, Y.-N. Liu, F. Zhou, Spectrofluorimetric determination of total free thiols based on formation of complexes of Ce (III) with disulfide bonds, Analytica chimica acta, 659 (2010) 238-242.

[38] E.L. Ferrer, A.P. Rollon, H.D. Mendoza, U. Lafont, S.J. Garcia, Double-doped zeolites for corrosion protection of aluminium alloys, Microporous and Mesoporous Materials, 188 (2014) 8-15.

[39] P. Larkin, IR and Raman Spectra-Structure Correlations: Characteristic Group Frequencies, Infrared and Raman spectroscopy; principles and spectral interpretation, Elsevier2011.

[40] K. Fuwa, B. Valle, The Physical Basis of Analytical Atomic Absorption Spectrometry. The Pertinence of the Beer-Lambert Law, Analytical Chemistry, 35 (1963) 942-946.

[41] S.A. Hayes, P. Yu, T.J. O'Keefe, M.J. O'Keefe, J.O. Stoffer, The Phase Stability of Cerium Species in Aqueous Systems I. E-pH Diagram for the Ce HClO 4 H 2 O System, Journal of the Electrochemical Society, 149 (2002) C623-C630.

[42] F. Maia, J. Tedim, A.D. Lisenkov, A.N. Salak, M.L. Zheludkevich, M.G. Ferreira, Silica nanocontainers for active corrosion protection, Nanoscale, 4 (2012) 1287-1298.

[43] S. Kallip, A.C. Bastos, K.A. Yasakau, M.L. Zheludkevich, M.G. Ferreira, Synergistic corrosion inhibition on galvanically coupled metallic materials, Electrochemistry Communications, 20 (2012) 101-104.

[44] K. Aramaki, Effects of organic inhibitors on corrosion of zinc in an aerated 0.5 M NaCl solution, Corrosion science, 43 (2001) 1985-2000.

Summary

Self-healing corrosion protective sol-gel coatings

The main objective of this thesis was to explore novel routes to self-healing corrosion protective sol-gel coatings via intrinsic and extrinsic healing approaches. The adopted approaches extend the service life of the coating and the underlying substrate by multiple damage closure/sealing and metal surface protection through incorporation of reversible tetra-sulfide groups and inhibitor loaded containers, respectively.

In *Chapter 2*, synthesis and characterization of first generation of healable organic-inorganic hybrid (OIH) sol-gel polymers containing reversible tetra-sulfide groups is described. Organically modified silicone alkoxides (OMSAs) including Bis[3-(triethoxysilyl)propyl]tetrasulfide (BS) and (3-Aminopropyl)trimethoxysilane (APS) were successfully employed to incorporate reversible tetra-sulfide groups and covalent bridges into a crosslinked Epikote 828 based epoxy matrix, respectively. The composition and architecture of the healable OIH sol-gel polymers were tuned by varying the content of the reversible groups and the crosslinking density of either inorganic or organic networks. The thermo-reversible tetra-sulfide groups with an average dissociation energy of 36 kcal mol^{-1} provided adequate chain mobility in the crosslinked network upon mild thermo-mechanical stimulus, enabling macroscopic flow. The macroscopic flow and hence the healing performance were strongly affected by the content of reversible tetra-sulfide groups, crosslinking density and healing temperature. Complementing the macroscopic flow studies with mechanical evaluation of the OIH sol-gel polymers revealed the dominant role of the reversible tetra-sulfide groups on the healing performance of the developed healable OIH sol-gel polymers.

In *Chapter 3* the macroscopic flow kinetics of the OIH sol-gel polymer exhibiting the highest healing efficiency in chapter 2 was further evaluated under air and nitrogen flow. To get an insight into the mechanisms involved in the healing process the evolution of

different functional groups in particular the reversible sulfur-sulfur (S-S) bonds was monitored using a hot-stage coupled Raman spectrometer during the temperature-induced healing process. Based on the thermo-mechanical analysis of the OIH sol-gel polymer complemented with Raman spectroscopic studies, the healing mechanism is believed to be based on the increased mobility of the system, achieved by thermally triggered selective breaking of the reversible S-S bonds with ulterior bond restoration after the trigger is removed.

In contrast to the increased polymer flow rates with an increase in the healing temperature under nitrogen flow, the maximum flow kinetics were acquired at 70 °C when the tests were performed under air flow. Faster flow kinetics at 70 °C compared to 80 °C and 90 °C in air revealed presence of two sets of competing phenomena in the polymer during the thermally triggered healing process; i) cleavage of reversible tetra-sulfide groups as well as increased chain mobility providing the required mobility for the polymeric network and therefore favoring macroscopic flow, ii) thermally accelerated oxidation of thiol groups resulting in formation of new thermo-reversible crosslinks (S-S bonds) and hindering the polymer flow. Yet, as a result of thermo-reversible nature of the new crosslinks, despite the lower kinetics, full gap closure was achieved at temperatures higher than the optimum healing temperature in air.

Based on the results presented in chapter 3, an effect of aging condition on the properties of the developed OIH sol-gel polymer was foreseeable. In *Chapter 4*, the time-resolved behaviour of the OIH sol-gel polymer containing thermo-reversible tetra-sulfide groups and the related deep impact on mechanical, viscoelastic and healing properties are presented. A hyphenated experimental procedure combining rheology and FTIR spectroscopy revealed an increase in the crosslinking density of the OIH sol-gel polymer during the thermally accelerated aging process due to formation of Si-O-Si bridges. The increased crosslinking density yielded a higher flow activation energy (E_a, extracted from the G' and G" master curves) lowering the macroscopic flow kinetics and hence postponing the onset of the healing processes in the aged polymer compared to the fresh (not aged) one. Yet the chemical species involved in the healing (i.e. the S-S and S-H groups) were not significantly affected by aging process, yielding an equivalent degree of interfacial healing based on the employed fracture mechanics based protocol (using DENT specimens) for the fresh and aged hybrid sol-gel polymer due to the availability of reversible groups at the fracture surface.

In *Chapter 5* application of the OIH sol-gel polymer as a protective coating for AA2024-T3 substrate is described. The prepared coating exhibited a hydrophobic surface with a static water contact angle of 94 °, strong adhesion to the AA2024-T3 panels demonstrated by mixed cohesive-adhesive failure mode of the specimens in the single lap shear test and an effective corrosion protection in 0.5 M NaCl solution illustrated by stable and high coating resistance values. Upon thermal treatment, the healable OIH sol-gel coating demonstrated 100% superficial healing efficiency, full adhesion recovery and complete restoration of its barrier properties. Although the long sealing performance of the coating was influenced by scratch geometry, the healed coating maintained same protective properties (illustrated by EIS spectra) as the intact coating for one year exposure to the aggressive electrolyte, as long as the scratch width to coating thickness ratio (w/t) was smaller than one.

In *Chapter 6* application of the AC/DC/AC procedure as a fast electrochemical technique for evaluation of the OIH sol-gel coating's durability and the healing extent of scratch induced interface is described. Local delamination processes governed by pore opening and cathodic reactions facilitated rapid assessment of the coating durability and sealing efficiency in less than 24 h using AC/DC/AC procedure compared to the conventional EIS measurement requiring more than one month. Full sealing of the scratch induced interface was achieved by annealing the scribed coatings at 70 °C independent of the healing time, as long as the healing time was longer than 2 h. Complementing the electrochemical evaluation (i.e. the EIS and AC/DC/AC) of the healed hybrid sol-gel coatings with optical and scanning electron microscopy disclosed their testing technique dependent failure modes. As a result of non-destructive nature of the EIS procedure, the healed interface preserved its integrity upon the measurement. Yet, the applied electrochemical stress in the form of cathodic polarization promoted evolution of ions, gaseous species and corrosion products on the metallic substrate during the AC/DC/AC procedure, facilitating coating failure at its weakest point i.e. the healed interface, giving an estimation of the extent of scratch healing in OIH sol-gel coatings.

In *Chapter 7*, development of extrinsic healing corrosion protective coatings containing combination of Ce^{3+} as inorganic and 2-Mercaptobenzothiazole (MBT) as organic inhibitor is described. To reduce the potential chemical/physical interactions of the corrosion inhibitors with the coating matrix, Ce^{3+} and MBT were successfully loaded in NaY zeolite and Zn-Al layered double hydroxide (LDH) containers via cation and anion

exchange processes, respectively, as confirmed by FTIR and EDS. Monitoring the inhibitor release profiles of the micro-/nano-containers as a function of NaCl concentration and solution pH validated stimuli-triggered release process, limiting the inhibitor leach out events to the corrosion processes involving release of ions and pH changes. The combination of the two employed inhibitors presented a constructive effect in the active protection of AA2024-T3 panels with 1:1 being the optimum Ce^{3+}:MBT molar ratio.

Incorporation of the single inhibitor doped containers in hybrid sol-gel and water-based epoxy coating provided active protection for the coated AA2024-T3 substrates. Yet, the combination of the inhibitor doped containers in the aforementioned coatings led to an improvement in the active protection of the substrate, confirming the synergy between the two inhibitor doped containers. The active protection offered by the combination of the two inhibitor doped containers was affected by the weight ratio of the NaY-Ce to LDH-MBT with 90:10 being the optimum ratio.

Samenvatting

Zelf-herstellende corrosie werende sol-gel coatings

Het doel van het onderzoek zoals beschreven in dit proefschrift was om zelfherstellende corrosie-werende sol-gel coatings te ontwikkelen. Het zelf-herstellende vermogen verlengt de levensduur van de coating en het onderliggende substraat doordat krassen in de coating in staat zijn zich meerdere keren te sluiten en daarmee het substraat beschermen. De nieuwe zelf-herstellende coatings zijn gebaseerd op intrinsieke en extrinsieke concepten en maken gebruik van tetra-sulfide groepen respectievelijk van microcontainers gevuld met inhibitoren.

Hoofdstuk 2 beschrijft de synthese en karakterisering van de eerste generatie zelf-herstellende organisch-anorganische hybride (OIH) sol-gel polymeren met daarin reversibele tetra-sulfide groepen. Gemodificeerde organo- siliconen-alkoxides (OMSAs) op basis van Bis[3-(triethoxysilyl)-propyl]tetrasulfide (BS) en (3-Aminopropyl)trimethoxysilane (APS) werden gebruikt om reversibele tetra-sulfide groepen en irreversibele covalente bindingen in te bouwen in een gecrosslinkte, op Epikote 828-gebaseerde epoxy matrix. De samenstelling van de zelf-herstellende coatings werd geoptimaliseerd door het gehalte aan reversibele groepen en de crosslink-dichtheid van het organische of het anorganische netwerk te variëren. De thermo-reversibele tetra-sulfide groepen, met een typische dissociatie-energie van 36 kcal mol^{-1}, gaven het netwerk voldoende moleculaire mobiliteit om de coatings bij lichte temperatuursverhoging enigszins te laten vloeien. Het macroscopische vloeigedrag en daarmee het zelf-herstellende vermogen bleek een sterke functie van het gehalte aan tetra-sulfide groepen, de crosslinkdichtheid en de temperatuur. De aanvullende mechanische karakterisering van de gesynthetiseerde materialen bevestigde nogmaals de belangrijke rol van de reversibele tetra-sulfide groepen in het herstellend vermogen.

In hoofdstuk 3 wordt de kinetiek van het macroscopische vloeigedrag van het OIH sol-gel polymeer uit hoofdstuk 2 met het beste zelf-herstellende vermogen in zowel lucht als

in een stikstof atmosfeer nader bestudeerd. Om meer inzicht in het moleculaire mechanisme en de rol van de verschillende chemische bindingen te verkrijgen, werd de temperatuursafhankelijkheid van de diverse chemische bindingen en in het bijzonder die behorende bij reversibele S-S binding, gemeten in een Raman spectrometer. Op basis van de thermomechanische analyse en de Raman spectra werd geconcludeerd dat het herstellende vermogen het gevolg is van de toegenomen beweeglijkheid van het netwerk als gevolg van het verbreken van de reversibele S-S bindingen die zich overigens na verwijdering van de thermische stimulus gewoon weer opnieuw vormen.

Bij verhitting in lucht vertoonde de sol-gel coating een maximale herstelsnelheid bij 70 ^{0}C, terwijl in het geval van verhitting in een stikstof milieu de beweeglijkheid nog verder toenam bij verdere temperatuursverhoging. Het maximum in snelheid van herstel in lucht bij 70 ^{0}C toont aan dat er tenminste twee reacties optreden: i) een toename in de beweeglijkheid van het netwerk door een verhoogde splitsingsgraad van de S-S bindingen bij hogere temperaturen en ii) een versnelde oxidatie van de thiol-groepen leidend tot de vorming van nieuwe bindingen en een verlaagde moleculaire mobiliteit. Omdat het thermo-reversibele karakter van de sol-gel coating behouden bleef, bleken krassen in de coating ook boven de optimale hersteltemperatuur goed dicht te vloeien, zij het met een lagere snelheid.

Op basis van de resultaten van hoofdstuk 3 was te voorzien dat de eigenschappen van de nieuw ontwikkelde OIH sol-gel coatings tijdsafhankelijk zouden zijn en dat de coatings dus een verouderingsgedrag zouden vertonen. Daarom is in hoofdstuk 4 onderzoek gedaan naar het tijdsafhankelijke gedrag van de tetra-sulfide bevattende sol-gel coatings. Speciale aandacht werd besteed aan het mechanisch en visco-elastisch gedrag alsmede aan het zelfherstellende vermogen. Door reologische waarnemingen te koppelen aan FTIR spectra werd duidelijk dat het thermische verouderingsgedrag het gevolg is van de vorming van Si-O-Si bindingen. De hogere crosslink dichtheid resulteerde in een hogere activeringsenergie voor vloei (E_a) waardoor het herstelproces in verouderde samples vertraagd werd ten opzichte van niet-verouderd materiaal. Ondanks de veroudering bleven de S-S en de S-H bindingen actief en werd een vergelijkbare mate van herstel gemeten tijdens breuk-mechanische testen aan verouderde en niet-verouderde DENT proefstukken. Het behoud van het zelf-herstellend vermogen werd toegeschreven aan een behoud van voldoende reversibele chemische bindingen aan het breukoppervlak.

In hoofdstuk 5 wordt het onderzoek aan beschermende coatings op basis van het OIH sol-gel polymeer beschreven. De geproduceerde coatings vertoonden een hydrofoob gedrag en een statische contact hoek van 94^0 voor water. De coatings hadden ook een goede hechting aan aluminium AA2024-T3 panelen hetgeen bleek uit het cohesieve-adhesieve karakter van het breukoppervlak van gebroken 'single lap' proefstukken. De coatings gaven ook een uitstekende corrosiebescherming in een waterig 0.5 M NaCl milieu hetgeen bleek uit de hoge elektrochemische weerstandswaarden. De OIH sol-gel coatings vertoonden volledig herstel van krassen in het oppervlak, hechting aan en elektrochemische bescherming van het substraat. Hoewel het lange-duurgedrag van de coating beïnvloed werd door de grootte van de aangebrachte krassen, bleef de corrosiewerende werking van de herstelde coating in dit agressieve milieu gedurende meer dan een jaar behouden. Dit gold alleen als de breedte van de kras tot op het substraat kleiner was dan de dikte van de coating.

In hoofdstuk 6 wordt het gebruik van de AC/DC/AC testmethode als versnelde test van de duurzaamheid en het herstellend vermogen van de OIH sol-gel coatings beschreven. De opgelegde AC/DC/AC condities leidden tot lokale onthechting als gevolg van het open gaan van poriën en het optreden van cathodische reacties op het grensvlak. In de 24 uur van een AC/DC/AC test kon het gedrag van een coating die meer dan een maand in een conventionele EIS test belast werd, goed nagebootst worden. Krassen in de coating werden volledig hersteld bij een temperatuur van 70 ^{0}C en een tijd van 2 uur of langer. Aanvullende optische en raster-elektronische waarnemingen lieten zien dat de EIS test geen aanvullende schade aan de coating toebracht. Ze lieten ook zien dat de cathodische polarisatie van het oppervlak tijdens de AC/DC/AC test aanleiding gaf tot de ontwikkeling van ionen, gassen en lokale corrosieproducten, vooral ter plaatse van de herstelde scheur.

Hoofdstuk 7 beschrijft het onderzoek aan de ontwikkeling van extrinsiek zelf-herstellende corrosiewerende coatings die zowel anorganische Ce^{3+} als organische 2-Mercaptobenzothiazole (MBT) inhibitoren bevatten. De Ce^{3+} en de MBT werden door middel van cation en anion uitwisselingsreacties ingebracht in NaY zeolieten en hydroxide containers met een gelaagde Zn-Al struktuur. FTIR en EDS werden gebruikt om het optreden van deze reacties te bevestigen. Metingen aan het release-gedrag van de micro- /nanocontainers als functie van het NaCl gehalte en de pH liet het gewenste schade-geïnitieerde gedrag zien, waarbij de inhibitoren pas vrijkwamen als de pH

veranderde als gevolg van het optreden van een corrosiereactie. De combinatie van twee afzonderlijke inhibitoren had een positief synergistisch effect op de corrosiebescherming van AA2014-T3 panelen. De beste resultaten werden verkregen bij een 1:1 (molaire)verhouding van Ce^{3+} en MBT. Ook het inbouwen van micro-containers met slechts een enkele inhibitor in zowel hybride sol-gel coatings als water-gedragen epoxy coatings gaf een actieve bescherming van het AA2024-T3 substraat. Duidelijk betere resultaten werden echter verkregen door beide inhibitoren te combineren. De beste resultaten werden verkregen bij een (massa)verhouding van (NaY-Ce):(LDH-MBT) van 90:10.

Acknowledgement

Notwithstanding the challenging nature of the Ph.D., working on Self-healing Sol-Gel coatings in NovAM group has been a great pleasure for the most part. Not only because of the interesting research topic, but also because of all the inspiring people I have met during this journey. They have contributed to this work in many different ways, and I sincerely want to thank them for that. I would like to mention some of them In particular.

I would like to thank my promoter, Prof. dr. ir. Sybrand van der Zwaag for his wisdom, support, excellent research guidance and commitment to the highest standards. I owe him gratitude for taking the time to discuss ideas and results no matter the time of day. Sybrand, I learned a lot from you about scientific writing, presenting and collaborating with other people. I want to thank my supervisor Dr. Santiago J. Garcia Espallargas for his guidance, Insightful comments and feedback towards my research. I learned a lot from his critical questions and comments. He taught me many things and provided opportunities for me to grow during varying stages of my career. Sybrand and Santiago, without your guidance my research and ultimately the dissertation would not have been possible. Thank you!

During my Ph.D. research I also had the opportunity to collaborate with many people in different groups. I would like to thank Charles de Boer from Kalvi Nanolab at Applied Science Faculty of TU Delft for the initial Raman measurements on my polymers. These measurements provided us with better understanding of temperature triggered phenomenon in the polymer and initiated a deeper research on the underlying mechanism.

Dr. A.C.C. Esteves and Prof. Jos Laven at the Eindhoven University of Technology, thank you for allowing us to use the facilities in SMG group. Your help and support in setting-up hot-stage coupled Raman spectrometer for characterization the OIH polymers is highly appreciated. I would like to mention Hesam, and Koen for their support and the fun discussions over the coffee breaks.

I express my gratitude to Dr. Mikhail Zheludkevich for giving me the opportunity to spent 3 months at CICECO labs in at University of Aviero. In particular, I would like to thank Dr. Alexandre Bastos. His deep knowledge on local electrochemical techniques has been invaluable in understanding complex electrochemical processes in extrinsic healing corrosion protective coatings. I want to mention Dr. J. Tedim, Dr. M. Maia and J. Caneiro for their help and support in the lab.

Curriculum Vitae

Mina Abdolah Zadeh was born on the 2nd of July 1983 in Macoo, Iran. Her academic studies started in 2001 at Petroleum University of Technology (PUT) where she received "National Iranian Oil Company" (NIOC) scholarship to pursue her undergraduate studies. Focusing on ultrasonic testing as a non-destructive testing technique, she obtained her B.Sc. in Technical Inspection and Safety Engineering.

After completion of B.Sc. in 2005, she started her M.Sc. at Sahand University of Technology (SUT), where she developed electrochemical routes for preparation of highly ordered nano-porous aluminum oxide as template for magnetic nanowires. In 2008, she received her M.Sc. in Material Science and Engineering (*cum laude*) with specialization in Nanotechnology.

Subsequent to graduation from SUT, she started to work as a junior research engineer at Research Institute of Petroleum Industry (RIPI) where she was involved in/responsible for nano-technology oriented research projects such as "Corrosion Protective Nano-Coatings".

In April 2011, she started her Ph.D. project at the Novel Aerospace Materials Group, Faculty of Aerospace Engineering at the Delft University of Technology under the supervision of Prof. dr. ir. van der Zwaag and Dr. Garcia. The results of her Ph.D. research on the "*Self-Healing Corrosion Protective Sol-Gel Coatings*" are presented in this thesis.

Since September 2015 Mina is employed as a R&D Scientist in AkzoNobel focusing on material science in the Scientific Support Group of AkzoNobel at Sassenheim.

List of Publications

Journal Papers

1. **M. Abdolah Zadeh**, N. Parvini-Ahmadi, M. Aliofkhazraei "Study of Nanopores Ordering in Anodic Aluminum Oxide Templates Achieved by Three Step Process", J. Nanosci. Nanotechnol. 10, 4743-4746 (2010).

2. **M. Abdolah Zadeh**, S. van der Zwaag, S.J. Garcia "Routes to extrinsic and intrinsic self-healing corrosion protective sol-gel coatings: a review", J. Smart & Stimuli Responsive Materials, 1, 1-18 (2013).

3. **M. Abdolah Zadeh**, A.C.C. Esteves, S. van der Zwaag, S.J. Garcia, "Healable dual organic–inorganic crosslinked sol–gel based polymers: Crosslinking density and tetrasulfide content effect", J. Polym. Sci., Part A: Polym. Chem., 52 (14), 1953-1961(2014).

4. **M. Abdolah Zadeh**, S. van der Zwaag, and S.J. Garcia, "Corrosion protective sol-gel coatings containing reversible tetra-sulphide groups showing intrinsic healing behavior", in Self-Healing Materials - Pioneering Research in the Netherlands, S. Van der Zwaag and E. Brinkman, Editors. 2015, Delft University Press: Delft, The Netherlands.

5. **M. Abdolah Zadeh**, S. van der Zwaag, S.J. Garcia, "Self-healing corrosion protective sol-gel coatings based on extrinsic and intrinsic healing approaches", J. Adv. Polym. Sci. (2015).

6. **M. Abdolah Zadeh**, S. van der Zwaag, S.J. Garcia "Assessment of healed scratches in intrinsic healing coatings by AC/DC/AC accelerated electrochemical procedure", Surf. Coat. Technol. (2015).

7. **M. Abdolah Zadeh**, S. van der Zwaag, S.J. Garcia "Adhesion and long-term barrier restoration of intrinsic self-healing hybrid sol-gel coatings containing tetrasulfide groups", submitted to ACS Appl. Mater. Interfaces.

8. **M. Abdolah Zadeh**, A. Grande, S. van der Zwaag, S.J. Garcia "Time resolved evaluation of healable dual organic-inorganic sol-gel based polymers", submitted to Polym. Chem..

9. **M. Abdolah Zadeh**, A. Grande, S. van der Zwaag, S.J. Garcia "Synergetic corrosion protection by combination of inhibitor doped zeolite and LDH nanocarriers", to be submitted to RSC Adv..

Selected Conference Papers

1. **M. Abdolah Zadeh**, F. Nasirpouri, N. Parvini Ahmadi and M. Javan Almasi, "A comparison between self- ordering of nanopores in anodic aluminum oxide templates achieved by two and three step anodic oxidation ", NanoKorea2007, Seoul, Korea.

2. **M. Abdolah Zadeh** , N. Parvini-Ahmadi, M. Aliofkhazraei "Study of Nanopores Ordering in Anodic Aluminum Oxide Templates Achieved by Three Step Process", ThinFilms2008, July 13-16, Singapore.

3. **M. Abdolah Zadeh**, H. Bargozin, M.M. Ahadian, "Development of anti-corrosion coatings by efflorescence of Nanotechnology in Oil & Gas Industry- A review", Nace International Corrosion 2010, 14-18 March, San Antonio, Texas, USA.

4. **M. Abdolah Zadeh**, S. van der Zwaag, S.J. Garcia, "Corrosion Trigerred Self- healing Sol-Gel Coatings", Coating Science International 2012, 26-29 June, Noordwijk, The Netherlands.

5. **M. Abdolah Zadeh**, S. van der Zwaag, S.J. Garcia, " On the healing mechanism of sol-gel derived hybrid materials containing dynamic di-sulfide bonds", International Conference on Self-Healing Materials 2013, 16-20 June, Ghent, Belgium.

6. **M. Abdolah Zadeh**, A.C.C. Esteve, S. van der Zwaag, S.J. Garcia, "Self-healing sol-gel coatings based on dynamic disulfide bonds", Coating Science International 2013, 25-28 June, Noordwijk, The Netherlands.

7. **M. Abdolah Zadeh**, S. van der Zwaag, S.J. Garcia, "Synergetic corrosion protection by combination of inhibitor doped zeolite and LDH nanocarriers", Coating Science International 2014, 24-27 June, Noordwijk, The Netherlands.

8. **M. Abdolah Zadeh**, S. van der Zwaag, S.J. Garcia, "Towards more reliable sol-gel coatings by combination of extrinsic and intrinsic healing approaches", European Technical Coating Congress 2014, 3-5 September, Cologne, Germany.